



UNIVERSITY OF
BIRMINGHAM

**AN INVESTIGATION INTO COORDINATE MEASURING MACHINE TASK SPECIFIC
MEASUREMENT UNCERTAINTY AND AUTOMATED CONFORMANCE ASSESSMENT OF
AIRFOIL LEADING EDGE PROFILES**

By

HUGO MANUAEL PINTO LOBATO

A thesis submitted to the
**School of Metallurgy and Materials, College of Engineering and Physical Sciences,
The University of Birmingham**

For the degree of
**Engineering Doctorate in Engineered Materials for High Performance
Applications in Aerospace and Related Technologies**

Structural Materials Research Centre
School of Metallurgy and Materials
The University of Birmingham
Birmingham
UK
August 2011

UNIVERSITY OF
BIRMINGHAM

University of Birmingham Research Archive

e-theses repository

This unpublished thesis/dissertation is copyright of the author and/or third parties. The intellectual property rights of the author or third parties in respect of this work are as defined by The Copyright Designs and Patents Act 1988 or as modified by any successor legislation.

Any use made of information contained in this thesis/dissertation must be in accordance with that legislation and must be properly acknowledged. Further distribution or reproduction in any format is prohibited without the permission of the copyright holder.

Abstract

The growing demand for ever more greener aero engines has led to ever more challenging designs and higher quality products. An investigation into Coordinate Measuring Machine measurement uncertainty using physical measurements and virtual simulations revealed that there were several factors that can affect the measurement uncertainty of a specific task. Measurement uncertainty can be affected by temperature, form error and measurement strategy as well as Coordinate Measuring Machine specification. Furthermore the sensitivity of circular features size and position varied, when applying different substitute geometry algorithms was demonstrated. The Least Squares Circle algorithm was found to be more stable when compared with the Maximum Inscribed Circle and the Minimum Circumscribed Circle. In all experiments it was found that the standard deviation when applying Least Squares Circle was of smaller magnitude but similar trends when compared with Maximum Inscribed Circle and the Minimum Circumscribed Circle. A Virtual Coordinate Measuring Machine was evaluated by simulating physical measurement scenarios of different artefacts and different features. The results revealed good correlation between physical measurements uncertainty results and the virtual simulations.

A novel methodology for the automated assessment of leading edge airfoil profiles was developed by extracting the curvature of airfoil leading edge, and the method led to a patent where undesirable features such as flats or rapid changes in curvature could be identified and sentenced. A software package named Blade Inspect was developed in conjunction with Aachen (Fraunhofer) University for the automated assessment and integrated with a shop floor execution system in a pre-production facility. The software used a curvature tolerancing method to sentence the leading edge profiles which aimed at removing the subjectivity associated with the manual vision inspection method. Initial trials in the pre-production facility showed that the software could sentence 200 profiles in 5 minutes successfully. This resulted in a significant improvement over the current manual visual inspection method which required 3 hours to assess the same number of leading edge profiles.

Dedication

I would like to dedicate this thesis to my daughter Daniela and my close family who have supported me in different ways during the duration of the Engineering Doctorate programme.

Acknowledgements

This thesis has been prepared as a requirement of the Engineering Doctorate (Eng.Doc) in Engineered Materials for High Performance Applications in Aerospace and Related Technologies. The research was carried out from December 2005 to December 2009 at the University of Birmingham School of Metallurgy and Materials, College of Engineering and Physical Sciences and Rolls-Royce plc Department of Manufacturing Technology (Measurement Team) under the supervision of Prof. Paul Bowen and Prof. Paul Maropoulos (University of Bath, Department of Mechanical Engineering) and Nicholas Orchard (Rolls-Royce plc). The Eng.Doc programme was funded by the Engineering and Physical Sciences Research Council (EPSRC) and Rolls-Royce plc.

During the majority of the programme I was based at Rolls-Royce plc (Derby, ManTech, Measurement Team) where I was supervised by Nicholas Orchard (Rolls-Royce plc Company Measurement Specialist).

I would like to thank my supervisors for their valuable contribution and inspiration towards my research .A sincere thanks is directed to Nicholas Orchard who introduced me and mentored me in the world of dimensional metrology.

Others have also helped and inspired me to complete this work. I would like to thank Metrosage and its developers (Prof. Kim Summerhays, John Baldwin and Daniel Campbell) for their support and discussions on VCMM's and specifically the help they

provided with simulations in Pundit/CMM. Prof. Alistair Forbes from the National Physics Laboratory (NPL) also provided me with help in further understating of virtual CMMs.

Mr. Stephan Bichman and Mr. Guilherme Mallaman developed the software production version of the work presented in Chapter 4 .A sincere thanks to Mr. Guilherme Mallaman who was a desk colleague at Rolls-Royce plc during a portion of my second year. I am grateful to him for discussions on programming and the algorithms which lead to the success of the work presented. Finally I would like to thank Prof. Paul Maropoulos who jointly supervised my research. A particular thanks to Miss Zhang Xi (Maria) and Dr. Carlo Ferri at University of Bath who through several discussions helped me tailoring the work presented in Chapter 2.

Motivation

Over the last decade the aerospace manufacturing industry has seen the introduction of lean manufacturing and concepts such as “six sigma” in an industry where tolerances for parts with critical conforming features can be as low as 0.005mm. Industry drivers aimed at reducing greenhouse emissions require products with ever tighter tolerances. Step changes in the way such tolerances are checked have been necessary to ensure the final product is 100% conformant and provides the customer 100% protection.

Step changes within the aerospace manufacturing environment include the introduction of digital dimensional measurement systems. Systems such Coordinate Measuring Machines (CMM) offered flexibility to measure a range of parts due to its multiple set ups coupled with high accuracy and high repeatability. Like most inspection systems its capability is questioned at the later stages of introduction of a new product rather than at early stages of product design. The introduction of Product Lifecycle Management (PLM) has provided the opportunity to integrate inspection system capability data with early stages of design development via Computer Aided Inspection Planning (CAIP) tools. Expertise in aerospace industries including Rolls-Royce plc will be required to understand to what extent CAIP tools can generate/collect data from dimensional measurement inspection systems such as CMMs including expanded uncertainty statements. Furthermore a low number of CMMs in industry today output expanded uncertainty statements as part of the feature/part conformance process.

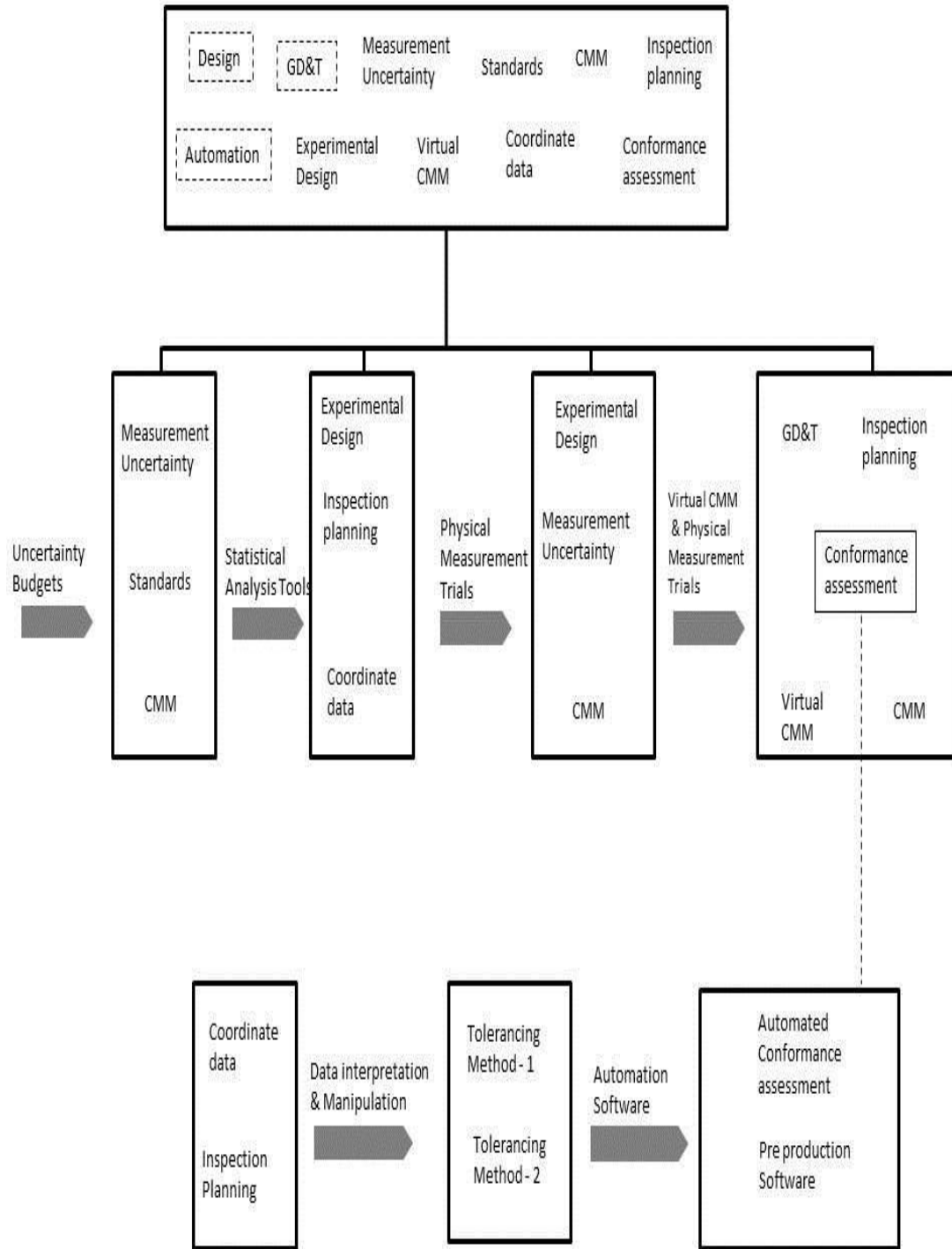
Aims and objectives

- The first aim of this research was to review available approaches for determining CMM task specific measurement uncertainty and evaluate key factors that could affect it using statistical analysis tools, physical measurements and a newly developed VCMM. To develop detailed knowledge of CMM systems , VCMMs and standards used to define their performance.
- The second aim of this work focused on the automation of a manual visual assessment task of leading edge profiles which feature on compressor blades of gas turbines engines. Removing the subjectivity associated with the use of current standards for leading edge assessment in an automated manner was required.

The two aims were split into the following six objectives:

- 1) To derive measurement uncertainty budgets for CMM using available standards.
- 2) To explore and integrate statistical analysis tools such as experimental design and Monte Carlo to aid the analysis of known fitting algorithms for circular features.
- 3) To investigate the impact of thermal effects during CMM measurements.
- 4) To perform comparative tests between physical CMM measurements of artefacts and real parts with a commercially available VCMM named Pundit/CMM.

- 5) To remove the subjectivity associated with the assessment of compressor blades leading edges via mathematical definition of a leading edge.
- 6) To automate the assessment of leading edge profiles in a production environment.



Outline of this thesis

Chapter 1 of this work reviews the state of the art literature in task specific measurement uncertainty of CMMs. Coordinate Metrology, Geometric Dimensioning and Tolerancing (GD&T) and Geometrical Product Specification (GPS) frameworks are reviewed in context of coordinate measurement systems. Previous work exploring the evaluation of CMM measurement uncertainty is reviewed; Physical measurement examples and estimations via virtual simulations are reviewed. An in depth review of Virtual CMMs describes the main concepts available today and key differences between such systems. The impact of measurement uncertainty is further reviewed in the context of conformance decisions.

Chapter 2 evaluates the application and comparison of two methods of estimating task specific measurement uncertainty using data from length bar measurements for coordinate measuring machines of different specifications. The two methods applied were the ISO-15530-3¹ and the Guide to the expression of uncertainty in measurement (GUM²). Standard uncertainties for both methods were derived and their impact on the expanded uncertainty calculation explained via uncertainty budgets. Although both methods could be used to aid point to point feature measurement, most geometrical features require a collection of points, therefore a different approach was required. A sensitivity study with integration of Design of Experiments (DOE) was proposed for circular features where it became difficult to apply the uncertainty budgets approach due

¹ ISO/TS 15530-3:2004 Geometrical Product Specifications (GPS) – Coordinate measuring machines (CMM): Technique for determining the uncertainty of measurement -- Part 3: Use of calibrated workpieces or standards, Geneva, 2004.

² ISO/IEC Guide 98:1995 Guide to the expression of uncertainty in measurement (GUM), Geneva, 1995.

to the factors being investigated. Firstly the impact of CMM specification and form error are evaluated when using different algorithms (Least Squares Circle, Maximum Inscribed Circle and Minimum Circumscribed Circle) to extract feature characteristics such as size, position and form. A Monte Carlo analysis was also integrated with a full factorial DOE to explore further how each of the algorithms used to extract the feature characteristics behave. The application of DOE was further explored by using a laboratory coordinate measuring machines to study the impact of the environment when measuring prismatic features on a calibrated artefact.

Chapter 3 describes the evaluation and application of a commercial (Pundit/CMM³) Virtual Coordinate Measuring Machine for the prediction of task specific measurement uncertainty. The first part of the chapter focused on comparison of length bars measurements obtained in chapter 2 with the recreated simulations in Pundit/CMM. Results obtained from chapters 2 and 3 indicated that there was a need to design and commission a multi feature artefact that could aid the investigation of task specific measurement uncertainty and also test the capabilities of Pundit/CMM. A multi feature artefact containing features with predefined form error was designed and commissioned at the Centre of Excellence in Customised Assembly (CECA, Nottingham). Finally a case study for the measurement of locating holes on a production part is presented. Estimations of measurement uncertainty are then compared for the different experiments to highlight possible discrepancies between the estimated magnitude values of expanded uncertainty among the different methods.

³ Volcano, CA, USA: Metrosage LLC. <<http://www.metrosage.com/punditcmm.html>>

Chapter 4 presents a novel way of assessing a free form feature in an automated manner. The free form feature studied was the leading edge of compressor blades. Such features are measured using coordinate measuring machines hence the final shape defined by the point coordinate data could contain some of the uncertainties previously mentioned in chapters 2 and 3. Methods for curve fitting and data smoothing are explored together with different quantities for expressing the quality of the leading edge profile. It was shown that the curvature change along the leading edge profile can be used to identify non desirable features such as flat regions or extremely sharp features. Sensitivity of the extracted curvature plots was investigated and two methods of sentencing the leading edge shape were developed. The first method focused on applying tolerance profiles to the curvature plot based on the nominal leading edge shape and a production standard (LESA 1) used during manual visual inspection of the profiles. The second method focused on parameterisation of the curvature plot by extracting some key features such maximum values of the peaks and valleys at fixed distances along the curvature plot. A pre production version of the software was developed in conjunction with Aachen University (Fraunhofer) and integrated in a production facility. Initial tests suggested that the software was capable of assessing 200 leading edge profiles in approximately 5 minutes. The manual visual inspection for the same number of leading edge profiles could last up to 3 hours. Furthermore the automated assessment results achieved showed very good conformance with quality requirements. A patent from this work was submitted including further applications in the analysis of free form features such as radius.

Nomenclature

$r(\theta)$ = Radius of a feature with symmetrical lobbing in polar coordinates

r_0 = Nominal radius

ρ = Magnitude of the feature radius roundness

$\omega\theta$ = Number of lobes

x = Cartesian workspace coordinate

y = Cartesian workspace coordinate

X = Cartesian coordinate with added random noise

Y = Cartesian coordinate with added random noise

γ, τ = Random noise generated from a normally distribution function

T_{ref} = Reference temperature

$\hat{\theta}_T$ = Measurand with

$\alpha_{T_{ref}}$ = Coefficient of thermal expansion

\hat{rmse} = Root square mean error

κ = Instantaneous curvature

K_{SMA} = Instantaneous curvature with moving average

m = Point to arc length convertor

C_{avg} = Specified distance along the arc length

XN = Normalised X axis

ϕ_i = Thickness/Arc length position

ϕ_{\max} = Maximum Thickness/Arc length position

ϖ_{up} = Skewed value pressure side

ϖ_{us} = Skewed value suction side

ψ_{xup} = Shift in X axis pressure side

ψ_{xus} = Shift in X axis suction side

δ_{up} = Curvature ratio pressure side

δ_{us} = Curvature ratio suction side

ψ_{yup} = Shift in Y axis pressure side

ψ_{yus} = Shift in Y axis suction side

ϖ_{lp} = Skewed value pressure side

ϖ_{ls} = Skewed value suction side

ψ_{xlp} = Shift in X axis pressure side

ψ_{xls} = Shift in X axis suction side

δ_{lp} = Curvature ratio pressure side

δ_{ls} = Curvature ratio suction side

ψ_{ylp} = Shift in Y axis pressure side

ψ_{yls} = Shift in Y axis suction side

λP_{ij} = Curvature Peaks

λV_{ij} = Curvature Valleys

$Area_{ij}$ = Area between curvature peaks and valleys

Abbreviations

ANSI	American National Standards Institute
ASME	American Society of Mechanical Engineers
CAIP	Computer-Aided Inspection Planning
CMM	Coordinate Measuring Machines
CMS	Coordinate Measuring Systems
CPD	Control Point Distance
CVNAL	Curvature Normalised by Arc Length
CVNTP	Curvature Normalised by Thickness Position
GD&T	Geometrical Dimensioning & Tolerancing
GPS	Geometrical product Specification
GUM	Guide to the expression of Uncertainty in Measurement
ISO	International Organization for Standardization
LESA	Leading edge standard assessment
LSC	Least Square Circle
MCC	Minimum Circumscribed Circle
MIC	Maximum Inscribed Circle
MPE	Maximum Permissible Error
NIST	National Institute for Standards and Technology
NPL	National Physics Laboratories
PLM	Product Lifecycle Management
PTB	Physikalisch-Technische Bundesanstalt
PUMA	Procedure for Uncertainty Management
VCMM	Virtual Coordinate Measuring Machine
VDI	Verein Deutscher Ingenieure
VIM	Vocabulary of Basic and General Terms in Metrology

Contents Listing

Chapter 1	Literature and state of the art review	1-1
1.1	Coordinate metrology and GPS framework.....	1-9
1.2	Measurement Uncertainty definition	1-12
1.3	Uncertainty in coordinate measurement	1-16
1.4	CMM based uncertainty assessment.....	1-32
1.4	Virtual coordinate measuring machines uncertainty estimation.....	1-35
1.5	Conformance decisions.....	1-46
1.6	Measurement uncertainty impact in airfoil leading edge conformance assessment	1-49
Chapter 2	ANOVA estimation of measurement uncertainty in CMM measurements	2-1
2.1	Comparison of two uncertainty methods during artefacts measurements	2-1
2.1.1	The GUM approach	2-1
2.1.2	ISO 15530-3.....	2-6
2.1.3	Impact of measurement uncertainty in conformance assessment	2-12
2.2	Sensitivity screening study of circular features with symmetrical lobbing	2-15
2.2.1	Monte Carlo simulation definitions	2-15
2.2.2	Three Lobe feature screening experiment results	2-18
2.2.3	Five Lobe feature screening experiment results	2-24
2.2.4	Descriptive statistics	2-28
2.3	Sensitivity study via Monte Carlo simulation integration with full factorial experimental design	2-33
2.3.1	Monte Carlo simulation integration with experimental design.....	2-33
2.3.2	Feature Size experimental design results.....	2-36
2.3.3	Feature centre coordinates experimental design results.....	2-48
2.4	Assessing the environmental impact.....	2-55
2.4.1	Experimental design set-up.....	2-55

2.4.2 Output responses	2-60
2.5 Summary	2-66
Chapter 3 Virtual estimations of task specific measurement uncertainty.....	3-1
3.1 Estimating uncertainty of length measurements with Virtual CMM.....	3-1
3.2 Manufacture and inter comparison measurements of a multi feature artefact.....	3-6
3.3 Experimental design.....	3-10
3.3 Physical measurements results.....	3-12
3.3.1 Machine M Physical measurement results - Size	3-14
3.3.2 Machine C Physical measurement results - Size	3-16
3.3.3 Machine W Physical measurement results - Size	3-19
3.3.4 Features Position results (M, C, W).....	3-22
3.4 VCMM multi feature artefact simulation	3-27
3.4.1 VCMM vs Physical measurement results – Size	3-28
3.4.2 VCMM vs physical measurement results – Position	3-32
3.4.3 Impact of form error definition within Pundit/CMM	3-33
3.5 A Case study for application of Pundit CMM during dowell hole measurement of shafts	3-37
3.5.1 Physical measurement results of the master shaft.....	3-42
3.5.2 Pundit/CMM simulation results.....	3-44
3.6 Impact of measurement uncertainty in conformance decision associated with circular features.....	3-46
3.7 Summary	3-47
Chapter 4 Automated conformance assessment of airfoil edges	4-1
4.1 Assessing the significance of leading edge shape.....	4-1
4.2 Mathematical modelling of leading edge shape.....	4-2
4.2.1 Data manipulation	4-4
4.2.2 Types of curvature	4-15
4.3 Automated sentencing of the Leading edge shape.....	4-24

4.3.1 Method 1 – Curvature Tolerancing.....	4-26
4.3.2 Industrial impact	4-41
4.3.3 Method 2 – Parameterisation of curvature plot features	4-45
Chapter 5 Conclusions	5-1
5.1 Conclusions.....	5-1
5.2 Future work.....	5-7
References.....	5-8

List of Figures

Figure 1. Product Lifecycle Management [1]	1-1
Figure 2. Contact points along the surface of a part	1-5
Figure 3. GD&T example for a positional tolerance [12].....	1-6
Figure 4. Example of hard gauging inspection routine.....	1-6
Figure 5. Example of CMM inspection routine	1-6
Figure 6. Features operations defined in the GPS project; (a) partition, (b) extraction, (c) filtration, (d) [14]	1-12
Figure 7. Precision vs Accuracy	1-13
Figure 8. Traceability chain for a CMM.....	1-16
Figure 9. Factors that may impact CMM uncertainty [51]	1-20
Figure 10. Different criteria for circular substitute features: (a) least	1-21
Figure 11. Effect of CMM uncertainty on circular features properties [67].....	1-22
Figure 12. Centre coordinates of all DOE runs [58].....	1-24
Figure 13. Example of a DOE framework for CMM measurement [73].....	1-24
Figure 14. Virtual CMM simulator (VCMM) [89].....	1-38
Figure 15. Expert CMM flow chart [92].....	1-41
Figure 16. Simulation by constraints flow diagram [114]	1-43
Figure 17. Conformance decision zones [19]	1-47
Figure 18. Impact of uncertainty on process capability	1-48
Figure 19. Leading edge of a fan blade airfoil section	1-50
Figure 20. Impact of leading edge bluntness on aerodynamic performance [124].....	1-52
Figure 21. Example of software package for airfoil analysis [128].....	1-53
Figure 22. Comparison of length bar measurements using CMM-1	2-8
Figure 23. a) Comparison of length bar measurements using CMM-2; b) Comparison of length bar measurements CMM-3	2-9
Figure 24. Measured parts conformance assessment types.	2-13
Figure 25. Circular feature with 3 lobes form error vs circular feature with no form error	2-19
Figure 26. Simulation results for the three lobed features	2-20
Figure 27. Simulation results for centre coordinates areas of the three lobed feature... ..	2-22
Figure 28. Impact on centre coordinates when applying MIC to a three lobed feature. ..	2-23
Figure 29. Simulation results for the three lobed feature.....	2-24
Figure 30. Simulation results for centre coordinates areas of the five lobed feature.....	2-26
Figure 31. Impact on centre coordinates when applying MIC to a five lobed feature ..	2-26
Figure 32. Example of three measurement runs of a three lobed feature	2-27
Figure 33. Normality test plots for r0 when applying LSC, MIC and MCC.	2-29
Figure 34. Normality test plots for X0 when applying LSC, MIC and MCC.....	2-31
Figure 35. Example of dowel hole size and position tolerances.....	2-33
Figure 36. Integration of experimental design with Monte Carlo simulation.....	2-36
Figure 37. Residual plots for LSC radius mean values.....	2-37
Figure 38. Main effects plots for LSC radius mean values.....	2-38

Figure 39. Main effects plots for MIC radius mean values	2-39
Figure 40. Main effects plots for MCC radius mean values	2-39
Figure 41. Main effects plots for LSC radius stdev	2-42
Figure 42. Interaction plot for LSC radius stdev values	2-43
Figure 43. Main effects plots for MIC radius stdev values.....	2-45
Figure 44. Interaction plot for MIC radius stdev	2-46
Figure 45. Main effects plot for MCC of radius stdev.....	2-48
Figure 46. a) Main effects plot for LSC X coordinate stdev; b) Main effects plot for LSC Y coordinate stdev	2-49
Figure 47. a) Main effects plot for MIC X coordinate stdev; b) Main effects plot for MIC Y coordinate stdev	2-50
Figure 48. a) Main effects plot for MCC X coordinate stdev; b) Main effects plot for MCC Y coordinate stdev	2-51
Figure 49. X,Y coordinates (Lobe type – 5; Lobe magnitude – 0.021; CMM uncertainty – 0.00433; Number of probing points – 4)	2-52
Figure 50. X,Y coordinates (Lobe type – 2; Lobe magnitude – 0.006; CMM uncertainty – 0.00144; Number of probing points – 17)	2-53
Figure 51. Main effects plot for % of form error captured	2-55
Figure 52. CMM set up for experimental design.....	2-56
Figure 53. a) Stdev vs Temperature results; b) Bias vs Temperature results	2-63
Figure 54. Interaction effect of the temperature and the type of feature measured (ring and sphere).....	2-64
Figure 55. Interaction effect of the stylus length and the probe extension	2-65
Figure 56. Interaction effect of the type of feature and the number of probing points..	2-65
Figure 57. Pundit/CMM simulation set up for length bar measurement.	3-1
Figure 58. a) Comparison of Pundit/CMM simulation with CMM-1 uncertainty budgets; b) Comparison of Pundit/CMM simulation with CMM-2 uncertainty budgets; c) Comparison of Pundit/CMM simulation with CMM-3 uncertainty budgets.....	3-5
Figure 59. a) Features specification for artefact A; b) Features specification for artefact B	3-7
Figure 60. a) Circular artefact with 5 harmonics; b) Fourier plot of the 5 harmonics.....	3-8
Figure 61. KernEvo CNC 5 axis machining center and Zeiss F25 CMM	3-9
Figure 62. Fully assembled Multi feature artefact	3-10
Figure 63. Day 1 I-Basic; a) Mean error of three repeats b) One standard deviation of three repeats	3-14
Figure 64. Three days I-Basic with 90 X,Y rotation about Datum-CS ; a) Mean error of three repeats b) One standard deviation of three repeats	3-15
Figure 65. Three days 3X-Basic; a) Mean error of three repeats b) One standard deviation of three repeats.....	3-16
Figure 66. I-Basic; a) Mean error of three repeats b) One standard deviation of three repeats	3-17
Figure 67. I-Basic with 90 X,Y rotation about Datum-CS ; a) Mean error of three repeats b) One standard deviation of three repeats	3-18
Figure 68. 3X-Basic; a) Mean error of three repeats b) One standard deviation of three repeats	3-19

Figure 69. I-Basic; a) Mean error of three repeats b) One standard deviation of three repeats	3-20
Figure 70. I-Basic with 90 X,Y rotation about Datum-CS ; a) Mean error of three repeats b) One standard deviation of three repeats	3-20
Figure 71. 3X-Basic; a) Mean error of three repeats b) One standard deviation of three repeats	3-21
Figure 72. a) Mean error of three repeats 1XBasic; b) Mean error of three repeats 1XBasic XY; c) Mean error of three repeats 3XBasic	3-23
Figure 73. a) Mean error of three repeats 1XBasic; b) Mean error of three repeats 1XBasic XY; c) Mean error of three repeats 3XBasic	3-24
Figure 74.a) Mean error of three repeats 1XBasic; b) Mean error of three repeats 1XBasic XY; c) Mean error of three repeats 3XBasic	3-26
Figure 75. Datum set up for Artefact B in Pundit/CMM	3-27
Figure 76. Probing strategy and form error definition in Pundit/CMM	3-28
Figure 77. Pundit Simulation comparison for Machine M feature sizes a) 1XBasic; b) 3XBasic	3-29
Figure 78. Pundit Simulation comparison for Machine W feature sizes a) 1XBasic; b) 3XBasic	3-30
Figure 79. Pundit Simulation comparison for Machine C feature sizes a) 1XBasic; b) 3XBasic	3-31
Figure 80. Pundit Simulation comparison for Machine W features position a) 1XBasic; b) 3XBasic	3-33
Figure 81. Pundit/CMM dense data option	3-34
Figure 82. Impact of dense data option using 1XBasic a) Feature position; b) Feature size	3-34
Figure 83. Impact of dense data option using 3XBasic a) Feature position; b) Feature size	3-35
Figure 84. Pundit Simulation comparison for Machine M features position a) 1XBasic; b) 3XBasic	3-36
Figure 85. Pundit Simulation comparison for Machine C features position a) 1XBasic; b) 3XBasic	3-37
Figure 86. Definition for measurement of dowell holes	3-38
Figure 87. Critical to quality characteristics (CTQC) diagram for the specific CMM..	3-38
Figure 88. Experimental workflow using the ISO 15530-3 approach	3-39
Figure 89. 3D visualisation of master shaft in Pundit/CMM	3-41
Figure 90. 10 repeated measurements of 12 holes on the master shaft	3-43
Figure 91. Pundit/CMM simulation shaft simulation set up	3-44
Figure 92. X,Y position uncertainty	3-45
Figure 93. Compressor blade airfoil sections	4-1
Figure 94. LESA standard for leading edge shape assessment	4-2
Figure 95. Leading edge curvature definition	4-3
Figure 96. a) Leading edge point cloud data; b) Instantaneous curvature for input data points	4-5
Figure 97. Linear interpolation vs Cubic spline interpolation	4-6
Figure 98. Cubic spline interpolation vs B-Spline interpolation	4-7
Figure 99. Instantaneous curvature profile using CPD of 0.2mm	4-9

Figure 100. a) B-spline fit error with CPD of 0.2mm; b) Histogram of error of fit	4-11
Figure 101. B-spline fit error with CPD of 0.02mm.....	4-12
Figure 102. Comparison of a) instantaneous curvature, and b) smoothed curvature a single pass simple moving average filter.....	4-13
Figure 103. Smoothed curvature using a two pass simple moving average filter	4-14
Figure 104. Generated ellipse with a=1,b=4.....	4-14
Figure 105. a) Instantaneous curvature b) Averaged curvature.....	4-15
Figure 106. Instantaneous curvature vs non-dimensionalisation options.....	4-16
Figure 107. Instantaneous curvature non-dimensionalisation options for two synthetic shapes.....	4-17
Figure 108. Examples of leading edge bias.....	4-18
Figure 109. a) Instantaneous curvature vs Thickness; b)Instantaneous curvature vs Arc Length	4-19
Figure 110. a) Instantaneous curvature vs Normalised Thickness position; b) Curvature NHT vs Normalised Thickness position.....	4-20
Figure 111. Section AA Leading edge plots for three different blades	4-21
Figure 112. a)Curvature NHT vs Normalised Thickness position; b)Curvature NHT vs Normalised Arc Length.....	4-22
Figure 113. Curvature plots shift as a function of the thickness line angle.....	4-23
Figure 114. Curvature of a non-ideal shape (LESA)	4-24
Figure 115. Flow chart for the automated leading edge assessment.....	4-25
Figure 116. Airfoil classification for 14 blades.....	4-26
Figure 117. Upper and Lower tolerance bands derived from nominal curvature.....	4-27
Figure 118. Curvature tolerancing sentencing method.....	4-28
Figure 119. Curvature tolerancing sentencing method applied to the 6 blades.....	4-30
Figure 120. Curvature tolerancing sentencing method applied to 6 blades with updated tolerance bands 2 nd pass.....	4-31
Figure 121. Curvature tolerancing method applied to LESA shapes.....	4-31
Figure 122. Curvature tolerancing sentencing method applied to 6 blades.....	4-32
Figure 123. Curvature tolerancing sentencing failing to capture 2 blades.....	4-33
Figure 124. Updated tolerance bands final iteration.....	4-34
Figure 125. a)Curvature tolerancing method applied to LESA shapes final iteration; b) Curvature tolerancing method applied to accepted shapes.....	4-35
Figure 126. Blade set curvature nominal curvature	4-37
Figure 127. Section “DC” curvature assessment	4-37
Figure 128. Section “DE” curvature assessment	4-38
Figure 129. a) Curvature plot of a failed blade; b) Leading edge profile of nominal and measured blade.....	4-39
Figure 130. Tolerancing methodology failure to capture a double peak feature	4-39
Figure 131. Failure to capture second double peak feature	4-40
Figure 132. Excel tool for displaying Blade Inspect outputs; b) Blade Inspect integration with CMM inspection	4-42
Figure 133. Detailed integration overview between Blade Inspect and inspection process operation sequence.....	4-43
Figure 134. Blade Inspect output for a blisk assessment using both CNTP and CNAL. ..	4-44

Figure 135. Parameterisation of curvature plot zones	4-46
Figure 136. Nominal airfoil section AA.	4-47
Figure 137. Curvature plots for the rejected airfoils section AA from classification summary.....	4-48
Figure 138. Parameterisation variables for all zones.....	4-49
Figure 139. LESA1 Leading edge shapes and corresponding curvature plots using CVNTP	4-53
Figure 140. LESA1 Leading edge shapes and corresponding curvature plots using CVNAL.....	4-57

List of Tables

Table 1. Historical development of GD&T and GPS [12].....	1-4
Table 2. Conventional Metrology vs Coordinate Metrology [17]	1-9
Table 3. Type b probability distributions [20]	1-15
Table 4. CMM performance standards	1-19
Table 5. Example of CMM factors used for an experimental design [58]	1-23
Table 6. Length bar measurement results	2-2
Table 7. Uncertainty contributors (GUM)	2-5
Table 8. Uncertainty components according to ISO 15530-3.....	2-6
Table 9. Uncertainty contributors (GUM, ISO 15530-3)	2-11
Table 10. CMM’s standard uncertainties.....	2-17
Table 11. Factors selected for the Monte Carlo simulation of features with systematic form error.	2-19
Table 12. Descriptive statistics table for radius (mm)	2-30
Table 13. Descriptive statistics for centre coordinate X0 (mm)	2-32
Table 14. Full factorial design factors and levels	2-34
Table 15. LSC experimental design P-values for Stdev results.....	2-41
Table 16. MIC experimental design P-values for Stdev results.....	2-43
Table 17. MCC experimental design P-values for Stdev results	2-47
Table 18. Properties of selected features	2-57
Table 19. Experimental design factors.....	2-59
Table 20. Experimental design ANOVA results.....	2-63
Table 21. CMM-3 UES length test	3-3
Table 22. CMM-2 UES length test	3-3
Table 23. CMM-1 UES length test	3-3
Table 24. CMM’s specifications.....	3-10
Table 25. Artefact A&B probing strategy.....	3-11
Table 26. Artefact B features plots from Zeiss F25 CMM measurements.	3-13
Table 27. Zeiss F25 CMM measurement plots for features 1A and 2A.	3-17
Table 28. Impact of control point choice on curvature smoothing	4-8
Table 29. Upper and Lower band variables definition 1 st pass.....	4-29
Table 30. Upper and Lower band variables definition 2 nd pass.....	4-30
Table 31. Upper and Lower band variables definition final iteration.....	4-33
Table 32. Upper and Lower band variables definition.	4-36
Table 33. Zone 1 variables and rules	4-50
Table 34. Zone 2 variables and rules	4-50
Table 35. Zone 3 variables and rules	4-50
Table 36. Sentencing results for the 6 rejected leading edges	4-51
Table 37. LESA1 sentencing results using curvature parameterisation method	4-54
Table 38. Zone 2 variables and rules using CVNAL.....	4-55
Table 39. Sentencing results for the 6 “Fail” blades and remaining RGL159 series “Pass”	4-56
Table 40. LESA1 results using CVNAL.....	4-58

Chapter 1

Literature and State of the Art Review

Traditionally designers have defined functional and operational requirements of parts based on ideal geometries with little understanding of how their requirements affected activities downstream of the Product Lifecycle Management (PLM) chain. This approach was due to both a lack of knowledge about the real part geometry and the fact that most software used to predict performance characteristics, did not accept non-ideal geometries.

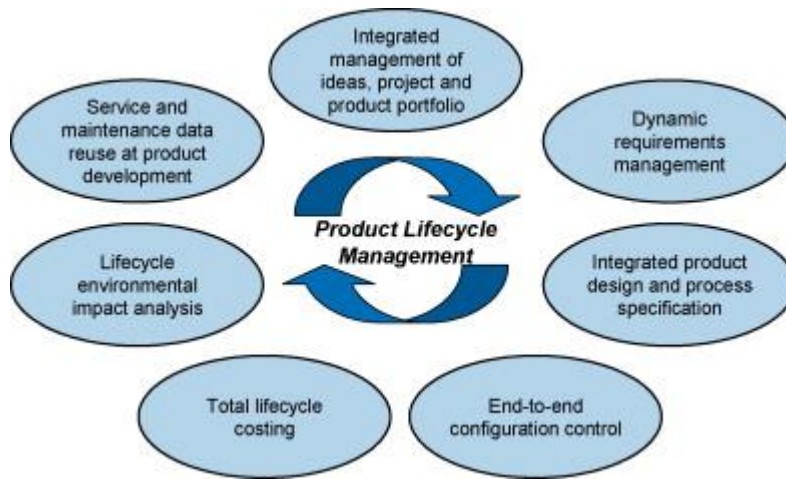


Figure 1. Product Lifecycle Management [1]

A key activity at any part of the PLM chain is integrated product design and process specification [1]. The intent of an integrated product design is to link digital tools at different stages of the design process with data from the physical world. This task is achieved via design verification and validation in the digital environment that exists within PLM. Design verification requires capability data driven by the capability of

manufacturing processes used to manufacture a particular product. This activity also requires information from a measurement process, which is used to describe inherent imperfections of manufacturing processes which can cause degradation of functional characteristics of the product, and therefore, of its quality [2]. Both the availability of capability data and integrated product design have driven manufacturers to standardise their designs.

Several authors have identified methodologies that could aid the standardisation of feature based designs [3] and manufacture [4]. Feature based design has made a direct and positive impact on part verification as it helped to codify and standardise both the manufacturing processes and the inspection methods used for types of features, thus improving design verification. Although digital design and manufacturing tools are becoming ever more sophisticated, digital measurement planning and modelling tools are still under development. It is important to stress that CAIP tools have been available for some time but of particular importance is the methods by which a user make a decision on the detailed inspection of a feature i.e micro planning as opposed to macro planning [5]. In general CAIP tools can be summarised in the following steps: (1) Computer Aided Design (CAD) interface and feature recognition, (2) determination of the inspection sequence of the features of a part, (3) determination of the number of measuring points and their locations, (4) determination of the measuring paths, and (5) simulation and verification [6, 7, 8, 9]. Unlike digital manufacturing planning tools which can have built in data such as manufacturing process capability for a specific feature, CAIP tools tend to rely on operators/inspectors experience as far digital measurement planning and modelling is concerned. The purpose of digital environment modelling and simulation is

to ensure standardisation and optimisation of designs and ultimately a better quality product. The tolerancing stage is the most critical stages within the digital design environment. Currently a designer can access manufacturing process capability data which allows a decision to be made with regards to tolerancing limits. Unfortunately manufacturing process capability data does not yet include the capability of the measurement method being used to measure a specific feature. This is a key consideration specifically with features which require coordinate measuring systems that could be subject to complex estimations of measurement uncertainties. International standards state that every feature should have tolerancing limits with an accompanying measurement uncertainty statement.

The definition of standards aiming at completely and coherently describe the geometrical characteristics of products includes GD&T (American Society of Mechanical Engineers (ASME) standards) and GPS (International Standards organisation (ISO) standards).

Geometric dimensioning and tolerancing is the language in which such constraints are explicitly defined. There are several standards that describe the symbols and define the rules used for GD&T. Both the ASME Y14.5M-1994 (Dimensioning and Tolerancing – Mathematical Definition of Dimensioning and Tolerancing Principles) [10] and the ISO/TR 14638: 1995, Geometric Product Specifications, define guidelines for 2D technical drawings [11].

GPS standards are group of standards which provide definitions and specifications according to the GPS matrix [12].

Table 1. Historical development of GD&T and GPS [12]

GD&T		GPS	
1905	Taylor Concept – Rule 1 Envelope Principle	1920s'	National standards on limits and fits (e.g.UNIM 24)
1939-45	MIL-STD 8A Form – positioning concepts	1940	ISA system on limits and fits (in Italy UNI 1088-1098:40)
		1962	ISO/R 286 “limits and fits”
1966	USASI Y14.5M First unified standard for dimensioning and Tolerancing	1969	ISO/R 1101/I Form-positioning concepts
1994	ASME Y14.5M Dimensioning and Tolerancing	1995	ISO/TR 14638 Geometrical Product Specifications (GPS) – Masterplan

These standards were developed with rules related to product definition rather than consideration given to the type of measurement system such coordinate measurement systems such as coordinate measuring machines. ASME Standard Y14.5M defines four primary form tolerances:

- Straightness
- Flatness
- Circularity
- Cylindricity

that are important characteristics for manufacturing and assembly. However, the current standard does not provide clear guidelines for CMM inspection and verification of these form tolerances. CMM users intuitively decide which sampling method to use, how many sample points to collect and which particular form-fitting criterion to use. The CMM users’ intuitions are derived from their experience of manufacturing those part features and their geometric relationships based on GD&T control frames.

When using a hard gauge such as a sine table, any form on the surface of the part will be taken into account by the table because all the high points of the surface of the part will be in contact with the table surface.

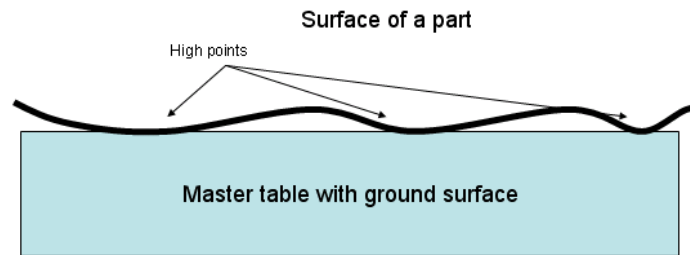


Figure 2. Contact points along the surface of a part

A Coordinate Measuring System (CMS) may only collect a number of points (also known as point cloud data) that will represent that same surface. Both methods aim at providing the same information according to the geometric specification but in the case of the hard gauge the instrument (sine table) performs the task of contacting the high points while in the case of a CMS the operator may make the decision on the number of points used to capture the surface. This difference could be described as the major challenge when designs that were and still are created based on standards that were developed with first principles measurements in mind. Even when the standard can be replicated by a CMS, its interpretation conversion into a CMS world can lead to decisions in measurement strategies which will ultimately affect the measurement results.

The example (Figure-3) extracted from the ISO 1101 [12] illustrates how both hard gauging and CMS systems can interpret the GD&T of a drawing during dimensional inspection.

The extracted (actual) median line shall be within a cylindrical zone of diameter 0,08, the axis of which coincides with the theoretically exact position of the considered hole, with respect to datum planes C, A and B.

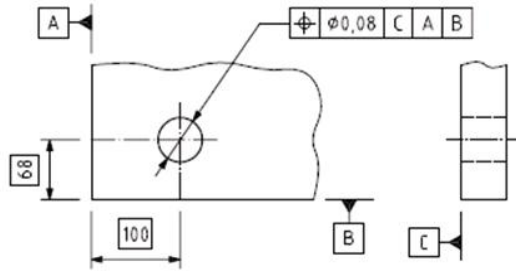


Figure 3. GD&T example for a positional tolerance [12]

First principles Inspection

- 1) Clamp datum C against box plate
- 2) Clock A for squareness
- 3) Use clock to find size of hole using points Y and Z
- 4) Clock from A to point X
- 5) Clock from B to point Y
- 6) Subtract the radii from the distance X to Y

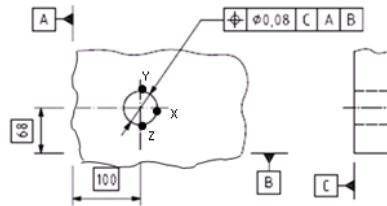


Figure 4. Example of hard gauging inspection routine

CMM Inspection

- 1) Use 3 points to define datum's A,B and C
- 2) Measure a circle/cylinder to determine hole position

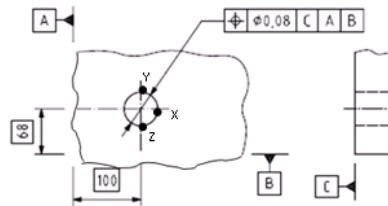


Figure 5. Example of CMM inspection routine

Both inspection systems (Figure-4, Figure-5) and methodologies satisfy the design definition in Figure-1 but both systems may impact the conformance of the part

differently. As an example the hard gauging method will ensure that the high points of the datum surfaces of the part will be in contact with a ground table or equivalent artifact. Most CMM users could opt for a simple datum set up using a plane, line and point. Furthermore it would be up to the CMM operator to choose the number of probing points to define the line and the plane. On the other hand the clock gauge used to check the position in X and Y coordinates would rely on another gauge such as a height gauge to set its starting position. Both approaches could therefore be valid inspection strategies but with completely different measurement results.

Although both systems are valid, for many years the components manufactured for the Aerospace industry have traditionally been verified on conventional measurement devices such as micrometers and height gauges to assess the conformance of manufactured parts to the engineering drawing. Such measurement devices, when used by skilled operators/inspectors, can assure confidence on the measurement results if standards and best practice are being followed. As the Aerospace market grew, it was no longer feasible in some instances to have skilled operators performing measurements of all parts due to constraints of lead time. With advances in machine automation, the aerospace industry started moving towards automated inspection methods in order to cut costs, improve lead times and in some cases increase their confidence on a measurement result.

These systems find the dimensions of a part via point locations on the object's desired surface. Coordinate data is then processed to determine the part's dimensions and the types and locations of variations in the surface. Once the coordinate data points are collected from the surface of the part by the CMS hardware, the information is processed

by software, which usually performs a geometric fit to the gathered data. This fitting software, which is usually integrated as part of the CMS, uses the coordinate data to, for instance, determine a part's location, orientation, concentricity, or deviation of the part from the corresponding perfect geometry. The software can apply appropriate processing of the data to determine if a part is within tolerances defined in the specifications [13-15]. Since a part is measured through only a sampling of points, its true surface can never be known exactly; instead, an approximation of the surface is known based on a finite sampling of coordinate points.

The software will often be required to compute “substitute geometry” based on the imperfect data. Imperfect data can be due to metrological characteristics of the measurement system including its environment and manufacturing defects also known as form error or due to uncertainty [16] of the measurement system itself while collecting the data. Over the past 20 years CMM's have improved in terms of flexibility, accuracy, and speed which led to a large expansion of its use within the aerospace industry. Whether the CMM is used in-process or at final verification stages there are few work pieces which cannot be inspected by this system. Such benefits coupled with evermore demanding aero engine designs have made the CMM one of the most powerful metrological instruments for the aerospace industry. Table-2 shows a comparison between conventional hard gauging metrology versus coordinate measurement.

Table 2. Conventional Metrology vs Coordinate Metrology [17]

Conventional Metrology	Coordinate Metrology
<p>Manual, time-consuming alignment of test piece</p> <p>Single-purpose and multi-point measuring instruments making it hard to adapt to changing measuring tasks</p> <p>Comparison of measurements with material measures, i.e, gauge blocks or kinematic standards</p> <p>Separate determination of size, form, location and orientation with different machines</p>	<p>Alignment of test piece not necessary</p> <p>Simple adaption to the measuring tasks by software</p> <p>Comparison of measurements with mathematical or numerical models</p> <p>Determination of size, form, location and orientation in one setup using one reference system</p>

1.1 Coordinate metrology and GPS framework

As previously mentioned, a key part of the PLM chain is design specification. A key issue during design specification is the lack of agreement between manufacturing engineers, quality engineers and design engineers which leads to ambiguity. Such

ambiguity can lead to rework and concessions therefore it is critical that every definition within a manufacturing drawing is understood by all parties.

The designer must make drawings free from ambiguity and possible to inspect at all stages of manufacture. Some of the reasons to why such events happen is due to possible misinterpretation of standards. In the case of the GPS, its basic philosophy can be difficult to interpret due to the number of standards involved. A key requirement for interpreting the GPS is the analysis of the GPS Matrix, which will be further explained. The GPS approach tends to detail every geometric characteristic separately, but with no emphasis on the underlying correlation between “specification” and the “verification”[18]. According to ISO 14660-1 [15], a geometrical feature is a point, line or surface. Such geometrical features exist in three “worlds”:

- The world of specification, where the designer has in mind several representations of the future workpiece;
- The world of the workpiece, the physical world;
- The world of inspection, where a representation of a given workpiece is used through sampling of the workpiece by measuring instruments.

The order in which the above stages are addressed is shown in the ISO 17450-1 [13]. The geometrical specification is a design stage where a range of permissible deviations of a set of characteristics of a workpiece related with its functional need. All the verification procedure must start from the defined tolerances and for generic tolerances the steps and feature operators involved are[14]:

1. A particular subset of the real surface is identified for each surface to be verified. This feature operation is called **partition**.
2. A subset of the real feature is approximated using a physical extraction process yielding to a finite set of point this feature operation is called **extraction**.
3. The feature **filtration** operation is then performed, sometimes it is embedded within the physical extraction process or applied subsequently, reducing the information of the set of points to describe only the frequencies of merit for the verification of the particular surface-tolerance combination.
4. The filtered point set is used to estimate the closest fitting substitute geometry through a process of **association**.
5. When two or more surfaces are influenced by one tolerance, the **collection** operation is used to consider all applicable surfaces at the same time.
6. When tolerance specifications depend on features coming from two or more surfaces, the **construction** operation is used to define these other ideal features. The tolerances specified for any particular feature define maximum or minimum values of characteristic.

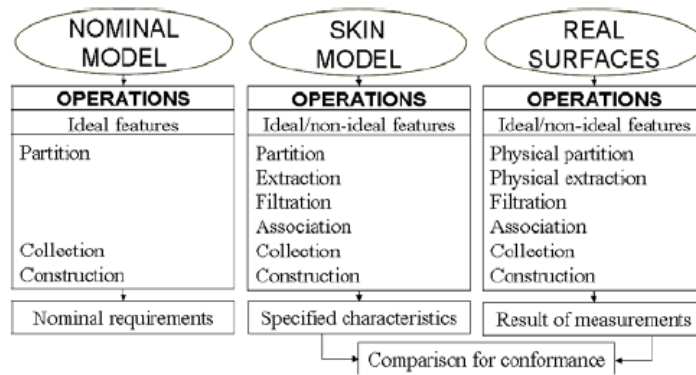


Figure 6. Duality principle in specification, production and verification phases

[14].

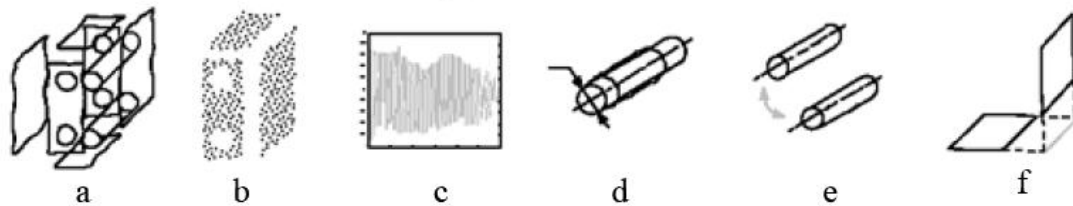


Figure 6. Features operations defined in the GPS project; (a) partition, (b) extraction, (c) filtration, (d) association, (e) collection, (f) construction [14]

1.2 Measurement Uncertainty definition

Every measurement process will have some extent of uncertainty. When reporting a measurement result, it is required in accordance with ISO14253-1[19] to report the uncertainty associated with the measurement. No perfect measurement exists. Instead, the result of measurement is only an approximation of the value of the quantity being reported [19]. Therefore, the measurement result is not complete without the accompaniment of a quantitative statement of its uncertainty.

The GUM [20] definition for uncertainty is a result of the evaluation aimed at characterizing the range within which the true value of a measurand is estimated to lie, generally with a given confidence. The concept of uncertainty is still relative new in the history of measurement while measurement error has long been part of the measurement science. Perhaps more concerning is the fact that the majority of CMM measurements produced by industry do not contain an uncertainty statement or the uncertainty statement is mostly derived from the machine specification. The Figure-7 illustrates two key quantities which form part of measurement uncertainty, precision and accuracy.

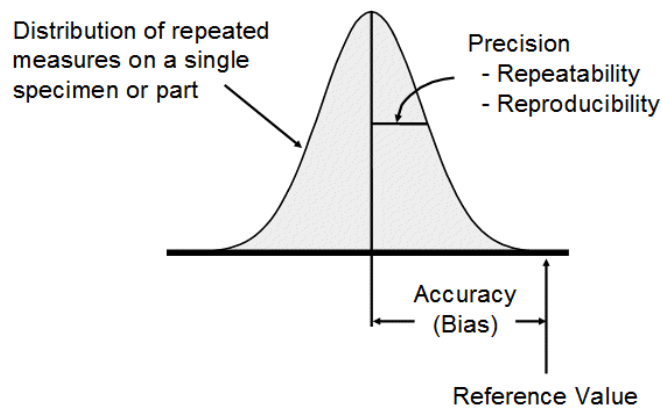


Figure 7. Precision vs Accuracy

Measurement uncertainty is made up of two components, a systematic error component and a random error component. In this context both precision and accuracy of the measurement instrument will therefore influence the measurement uncertainty. Measurements with low precision and accuracy are therefore likely to produce higher uncertainties when compared with high precision and high accuracy. Similarly a measurement system with high repeatability could be systematically wrong. This case presents a better scenario when compared with a system that is systematically right and

randomly wrong because random errors by their nature are difficult if not impossible to compensate unlike the systematic ones. Accuracy by definition [20] is the closeness of agreement between the result of a measurement and a true value of a measurand. Precision is the degree to which further measurements or calculations show the same or similar results. In this sense precision is normally determined by the standard deviation of repeated measurements and can be the measurement uncertainty of a system if the system is accurate. In most cases precision will be used for the calculation of the random error component of measurement uncertainty as previously defined. The term measurement uncertainty is often used without attention to the context. Standard uncertainties represent where possible the Type A uncertainties (random components) and Type B uncertainties (systematic components). Type A uncertainty is derived from independent statistical observations $X_{i,k}$ of X_i under repeatable conditions with x_i being the input estimate and $q(\bar{X}_i)$ the standard uncertainty to be associated with x_i .

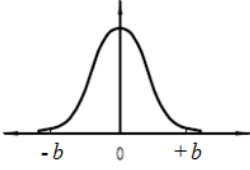
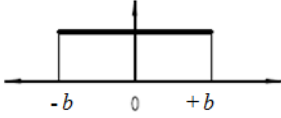
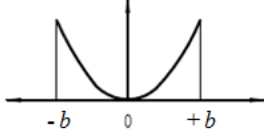
$$\bar{x} = \frac{1}{n} \sum_{i=1}^n x_i$$

$$u(x) = \sqrt{\frac{1}{n(n-1)} \sum_{i=1}^n (x_i - \bar{x})^2}$$

In most cases Type B evaluation of standard uncertainty is based on scientific judgement using all relevant information of the measurement system. This may include the manufacturer's specification, historical data, calibration data and general knowledge of

the measurement system. Three [20] probability distributions (Table-3) are used to transform the limits of the relevant information b into a standard uncertainty.

Table 3. Type b probability distributions [20]

 <p>A graph of a Gaussian distribution centered at 0 on a horizontal axis. The curve is bell-shaped and symmetric, with labels $-b$, 0, and $+b$ on the axis.</p>	 <p>A graph of a rectangular distribution centered at 0 on a horizontal axis. The distribution is a flat-topped rectangle with labels $-b$, 0, and $+b$ on the axis.</p>	 <p>A graph of a U distribution centered at 0 on a horizontal axis. The distribution is a curve that is zero at 0 and increases to a peak at $-b$ and $+b$, with labels $-b$, 0, and $+b$ on the axis.</p>
a) Gauss distribution	b) Rectangular distribution	c) U distribution

Once all standard uncertainties are identified for the particular measurand, a combined uncertainty can be derived using the following:

$$u_c(y) = \sqrt{\sum_{i=1}^n \left(\frac{\partial f}{\partial x_i}\right)^2 u^2(x_i) + 2 \sum_{i=1}^n \sum_{j=i+1}^n \frac{\partial f}{\partial x_i} \frac{\partial f}{\partial x_j} u(x_i, x_j)}$$

The Expanded measurement uncertainty can be derived as follows:

$$U = k \cdot u_c(y)$$

Where k is the coverage factor derived from the t distribution table [20] by deriving the degrees of freedom of the combined uncertainty in cases where Type B standard uncertainties were derived using a rectangular distribution according to the GUM.

$$v_{eff}(y) = \frac{u_c^4(y)}{\sum_{i=1}^N \frac{(\partial f / \partial x_i)^4 \cdot u^4(x_i)}{v(x_i)}}$$

1.3 Uncertainty in coordinate measurement

According to the International Vocabulary in Metrology (VIM), a key property of a measurement result is traceability. “The property of the result of a measurement or the value of a standard whereby it can be related to stated references, usually national or international standards, through an unbroken chain of comparisons all having stated uncertainties[19].”

In the case of coordinate measuring machines the traceability chain can be described in the Figure-8.

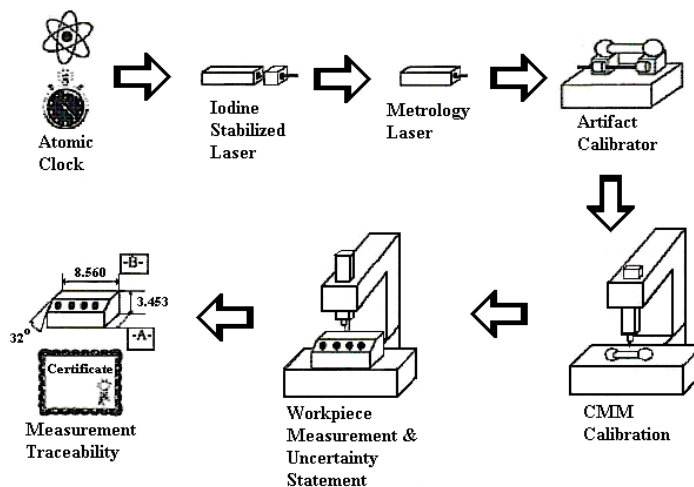


Figure 8. Traceability chain for a CMM

A key part of the CMM traceability chain shown above is the CMM calibration also known as performance verification tests. Over the years several national and international standards have been developed to aid CMM verification tests [21-45]. Such tests are strongly dependant on the artefact calibrator as shown in Figure-8 above. Furthermore the tests only reflect in the majority of cases the machine performance when dealing with a point to point measurement along predefined positions within the machine volume. Other tests using artefacts or non-contact metrology can be used to extract the full error map of the machine. In the case of artefacts these are calibrated in accordance with the rules set by the ISO/IEC 17025:2005 [46]. Due to the number of variables [47-53] present in a CMM system the evaluation of task specific measurement uncertainty can be a very complex task. However there are different approaches which can aid the estimation of measurement uncertainty:

Sensitivity analysis – Sensitivity analysis also known as uncertainty budgeting, consists of listing each uncertainty source, its magnitude, effect on the measurement result, correlation with other uncertainty sources, and combining appropriately.

Expert Judgement – Used when there is lack of a mathematical model or measurement data.

Substitution – Applied via repeated measurements of a calibrated master part. The output results of the repeated measurement yield a range of errors and uncertainty.

Simulation – Modeling and simulating the measurement process. All known errors are modeled via a statistical process and the outputs converted to an uncertainty statement.

Measurement History – A large numbers of measurements over time can place an upper bound on measurement uncertainty. In this case only variability contributes to the uncertainty estimation and no bias.

Governing all the approaches previously mentioned is the GUM (except Expert judgement, Measurement history). The substitution method provides a practical approach to uncertainty estimation in coordinate metrology as described by the ISO 15530-3[55], which is part of a collection of standards under development by ISO TC213comitee WG10 [54-57]. The simulation approach provides a more comprehensive approach to the estimation of measurement uncertainty because all or most contributors to the estimation can be described individually or described under expert assumptions. Such approach allows the user to determine how significant each of the individual factors contributes towards the expanded uncertainty. It is important to recognise that measurement uncertainty is task specific and as such there will be factors which remain constant in terms of their influence during the measurement process and factors that may vary from task to task. The Design of experiments approach to uncertainty estimation is focused on understanding how the selected input factors of the CMM system affect the output response [58-63]. Furthermore the design of experiments approach also allows the experimenter to study the interactions between such factors depending on the type of DOE method selected for the study.

Table 4. CMM performance standards

Standard	Part	Description	Issued
JIS B 7440	1	General Terms	2003/4
	2	Dimensional measurement	2003/4
	3	Rotary table-equipped CMM	2003/4
	4	Scanning measurement	2003/4
	5	Multiple stylus probing systems	2004
	6	Errors in computing Gaussian associated features	2004
VDI/VDE 2617	1	General Terms	2005
	2.1.2.2	Performance assessment	2005
	2.3	Performance assessment of Large CMMs	2006
	3	Determining parametric errors	1989
	4	CMMs with additional axes of rotation	2006
	5	Interim checks with artefacts	2010
	5.1	Interim checks with ball plates	2011
	6.1.6.2	Testing guidelines for CMMs with optical probes/sensors	2007/5
	6.3	CMMs with multiple probing systems	2008
	7	CMM uncertainty estimation by simulation	2008
	8	CMM measurements suitability testing	2006
	9	AACMM performance and acceptance testing	2009
	10	Laser trackers acceptance testing	2011
11	CMM uncertainty estimation using uncertainty budgets	2011	
12.1	Testing guidelines for CMMs measuring micro geometries	2011	
13	Testing guidelines for CMMs with CT sensors	2009	
ASME B89.4.10360.2		Performance assessment	2008
ASME B89.4.19		Performance Evaluation of Laser-Based Spherical CMM	2006
ASME B89.4.22		AACMM performance and acceptance testing	2004
ASME B89.4.10		Evaluation of Coordinate Measuring System Software	2000
ISO 10360	1	General Terms	2000
	2	Performance assessment	2009
	3	CMMs with rotary tables	2000
	4	CMMs with scanning modes	2000
	5	CMMs with multiple probing systems	2010
	6	Evaluation of Coordinate Measuring System Software	2001
	7	CMMs with imaging probing systems	2011

This aspect is in agreement with the PUMA as defined by the ISO 14253-1 which is part of a collection of standards related to uncertainty and conformance decisions [19, 64, 65]. CMM users are aware of the existence of measurement uncertainty but the uncertainty model is either studied as a separate factor from the model or included in a segregated fashion which shows no correlation with pertinent factors identified. Recent research on CMM inspection techniques using DOE methods have been aimed at developing CMM

inspection guidelines. These may combine factors such as form-fitting criterion; sampling method; sample size; type of form error due to various manufacturing processes; and CMM measurement uncertainty.

Form error and sampling strategy are directly related because the information available for one parameter should drive the other. In this sense if a feature contains a form tolerance, the sampling strategy should reflect such tolerance. Form error itself by definition should be the representation of the true surface of a feature and as such in most cases is a function of the process used to manufacture such feature. On the other hand even for a feature with perfect form, form error can still occur but in this case it is induced by the measurement system in specific by a CMM. The Figure-9 shows various factors that can effect CMM measurements.

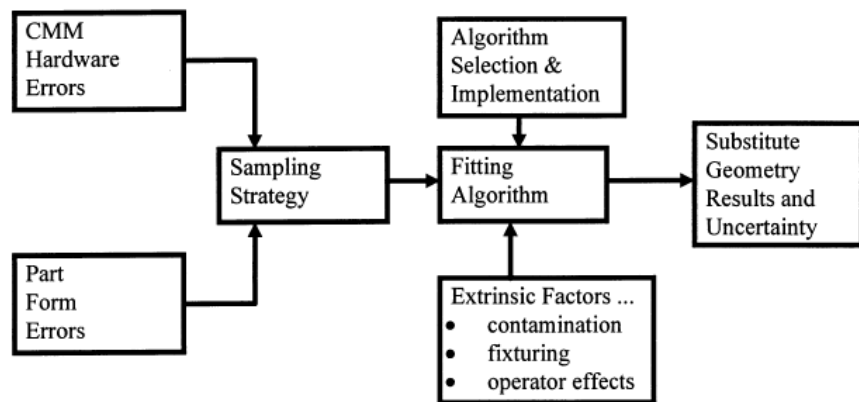


Figure 9. Factors that may impact CMM uncertainty [51]

It important to specify at this point that although measurement uncertainty estimation for coordinate measuring machines can be very complex, feature metrology may become even more complex if ambiguity or standards adoption is not taken into

account when performing measurement uncertainty experiments [61-66]. Danish et al [67] used a standard data set of 22 points with a non ideal form circular feature. The author then performed a Monte Carlo analysis on the data set by perturbing the data set with different measurement uncertainty magnitudes which could potentially represent different CMM's. Four different criteria were then used to perform the substitute geometry task. The Figure-10 highlights the different criteria used:

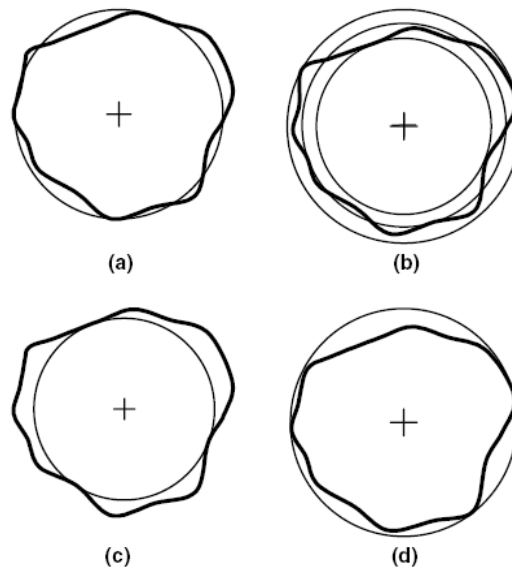


Figure 10. Different criteria for circular substitute features: (a) least square circle; (b) minimum zone circle; (c) maximum inscribed circle; (d) minimum circumscribing circle. [67]

The results below clearly show that depending on the criteria chosen for the substitute geometry, both the mean and uncertainty values will vary. In most cases least squares estimation provided the less sensitive results with increment in CMM measurement uncertainty, but depending on the feature functionality the result could be miss leading. According to ISO 14 660-2 rules when an actual axis/size is required

for a particular measurement task the Least Squares algorithm is preferred due to its stability. The Gaussian regression circle has the advantage of needing the least number of traced points and always being unique. The Chebyshev substitute circle has the advantage of being standardized in ISO 1101 for the assessment of roundness but the disadvantage of needing a much larger number of traced points and not always being unique. The contacting substitute circle (maximum inscribed or minimum circumscribed) has the advantage of being in conformance with ISO 5459 [68] for the definition of datums, but has the disadvantage of not always being unique. Further details on filters when applying substitute geometries are covered by the ISO TS 16610 [69, 70] series.

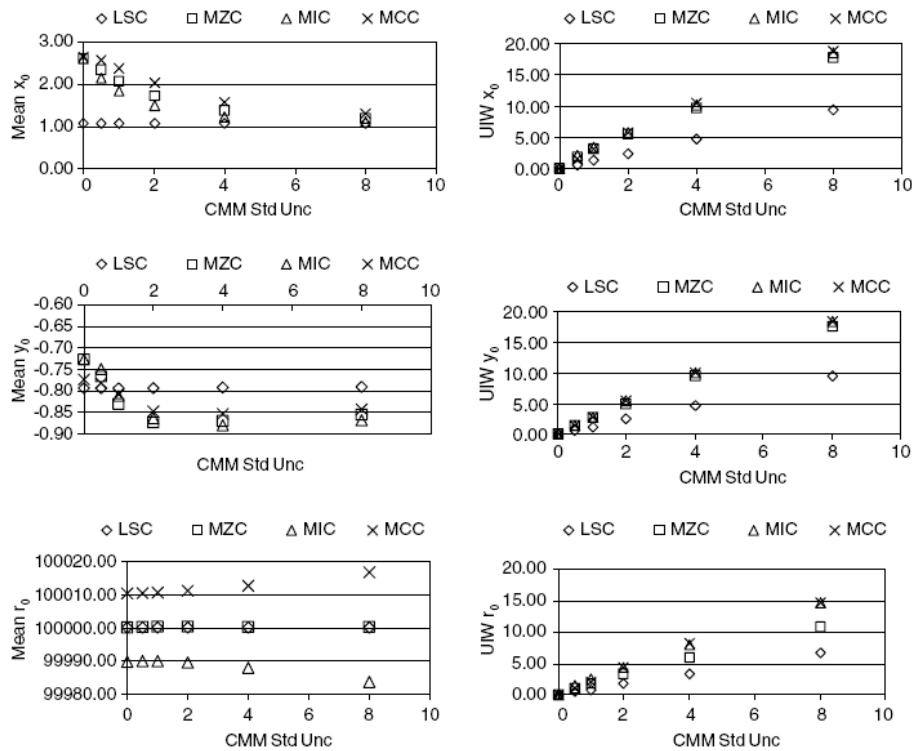


Figure 11. Effect of CMM uncertainty on circular features properties [67]

This effect can be due to the residual errors within the volume of the machine and lobbing effects in the case of kinematic probes [71,72]. Feng et al [58] research applied factorial design approach to the estimation of measurement uncertainty using CMM's. The factors chosen for the study are shown in the Table-5 .

Table 5. Example of CMM factors used for an experimental design [58]

Factors	Levels		
	Low	Medium	High
(A) Speed [%]	50	62.5	75
(B) Stylus Length [mm]	31		51
(C) Probe Ratio (_:1)	9		22
(D) Measurement Points	12	19	26
(E) Starting Position (% Offset)	0	40	60

The confirmation experiment showed that uncertainty was minimized when the speed was highest, stylus length was shortest, probe ratio was largest, and the number of pitch points was largest. The results presented in this study only addressed variability (standard deviation). The Figure-12 showed the entire centre coordinates for the artefact used during all factorial design experiments.

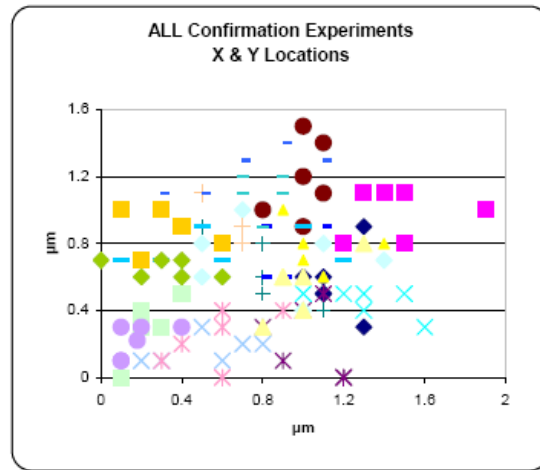


Figure 12. Centre coordinates of all DOE runs [58]

Sun et al [73] explored the development of a comprehensive framework for application of experimental design in determining CMM measurement uncertainty.

Figure-13 shows the split between the key factors used in the DOE.

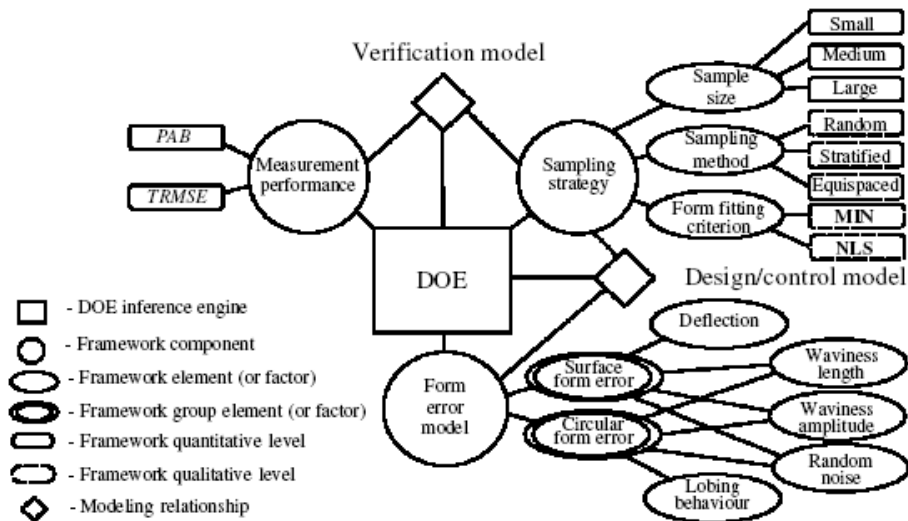


Figure 13. Example of a DOE framework for CMM measurement [73]

Experimental designs have been used in many applications to aid the understating of the behaviour of a particular process or variable. Several studies [74-78] have investigated in detail one of the key stages (Sampling strategy) in the verification model shown in Figure-13 where the measurement strategy proved to be of very important consideration when studying measurement uncertainty and its impact in conformance decisions. Although there can be several approaches to design of experiments [58-62] the list below provides a comprehensive introduction on how to set up [79-84] an experimental design:

(a) Define the objectives of the experiment. At this stage it is very important to understand the specification of the process which the experiment tries to address and in particular a good overview of the input and output factors.

(b) Identify all sources of variation, including:

(i) treatment factors and their levels, as with most variables not every value attributed to it may have an effect on the outcome of a particular event therefore it is critical that the factors and treatment levels are selected in accordance to the objectives of the experiment.

(ii) experimental units, it is not always possible to attribute a numerical value to the treatment levels

(iii) blocking factors, noise factors, and covariates.

(c) Choose a rule for assigning the experimental units to the treatments.

(d) Specify the measurements to be made, the experimental procedure, and the anticipated difficulties.

(e) Run a pilot experiment.

- (f) Specify the model.
- (g) Outline the analysis.
- (h) Calculate the number of observations that need to be taken.

Experimental designs are rules that help determine the assignment of the experimental units to the treatments. Although experiments differ from each other greatly in most respects, there are some standard designs that are used frequently.

Completely Randomized Designs

A completely randomized design is the name given to a design in which the experimenter assigns the experimental units to the treatments completely at random, subject only to the number of observations to be taken on each treatment. Completely randomized designs are used for experiments that involve no blocking factors.

The statistical properties of the design are completely determined by specification of r_1, r_2, \dots, r_v , where r_i denotes the number of observations on the i th treatment, $i = 1, \dots, v$.

Such models are of the form:

$$\text{Response} = \text{constant} + \text{effect of treatment} + \text{error} .$$

Factorial experiments often have a large number of treatments. This number can even exceed the number of available experimental units, so that only a subset of the treatment combinations can be observed.

Block Designs

A block design is a design in which the experimenter partitions the experimental units into blocks, determines the allocation of treatments to blocks, and assigns the experimental units within each block to the treatments completely at random.

In the analysis of a block design, the blocks are treated as the levels of a single blocking factor even though they may be defined by a combination of levels of more than one nuisance factor.

Such models are of the form:

$$\text{Response} = \text{constant} + \text{effect of block} + \text{effect of treatment} + \text{error} .$$

The simplest block design is the complete block design, in which each treatment is observed the same number of times in each block. Complete block designs are easy to analyze. A complete block design whose blocks contain a single observation on each treatment is called a randomized complete block design or, simply, a randomized block design.

When the block size is smaller than the number of treatments, so that it is not possible to observe every treatment in every block, a block design is called an incomplete block

design. The precision in which treatment effects can be compared and the methods of analysis that are applicable will depend on the choice of the design:

- (i) Crossed Blocking
- (ii) Nested Blocking

Split-Plot Designs

A split-plot design is a design with at least one blocking factor where the experimental units within each block are assigned to the treatment factor levels as usual, and in addition, the blocks are assigned at random to the levels of a further treatment factor. This type of design is used when the levels of one (or more) treatment factors are easy to change, while the alteration of levels of other treatment factors are costly, or time-consuming.

Split-plot designs also occur in medical and psychological experiments. For example, suppose that several subjects are assigned at random to the levels of a drug. In each time-slot each subject is asked to perform one of a number of tasks, and some response variable is measured. The subjects can be regarded as blocks, and the time-slots for each subject can be regarded as experimental units within the blocks. The blocks and the experimental units are each assigned to the levels of the treatment factors—the subject to drugs and the time-slots to tasks. In a split-plot design, the effect of a treatment factor whose levels are assigned to the experimental units is generally estimated more precisely than a treatment factor whose levels are assigned to the blocks.

A model [63] is an equation that shows the dependence of the response variable upon the levels of the treatment factors. (Models involving block effects or covariates are considered in later chapters.) Let Y_{it} be a random variable that represents the response obtained on the t th observation of the i th treatment. Let the parameter μ_i denote the “true response” of the i th treatment, that is, the response that would always be obtained from the i th treatment if it could be observed under *identical* experimental conditions and measured without error. Of course, this ideal situation can never happen—there is always some variability in the experimental procedure even if only caused by inaccuracies in reading measuring instruments. Sources of variation that are deemed to be minor and ignored during the planning of the experiment also contribute to variation in the response variable. These sources of nuisance variation are usually represented by a single variable ϵ_{it} , called an *error variable*, which is a random variable with zero mean. The model is then:

$$Y_{it} = \mu_i + \epsilon_{it}, \quad t = 1, \dots, r_i, \quad i = 1, \dots, v,$$

where v is the number of treatments and r_i is the number of observations to be taken on the i th treatment. An alternative way of writing this model is to replace the parameter μ_i by $\mu + \tau_i$, so that the model becomes:

$$Y_{it} = \mu + \tau_i + \epsilon_{it}, \quad t = 1, \dots, r_i, \quad i = 1, \dots, v.$$

In this model, $\mu + \tau_i$ denotes the true mean response for the i th treatment, and examination of differences between the parameters μ_i in the first model is equivalent to

examination of differences between the parameters τ_i in the second model. It will be seen in Section 3.4 that unique estimates of the parameters in the second formulation of the model cannot be obtained. Nevertheless, many experimenters prefer this model. The parameter μ is a constant, and the parameter τ_i represents the positive or negative deviation of the response from this constant when the i th treatment is observed. This deviation is called the “effect” on the response of the i th treatment. The above models are *linear models*, that is, the response variable is written as a linear function of the parameters. Any model that is not, or cannot, be transformed into a linear model cannot be treated by the methods in this book. Linear models often provide reasonably good approximations to more complicated models, and they are used extensively in practice. The specific forms of the distributions of the random variables in a model need to be identified before any statistical analyses can be done. The error variables represent all the minor sources of variation taken together, including all the measurement errors. In many experiments, it is reasonable to assume that the error variables are independent and that they have a normal distribution with zero mean and unknown variance σ^2 , which must be estimated. Proceeding with the analysis when the constant variance, normality, or independence assumptions are violated can result in a totally incorrect analysis. A complete statement of the model for any experiment should include the list of error assumptions. Thus, for a completely randomized design with v specifically selected treatments (fixed effects), the model is:

$$Y_{it} = \mu + \tau_i + \epsilon_{it},$$

$$\epsilon_{it} \sim N(0, \sigma^2),$$

ϵ_{it} 's are mutually independent,

$t = 1, \dots, r, i = 1, \dots, v,$

where " $\sim N(0, \sigma^2)$ " denotes "has a normal distribution with mean 0 and variance σ^2 ."

This is sometimes called a *one-way analysis of variance model*, since the model includes only one major source of variation, namely the treatment effect, and because the standard analysis of data using this model involves a comparison of measures of variation. Notice that it is unnecessary to specify the distribution of Y_{it} in the model, as it is possible to deduce this from the stated information. Since Y_{it} is modeled as the sum of a treatment mean $\mu + \tau_i$ and a normally distributed random variable ϵ_{it} , it follows that:

$$Y_{it} \sim N(\mu + \tau_i, \sigma^2).$$

Also, since the ϵ_{it} 's are mutually independent, the Y_{it} 's must also be mutually independent. Therefore, if the model is a true representation of the behaviour of the response variable, then the data values y_{it} for the i th treatment form a random sample from a $N(\mu + \tau_i, \sigma^2)$ distribution. To aid the analysis of experimental designs tools [84, 85] have been developed over the years.

1.4 CMM based uncertainty assessment

The ISO 15530 series aims at providing terminology, techniques, and guidelines for estimating the uncertainty of CMM measurements. The complexity associated with the topic of CMM measurement uncertainty is reflected by the progress achieved in the last decade by the ISO TC 213 working group. The techniques presented in the ISO 15530 series are compliant with the GUM.

The ISO 15530 series consist of 5 parts as follows:

- Part 1: Overview and metrological characteristics.
- Part 2: Use of multiple strategies in calibration of artefacts.
- Part 3: Use of calibrated work pieces or standards.
- Part 4: Use of computer simulation.
- Part 5: Use of expert judgement, sensitivity analysis and error budgeting

Part 1 provides an overview and metrological characteristics via the introduction of techniques for determining the uncertainty of measurement for a CMM. A list of factors that can potentially affect the measurements produced by a CMM are provided although the document is still in draft version.

Part 2 (the document is still in a draft version) introduces a technique where multiple measurement strategies of the same work piece are used for determining the uncertainty associated with the CMM task. The multiple measurement strategy combines multiple

different orientations as well as different point distributions replicated in each orientation. The calibration value, and related calibration uncertainty are determined by proper calculation based on the database generated by all of the measuring results obtained.

Part 3 introduces the use of calibrated work pieces for a simple uncertainty evaluation of measurements performed by a CMM. The technique applies to specific measuring tasks and to CMM results obtained from both uncorrected and corrected measurements. The standard includes a methodology for non-substitution, where measurements are results in which the CMM indication is not corrected by systematic errors. It also includes a methodology where substitution measurement is used to determine task specific measurement uncertainty. In the case of substitute methodology the CMM indication is corrected by systematic errors, where both the work piece and a proper material standard of size are measured. Guidelines are provided in terms of number of measurements to be taken and which contributors from the measurement process can be used to estimate the task specific measurement uncertainty:

- the calibration uncertainty stated in the artefact certificate;
- the standard uncertainty assessed by the above procedure;
- the standard uncertainty resulting from the variations of form errors,

roughness, CTE, and other relevant parameters in different corresponding workpieces.

Part 4 provides guidelines on estimating task-specific measurement uncertainty using virtual simulations tools. The main sections within the ISO 15530-4 are broken down as follows:

A - UES: Uncertainty Evaluating Software

B - UES model.

C - UES validation.

The Uncertainty Evaluating Software is a software tool used to provide uncertainty evaluation by simulating the overall CMM measuring process of a work piece. UES tools may reside in the CMM OEM software or they can be off-line tools. UES tools suppliers have to provide a list of key attributes of the UES which includes:

- List of CMM metrological characteristics (see some examples below):

Geometric errors, Environmental characteristics, probing system, probing strategy

- Documented techniques used for the uncertainty evaluation.

Algorithms

The standard describes how the UES can be validated:

1 - CMM testing on a calibrated artefact with uncertainty statements. This may consist of simple point to point measurements where the main influence factors could be the

CMM probe and error map if known or known scale errors. The output results should be smaller or equal to 1 in order to pass the test.

2 - Computer-aided techniques where known uncertainty statements based on factors such as form error can be used to check the uncertainty estimated by the UES. It is expected that for known case scenarios the uncertainty output U from the UES should be higher when compared with absolute error E.

3 – Comparison of UES uncertainty with a known reference uncertainty from a calibrated artefact.

4 – Long term statistical investigation. Similarly to method 1 but over a long time period.

Part 5 provides guidelines on the use of expert judgement, sensitivity analysis and error budgeting. In the case of expert judgement it is expected that its use will require the CMM operator/Inspector to be qualified to a particular academic standard. This standard is still under development.

1.4 Virtual Coordinate measuring machines uncertainty estimation

Section 2.2 described both approaches to measurement uncertainty estimation and potential factors that affect the measurement uncertainty quantity within coordinate measuring machines task. Although measurement uncertainty estimation can be derived

from first principles using the GUM approach and or experimental methods, for more complex measurands it may be difficult if not impossible to derive such budgets. Furthermore in the majority of cases in the aerospace industry parts being measured may contain several hundred dimensions all of which may require CMM inspection and an uncertainty statement. Experimental methods as an approach to quantifying uncertainty may therefore become economically unviable for such cases due to both the cost in time used for the experiments and cost associated with a representative reference artefact which would have to be used in the experimental purpose. To overcome the challenges associated with task specific measurement uncertainty in CMM's simulation tools that aim at replicating the measurement task have been developed. Such tools may consist of an algorithm [62, 67, 86 ,87] which may replicate the measurement of a circular feature to full software packages with intuitive user interfaces [88]. The development VCMM tools coupled with advances in CAIP tools within the PLM environment will eventually lead to their integration due to the challenges presented in section 1.1 of this document.

Virtual CMM's such as the Virtual CMM [89] Simulation by constraints [88, 90], Virtual Instrument [91] and Expert CMM [92] were developed to aid the evaluation of task specific measurement uncertainty of complex measurands using Monte Carlo theory. All of the methods work on the basis of propagating the uncertainty from the different sources to the measurement results. Each method may operate in a slightly different approach, for example the Virtual CMM relies heavily on the error map information of the CMM and the uncertainty associated with the error map measurements while PUNDIT/CMM is able to generate a population of machine errors maps that will fall within a particular type of machine specification chosen by the user and its uncertainty

before making any real measurement. Underlying the use of virtual CMM's [93,94] will be good practice in terms of environment of where the machine is kept and general good practice to ensure that the CMM system as a whole is very similar to the virtual simulations.

The Virtual CMM (VCMM)

The virtual coordinate measuring machine (VCMM) approach estimates task specific measurement uncertainty for a specific CMM. The process starts by assigning virtual probing points to an ideal geometry representing a nominal design specification. At each probing point on a particular feature, the VCMM generates a perturbed point [95]. The perturbed point is generated by modelling variations coming from the different contributors to the measurement task. Each contributor is simulated using a probability density function (PDF) and each perturbed point is simulated by combining the information from all input contributors (PDF's).

As with any simulation software the inputs (uncertainty associated with each contributor) should be assessed completely but some of them cannot be easily or economically measured and must be estimated. Contributors such as form error, cleanliness, fixturing variability and operators are not included in the VCMM [96, 97] although cleanliness and fixturing variability can be very hard to model. The Virtual CMM requirements imply that its use may be restrained to CMM's under laboratory conditions rather than shop floor CMM's due to better control of key input contributors in laboratory conditions. Furthermore its application would be better suited for artefacts or parts with very low form error.

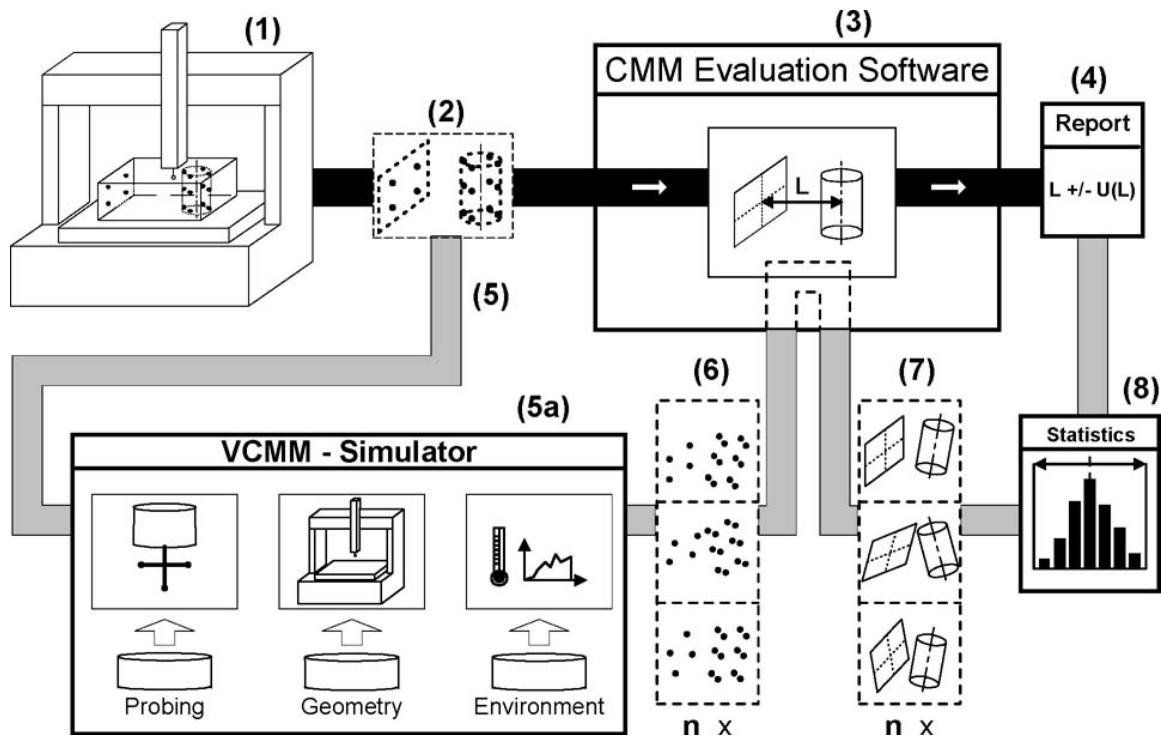


Figure 14. Virtual CMM simulator (VCMM) [89]

The Figure-14 above shows the sequence of events related to both the physical CMM measurements and the Virtual CMM simulator. Steps (1) to (3) represent the collection of data points, the application of substitute geometry to the collected data points and the computation of the specified tolerances. The Virtual CMM simulator shows three typical input factors:

- 1 Probe uncertainty
- 2 CMM geometric errors information
- 3 Environment

The input factors are used to perturb (5a) the original data points collected from the physical measurements via Monte Carlo simulation. This task allows several data sets to be created within the bounds set by the collective uncertainty due to the three input factors. A set of substitute geometries is then computed by the CMM software on the generated data. Statistical analysis (8) can then be used to report the uncertainty results. Although the Figure-15 above provides an example of what could be described as an online Virtual CMM solution, such tools have off-line capability. It is worth noting that the Virtual CMM is very dependent on accurate description of its geometric errors [98, 99]. The accuracy of such errors is directly related to the method used to extract such errors. These methods include reference artefacts [100-102] and laser interferometry/tracking systems [103-105]. The International Joint Research project [106] summarises a collection of projects from different working groups on VCMM's including the PTB (Physikalisch-Technische Bundesanstalt) Germany, NMIJ (National Metrology Institute of Japan) Japan, NML: CSIRO (National Measurement Laboratory) Australia, UT (The University of Tokyo) Japan and TDU (Tokyo Denki University) Japan. guidelines [107,108] of how the Virtual CMM concept could be generalised together with a general methodology to take into account prior calibration information in uncertainty estimation was also proposed by the NPL (National Physics Laboratory). Other VCMM's have been developed [109,110] to include enhanced user interfaces and 3D simulation of the specific measurement task.

The Expert CMM (ECMM)

The Expert CMM project (ECMM) consisted of a collaboration between a national metrology institute and industry [90]. Early testing of the ECMM software was done via measurements on a hole plate that was measured in 100 positions. Its length and its uncertainty were computed with 89% success rate of the calibrated length being within the computed uncertainty with a coverage factor of 2. The result was also a reflection of the well-controlled metrological conditions of the CMM such as environment where the machine was located.

Some of the key characteristics of the ECMM were as follows:

- being consistent with the ISO-GUM;
- being task specific;
- requiring minimum involvement of the user;
- working on line for immediate checks, and off line for comparative evaluations of alternative procedures;
- keeping groups of contributors (CMM, environment, piece) separate, so as to ease troubleshooting in the case of poor accuracy of measurement. The method proposed, as the other parametric methods, once evaluated the parametric errors of the specific CMM, is divided into two parts:
 - the first consists on the superimposition of adequate errors to the measured points; this errors came up from a Monte Carlo simulation of the error model's parameters.

· the second is the propagation of error through the CMM measurement program (called part program) as the two step are included in the same procedure so a Monte Carlo simulation is used in this case also.

A scheme of the proposed methodology is shown in Figure-15.

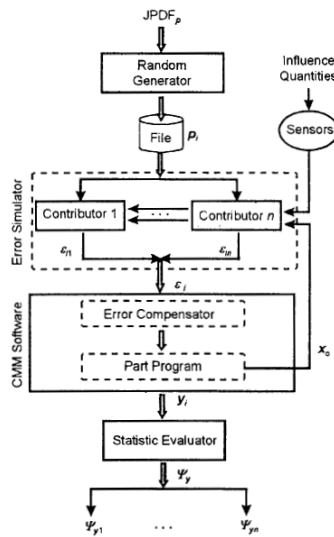


Figure 15. Expert CMM flow chart [92]

The simulator was based on a model $\epsilon_i = g(p_i)$ where p_i are the model parameters with a joint probability density function JPDF_p. The simulator contains the mathematical error model of the specific CMM and it is pretty similar to the compensation model used to compensate the CMM by the manufacturer. The standard CMM software is embedded into additional ECMM software, the error simulator and a statistic evaluator. The error simulator takes an input population of parameters p_i (vector of parameters) from a file generated at random according to a known JPDF_p. The simulator takes also actual information about the measurement in progress: geometrical information x_0 () from the part program, and auxiliary measurement values of influence quantities (typically

temperatures, on line ECMM only). The error simulator outputs the point coordinate perturbations ϵ_i , one for each instance p_i ; this is done separately for different contributor groups $1 \dots n$. The CMM software may have facilities for compensating errors; the (compensated) points are input to the part program, which reduces them to the final results y_i . Finally the variance-covariance matrix Ψ_y is evaluated, separately.

Simulation by constraints - Pundit/CMM

The two previously described virtual CMMs methods require the assessment of the individual parametric errors of the CMM - information that is usually not immediately available and is not included in National or International Standards regarding CMM performance specifications. The simulation by constraints technique [111] which generalizes the virtual CMM simulation concept allows the calculation of task specific measurement uncertainty based on standardized performance data such as ANSI B89.4.1 and ISO 10360 CMM performance specifications. This method treats performance tests specifications as mathematical constraints on the (infinite number) of possible virtual CMM states (each defined by specific parametric errors) that are allowed by the performance data [112]. These constraints, together with reasonable assumptions, such as the parametric errors are smoothly varying functions; greatly limit the number of permissible states that the CMM may occupy. A key feature within Pundit/CMM [113,114] is the possibility to use either the machine specification or its error map if known. This is a key advantage for this type of virtual CMMs because the ISO 10360 tests don't necessarily fully reflect a machine capability. For example, the ANSI B89.4.1

Standards volumetric performance test includes the measurement of ball bar lengths near the extremes of the CMM work zone. This is, in effect, a boundary condition on the allowed parametric error functions. In order to be self consistent, the constrained parametric errors, i.e. the permissible virtual CMM states, must faithfully reproduce the original performance specifications when a simulation of the performance test is computed. The expectation is that the standard specifications should provide sufficient constraints to allow the reasonable calculation of task specific uncertainty.

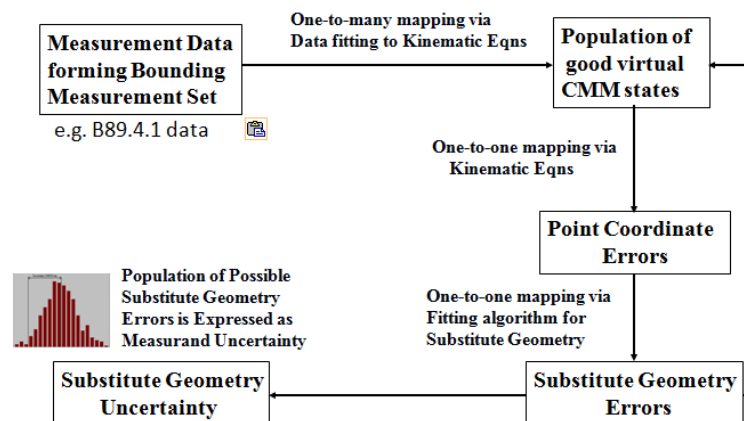


Figure 16. Simulation by constraints flow diagram [114]

A comparison between the VCMM method and Simulation by constraints [87] found that both methods approximated the experimental uncertainty values calculated from the physical measurements of two ring gauges. Furthermore the main difference between the two methods is highlighted by the author in the sense that the VCMM was likely to have a better description of the machine geometry when compared with the MPE values used to describe the machine geometry in the simulation by constraints method.

Hybrid methods

An Early method presented by Hamburg-Piekar et al [115], where for a specific geometrical or dimensional tolerance an uncertainty assessment model is developed making use of known techniques such point wise averaging and reversal methods. The GUM approach was the basis used for the proposed method with Monte Carlo simulations checking the output uncertainties from the GUM approach. The methodology considered five major uncertainty contributors to six general groups of tolerances:

- Repeatability
- Machine
- Probing
- Work piece
- Temperature

Each tolerance model included up to the five major contributors depending on the tolerance being examined. This particular method made use of a database where several test cases were recorded and could be accessed by the operators. A case study was presented by the author for the calibration uncertainty of a reference production part. In the case study the Hybrid method was compared with Pundit/CMM and the results obtained were somewhat mixed with Hybrid method overestimating in the case of parallelism and perpendicularity tolerances while Pundit/CMM overestimated the size

tolerances for diameters. Of particular importance was the range of uncertainties varied between 0.002mm and 0.02mm.

A later patented method [116,117] developed by Politecnico di Torino exploits Monte Carlo technique to calculate the errors in the measured coordinates of each single measured point while using the CMM part programme to propagate the measurement uncertainty. This is a key difference when compared with VCMM's where parametric errors are required; instead the CMM is not modelled. In the simulation the machine specification uncertainty is used similarly to the simulations by constraint approach. The proposed method is an approximated one, providing a reasonable uncertainty evaluation that fits for industrial environment much more than calibration laboratories. The basis of this approach stands on the fact that every CMM measuring task can be divided in to two elementary steps:

1. Measurement of the coordinates of a certain number of points on the surface of the work piece;

2. Evaluation of the measurements in order to calculate one or more substitute features and eventually verify tolerances as stated in the part program. The first step is the one influenced by the effect of uncertainty contributors pertaining to:

- Hardware;
- Sampling strategy;
- Work piece;
- Extrinsic factors.

The second is influenced by uncertainty factors as well but by those contributors related with the fitting algorithms. Its role in the measurement process is to translate the

information contained in the coordinate of point into intrinsic or relational parameters of substitute features in order to calculate the measurands as defined in the measurement program. An additional uncertainty source must be added: it is related with the accuracy of the machine: this term, neglected in the case of comparative measurements as stated in ISO 15530-2, should be here taken into consideration and it is requested as an input quantity by the algorithm. Another remark concerns the uncertainty due to the interaction between the form error of the measurand and the incomplete sampling of surface: this term is usually provided as an input quantity for simulative methods and it's also hard to be taken into account if poor information on measurand is provided. The developed method does not require any input regarding this contributor: its particular algorithm for generating the perturbed data is able to account for it.

1.5 Conformance decisions

Conformance decisions are required to ensure a product meets its required specification but neither the production nor measurement processes are perfect, there will always be some dispersion in the observed product value either for repeated measurements of one item or for measurements of a series of items.

Conformity assessment focuses on determining actual product errors: apparent dispersion due to limited measurement capability should normally be small. Questions of appropriate rules for decision-making in conformity assessment with due account of

measurement uncertainty raise questions which ultimately can be resolved by economic considerations.

Tolerance verification requires a comparison between nominal value and a measured value. The decisions on conformance to specifications are either “acceptance” or “rejection” at final inspection stage. A clear normative framework on conformance decisions has been defined by the ISO 14253. To support such decision rules in order to avoid misunderstanding and disagreement between customer and supplier the concept of measurement uncertainty was introduced. The ISO 14253-1 implements and expands the concept of measurement uncertainty as defined by the GUM Guide to the expression of Uncertainty in Measurement. According to the decision rules shown in Figure-17 . Only measured values in the conformance zone can prove conformance, and only measured values in the non-conformance zone can prove non-conformance.

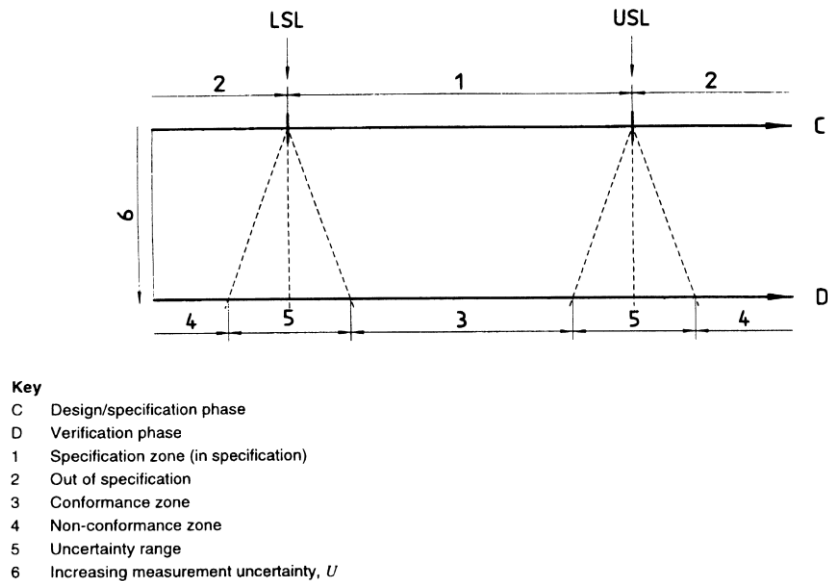


Figure 17. Conformance decision zones [19]

If measured values are within “zone-5” as shown in the Figure-19 above, than it is neither possible for the customer to reject the part, nor for the supplier to accept the part. Rules defined by the ISO 14253-3 were developed to aid situations where measured values are found to be within “Zone-5”. In order to manage measurement uncertainty statements rules have been developed by the ISO 14253-2 in the form of PUMA (Procedure for uncertainty management). PUMA is a procedure developed for calculating and managing uncertainty budgets. Each contributor of the uncertainty budget is clearly identified so that the impact of a particular contributor can be monitored and used to define potential improvements/costs [118] associated with improvements to the overall uncertainty budget and its impact in economic decisions surrounding conformance decisions. An approach [119] to identify the economic impact on uncertainty intervals can be seen in the Figure-18.

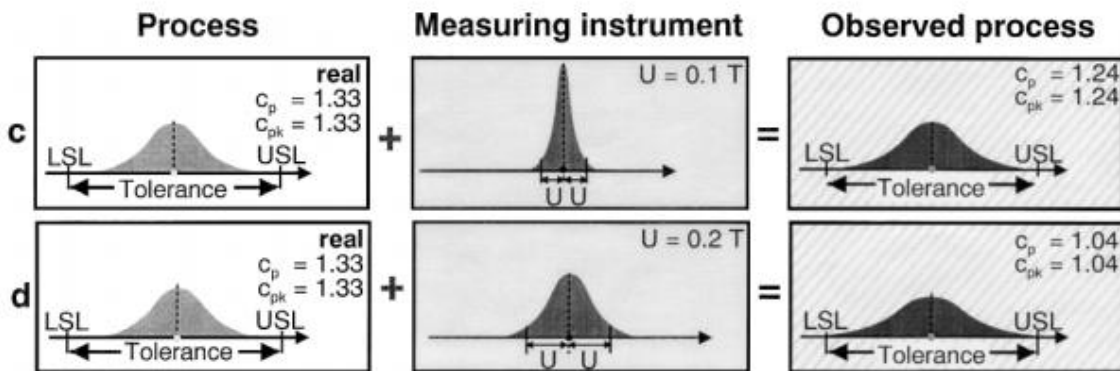


Figure 18. Impact of uncertainty on process capability

The Figure-18 shows that as the uncertainty interval increases and assuming that the rules of the ISO 14253 are being adhered to, the Cp value decreases. According to the chart above if the uncertainty interval was 20% of the tolerance limits the number of

defective parts would increase. This leads to investigations [120, 121] into the production process to try and improve some of the variation that causes the C_p value to decrease or an improvement in the measurement capability could be required. Economics of how to make a decision on the two approaches can in some cases be difficult to evaluate but with the aid of tools such as PUMA it should become clear to the user whether the focus of the measurement capability improvement should be the system itself or the environment it sits on as an example.

1.6 Measurement uncertainty impact in airfoil Leading edge conformance assessment

As mentioned in the previous sections of this document coordinate measurement is required to meet some of the most demanding tolerances in aerospace components. Compressor blades are a group of parts which require coordinate measurement due to its free form features but also due to stringent accuracy requirements specifically surrounding the airfoil shape. Both non-contact and contact measurement systems such as CMM's are used to digitise the airfoil. In the case of CMM's both touch trigger probes and scanning probes can be used to extract the airfoil geometry so that key features within the airfoil profile can be assessed for conformance. As pointed out by Goodhand [108], geometric variability in the form of leading-edge erosion in core compressor airfoils may account for an increase of 3% or more on thrust-specific fuel consumption.

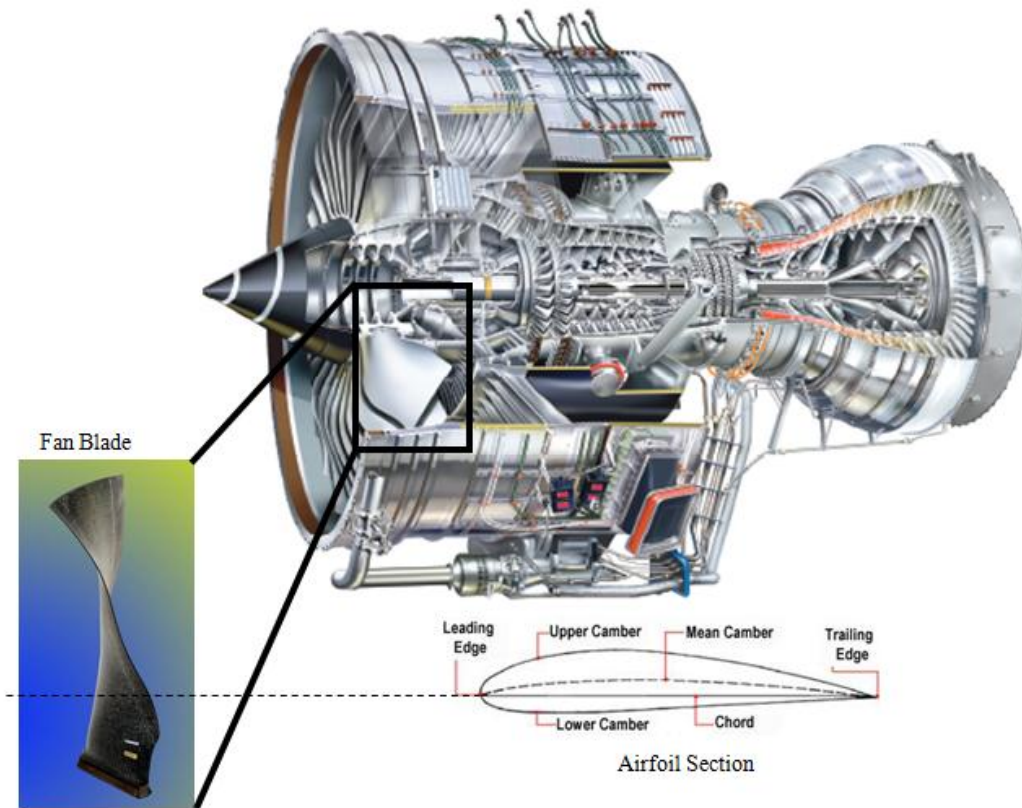


Figure 19. Leading edge of a fan blade airfoil section

As pointed out by Goodhand [108], geometric variability in the form of leading-edge erosion in core compressor airfoils may account for an increase of 3% or more on thrust-specific fuel consumption. A typical approach to aid such potential performance benefits is by tightening manufacturing tolerances to reduce the amount of geometric uncertainty. Unfortunately such approach could become exceedingly costly or otherwise impractical to achieve. Furthermore, normal engine operation leads to changes in compressor and fan airfoil shapes through erosion, corrosion and other means. In addition to geometric variability, perturbations in operating conditions may be simply unavoidable due to the variable environments in which gas turbine engines must operate. In addition to

geometric variability, perturbations in operating conditions may be simply unavoidable due to the variable environments in which gas turbine engines must operate. Leading-edge shape studies focusing on variability of leading edges [122, 123] have taken into account both manufacturing imperfections and wear. Concepts of such effects have been modelled via the bluntness mode described in Section 2.4. The degradation in performance is shown in the Figure-20 as an increase in loss coefficient and a decrease in turning. It has been shown when the bluntness parameter increased to three, the loss coefficient had gone up by approximately 8% while the turning had decreased by about 1.5%. The larger relative impact on the loss coefficient is to be expected since the loss generation for this low-Mach-number transonic case is primarily due to viscous effects, and the leading edge shape will directly impact the boundary layer transition and growth. The effect of leading-edge bluntness can be expected to be more pronounced for higher Mach number cases, as the loss due to leading-edge thickness has been shown to scale with M_{2inlet}^2 [124]. Other authors [125,126] have studied the effect of smoothing the leading edge apex with the remaining of the airfoil using curvature resulting in smoother boundary layer flows, affecting aerodynamic as well as heat transfer performance. It is worth noting although literature clearly indicates benefits specific to a leading edge shape and particular operating conditions, it does not necessarily takes into consideration the uncertainties associated with processing/manufacturing of such shapes and its dimensional measurements. Because of the importance of the leading edge shape, its inspection technique requires very high accuracy which tends to lead most manufacturers to the use of either CMM's or non-contact systems such as GOM [127].

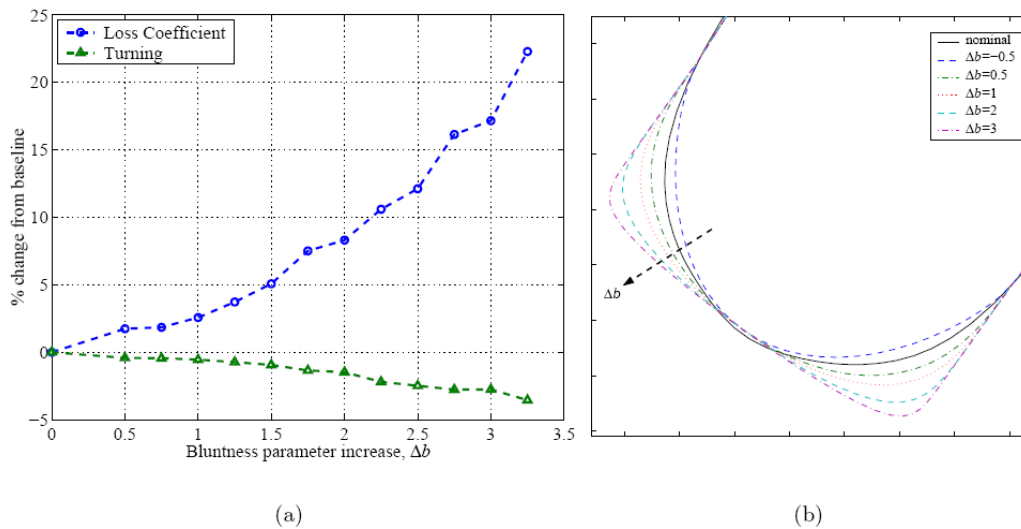


Figure 20. Impact of leading edge bluntness on aerodynamic performance [124]

Assuming a coordinate measuring system such as a CMM was used to digitised a leading edge of an airfoil section of a blade, such data tends to be used for two key activities:

- 1 – Conformance assessment of the airfoil shape
- 2 – Verification of aerodynamic performance

Conformance assessment of airfoils can be performed using standard software packages such as Mitutoyo MAFIS [128] and Zeiss Blade Pro [129]. Such software packages have the capability to perform standard airfoil checks such as cord length, Leading/Trailing edge radius and profile tolerance of the overall shape.

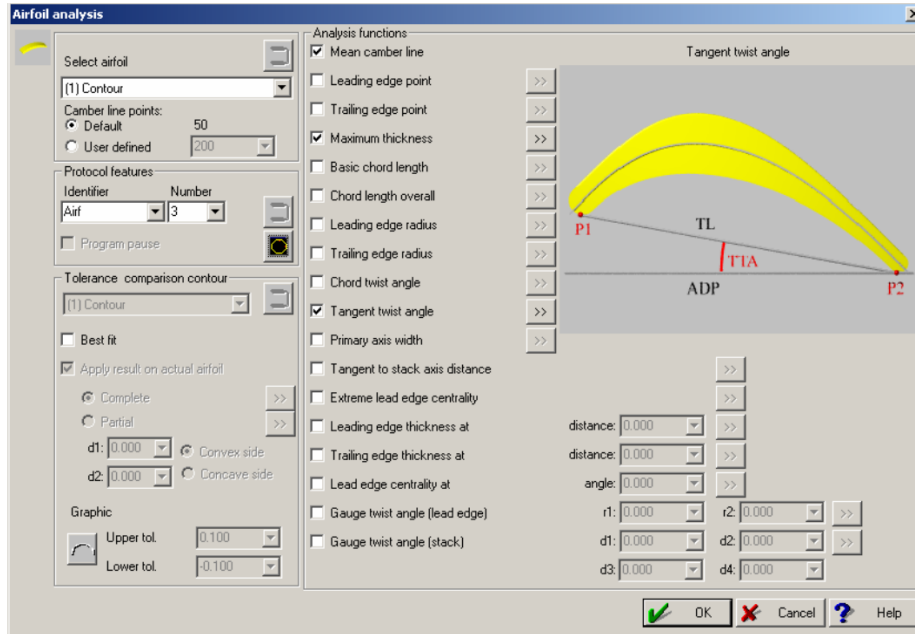


Figure 21. Example of software package for airfoil analysis [128]

Verification of aerodynamic performance could consist of feeding back the original coordinate data captured during the measurement process into a software package such as MISES [130]. In both cases (conformance assessment of airfoil; Simulation of collected data) the raw data output of the measurement system may consist of raw data points or interpolated data such a plane curve. Plane curves [131] are very important and can generally be described mathematically in the following manner:

explicit form: $y = f(x)$ (as a function graph);

implicit form: $f(x, y) = 0$

parametric form: $r(t) = [x(t), y(t)]$

For each of the above plane curves curvature can be derived in the following manner:

parametric form Curvature: Considering a parameterised curve $r(t)=(x(t),y(t))$, the curvature $k(t)$ is given by:

$$k(t) = \frac{\dot{x}\ddot{y} - \ddot{x}\dot{y}}{(\dot{x}^2 + \dot{y}^2)^{3/2}}$$

explicit form Curvature: Considering a plane curve that could be provided as a graph of a function $y=f(x)$, the curvature $k(t)$ is given by:

$$k(t) = \frac{f''(x)}{(1 + f'(x)^2)^{3/2}}$$

This formula for the curvature can easily be derived from the previous one if we represent the curve in the following parametric form:

$$x = t, y = f(t)$$

Implicit form Curvature: Considering a plane curve provided by an equation $F(x,y)=0$:

$$K = kn = -\frac{F_{xx}F_y^2 - 2F_xF_yF_{xy} + F_{yy}F_x^2}{(F_x^2 + F_y^2)^{3/2}}n$$

$$n = \frac{[F_x, F_y]}{(F_x^2 + F_y^2)^{1/2}}$$

Interpolation is used to estimate the value of a function between known data points without knowing the actual function. Interpolation methods can be divided into two main categories [132, 133]:

1 - Global interpolation. These methods rely on a constructing single equation that fits all the data points. This equation is usually a high degree polynomial equation. Although these methods result in smooth curves, they are usually not well suited for engineering applications, as they are prone to severe oscillation and overshoot at intermediate points.

2 - Piecewise interpolation. These methods rely on constructing a polynomial of low degree between each pair of known data points. If a first degree polynomial is used, it is called linear interpolation. For second and third degree polynomials, it is called quadratic and cubic splines respectively. The higher the degree of the spline, the smoother the curve. Splines of degree m , will have continuous derivatives up to degree $m-1$ at the data points.

3 - Linear interpolation result in straight line between each pair of points and all derivatives are discontinuous at the data points. As it never overshoots or oscillates, it is frequently used in chemical engineering despite the fact that the curves are not smooth. To obtain a smoother curve, cubic splines are frequently recommended. They are generally well behaved and continuous up to the second order derivative at the data points. Considering a collection of known points (x_0, y_0) , (x_1, y_1) , ... (x_{i-1}, y_{i-1}) , (x_i, y_i) ,

$(x_{i+1}, y_{i+1}), \dots (x_n, y_n)$. To interpolate between these data points using traditional cubic splines, a third degree polynomial is constructed between each point. The equation to the left of point (x_i, y_i) is indicated as f_i with a y value of $f_i(x_i)$ at point x_i . Similarly, the equation to the right of point (x_i, y_i) is indicated as f_{i+1} with a y value of $f_{i+1}(x_i)$ at point x_i . Traditionally the cubic spline function, f_i , is constructed based on the following criteria:

- Curves are third order polynomials,

$$f_i(x) = a_i + b_i x + c_i x^2 + d_i x^3$$

- Curves pass through all the known points,

$$f_i(x_i) = f_{i+1}(x_i) = y_i$$

- The slope, or first order derivative, is the same for both functions on either side of a point,

$$f_i'(x_i) = f_{i+1}'(x_i)$$

- The second order derivative is the same for both functions on either side of a point,

$$f_i''(x_i) = f_{i+1}''(x_i)$$

This results in a matrix of $n-1$ equations and $n+1$ unknowns. The two remaining equations are based on the border conditions for the starting point, $f_1(x_0)$, and end point, $f_n(x_n)$. Historically one of the following border conditions have been used [134,135]:

- Natural splines. The second order derivatives of the splines at the end points are zero.

$$f_1''(x_0) = f_n''(x_n) = 0$$

- Parabolic run out splines. The second order derivative of the splines at the end points is the same as at the adjacent points. The result is that the curve becomes a parabolic curve at the end points.

$$f_1''(x_0) = f_1''(x_1)$$

$$f_n''(x_n) = f_n''(x_{n-1})$$

- Cubic run out splines. The curve degrades to a single cubic curve over the last two intervals by setting the second order derivative of the splines at the end points to:

$$f_1''(x_0) = 2f_1''(x_1) - f_2''(x_2)$$

$$f_n''(x_n) = 2f_n''(x_{n-1}) - f_{n-1}''(x_{n-2})$$

- Clamped spline. The first order derivatives of the splines at the end points are set to known values.

$$f_1'(x_0) = f'(x_0)$$

$$f_n'(x_n) = f'(x_n)$$

In traditional cubic splines equations 2 to 5 are combined and the n+1 by n+1 tridiagonal matrix is solved to yield the cubic spline equations for each segment [136]. As both the first and second order derivative for connecting functions are the same at every point, the result is a very smooth curve. The above literature review revealed that the application of plane curves to extraction of curvature profiles of Leading edges has been applied in the context of computational fluid dynamics, specifically design intent versus performance behaviour of particular Leading edge profiles under particular working conditions.

Chapter 2

ANOVA estimations of uncertainty in CMM measurements

2.1 Comparison of two uncertainty methods during artefacts measurements

2.1.1 The GUM approach

Three CMMs were chosen for comparison of uncertainty budgets when performing a point to point measurement using calibrated lengths bars. Using the output data of the artefact measurements and applying the GUM approach, the expanded uncertainty was determined in the following way:

- 1 – Calculation of the type A uncertainties
- 2 – Calculation of the type B uncertainties
- 3 – All type A and Type B uncertainties were combined in quadrature to derived the combined standard uncertainty
- 4 – Calculation of effective degrees of freedom to derive the appropriate K value from a t distribution table

Table-6 shows all the measurements runs taken by the CMM-1.

Table 6. Length bar measurement results

Nominal (mm)	30.000	110.000	410.000	609.999	809.999
Run 1	29.999	110.000	410.000	610.000	810.000
Run 2	30.000	110.000	410.001	610.001	810.001
Run 3	30.000	110.000	410.001	610.001	810.000
Run 4	30.000	110.000	410.000	610.000	810.000
Run 5	29.999	110.000	410.000	610.000	810.001
Run 6	30.000	110.000	410.000	610.000	810.000

Determining Type A uncertainties:

The equation 1 was used to derive the type A uncertainty u_{A1} where the subscript A indicated the uncertainty type.

$$u_{A1} = \frac{\sqrt{\frac{1}{n-1} \sum_{i=1}^n x_i (x_i - \frac{1}{n} \sum_{i=1}^n x_i)}}{\sqrt{n}} \quad (2.1)$$

By applying equation 1 to the measurements runs for the 30.0005 mm length bar u_{A1} was found to be 0.00006 mm.

Determining Type B uncertainties:

Machine specification:

The Maximum permissible error statement $\pm(0.6+1.5L/1000)$ μm was interpreted as the envelope in which any measurement result should lie in. For such assumption a rectangular distribution was used to convert the MPE statement into a type B uncertainty in the following manner:

$$u_{B1} = \frac{0.6 + (1.5 \times 30.0005 / 1000)}{\sqrt{3}} = 0.372 \mu\text{m} \quad (2.2)$$

Temperature effects:

The difference between the coefficients of thermal expansion between the CMM and the part to be measured was found to be:

$$CTE_{|CMM-Part|} = 11.5 - 0.15 = 11.35 \text{ ppm} / \text{C} \quad (2.3)$$

Temperature uncertainty for the room where the measurements took place was ± 0.2 C.

$$u_{B2} = \frac{(11.35 \times 30.0005 \times 0.2)}{\sqrt{3}} = 0.0393 \mu\text{m} \quad (2.4)$$

Three other standard uncertainties were derived from temperature effects. Two standard uncertainty terms due to the uncertainty in the coefficients of thermal expansion of the CMM and the part were derived assuming a 10% uncertainty for the CTE values.

$$u_{B3} = \frac{(1.15 \times 30.0005 \times 0.2)}{\sqrt{3}} = 0.00398 \mu\text{m} \quad (2.5)$$

$$u_{B4} = \frac{(0.015 \times 30.0005 \times 0.2)}{\sqrt{3}} = 0.00006 \text{ } \mu\text{m} \quad (2.6)$$

A third standard uncertainty at the time of measurement:

$$u_{B5} = \frac{(11.35 \times 30.0005 \times 0.07)}{\sqrt{3}} = 0.0137 \text{ } \mu\text{m} \quad (2.7)$$

Because no temperature records were available at the time of measurement the same value for temperature uncertainty was used for both u_{B2} and u_{B3} . In most cases it would be expected that the temperature uncertainty at the time of measurement would be of smaller magnitude when compared with the room's temperature uncertainty. Such assumption was valid because the time period for actual measurements was likely to be less than the time period used to determine the room temperature uncertainty. The final standard uncertainty to be used for the combined uncertainty calculation was the calibration uncertainty of the artefact as described in Table-8 (section 2.1.2 of this document).

$$u_{B6} = 0.000085 \text{ } \mu\text{m} \quad (2.8)$$

The combined uncertainty was derived by combining all type A and type B uncertainties in quadrature:

$$u_{AB} = \sqrt{u_{A1}^2 + u_{B1}^2 + u_{B2}^2 + u_{B3}^2 + u_{B4}^2 + u_{B5}^2 + u_{B6}^2} = 0.384 \text{ } \mu\text{m} \quad (2.9)$$

The effective degrees of freedom V_{eff} :

$$V_{eff} = \frac{u_{AB}^4}{\left(\frac{u_A}{n-1}\right)^4} \Rightarrow 30 \quad (2.10)$$

Therefore from the t distribution table $K_{95}=2$. By multiplying the K_{95} value by the combined standard uncertainty u_{AB} the expanded uncertainty was found to be:

$$U_{95} = 2 \times 0.384 = 0.7685 \text{ } \mu\text{m} \text{ (2.11)}$$

Table-7 summarises the GUM uncertainty budget contributors.

Table 7. Uncertainty contributors (GUM)

Uncertainty component	Uncertainty source	Distribution type	Standard Uncertainty type	Magnitude (μm)	DOF
UA1	repeated measurements	N/A	A	0.06	5
UB1	Machine specification	rectangular (1.732)	B	0.372	∞
UB2	Difference between machine CTE (scales) and part CTE using overall temperature uncertainty	rectangular (1.732)	B	0.0393	∞
UB3	Uncertainty in machine CTE	rectangular (1.732)	B	0.00006	∞
UB4	Uncertainty in part CTE	rectangular (1.732)	B	0.00398	∞
UB5	Difference between machine CTE (scales) and part CTE using temperature uncertainty at the time of measurement	rectangular (1.732)	B	0.0137	∞
UB6	Calibration uncertainty of the reference artefact	normal (2)	B	0.000085	∞
UAB	Combined Uncertainty			0.379120075	>30
U95	Expanded Uncertainty			0.75824015	

The major contributor in the above GUM budget was found to be the Machine specification followed by the artefact calibration uncertainty contributor.

2.1.2 ISO 15530-3

According to the ISO 15530-3 the expanded uncertainty U_{95} can be calculated from the following standard uncertainties:

$$U_{95} = k \sqrt{u_p + u_{B6} + u_w} + |e_s| \quad (2.12)$$

The uncertainties of the measurement task were described in Table-8 as follows:

Table 8. Uncertainty components according to ISO 15530-3

Uncertainty component	Uncertainty type according to GUM	Variable
Geometrical errors of CMM Temperature of CMM Drift of CMM Temperature of workpiece Systematic errors of probing system Repeatability of the CMM Scale resolution of the CMM Temperature gradients of the CMM Random errors of the probing system Probe changing uncertainty Errors induced by the procedure (clamping, handling, etc.) Errors induced by dirt Errors induced by the measuring strategy	A	u_p
Calibration of the calibrated workpiece	B	u_{B6}
Variations among workpieces and calibrated workpiece in roughness form expansion coefficient elasticity	A&B	u_w

The uncertainty budget derived was based on the same length bar measurements (30.0005m) as shown in the previous section of this document. The standard uncertainty u_w was derived in the following way:

$$u_w = (20.6 - 20) \times 30.0005 \times 1.15 = 0.000021 \text{ } \mu\text{m} \quad (2.13)$$

Where 20.6 C was the average temperature during the measurements of the length bar and 1.15 ppm/C the uncertainty on the CTE of the part.

The standard uncertainty u_p :

$$u_p = \sqrt{\frac{1}{n-1} \sum_{i=1}^n x_i (x_i - \frac{1}{n} \sum_{i=1}^n x_i)} = 0.00013784 \text{ } \mu\text{m} \quad (2.14)$$

The artefact calibration uncertainty:

$$u_{B6} = 0.000085 \text{ } \mu\text{m} \quad (2.15)$$

The systematic error:

$$|e_s| = 0.00045 \text{ } \mu\text{m} \quad (2.16)$$

The expanded uncertainty U_{95} :

$$U_{95} = 0.777 \text{ } \mu\text{m} \quad (2.17)$$

Other uncertainties such as rounding, probe ball diameter, lack of parallelism of faces, dust could also be considered within the uncertainty budget although their contribution in

this particular example was relatively small. Appendix 2.1 contains all the data for the three CMM's.

The Figures-22, 23 a);b) show the comparison between the ISO 15530-3 and the GUM budgets for three CMMs using length bar measurements data. All three machines were housed in controlled environments. CMM-1 and CMM-2 were used as reference machines for calibration purposes while CMM-3 was a production machine. CMM-1 specification (0.6+1.5L/1000 μ m), repeatability and systematic error were also shown on the chart:

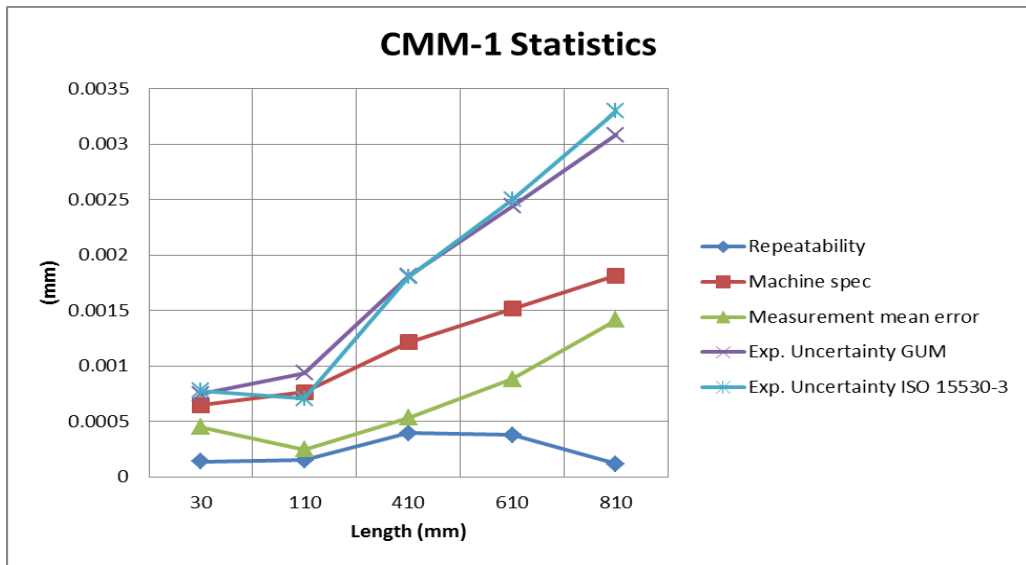
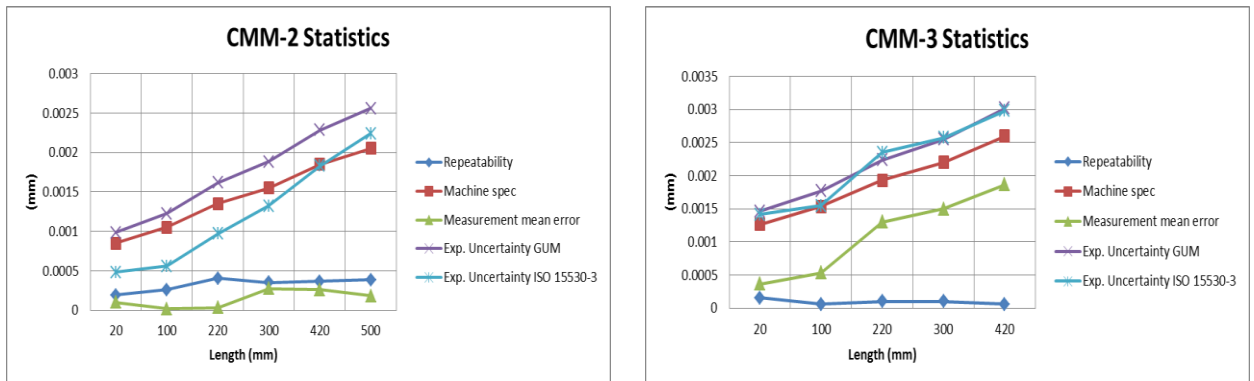


Figure 22. Comparison of length bar measurements using CMM-1

From the Figure-22 above both the ISO 15530-3 and the GUM budget results follow the same trend and magnitudes above the machine specification and mean error values. The Figure-23 shows the same methodology applied to two other coordinate measuring machines. The results shown for CMM-2 indicate that there were some differences between the two uncertainty budgets. While the GUM budget trend was found to be

above the machine specification, the ISO 15530-3 budget was found to be below the machine specification.



a) Machine specification: $0.8+L/400$ (μm)

b) Machine specification: $1.2+3.3L/1000$ (μm)

Figure 23. a) Comparison of length bar measurements using CMM-2; b) Comparison of length bar measurements CMM-3

CMM-3 statistics were found to very similar to CMM-1 statistics in the sense that both uncertainty budgets followed similar trends and magnitudes above the machine specification. For both CMM-1 and CMM-3 the measurement mean error values were found to be above the repeatability values. CMM-2 showed repeatability values above the measurement mean error. The results highlighted some key differences between the two approaches investigated for deriving CMM uncertainty budgets. While the GUM approach focused on using specification information to derive standard uncertainties the ISO 15530 approach relied heavily on the output measurement data. This implied that the ISO uncertainty budget would always be more sensitive to the uncertainties associated with the measurement task. While the major contributor to the uncertainty budget in the

GUM approach was consistently the machine specification (*UBI*), the ISO budget revealed that the contributors relative importance varied with the calibration uncertainty becoming the major contributor for the 500mm length measurement (Table-9).

Table 9. Uncertainty contributors (GUM, ISO 15530-3)

Nominal (mm)		20.0008		100.0032		500.0468			
Nominal (mm)		20.0008		100.0032		500.0468			
GUM (um)	Contribution to Expanded Uncertainty %	GUM (um)	Contribution to Expanded Uncertainty %	GUM (um)	Contribution to Expanded Uncertainty %	GUM (um)	Contribution to Expanded Uncertainty %		
Type B		Type B		Type B		Type B			
LS1	LSM	LS1	LSM	LS1	LSM	LS1	LSM		
0.490746884	50	0.001381611	0	0.034617718	48	1.183534688	46	0.874663511	36
LS2	LSM	LS2	LSM	LS2	LSM	LS2	LSM		
0.019557325	2	0.190932516	40	0.077801894	6	0.388769024	15	0.383336627	17
LS4	LSM	LS4	LSM	LS4	LSM	LS4	LSM		
0.009543822	1	0.1	21	0.028224544	2	0.019666667	3	0.183333333	8
LS5	LSM	LS5	LSM	LS5	LSM	LS5	LSM		
0.009151396	1	0.015180607	3	0.045769524	4	0.079517609	14	0.379551142	17
LS3	LSM	LS3	LSM	LS3	LSM	LS3	LSM		
0.004058095	0	0.020443868	2	0.10207615	4				
LS0	LSM	LS0	LSM	LS0	LSM	LS0	LSM		
1.38161E+05	0	3.49177E+05	0	0.874663511	34				
4.7	4.7	4.7	4.7	4.7	4.7	4.7	4.7	4.7	4.7
4.36436E+05	0	8.73872E+05	0	7.21E+05	0				
Expanded Uncertainty of 95% (k=2)	Expanded Uncertainty of 95% (k=2)	Expanded Uncertainty of 95% (k=2)	Expanded Uncertainty of 95% (k=2)	Expanded Uncertainty of 95% (k=2)	Expanded Uncertainty of 95% (k=2)	Expanded Uncertainty of 95% (k=2)	Expanded Uncertainty of 95% (k=2)	Expanded Uncertainty of 95% (k=2)	Expanded Uncertainty of 95% (k=2)
0.68200215	0.463016	1.27848165	0.96959576	2.567307214	2.26933002				

2.1.3 Impact of measurement uncertainty in conformance assessment

In the previous section two methods for deriving uncertainty budgets during CMM linear point to point measurements were derived and compared. The ISO 14253-1 defines the rules for conformance and non-conformance specification by recommending that rules be applied for the most important specifications controlling the function of the work piece or the measuring equipment. At a design stage the terms “in specification” and “out of specification” refer to areas separated by the upper and lower tolerance (double sided) or either LSL or USL for a one sided specification. When dealing with the manufacturing or measurement stages of the process the LSL and USL are added to by the measurement uncertainty. The conformance or non-conformance ranges are reduced due by the uncertainty. Such rules are to be applied when no other rules are in existence between supplier and customer. ISO 14253 allows for other rules to be agreed between customer and supplier. Such rules should be fully documented. During the verification stage the uncertainty range separates the conformance zone from the non- conformance zone.

Assuming that CMM-1 (section 2.1) was to be used to measure parts with linear dimensions of nominal size 30mm and a tolerance of $\pm 0.003\text{mm}$, the application of conformance decisions could be applied since the uncertainty values required for the verification stage were previously evaluated in section 2.1 of this document.

A part was measured as 30.0025mm. The expanded uncertainty derived for CMM-1 for a nominal length of 30.0005mm was found to be $0.77\mu\text{m}$ according to both the GUM and ISO 15530-3 standards. Such result implied that the actual measurement lied between

30.0018mm and 30.0032mm. Two other parts were measured with values of 30.005mm and 30.001mm respectively.

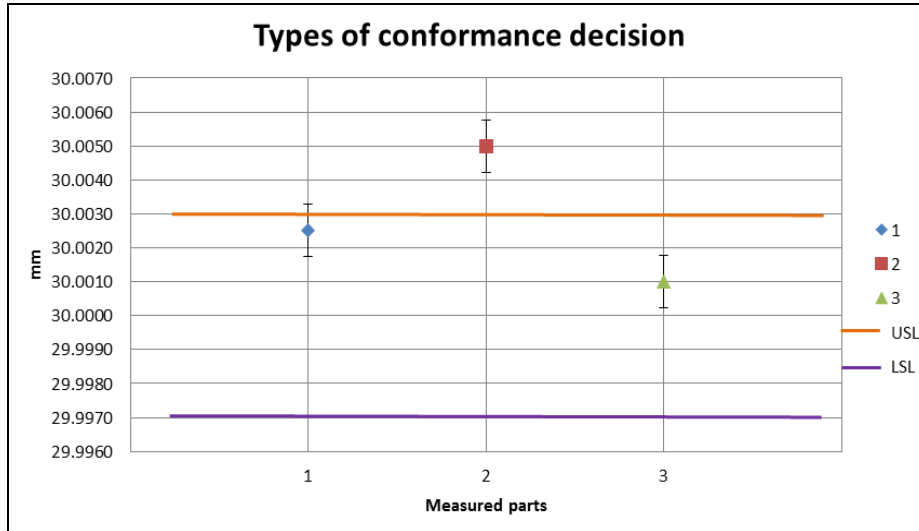


Figure 24. Measured parts conformance assessment types.

By applying the conformance decision rules in accordance with the ISO 14253-1 the following results were obtained:

For measured part 1 the result of the measurement was found to be neither conformance nor non-conformance with a specification can be proven. In the case of part 2 the result of the measurement was found to be above the USL and so non-conformance was proven. Part 3 result of measurement was found to be above the LSL and below the USL and so conformance was proven. From the results shown in Figure-24 it was clear that only the 3rd part measured conformed to verification specification in the case of using CMM-1. All the above results indicated that a CMM specification was the major key contributor to the measurement uncertainty and that for the machines investigated. Under the circumstances above it could be acceptable using the machine specification standard

uncertainty as the only quantity towards the expanded uncertainty budget but in cases where a CMM temperature could vary in the +/-2 C range this would no longer be acceptable as shown by the change:

$$u_{B2} = \frac{(11.35 \times 30.0005 \times 2)}{\sqrt{3}} = 0.393 \text{ } \mu\text{m} \text{ (2.18)}$$

The *UB2* contribution would be as high as the CMM specification of 0.372 μm .

Two options could be explored to improve the impact of measurement uncertainty on conformance decisions:

- 1- Assuming that such prior knowledge existed in terms of expanded uncertainty, the information provided in the chart above could be used as a measurement capability feedback to the design authority because in principle further work could be carried out by designers to study the impact of altering the design specifications (USL,LSL). As such, potentially all 3 measured parts could become conformant with specification.

- 2- A second option assuming that design specification could not be changed would be the use of the PUMA method. The ISO 14253-4 provides guidelines for management of uncertainty statements via the Procedure for uncertainty of measurement management (PUMA).

2.2 Sensitivity screening study of circular features with symmetrical lobbing

2.2.1 Monte Carlo simulation definitions

The impact of CMM point coordinate uncertainty has been investigated by previous authors [58,59] when determining the size and location of prismatic features such as circles and planes. Their work demonstrated how the impact of point uncertainty applied to a feature with predefined fixed form error affected the output response when applying different substitute geometry algorithms. This approach is based on only a single variable perturbing each measurement point represented by a normal distribution with specific standard deviation values.

Factors such as form error and sampling strategy could be directly related because the information available for one parameter could influence the other. In this sense if a feature contains a form tolerance, the sampling strategy should reflect such tolerance. Form error itself by definition should be the representation of the true surface of a feature and as such in most cases is a function of the process used to manufacture such feature. On the other hand even for a feature with perfect form, form error can still occur but in this case it is induced by the measurement system in specific by a CMM. This effect can be due to the residual errors within the volume of the machine and lobbing effects in the case of kinematic probes. Random effects associated with coordinate measuring machines can be assumed (CMM in a measurement room under controlled environment) to be normally distributed with a standard deviation (repeatability) of 1 micron [50,51].

In a production environment the form of a feature is process specific therefore a good sampling strategy [51, 67] for a feature with three lobes may not be ideal for a feature with four lobes. Furthermore the lobes may have different magnitudes and CMMs of different specifications may be used to measure such features. In order to explore the impact of such factors on CMM measurement uncertainty it was decided to firstly distinguish the different types of lobbing effects by grouping them into two categories:

- 1 - Symmetrical lobbing
- 2 - Non symmetrical lobbing

Symmetrical lobbing can be expressed in polar coordinates using:

$$r(\theta) = r_0 + \rho \cos(\omega\theta) \quad (2.19)$$

Where 2ρ is the roundness of the circle also known as form and $\omega\theta$ the number of lobes (periodic function). In the Cartesian workspace equation (2.19) can be expressed using:

$$\begin{aligned} x &= r \cos(\theta) \\ y &= r \sin(\theta) \end{aligned} \quad (2.20)$$

Some random noise can be added to equations (2.20) using:

$$\begin{aligned}
 X &= x + \gamma \\
 Y &= y + \tau
 \end{aligned}
 \tag{2.21}$$

where $\gamma, \tau \in N(0, \sigma^2)$

Random noise in this study represented the CMM uncertainty by converting the machine MPE value to a standard uncertainty (Table-10). This conversion followed the guidelines set by ISO 14253-2 (section 8.4.5) where:

$$\gamma, \tau = MPE \times b
 \tag{2.22}$$

Where b represented a rectangular distribution.

Table 10. CMM's standard uncertainties

Machine	MPE (μm)	b (Distribution)	Standard uncertainty (Feature(μm))
CMM A	$2.5+3L/1000$	0.6	1.529
CMM B	$5+3L/1000$	0.6	2.973
CMM C	$7.5+3L/1000$	0.6	4.416

During each run of the Monte Carlo simulation the phase angle of the probing points was also randomised. This assumption was made due to the fact that in a production

environment it was likely that the phase angle of a particular form error could change with time. Of particular importance was to understand the behaviour of a circular feature given two types of systematic lobbing, fixed number of probing points and three measurement uncertainty values which represented three different CMM specifications.

The quantities investigated were as follows:

- a) Mean error

$$\text{Mean error} = \frac{1}{n} \sum_{i=1}^n x_i - x_{\text{nominal}} \quad (2.23)$$

- b) Standard deviation

$$\text{stdev} = \sqrt{\frac{1}{n-1} \sum_{i=1}^n x_i (x_i - \frac{1}{n} \sum_{i=1}^n x_i)} \quad (2.24)$$

- c) % of form captured

$$\% \text{ form} = \left(\frac{\text{Min}(r) - \text{Max}(r)}{2\beta} \right) \times 100 \quad (2.25)$$

2.2.2.3 Lobe feature screening experiment results

The Table-11 summarises the implementation of the above methodology for two circular features with centre coordinates X,Y (50,50(mm)).

Table 11. Factors selected for the Monte Carlo simulation of features with systematic form error.

Lobe Type	Radius Lobe Magnitude (mm)	CMM U (mm)	N. probing points	X,Y centre coordinates (mm)
3	0.021	0.00152	17	50,50
3	0.021	0.00297	17	50,50
3	0.021	0.00441	17	50,50
5	0.021	0.00152	17	50,50
5	0.021	0.00297	17	50,50
5	0.021	0.00441	17	50,50

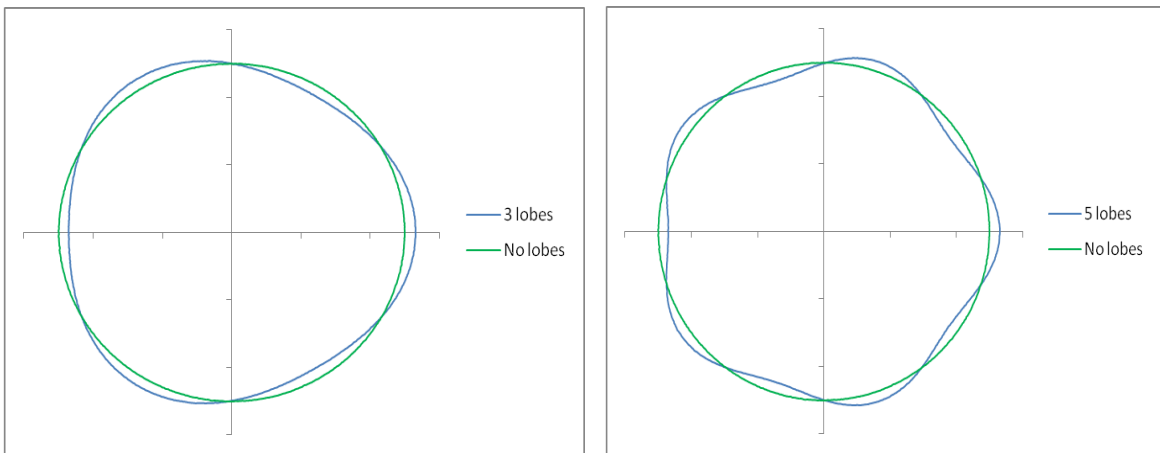
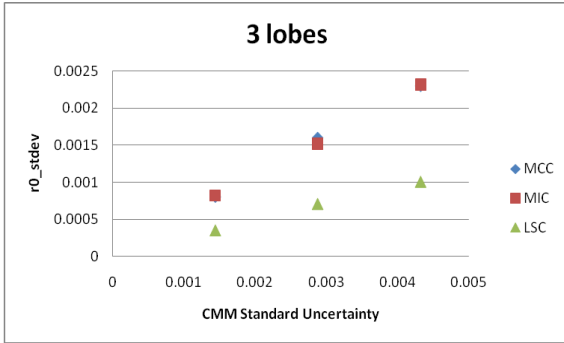
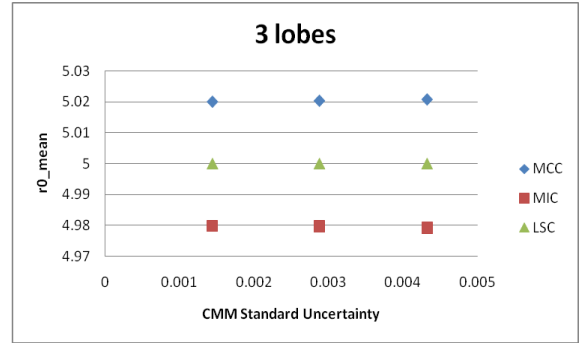


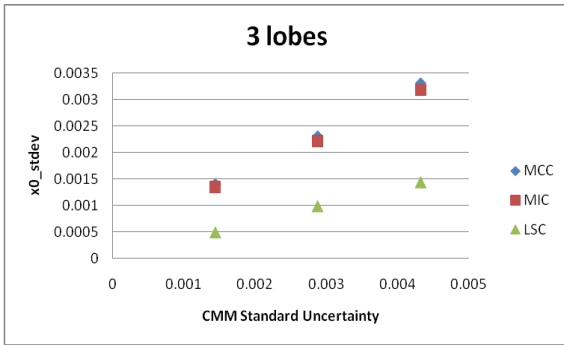
Figure 25. Circular feature with 3,5 lobes form error vs circular feature with no form error



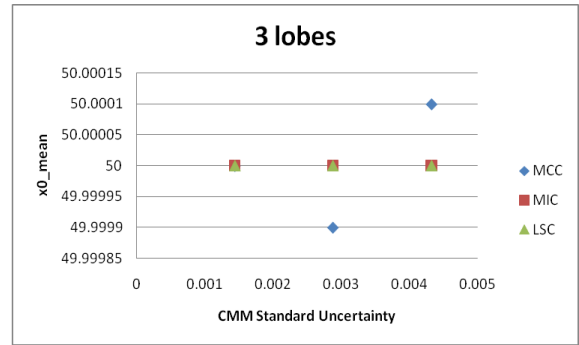
a)



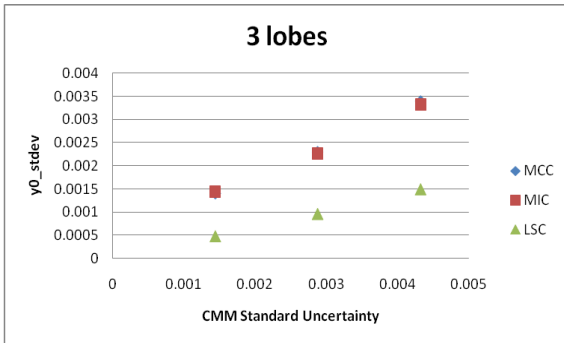
d)



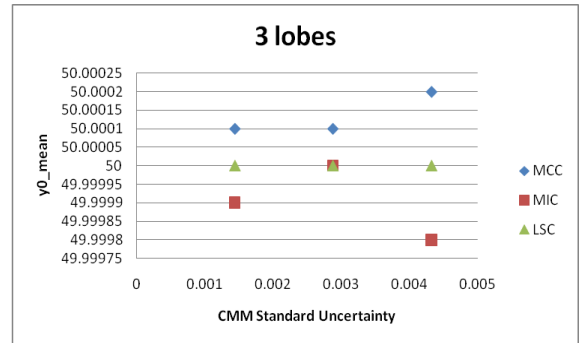
b)



e)



c)



f)

Figure 26. Simulation results for the three lobed features

From the Figure-26 above it was clear that the stdev values of r0, x0 and y0 increased with increment in the CMM standard uncertainty values almost linearly for all criteria.

The stdev values for r0, x0 and y0 were found to be smaller for LSC when compared with MIC and MCC criteria. This result showed that with increment in CMM standard uncertainty all stdev parameters also increased. Of particular interest was the difference between y0_stdev value for LSC between 0.00159mm and 0.00416mm which was found to be approximately 0.001mm. The same comparison when done for MCC or MIC was found to be 0.002mm. The stdev results presented can be converted to an expanded uncertainty interval at 95% confidence. This could be achieved by determining the interval of the distribution between 2.5% and 97.5% or the equivalent 2sigma.

The mean error results obtained show slightly different behaviour in comparison to the Stdev results. For the LSC criteria the x0 and y0 values did not vary with increments in the CMM standard uncertainty values. The r0 value was found to be stable for the LSC criteria with a slightly increase for the MCC and decrease for MIC with increments in CMM standard uncertainty.

Figure-27 shows the calculated area resultant from 1000 Monte Carlo runs for the centre coordinates of the 3 lobed circular feature for the different criteria. Area values reflected the maximum envelope size defined by the maximum X centre coordinate and maximum Y centre coordinate.

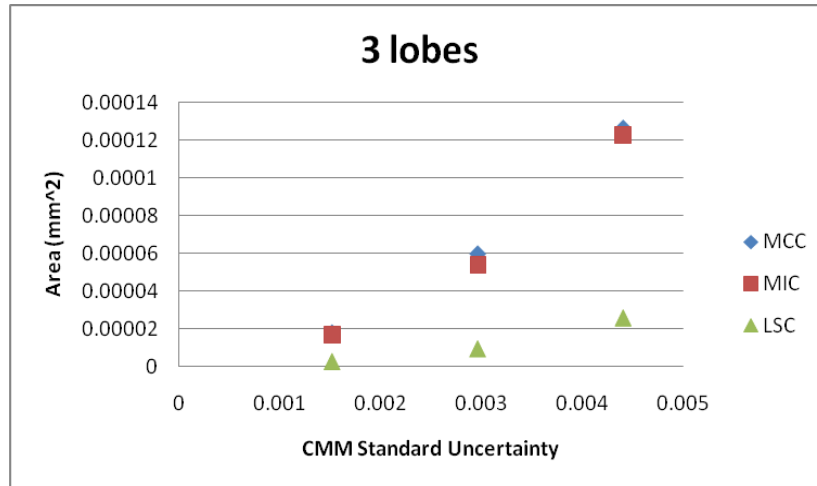


Figure 27. Simulation results for centre coordinates areas of the three lobed feature

The positional area values appeared to increase almost linearly for all the criteria. The difference between the LSC values and the MIC/MCC also increased with increments in the CMM standard uncertainty values. Of particular interest was the difference between the areas for CMM B between LSC and MIC/MCC and the area for CMM C between LSC and MCC/MIC, where the area difference doubled between the two CMMs. The Figure-28 shows all the centre coordinates for the MIC criteria using the CMM B standard uncertainty value.

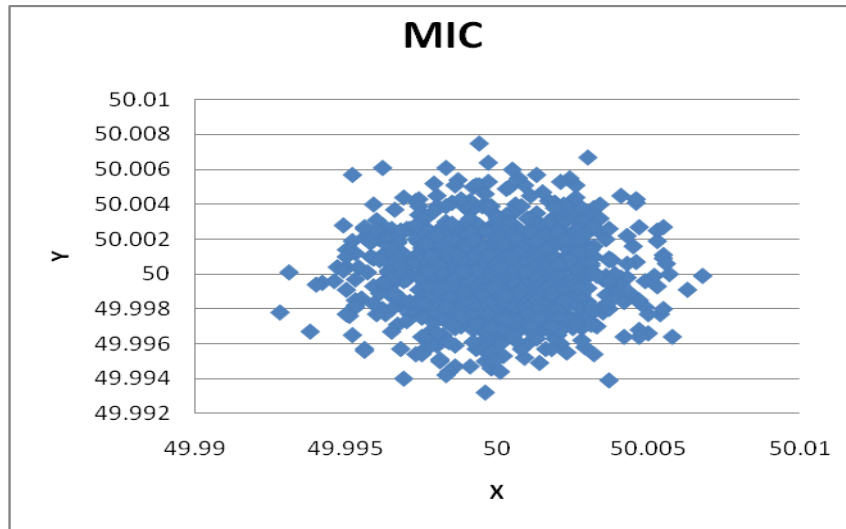
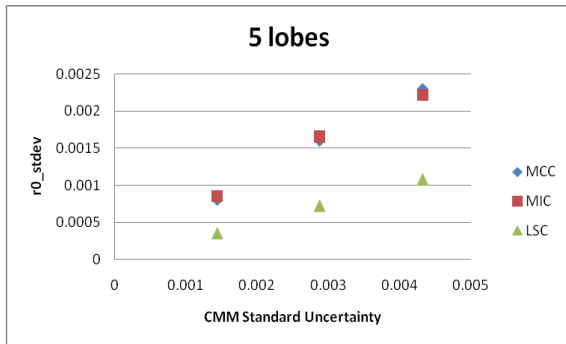


Figure 28. Impact on centre coordinates when applying MIC to a three lobed feature

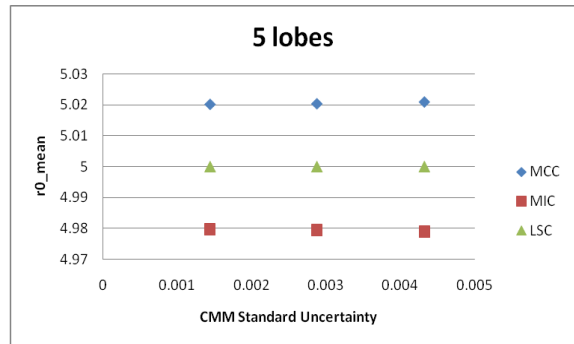
The maximum X,Y centre coordinate deviation from nominal was found to be 0.007mm. From the figure above it was found that the majority of the centre coordinate values for the Y coordinate remained between 50.004 and 49.996mm while the values of the X coordinate remained between 50.003 and 49.997. This result showed the potential uncertainty associated with position of circular features in the measurement space. This result only represented the variation in position of a particular circular feature due to the uncertainties associated with the measurement strategy for the feature. It is foreseen that a Datum feature to which this feature could be referenced to undergoing a similar measurement strategy, could increase the above variation in position uncertainty because both Datum and feature would now vary in a similar manner as observed in the Figure-28.

2.2.3 5 Lobe feature screening experiment results

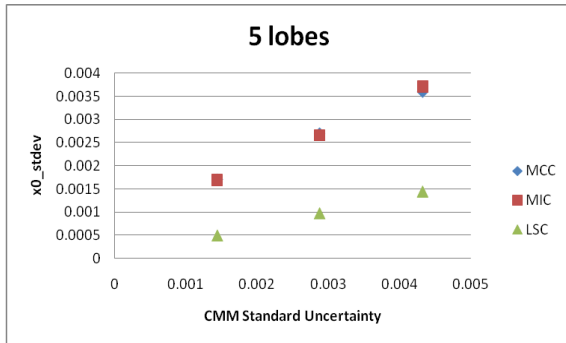
Below are the results for the 5 lobed circular features under the same input conditions as the 3 lobed features in the previous section.



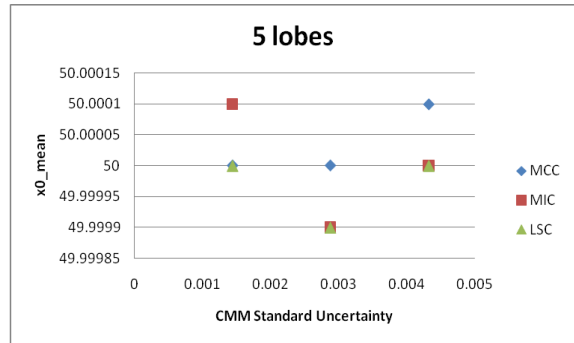
a)



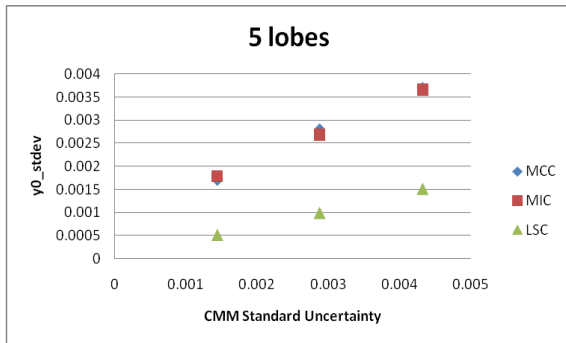
d)



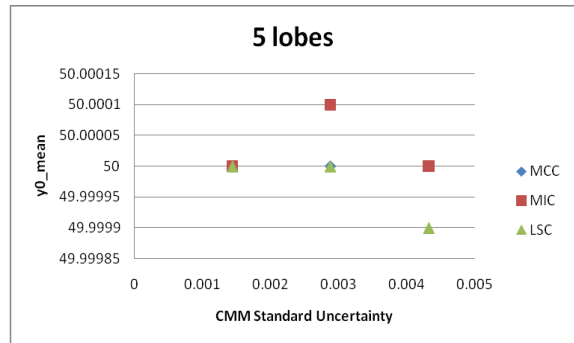
b)



e)



c)



f)

Figure 29. Simulation results for the three lobed feature

From the Figure-29 it was found that the stdev values of r_0 , x_0 and y_0 increased with increment in the CMM standard uncertainty values almost linearly for all fitting criteria. The stdev values for r_0 , x_0 and y_0 were found to be smaller for LSC when compared with MIC and MCC criteria, a similar result to the one obtained for the 3 lobed feature. The maximum stdev value for r_0 was found to be 0.022mm for the MIC/MCC criteria and 0.001mm for the LSC criteria. The maximum value for the stdev for the centre coordinates for MIC/MCC was found to be 0.0037mm and for LSC 0.0015mm.

A different set of results were found for the mean error values of r_0 , x_0 and y_0 . Unlike the results obtained for the 3 lobed feature, the x_0 and y_0 values varied randomly with increments in the CMM standard uncertainty values. The r_0 values were found to be stable for the LSC criteria and slightly increase for the MCC and decrease for MIC with increments in CMM standard uncertainty.

The Figure-30 shows the area values determined from the Monte Carlo runs for all criteria for the three CMM standard uncertainty values. The area values for LSC criteria were found to be smaller when compared with MIC/MCC. The difference between the LSC values and the MIC/MCC values increased with increments in the CMM standard uncertainty values. When compared with the area values obtained for the three lobed feature, the 5 lobed feature results were found to be almost 100% higher in magnitude but of very similar trend to the trend displayed in Figure-27.

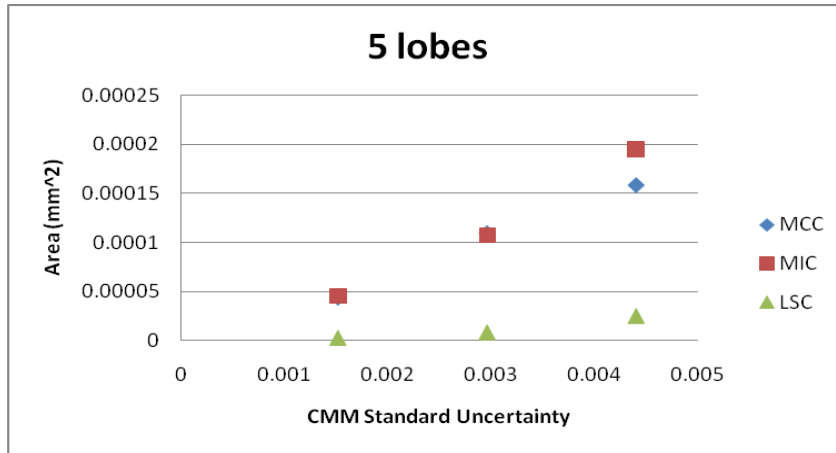


Figure 30. Simulation results for centre coordinates areas of the five lobed feature

Figure-31 shows all the centre coordinates for the MIC criteria for CMMB.

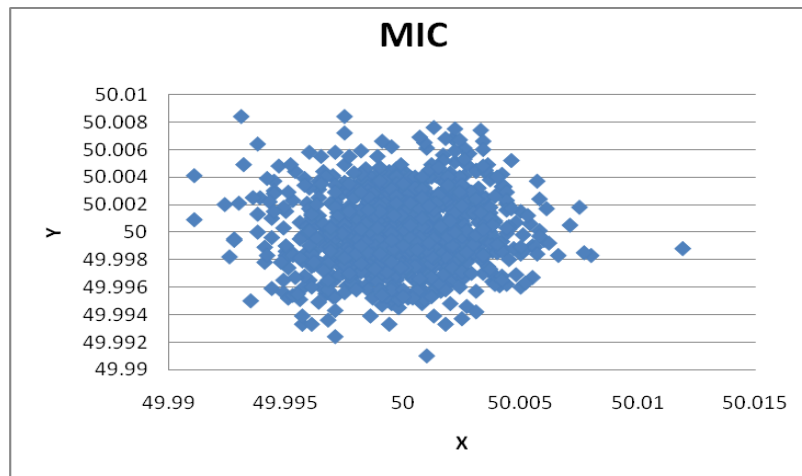


Figure 31. Impact on centre coordinates when applying MIC to a five lobed feature

When comparing the area figures obtained in Figure-31 for the five lobed feature with Figure-28 (3 lobed feature) it can be seen that its area values were of higher magnitude. This result was also visible when comparing the maximum X,Y centre coordinates where the five lobed feature maximum X coordinate deviation was found to be 0.011mm when compared with the 3 lobed feature value of 0.007mm.

The results obtained clearly highlighted the impact of a particular number of factors on the standard uncertainty of a feature size and position for three different criteria. Of particular importance is that all values showed above (Stdev) reflected one standard uncertainty (1 sigma). Furthermore the lobes used to simulate feature form error were assumed to be systematic.

Although 1000 Monte Carlo runs were used in this screening study to simulate measurements of a particular feature, in a production environment a set of three repeated measurements could be represented by the Figure-32. This assumption tries to illustrate how the cost associated with such experiments can output results with high uncertainties.

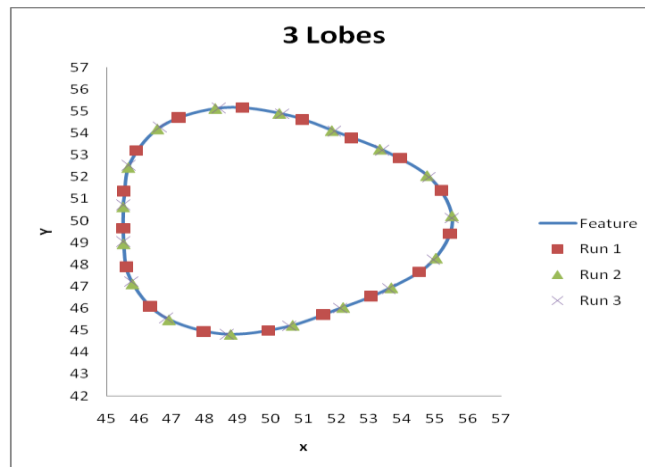


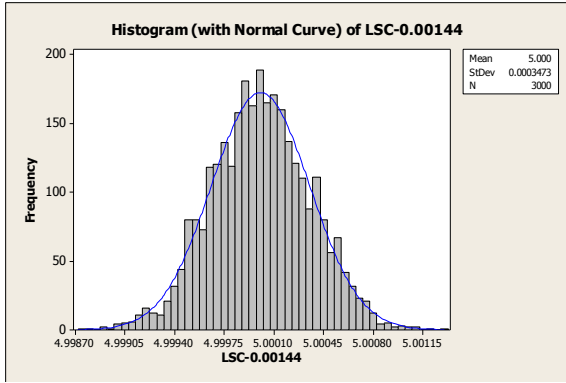
Figure 32. Example of three measurement runs of a three lobed feature

The three runs represented three features manufactured during a process in which the phase angle changed between each feature but the form and magnituded remained constant. Hence during the inspection process the output size for the feature in Run 1 could be different from the outputs from Runs 2 and 3. The same principle would be applied to the centre coordintaes of the three runs. Due to the fact that only 3 runs took

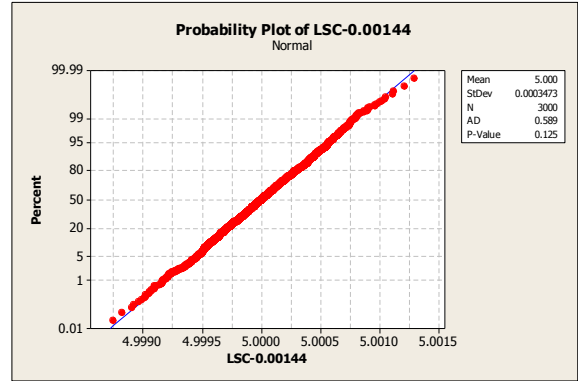
place it would be likely that any output statistical information could be of higher magnitude than the results so far presented in the screening study.

2.2.4 Descriptive statistics

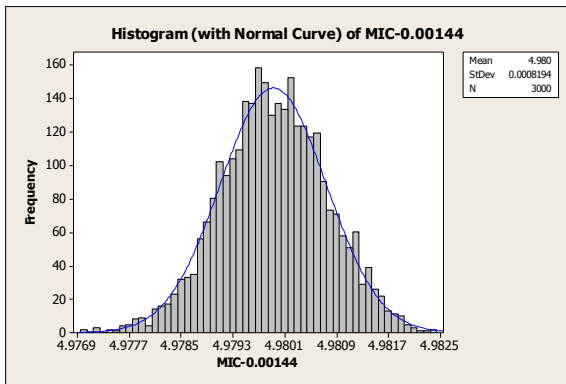
Figure-33 shows the histograms and corresponding normality test plots using the Anderson Darling technique for the different uncertainties used in section 2.2.1 for the three lobed feature. The histograms in Figure-33 shows the distribution for the r_0 parameter when using LSC. According to the probability plot shown in Figure-33(b) the Anderson Darling test revealed a P value of 0.125, therefore we can reject the hypothesis that the data did not come from a normal distribution, at a significance level of 0.05. The skewness value obtained for the Figure-33(c) above was found to be -0.00. For a normal distribution the value is zero, and any symmetric data should have a skewness near zero. Negative values for the skewness indicate data with the left tail heavier than the right tail and positive values for the skewness indicate data with the right tail heavier than the left tail. Kurtosis analysis revealed a value of 0.02. A value of 0 typically indicates normally peaked data while negative values indicate a distribution flatter than normal while positive values indicate a distribution sharper than normal. Table-12 summarises the descriptive statistics of r_0 for all measurement uncertainty values.



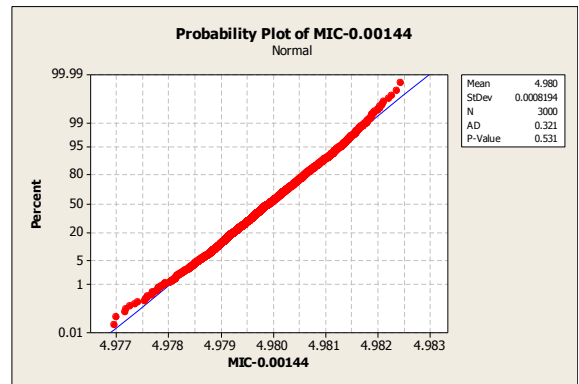
a) LSC



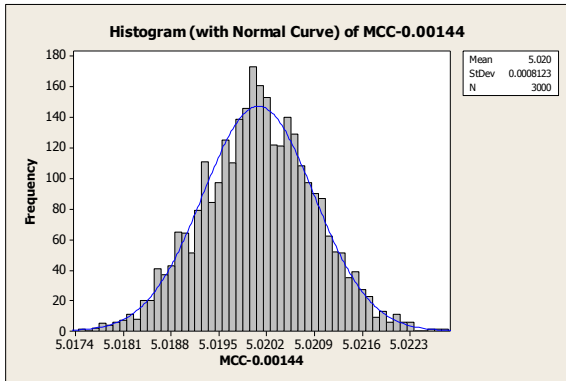
b) LSC



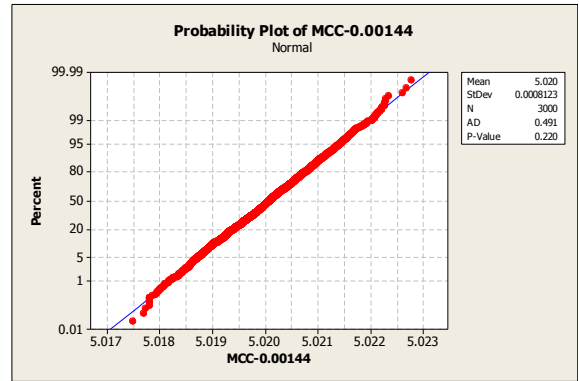
c) MIC



d) MIC



e) MCC

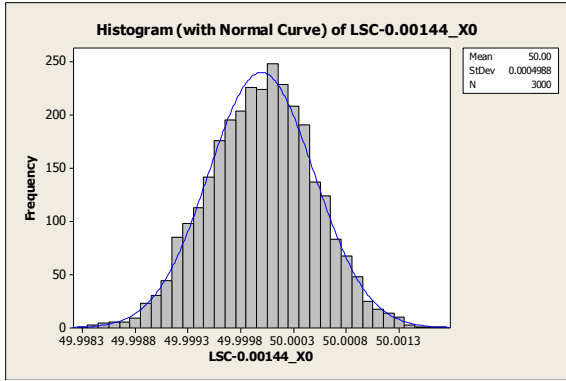


f) MCC

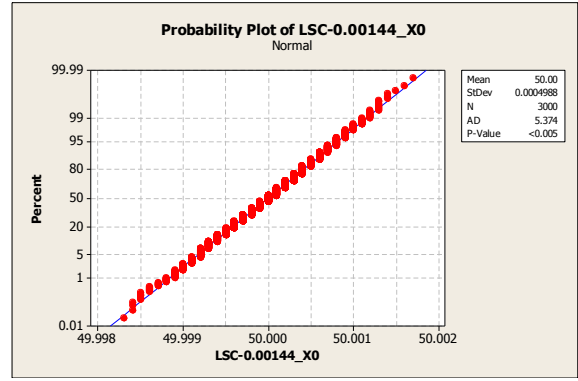
Figure 33. Normality test plots for r_0 when applying LSC, MIC and MCC.

Table 12. Descriptive statistics table for radius (mm)

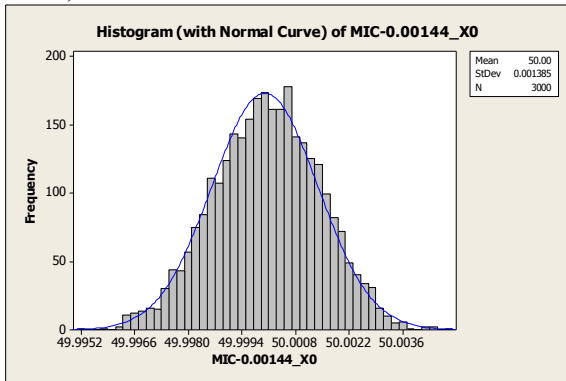
	Uncertainty	Nominal	SE Mean	StDev	Minimum	Q1	Median	Q3	Maximum	Skewness	Kurtosis	Anderson Darling Statistic
LSC	0.0014	5.0000	0.0000 1	0.0003 5	4.99870	4.99980	5.00000	5.00020	5.00130	0.00000	0.02000	0.589
LSC	0.0029	5.0000	0.0000 1	0.0007 0	4.99780	4.99960	5.00000	5.00050	5.00260	-0.08000	-0.09000	0.528
LSC	0.0043	5.0000	0.0000 2	0.0010 4	4.99660	4.99930	5.00000	5.00070	5.00340	0.08000	-0.02000	0.359
MIC	0.0014	5.0000	0.0000 15	0.0008 19	4.977	4.9794	4.9799	4.9805	4.9824	-0.08	0.01	0.321
MIC	0.0029	5.0000	2.82E- 05	0.0015 4	4.9747	4.9787	4.9797	4.9808	4.9844	-0.08	-0.08	0.455
MIC	0.0043	5.0000	4.15E- 05	0.0022 7	4.9721	4.9777	4.9793	4.9809	4.987	-0.09	-0.22	1.394
MCC	0.0014	5.0000	1.48E- 05	0.0008 12	5.0175	5.0195	5.0201	5.0206	5.0228	-0.02	-0.11	0.491
MCC	0.0029	5.0000	2.85E- 05	0.0015 6	5.0146	5.0193	5.0203	5.0214	5.026	0.01	0.05	0.234
MCC	0.0043	5.0000	4.01E- 05	0.0022 05	5.0125	5.0192	5.0207	5.0222	5.029	0.01	0.01	0.171



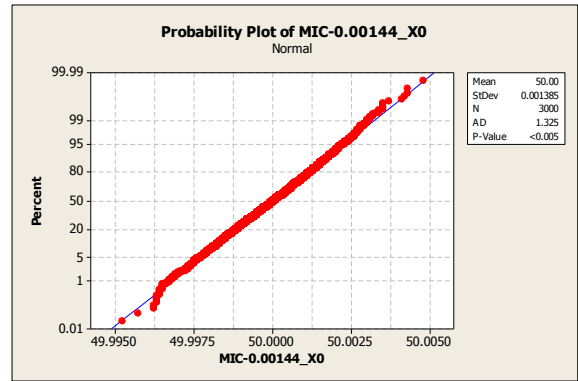
a) LSC



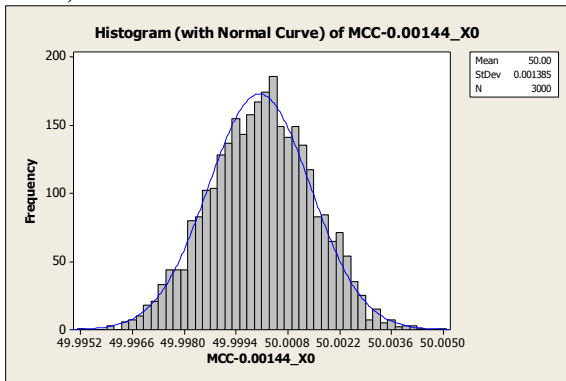
b) LSC



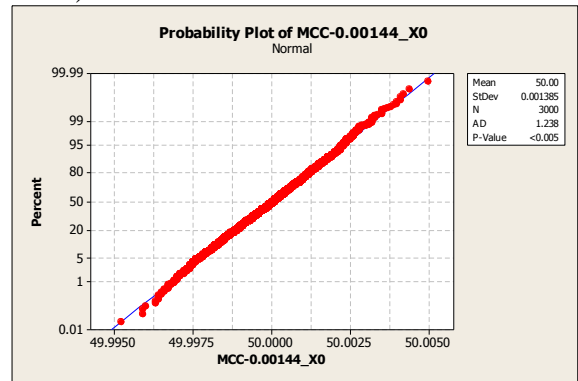
c) MIC



d) MIC



e) MCC



f) MCC

Figure 34. Normality test plots for X0 when applying LSC, MIC and MCC

Table 13. Descriptive statistics for centre coordinate X0 (mm)

	Uncertainty	Nominal	SE Mean	StDev	Minimum	Q1	Median	Q3	Maximum	Skewness	Kurtosis	Anderson Darling Statistic
LSC	0.0014	50.0000	2.53E-05	0.00138	49.995	49.999	50.00000	50.001	50.005	-0.04	-0.19	5.374
LSC	0.0029	50.0000	1.79E-05	0.000982	49.997	49.999	50.00000	50.001	50.004	-0.01	-0.14	1.970
LSC	0.0043	50.0000	2.68E-05	0.00147	49.995	49.999	50.00000	50.001	50.005	0.06	-0.14	1.057
MIC	0.0014	50.0000	0.0000	0.0014	49.9950	49.999	50.00000	50.0010	50.005	-0.08	-0.18	1.325
MIC	0.0029	50.0000	0.000042	0.0023	49.992	49.998	50.00000	50.002	50.007	0.04	0.11	0.726
MIC	0.0043	50.0000	5.86E-05	0.00321	49.988	49.998	50.00000	50.002	50.01	-0.04	0.01	0.338
MCC	0.0014	50.0000	2.53E-05	0.00138	49.995	49.999	50.00000	50.001	50.005	-0.04	-0.19	1.238
MCC	0.0029	50.0000	4.13E-05	0.00226	49.992	49.999	50.00000	50.002	50.008	-0.02	0.01	0.401
MCC	0.0043	50.0000	5.91E-05	0.00323	49.99	49.998	50.00000	50.002	50.011	0.02	-0.19	1.005

2.3 Sensitivity study via Monte Carlo simulation integration with full factorial experimental design

2.3.1 Monte Carlo simulation integration with experimental design

The main objective of this experiment was to understand the sensitivity of form, size and position of circular features using LSC, MCC and MIC. To investigate how the three algorithms react to the same input factors and respective levels.

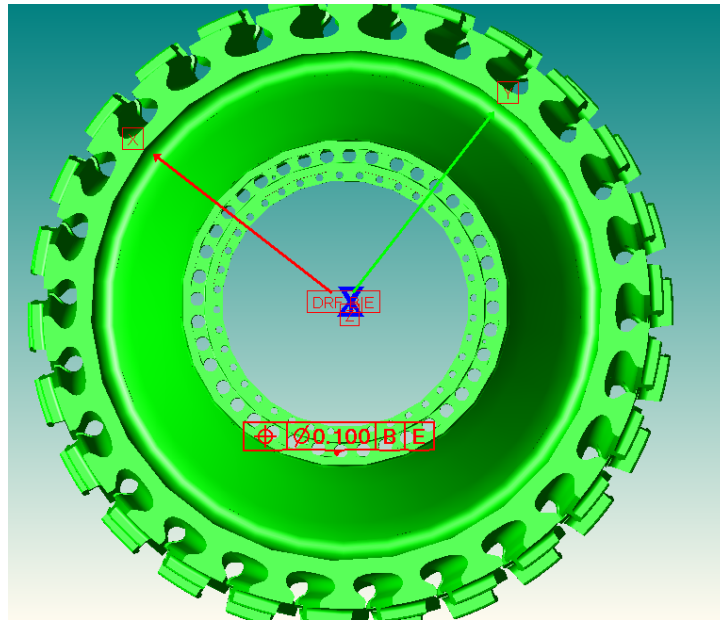


Figure 35. Example of dowel hole size and position tolerances

The output responses chosen for the experimental design study were the mean values and the standard deviation. Both quantities represented both a random (Type A) component of uncertainty and a systematic component (Type B) of uncertainty.

Feature Design Of Experiments definition

The following factors were selected for the feature experimental design:

- a) Lobe type (α)
- b) Lobe magnitude (β)
- c) CMM Uncertainty (ε)
- d) Number of probing points (η)

Table 14. Full factorial design factors and levels

Factors	Label	Levels		
Lobe type	$\alpha_i \ i = 1,2,3$	2	3	5
Lobe magnitude(mm)	$\beta_j \ j = 1,2,3$	0.006	0.013	0.021
CMM Uncertainty (mm)	$\varepsilon_k \ k = 1,2,3$	0.0014	0.0028	0.0043
Number of probing points	$\eta_l \ l = 1,2,3$	4	9	17

A 3^k factorial design was selected for this experiment. For the four factors selected using the three level factorial design resulted in 81 experimental runs. Each run was replicated three times resulting in a total of 243 experimental runs. For each of the 243 experimental

runs 1000 Monte Carlo runs were generated. For the three level full factorial design a three way model can be used:

$$y_{ijklmt} = \mu + \tau_{ijklm} + \delta_{ijklmt}$$

where (2.26)

$$\delta_{ijklmt} \sim N(0, \sigma^2)$$

μ is the overall mean effect and τ the treatment combinations. All treatment combinations were modelled as:

$$\tau_{ijklm} = \alpha_i + \beta_j + \varepsilon_k + \eta_l + \vartheta_m + (\alpha\beta)_{ij} + (\alpha\varepsilon)_{ik} \dots (\varepsilon\eta\vartheta)_{klm} \quad (2.27)$$

where $\alpha_i, \beta_j, \varepsilon_k$ are the effects (positive or negative) on the response of factors A, B, C at levels i, j, k , respectively, $(\alpha\beta)_{ij}, (\alpha\varepsilon)_{ik}$, and $(\beta\varepsilon)_{jk}$ are the additional effects of the pairs of factors together at the specified levels, and $(\varepsilon\eta\vartheta)_{klm}$ is the last additional effect of the last three factors together at levels, k, l, m . In this experiment only up to third order interactions were investigated therefore the three effect treatment combination described above.

By replacing the variable τ_{ijklm} in (2.27) the four way model became:

$$y_{ijklmt} = \mu + \alpha_i + \beta_j + \varepsilon_k + \eta_l + (\alpha\beta)_{ij} + (\alpha\varepsilon)_{ik} \dots (\beta\varepsilon\eta)_{jkl} + \delta_{ijklt} \quad (2.28)$$

Where the symbol represented all the other two level and three level interactions. The flow diagram (Figure-36) shows the integration of the simulation method with the experimental design model. This model could be developed further to contain other factors such as temperature.

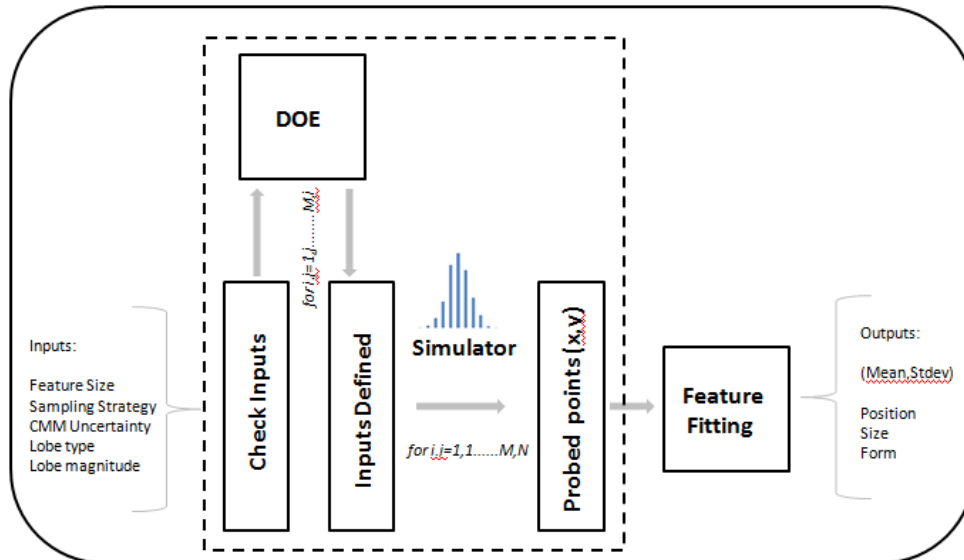


Figure 36. Integration of experimental design with Monte Carlo simulation

2.3.2 Feature Size experimental design results

The results below show the outputs for the feature size mean error quantity for the three substitute geometry algorithms (LSC, MIC & MCC).

Feature size mean error

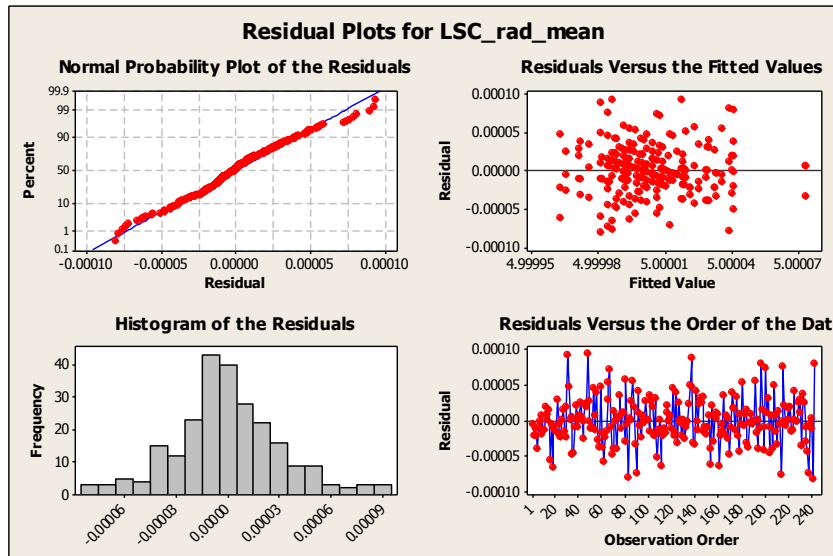


Figure 37. Residual plots for LSC radius mean values

The Figure-37 above shows the residual plots for the LSC results. From the plot containing the fitted values it was clear that the experimental design values were randomly scattered which indicated that there were no systematic effects introduced by the DOE. Figure-38 shows the main effects plot for the LSC mean values output response. It was clear that the number of probing points and lobe magnitude had a greater impact on the magnitude of the mean values obtained when compared with the lobe type and CMM uncertainty. The magnitude of the mean error values indicated that the mean size of the circular features when extracted using LSC, was not sensitive to factors chosen for the experimental design. The results shown in Figure-39 indicated that when applying the MIC algorithm, lobe type, lobe magnitude and number of probing points have an effect on the mean radius values. The mean values range was found to be 0.010mm according to the main effects plot. As the lobe magnitude increased the MIC

mean values decreased. The same result was obtained for the number of probing points variable. The results obtained for the main effect plots using MCC were similar to the results obtained for MIC. The range of the mean radius for MCC was found to be 0.010mm. As the lobe magnitude increased the mean radius decreased. This result was found to be the symmetrically opposite to the MIC result. For all the main effects plot variables for MCC the results were found to be symmetrically opposite.

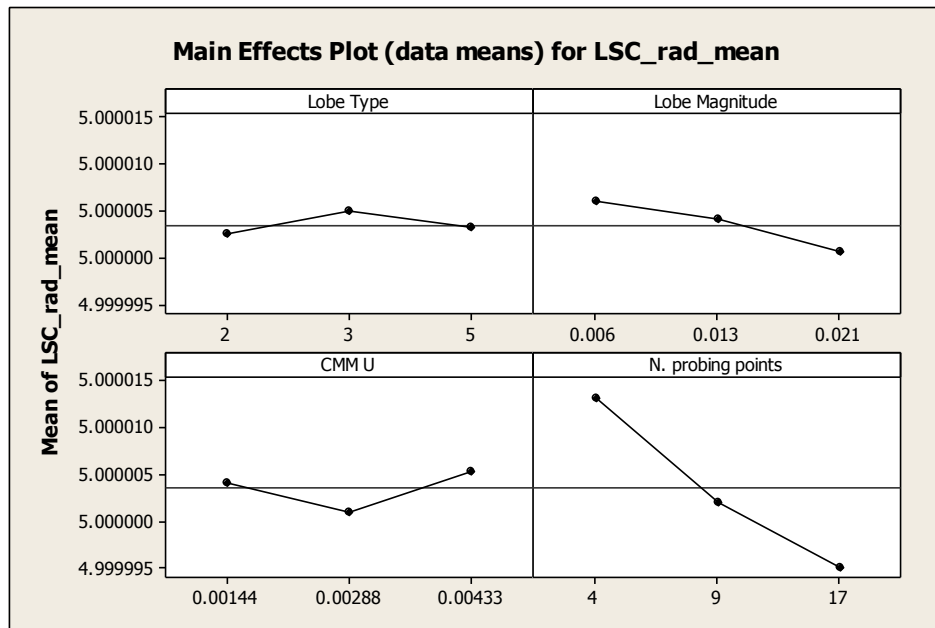


Figure 38. Main effects plots for LSC radius mean values

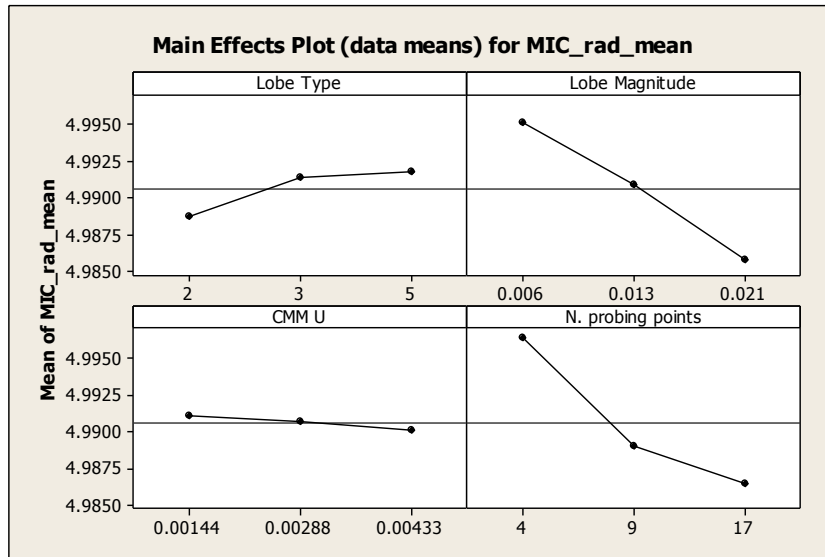


Figure 39. Main effects plots for MIC radius mean values

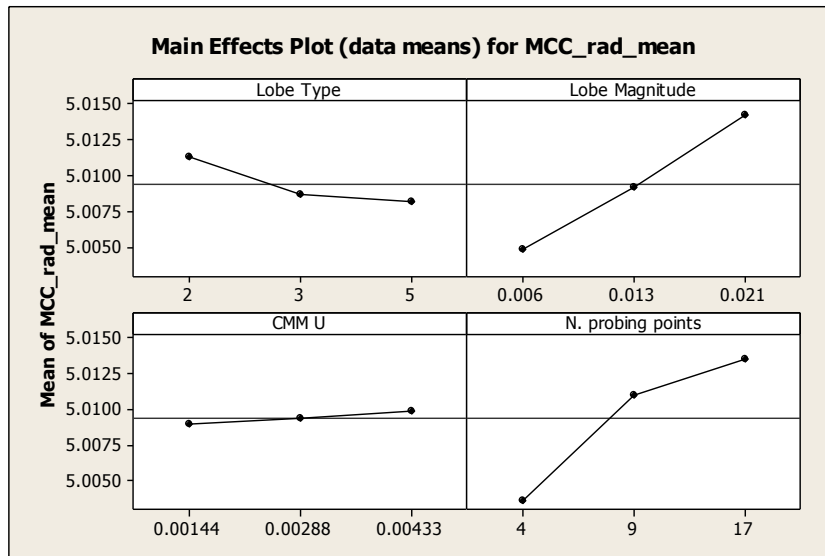


Figure 40. Main effects plots for MCC radius mean values

The results obtained for the means of the centre coordinates indicated that the means of the centres coordinates for LSC, MIC and MCC were not affected by the any of the four factors selected for the experimental design (Appendix 2.3).

Feature size stdev

Table-15 shows the P-values for the full factorial design model used in this study. The calculated F-statistic (F) is the value which would be used to compare with tables containing original data using degrees of freedom. The calculated p-value (P) determines the significance of the test. If the value lies below 0.05 the test is significant at the 5% level and there is evidence that the population means are not the same. If the value is less than 0.1 but greater than 0.05 then there is weak evidence in favour of the alternative hypothesis. Finally, if the p-value is greater than 0.1 there is no evidence to reject the null hypothesis that the population means are the same. The factors found to be statistically significant when using LSC were the CMM uncertainty and the number of probing of points. The interaction between the CMM uncertainty and the number of probing points was also found to be statistically significant. The main effects plot for the stdev shows that the range of the standard deviation values when using LSC was between 0.0015mm and 0.0005mm. As the CMM uncertainty increased so did the stdev values. An opposite result was found for the number of probing points factor, as the number of probing points increased the stdev values decreased.

Table 15. LSC experimental design P-values for Stdev results

Source	F	P
Lobe Type	0.53	0.589
Lobe Magnitude	2.84	0.061
CMM U	35485.21	0.000
N. probing points	18806.25	0.000
Lobe Type*Lobe Magnitude	0.15	0.962
Lobe Type*CMM U	1.18	0.322
Lobe Type*N. probing points	0.55	0.701
Lobe Magnitude*CMM U	1.88	0.116
Lobe Magnitude*N. probing points	1.00	0.406
CMM U*N. probing points	1508.80	0.000
Lobe Type*Lobe Magnitude*CMM U	0.83	0.576
Lobe Type*Lobe Magnitude* N. probing points	0.54	0.822
Lobe Type*CMM U*N. probing points	0.72	0.673
Lobe Magnitude*CMM U* N. probing points	1.46	0.177
Error		
Total		
S = 0.0000247330 R-Sq = 99.85% R-Sq(adj) = 99.79%		

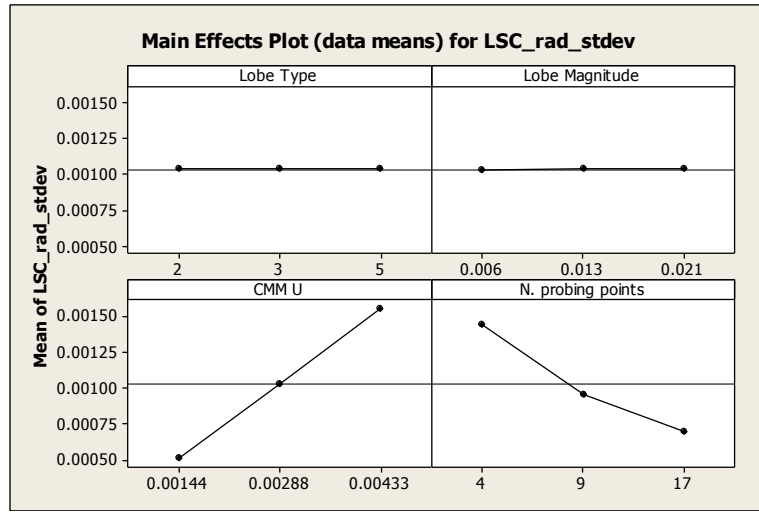


Figure 41. Main effects plots for LSC radius stdev values

The Figure-42 shows the interaction between the CMM uncertainty and the number of probing points. The plot indicated that the change from 9 probing points to 4 probing points increased the magnitude of stdev when compared with the change from 17 probing points to 9. A similar result was obtained for the CMM uncertainty values where there was a step change observed for the 0.00433mm when compared with other CMM uncertainty values.

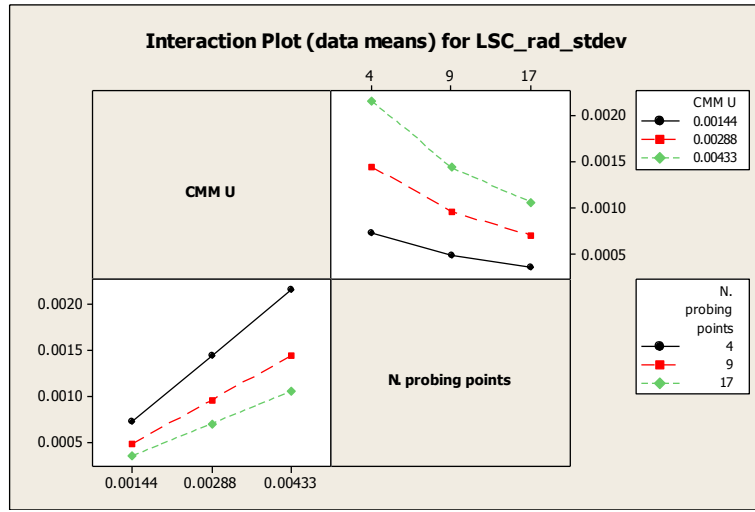


Figure 42. Interaction plot for LSC radius stdev values

The P-values in the Table-16 indicate that when using MIC as the fitting algorithm all the factors used in the experimental design study were statistically significant. All the interactions were found to statistically significant with the exception of the two level interactions between lobe magnitude and CMM uncertainty. The R-sq value obtained indicated a good fit of the statistical model used.

Table 16. MIC experimental design P-values for Stdev results

Source	F	P
Lobe Type	4548.97	0.000
Lobe Magnitude	2319.12	0.000
CMM U	7395.34	0.000
N. probing points	5721.36	0.000
Lobe Type*Lobe Magnitude	652.42	0.000
Lobe Type*CMM U	26.72	0.000
Lobe Type*N. probing points	6234.00	0.000
Lobe Magnitude*CMM U	1.15	0.335
Lobe Magnitude*N. probing points	479.83	0.000
CMM U*N. probing points	8.81	0.000
Lobe Type*Lobe Magnitude*CMM U	2.38	0.019

Lobe Type*Lobe Magnitude*	1173.41	0.000
N. probing points		
Lobe Type*CMM U*N. probing points	94.56	0.000
Lobe Magnitude*CMM U*	5.98	0.000
N. probing points		
Error		
Total		
S = 0.0000699205 R-Sq = 99.78% R-Sq(adj) = 99.70%		

The main effects plot in Figure-43 shows a range for the stdev values between 0.0027mm and 0.0015mm. This range was found to be almost double of the range obtained when using the LSC algorithm clearly indicating that MIC as an algorithm was more sensitive to the factors chosen for this study. Unlike the main effects plot obtained for LSC, where lobe type and lobe magnitude were not significant factors, the MIC main effect plots revealed that such factors are of significance.

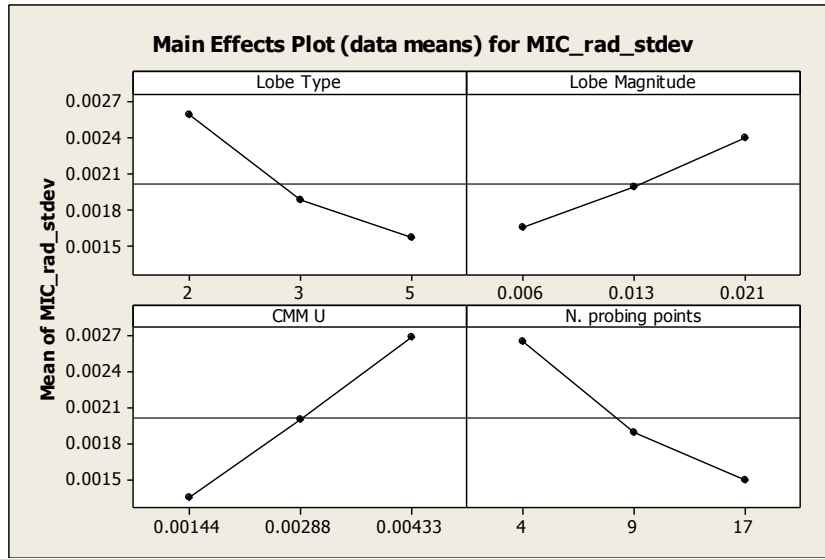


Figure 43. Main effects plots for MIC radius stdev values

The Figure-44 shows the interactions plot for the MIC model. The interaction between lobe type and number of probing points indicated that when the number of probing points was 4 there was a significant change in the relationship between the two factors which was reflected in a higher Stdev value. Furthermore when the number of probing points level was 9 and the number of probing points level 3, a step change in the Stdev value was found and reflected in the second heights magnitude value for the Stdev. Another significant interaction was observed in the interaction plots between lobe magnitude and lobe type and lobe magnitude and number of probing points. In the case of both interactions when the factors were at their highest level a step change could be observed in the interaction plot lines.

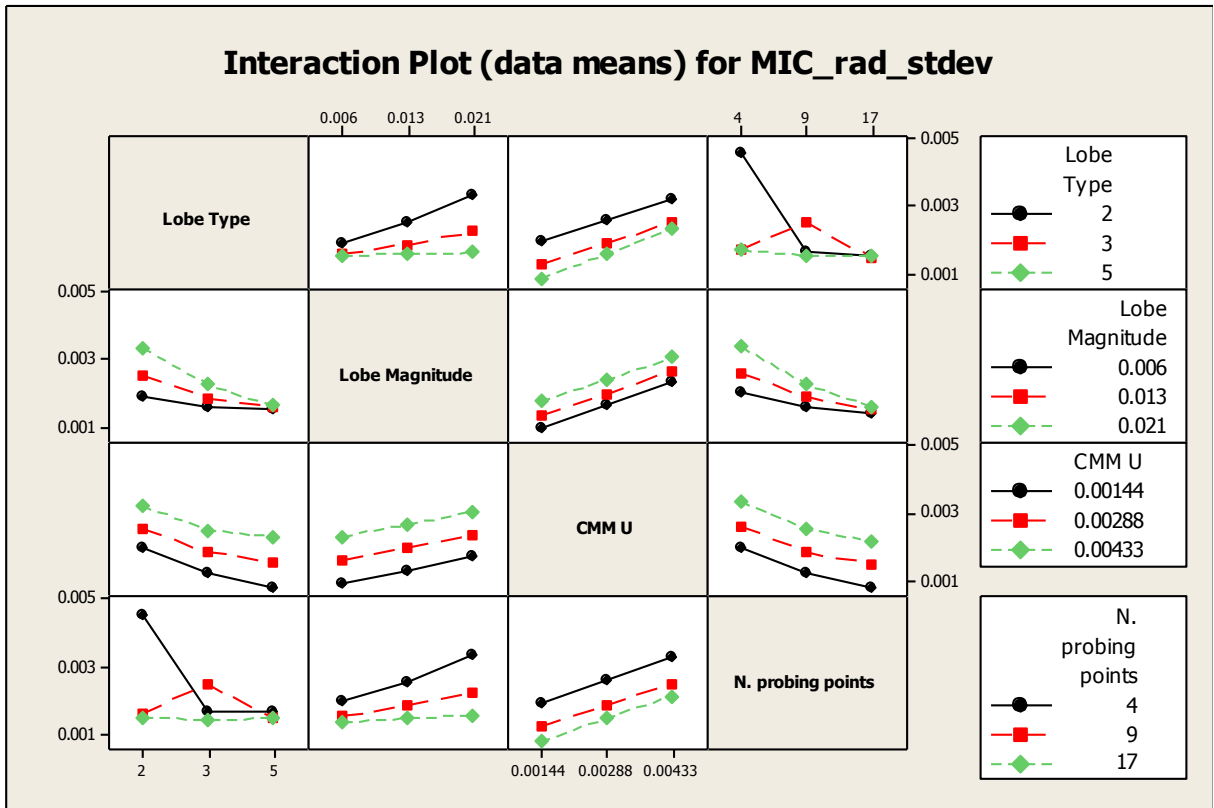


Figure 44. Interaction plot for MIC radius stdev

The P-values in the Table-17 indicated that when using MCC as the fitting algorithm all the factors used in the experimental design study were statistically significant. All the interactions were found to statistically significant with the exception of the two level interaction between lobe magnitude and CMM uncertainty. The R-sq value obtained indicated a good fit of the statistical model used.

Table 17. MCC experimental design P-values for Stdev results

Source	F	P
Lobe Type	5796.70	0.000
Lobe Magnitude	2951.73	0.000
CMM U	9084.64	0.000
N. probing points	7251.58	0.000
Lobe Type*Lobe Magnitude	831.76	0.000
Lobe Type*CMM U	35.05	0.000
Lobe Type*N. probing points	7884.74	0.000
Lobe Magnitude*CMM U	0.46	0.766
Lobe Magnitude*N. probing points	646.60	0.000
CMM U*N. probing points	11.11	0.000
Lobe Type*Lobe Magnitude*CMM U	3.67	0.001
Lobe Type*Lobe Magnitude* N. probing points	1496.70	0.000
Lobe Type*CMM U*N. probing points	109.21	0.000
Lobe Magnitude*CMM U* N. probing points	6.74	0.000
Error		
Total		
S = 0.0000630575 R-Sq = 99.82% R-Sq(adj) = 99.76%		

The main effects plot results obtained using the MCC algorithm was very similar to the one obtained using MIC. A maximum value of 0.0027mm and a minimum value of 0.0015mm define the range of the stdev values obtained.

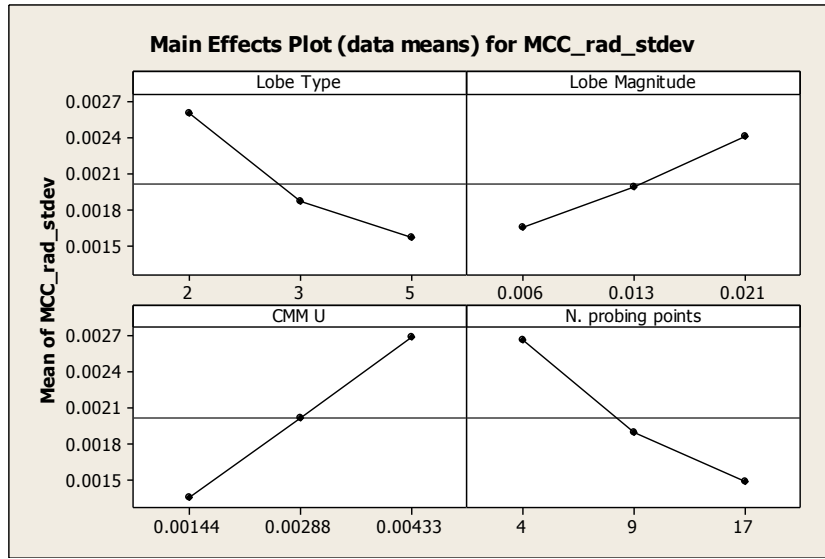


Figure 45. Main effects plot for MCC of radius stdev

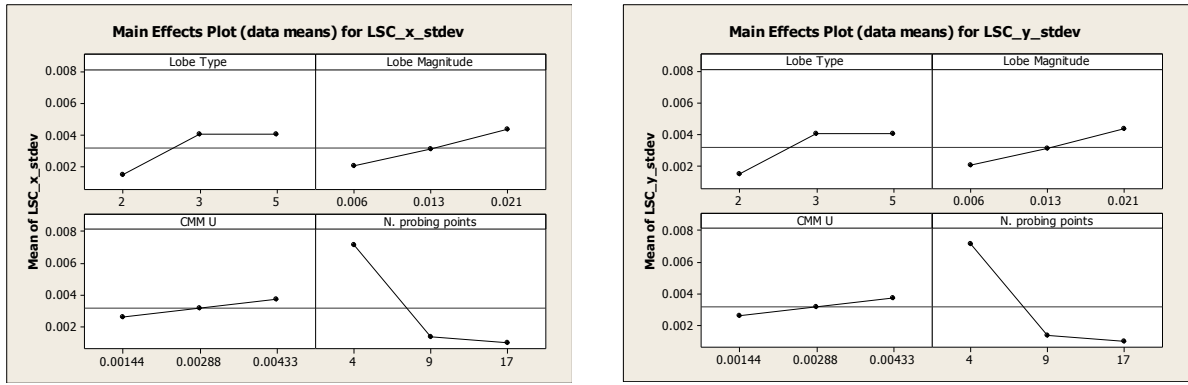
As the CMM uncertainty magnitude increased so did the magnitude of the Stdev for the MCC substitute geometry. As the number of probing points increased the Stdev values decreased. The lobe type factor showed a similar trend to the number of probing points response. Appendix 2.3 contains the interaction plots for the factors and respective levels shown in Figure-45.

2.3.3 Feature centre coordinates experimental design results

Feature centre coordinates Stdev

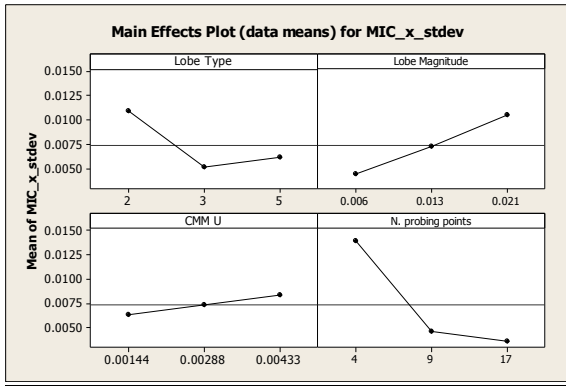
The Figure-46 shows the main effects plot for the variation within the centre coordinates of the circular features when using LSC. Both X,Y coordinates show similar trends in the main effects plots. Both the Lobe Magnitude and CMM uncertainty factors do not appear to have a significant impact in the variation of the centre coordinates. The lobe type plot

indicated that the variation increased with the number of lobes. A two lobe feature was found to have half the variation at 0.002mm of the three and five lobe features. The use of 4 probing points recorded the highest variation from all the factors within the main effects plot with a magnitude of 0.0075mm.

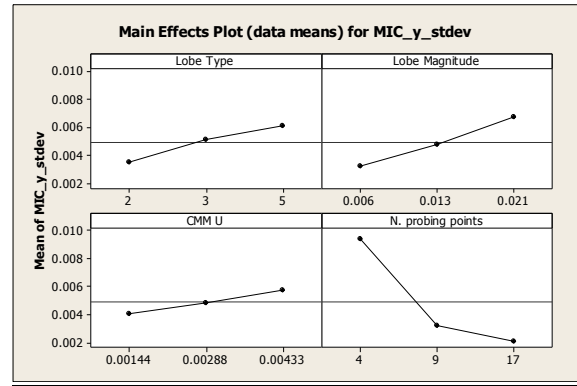


a) b)
Figure 46. a) Main effects plot for LSC X coordinate stdev; b) Main effects plot for LSC Y coordinate stdev

The MIC results shown in the Figure-47 indicated that the magnitude of the variation of the centre coordinates was higher when compared to the LSC main effects plot. In terms of which factors affected the variation results the most, the number of probing points recorded a variation of approximately 0.0125mm when using 4 probing points. It is worth noting that unlike the LSC results where the main effects plot were very similar for both the X,Y coordinates, the MIC main effects plots appear to be different both in terms of magnitudes and the trends that each factors displayed. The X coordinate main effects plot showed higher magnitudes of the standard deviation for all factors (with the exception of the CMM uncertainty) when compared to the Y coordinate plot.



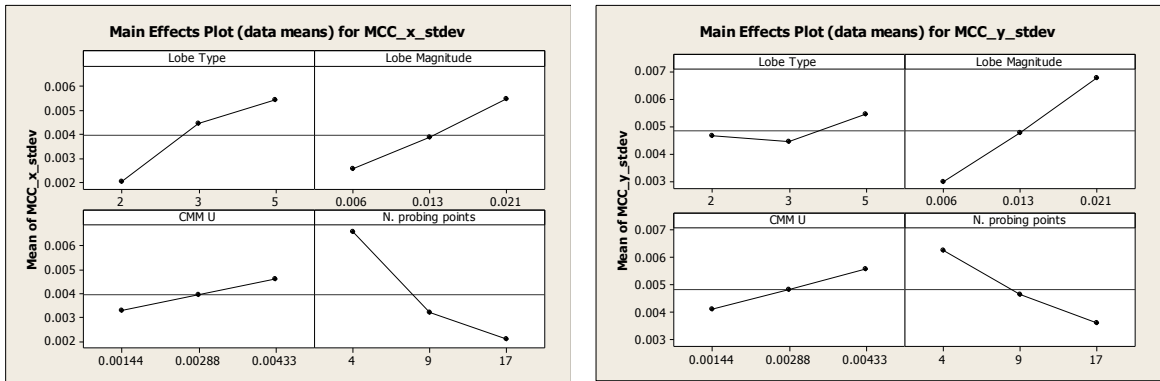
a)



b)

Figure 47. a) Main effects plot for MIC X coordinate stddev; b) Main effects plot for MIC Y coordinate stddev

The main effects plot for MCC indicates that the lobe magnitude and the number of probing points are key factors that affect the magnitude of the standard deviation for the centre coordinates. The maximum value for the standard deviation recorded was 0.007mm when the lobe magnitude of was set at 0.021mm. A similar trend was found between the lobe type for the X,Y coordinates when using MIC and MCC. In both cases the X coordinate trend was different from the Y coordinate for the lobe type factor.

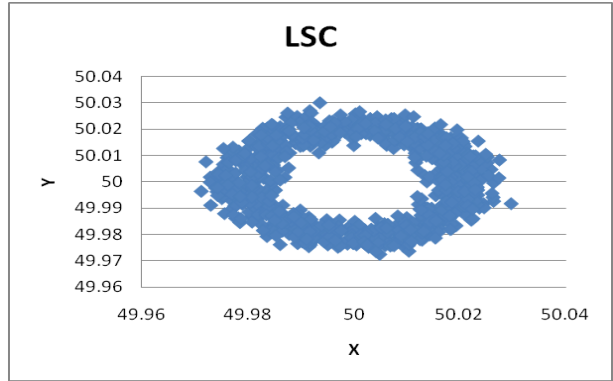


a)

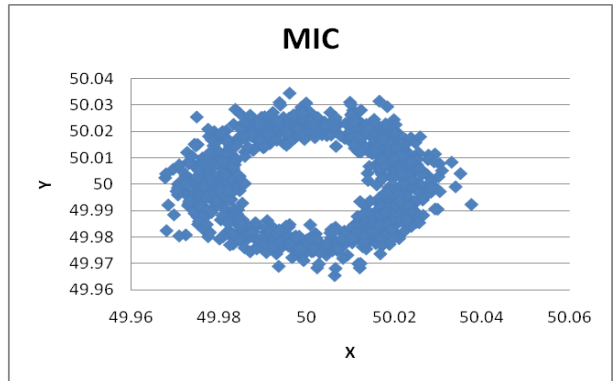
b)

Figure 48. a) Main effects plot for MCC X coordinate stdev; b) Main effects plot for MCC Y coordinate stdev

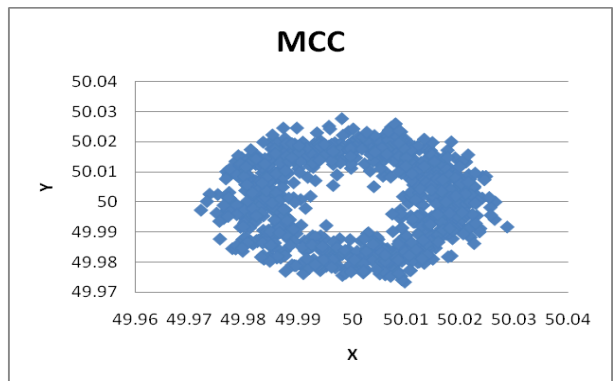
From the main effects plot above it was observed that there were two extreme cases for the stdev values obtained. The plots show all the centre coordinates obtained for the two experimental design runs that represented the two extreme cases of stdev for the three algorithms selected. The Figure-49 shows the all the centre coordinates obtained for the experimental design run with factors set as follows: Lobe type – 5; Lobe magnitude – 0.021; CMM uncertainty – 0.00433; Number of probing points – 4. The plots obtained for all three algorithms indicated that the majority of the centre coordinates obtained were at an interval from the nominal value (50,50 (mm)) varying from 0.005mm to 0.0015mm in both X,Y directions. In all three cases an X coordinate value close to 50.03mm was obtained. This magnitude represents a difference of 0.030mm when compared with the nominal X coordinate value. A similar result was obtained for the Y coordinate with a maximum difference of 0.04mm was registered when applying MIC.



a)

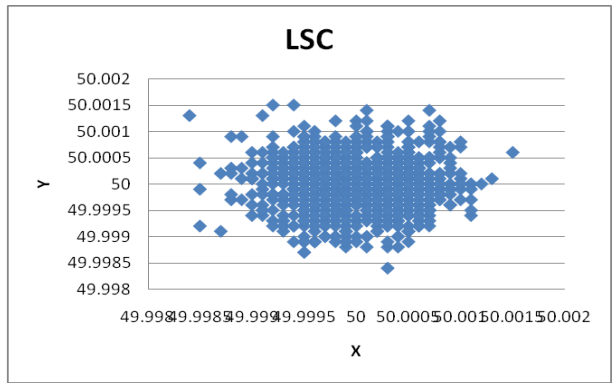


b)

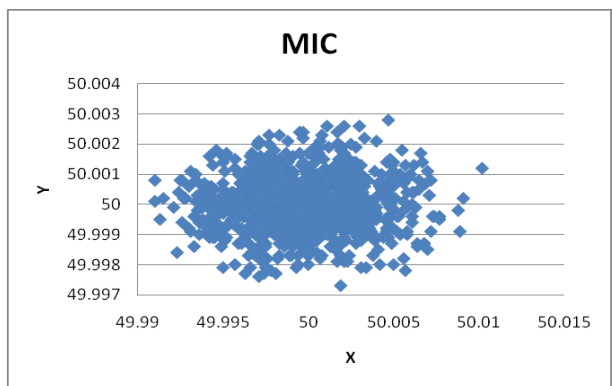


c)

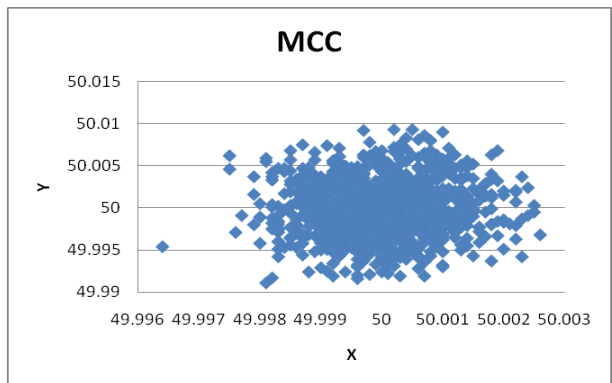
Figure 49. X,Y coordinates (Lobe type – 5; Lobe magnitude – 0.021; CMM uncertainty – 0.00433; Number of probing points – 4)



a)



b)



c)

Figure 50. X,Y coordinates (Lobe type – 2; Lobe magnitude – 0.006; CMM uncertainty – 0.00144; Number of probing points – 17)

The Figure-50 shows the all the centre coordinates obtained for the experimental design run with factors set as follows: Lobe type – 2; Lobe magnitude – 0.006; CMM uncertainty – 0.00144; Number of probing points – 17. Unlike the results obtained in Figure-49 there was no interval found between the nominal centre coordinates and the cluster of points shown in the charts. For LSC and MCC the maximum difference for the Y coordinate and nominal Y value was 0.0015mm. MIC recorded a maximum Y coordinate of 50.003mm. In all three cases the maximum difference found between the X coordinate and nominal value was 0.0014mm.

The two extreme cases shown above indicated potential case scenarios where any assumptions made about the factors and its respective levels could have an impact on the measurement uncertainty associated with the centre coordinates of a circular feature.

Appendix 2.3 contains the main effects plots for mean values of the centre coordinates of the three algorithms.

Lobe magnitude captured (Form error)

From the results presented in this section it was clear that lobe magnitude was an important factor. The Figure-51 shows the main effects plot for the percentage of form error captured. From the four factor used in this study the number of probing points appeared to have the highest magnitude of effect on the main effect plot. For the three remaining factors the main effects plot indicated that in most cases the percentages of form error captured interval was between 60 and 80%.

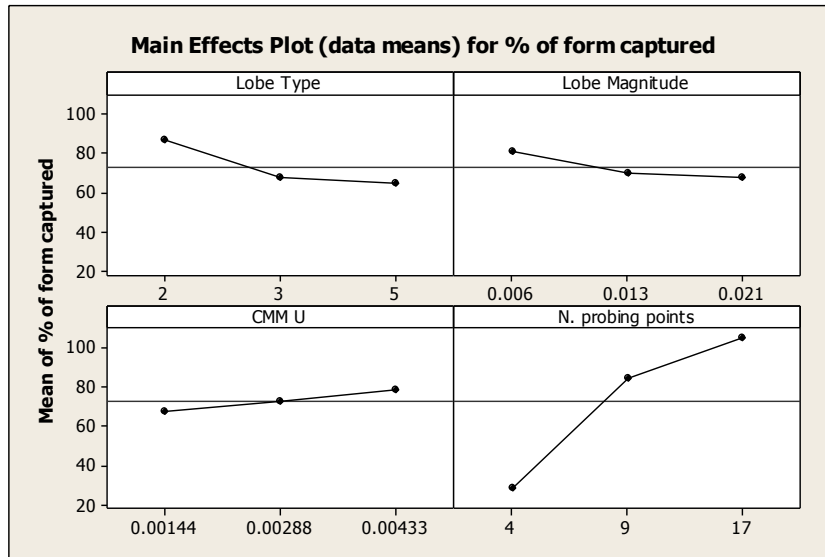


Figure 51. Main effects plot for % of form error captured

2.4 Assessing the environmental impact

2.4.1 Experimental design set-up

A commercially available CMM was used for the experimental study. The machine was a moving bridge with a specification $MPE=(3.5+L/250)\mu\text{m}$ (L being a length in mm) according to ISO 10360-2. The experimental set-up is shown in the Figure-52. The machine was located in a temperature controlled room where the temperature could be set at a pre-specified reference value within an uncertainty of $\pm 1\text{ }^\circ\text{C}$ at 95 % significance level. Therefore, by setting different levels of room temperature it was possible to simulate measurement tasks performed in workshop environments where the temperature could vary considerably throughout a working day during normal operating conditions.

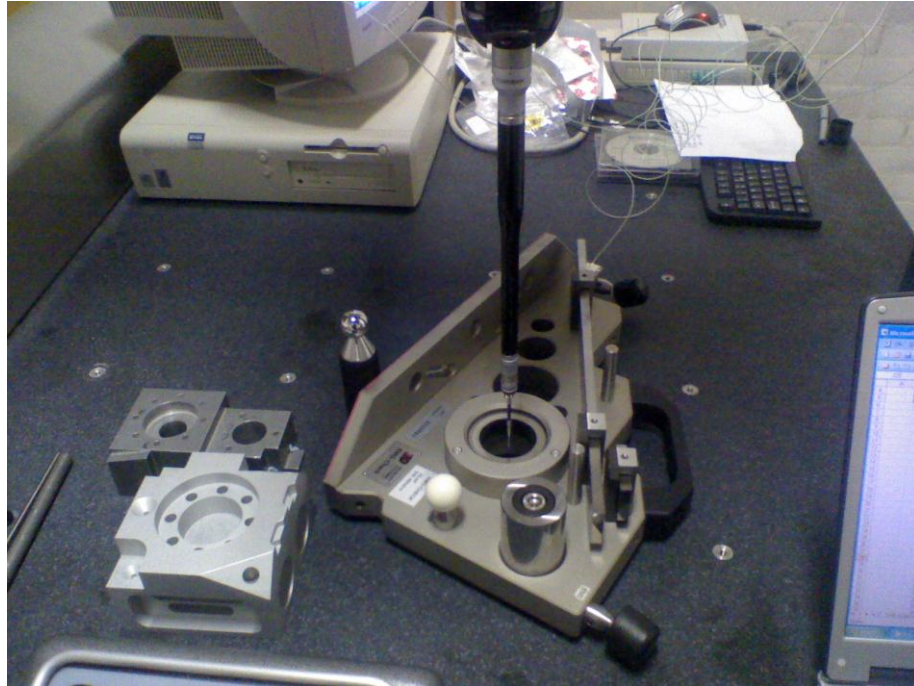


Figure 52. CMM set up for experimental design

In this investigation, two levels of room temperature were selected, 21 and 24 °C, respectively, and no temperature compensation settings were enabled on the CMM throughout the whole experimental activity. The stability of the machine temperature at each of the two levels of air temperature considered was monitored using K type thermocouples applied in a number of points of the machine structure.

Two different features were selected for this study: a ring gauge (R) and a sphere (S) to represent two and three dimensional features, respectively. In both cases, the measurand was defined as the diameter of the part at each of the two examined levels of air temperature.

The values of both the measurands were valid at a reference temperature T_{ref} that was also stated in the artefact calibration certificate. For the measurand in this study, as is

typical with any length, $T_{ref} = 20\text{ }^{\circ}\text{C}$. Thermal expansion for the sphere (external feature) and thermal contraction for the ring gauge (internal feature) was expected to affect the values provided by the certificate when the operating temperature of the CRM was higher than T_{ref} . Consequently, new estimates $\hat{\theta}_T$'s for the values of the measurands valid when the temperature of the measurand T were produced using the following equation, under the assumption of linear thermal expansion of the CRM:

$$\hat{\theta}_T = \hat{\theta} + \alpha_{T_{ref}} \cdot (T - T_{ref}) \cdot \hat{\theta} \quad (2.29)$$

In equation 2.29 $\alpha_{T_{ref}}$ was the coefficient of linear thermal expansion when the CRM was at the temperature T_{ref} . The temperature T of the CRM when the air temperature was set at 21 and 24 $^{\circ}\text{C}$ respectively, was monitored attaching K type thermocouples to the CRM at a number of points. Some of the information available on the calibration certificate of the CRM used have been summarised in Table-18.

Table 18. Properties of selected features

FEATURE	CALIBRATED VALUE (mm)	UNCERTAINTY (mm)	COEFFICIENT OF THERMAL EXPANSION (pp/mC)
Ring Gauge	49.9994	0.4	11.5
Sphere	29.9992	0.4	5.5

Ultimately, an estimate $\hat{m}se$ of a series of measurement results taken in the i -th experimental condition was obtained using $\hat{\theta}_T$ from equation 2.29.

$$rmse (\bar{x}_i, \theta, n) = \sqrt{\frac{\sum_{i=1}^n (\bar{x}_i - \bar{x})^2}{n} + \frac{\sum_{i=1}^n (\bar{x} - \theta)^2}{n}} \quad (2.30)$$

The series of measurements was taken in repeatability conditions. The results \bar{x}_i and \bar{x}_{i+1} have not been obtained one after the other in a temporal sequence, but were assigned to the run order by randomly selecting them from all the measurements in all the investigated experimental conditions at a pre-specified temperature. Differently stated, the measurements results were replicates and not repetitions of the measurement process.

The set-up parameters chosen as discretionary factors were the probe extension, the stylus length [138] and the number of probing points. For the probe extension, three different set-ups of the analysed CMM were considered: without any probe extension, with probe extensions of length 100 mm and 200 mm. Three styli of the same type and geometrical characteristics (e.g. material, tip size), but with lengths 20, 60 and 110 mm, respectively, were chosen. Regarding the planning of the measurements, the potential effects on the uncertainty of measurement due to two different numbers of probing points (seven and eleven) were examined.

A kinematic probe with a standard force module [113] was used throughout this experiment. The factors examined in this study with their levels are displayed in Table-19.

Table 19. Experimental design factors

FACTORS	LABELS		LEVELS		
Room temperature (°C)	$temp_{(j)}$	$j = 1, \dots, 72$	20	24	
Feature	$fea_{(j)}$	$j = 1, \dots, 72$	Ring (R)	Sphere (S)	
Probe extension (mm)	$pe_{(j)}$	$j = 1, \dots, 72$	0	100	200
Styli length (mm)	$sl_{(j)}$	$j = 1, \dots, 72$	20	60	110
No. of probing points	$np_{(j)}$	$j = 1, \dots, 72$	7	11	

A fully randomized experimental design with three factors at two levels each and two factors at three levels each identified 72 different experimental conditions, henceforth also referred to as treatments or cells of the design. Three replicates of the design were considered, i.e. $r = 1, 2, 3$. This resulted in an overall experimental effort of 216 measurement tasks, i.e. 648 measurement tests. All the measurement tasks at one level of temperature were carried out first, and then all the others were performed at the remaining level of temperature investigated. Therefore, if some nuisance factor occurred while performing the measurement task at a certain temperature, it would lead the experimenter to attribute incorrectly such effects on the response variable (\hat{rmse}) to the temperature.

The two types of the features, ring and sphere, were not randomly assigned to the run order. In fact, the sequence of measurement tasks was constructed as a sequence of pairs, each consisting of one measurement of the ring and one of the sphere in identical experimental conditions. This experimental strategy was adopted with the intent of counteracting the potential presence of nuisance factors that increase the variability of the response variable, thus making it more difficult to identify any significant effect on the

response variable due to the type of the feature measured. Once, the room temperature was set and the constraint on the run order for the type of features was introduced, all the others combinations of factors were randomly assigned to the sequence of the measurement tasks.

When changing the probe extension or the stylus length a calibration procedure was run. Consequently, the random assignment of the experimental conditions to the order of the measurement tasks may result some times in a calibration procedure being run, but in some other time in no calibration procedure being run. The last circumstance happened when the probe extension or the stylus length were not changed between two consecutive conditions. This was considered acceptable because this experiment was meant to be representative of the actual operational conditions in which the measuring system was used. In such circumstances, the random sequence of calibration and non-calibration was most likely to happen depending on the variety of measuring tasks performed.

2.4.2 Output responses

It was moreover argued that performing calibration procedures during the experiment may increase the overall measured uncertainty of the system in comparison with ideal laboratory conditions. A suitable statistical model to describe the experimental results was as follows:

$$r\hat{m}se_j = \mu + temp_{(j)} + fea_{(j)} + pe_{(j)} + sl_{(j)} + np_{(j)} + temp : fea_{(j)} + \dots + er_j \quad (2.31)$$

In equation (2.31), the symbol μ represented the mean of the response variable \hat{rmse}_j over all the experiment and $j=1,\dots,72$ was the index associated with each of the experimental conditions. The meaning of the other symbols are summarised in Table-19, whereas the colon was used to identify an interaction effect on the response variable due to the factors it divided. The parenthesised subscripts mapped the rows in the data to the levels of the factor used in that row. For example, $temp_{(j)}$ corresponded to the temperature used for that j . For brevity, the ellipsis stands for all the remaining possible second order interactions. Interactions of higher order, i.e. involving more than two factors, were not considered because it was difficult to foresee how the experimental conditions considered could possibly cause them. Moreover, from a practitioner's point of view, it was also difficult to see how the awareness of the significance of a third, fourth or fifth order interaction could enrich the knowledge of the measuring system investigated. The terms er_j 's were random variables that, without losing generality, were assumed to be independent and identically distributed with mean zero and constant variance σ_{er}^2 . If they were also normal statistical inferences regarding the parameters of the model was facilitated. In the previous section it was observed that the realisations of \hat{rmse}_j were distributed asymmetrically. Such circumstance made it very unlikely that the errors of the model to follow a symmetrical distribution such as the normal. For this reason, it would make the inferential process easier if the response variable were transformed in such a way to assume a more symmetrical distribution. A transformation that appears to suits this purpose was the logarithm transformation shown in the equation :

$$\log(\hat{rmse})_j = \mu + temp_{(j)} + fea_{(j)} + pe_{(j)} + sl_{(j)} + np_{(j)} + temp_{(j)} : fea_{(j)} + \dots + er_j \quad (2.32)$$

Equation (2.32) represented a multiplicative model in the domain of the untransformed response variable. It can therefore be rewritten as in its equivalent form:

$$\hat{rmse}_j = e^\mu \cdot e^{temp_{(j)}} \cdot e^{fea_{(j)}} \cdot e^{pe_{(j)}} \cdot e^{sl_{(j)}} \cdot e^{np_{(j)}} \cdot e^{temp_{(j)}:fea_{(j)}} \cdot e^{temp_{(j)}:pe_{(j)}} \cdot \dots \cdot e^{er_j} \quad (2.33)$$

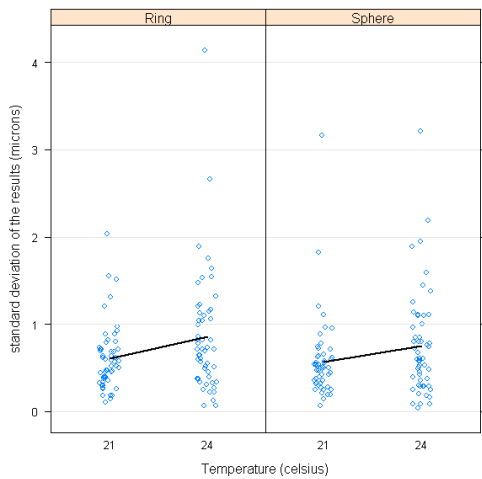
This model was fitted to the experimental data using the ordinary least squares method (OLS) as implemented in R [85]. A large number of two-way interactions were found not to be statistically significant resulting in the following final model:

$$\begin{aligned} \log(\hat{rmse})_j = & \mu + temp_{(j)} + fea_{(j)} + pe_{(j)} + sl_{(j)} + np_{(j)} + \\ & + temp_{(j)} : fea_{(j)} + pe_{(j)} : sl_{(j)} + fea_{(j)} : np_{(j)} + er_j \end{aligned} \quad (2.34)$$

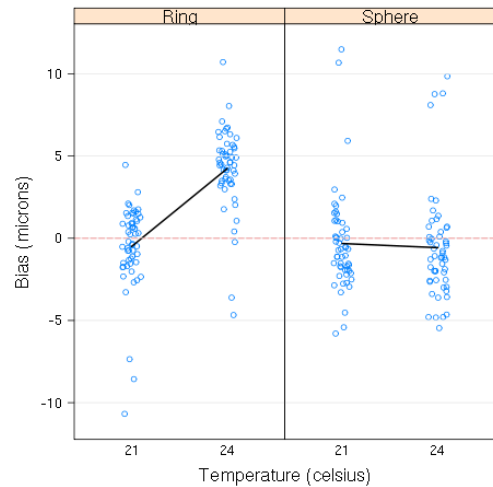
The coefficient of determination (R^2), was equal to 40.9 %. This means that about 60% of variability of the response variable was not accounted for by this model and must be due to other unknown sources. The ANOVA table that shows the significance of each of the factors included in equation (2.34) is shown in Table-20.

Table 20. Experimental design ANOVA results

	Degree s of freedom	Sum of squares	Means of squares	F value	Pr(> F)
Temperature $temp_{()}$	1	5.78	5.78	30.43	$8.41 \cdot 10^{-7}$
Probe extension $pe_{()}$	2	4.06	2.03	10.67	$1.13 \cdot 10^{-4}$
Stylus length $sl_{()}$	2	2.28	1.14	5.99	$4.31 \cdot 10^{-3}$
Type of feature $fea_{()}$	1	0.879	0.879	4.63	$3.56 \cdot 10^{-2}$
Number of probing points $np_{()}$	1	0.783	0.783	4.12	$4.70 \cdot 10^{-2}$
$temp_{()} : fea_{()}$	1	3.57	3.57	18.8	$5.83 \cdot 10^{-5}$
$pe_{()} : sl_{()}$	4	4.52	1.13	5.95	$4.39 \cdot 10^{-4}$
$np_{()} : fea_{()}$	1	1.18	1.18	6.22	$1.55 \cdot 10^{-2}$
Residuals	58	11.0	0.190		



a)



b)

Figure 53. a) Stdev vs Temperature results; b) Bias vs Temperature results

Figure-54, 55 and 56 show the interaction plots corresponding to the three significant interaction effects in the final model. These show the mean \hat{rmse} for each combination of the interacting factors and are useful in interpreting the combined effect of these factors. Figure-56 shows that in the selection of the stylus length to obtain improved uncertainty performance, the probe extension must be also considered. For different probe extensions, different styli may be preferable from the point of view of limiting the uncertainty. Stylus length and probe extension should therefore be chosen together. In Figure-55, this is demonstrated observing that with the same probe extension of length 200 mm, uncertainty of measurement could be greatly improved if the stylus length was carefully chosen (stylus length 60 mm). Appendix 2.4 contains the full published technical paper.

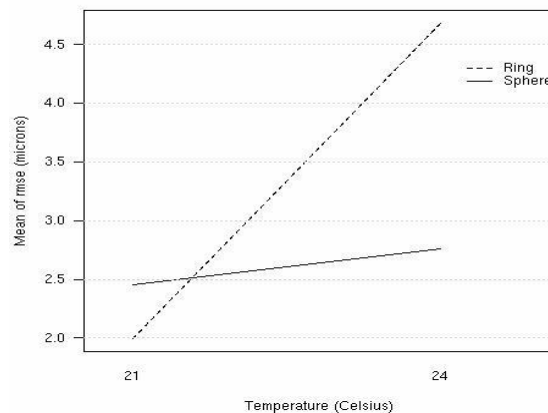


Figure 54. Interaction effect of the temperature and the type of feature measured (ring and sphere)

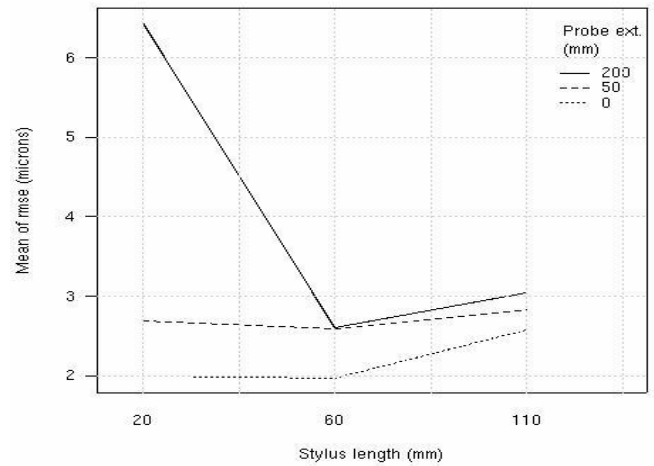


Figure 55. Interaction effect of the stylus length and the probe extension

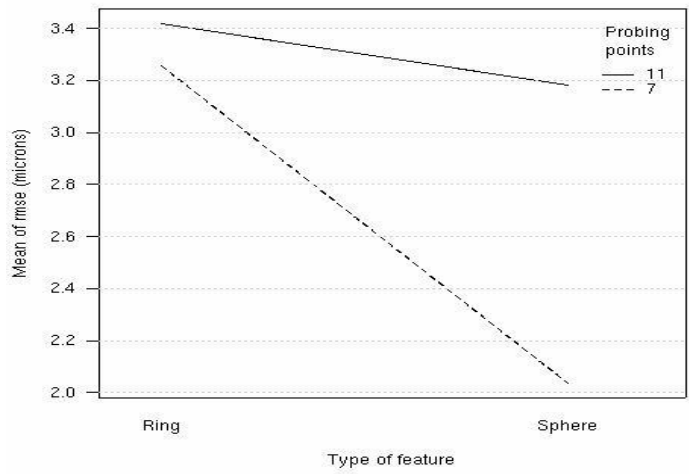


Figure 56. Interaction effect of the type of feature and the number of probing points

2.5 Summary

In this chapter two uncertainty estimation methods were compared using calibration data from CMM length measurements. Although both methods showed similar results for CMM-1 and CMM-3, CMM-2 showed a difference between the methods. In the case of ISO 15530-3 approach, the expanded measurement uncertainty results were found to be particularly sensitive to the standard deviation calculations when compared with the GUM approach where the same quantity is used to derive the Type A standard uncertainty. Although such approaches can easily be applied to length measurements, they may not necessarily describe how the sensitivity of other geometrical features varies with changes to certain input factors.

The sensitivity of CMM point coordinate uncertainty on a circular feature while applying different substitute geometry criteria (least squares circle, minimum zone circle, maximum inscribed circle and minimum circumscribing circle) was investigated. The sensitivity results can provide some guidance in selection of a CMM for a specified tolerance. For the generated features with three and five lobes the LSC algorithm stdev was always found to be of smaller magnitude when compared with MIC and MCC. The Area position results revealed that the three lobed feature was less sensitive to the input factors when compared with the five lobed feature.

It was shown that the random uncertainties associated with the CMM measurements will generally increase the magnitude of form error derived from the measurement points, with the increase roughly proportional to the measurement uncertainty. The uncertainty associated with the estimate of the circularity has two contributing components, one due to finite sampling, and the other due to CMM uncertainty.

It was also shown that the different criteria chosen for the study react differently to the inputs chosen for the DOE. While the systematic error main effects plots show expected trends for the determined radius, the standard deviation main effect plots indicated that when using LSC lobe magnitude and lobe type factors effect was constant at the different levels chosen for the DOE. When using MIC and MCC the same factors did not behave in a constant manner when using different levels for the two factors. Main effects plots for the X,Y centre coordinates for the different criteria also showed how the standard deviation behaviour changed with the different levels of the input factors. Of particular importance were the differences between two extreme cases of the DOE runs where the centre coordinates variation changed from 0.003mm for the run using a two lobed feature to 0.03mm when using the five lobed feature. Furthermore the five lobed feature results showed that in none of the 1000 runs the nominal coordinates were ever replicated.

Chapter 3

Virtual estimations of task specific measurement uncertainty

3.1 Estimating uncertainty of length measurements with Virtual CMM

In this section the results presented in section 2.1.1 were used to create simulation models in Pundit/CMM. The Figure-57 shows the gauge model created in Pundit/CMM with all the settings using the information provided in section 2.1.1.

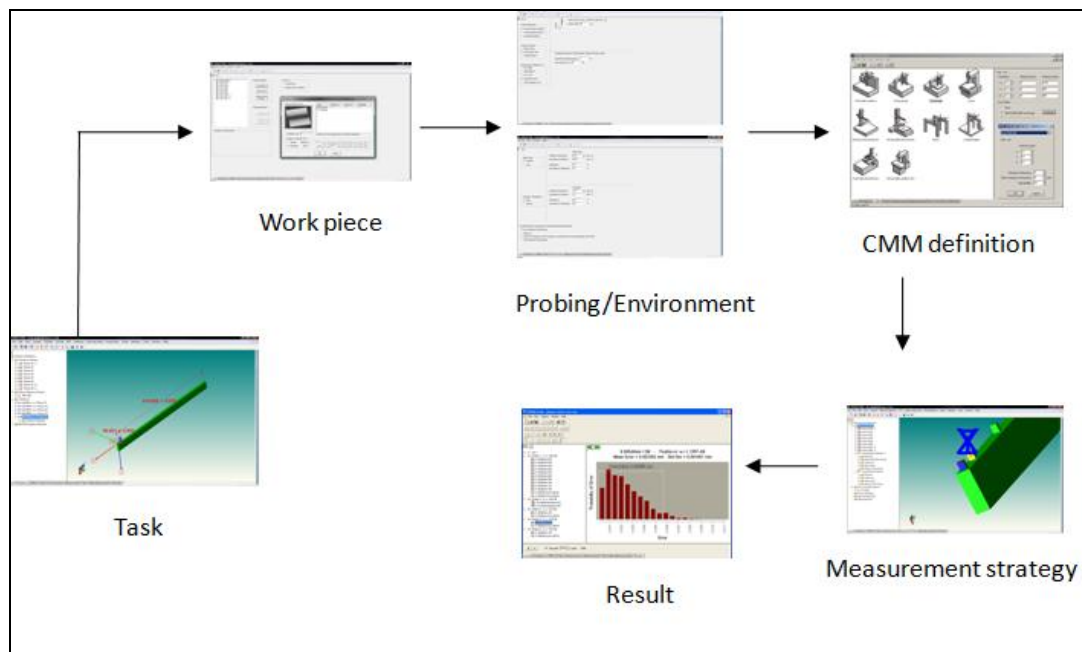


Figure 57. Pundit/CMM simulation set up for length bar measurement.

Firstly a comparison between Pundit/CMM and the physical measurement results from section 3.1.1 was used to test the UES in accordance to section C.2 of the ISO 15530-4.

Although it is recommended that for the measurement of the recommended artefacts to vary the measurement strategy (position and orientation of the test object, distribution of measurement points) in order to check the influence on the measurement uncertainty stated, this was not possible due to the fact that the data already existed. For all CMMs the MPE0 was used with all length bar measurement set up within the simulations along the X-axis of the individual CMMs which reflected the physical data measurements. The tables of results below indicate that for all of the length measurements performed by the different CMMs the UES conformed to the test [57]:

$$|Y_m - Y_{cal}| / \sqrt{U_{cal}^2 + U_{sim}^2} \leq 1 \quad (3.1)$$

where:

Y_m was the measurement result (for all measurements the maximum error from all the measurements was used)

Y_{cal} was the calibrated value

U_{cal} was the expanded uncertainty of calibrated artefact

U_{sim} was the task specific expanded uncertainty of the simulated measurement

CMM-3 results showed that for the length measurement of 20mm the UES test was very close to 1. Appendix 3.1 contains all the input data used for creating the simulations in Pundit/CMM. Section C.3 of the ISO 15530-4 provides guidance on how to use computer aided verification to check the UES by comparing the absolute error of measurement with the uncertainty reported from the UES.

Table 21. CMM-3 UES length test

Ycal (mm)	Ym (mm)	Ucal (mm)	U _{sim} (mm)	≤ 1
20.001	20.0015	2.36E-06	0.0005	0.999989
99.9949	99.9955	5.98E-05	0.000966	0.619931
220.018	220.0194	0.00029	0.00178	0.776281
300.0091	300.0107	0.000539	0.00229	0.680076
420.0021	420.004	0.001058	0.00299	0.599081

Table 22. CMM-2 UES length test

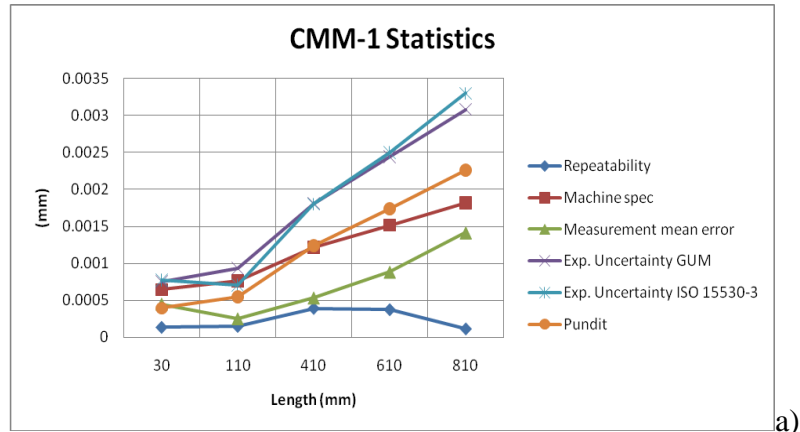
Ycal (mm)	Ym (mm)	Ucal (mm)	U _{sim} (mm)	≤ 1
20.0008	20.0004	2.76E-06	0.00046	0.86955
100.0232	100.0227	6.98E-05	0.000582	0.852988
220.0322	220.0315	0.000338	0.000925	0.710676
300.0564	300.0573	0.00063	0.0012	0.66413
420.0494	420.0501	0.001234	0.00158	0.349138
500.0463	500.0455	0.001749	0.00182	0.316908

Table 23. CMM-1 UES length test

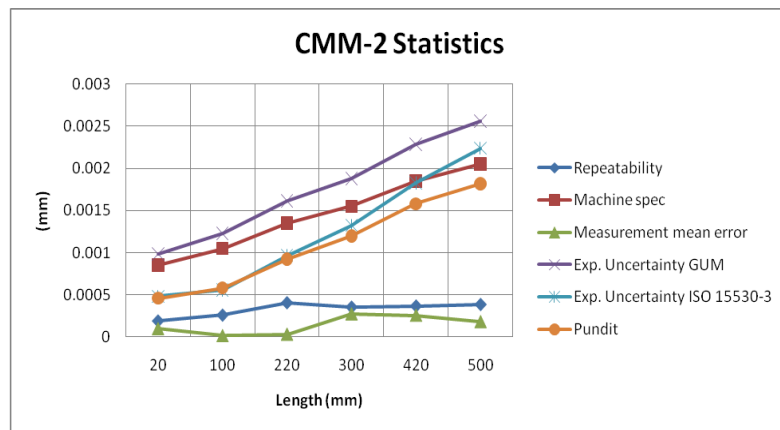
Ycal (mm)	Ym (mm)	Ucal (mm)	U _{sim} (mm)	≤ 1
30.000500	30.000200	0.000171	0.000395	0.696984
110.000600	110.000100	0.000307	0.000545	0.799336
410.000200	410.001200	0.000817	0.001240	0.673421
609.999900	610.000200	0.001157	0.001740	0.143571
809.999500	810.001100	0.001497	0.002260	0.590225

Section C.4 provides guidelines on experiments where a known reference expanded uncertainty statement could be compared with a simulated experiment.

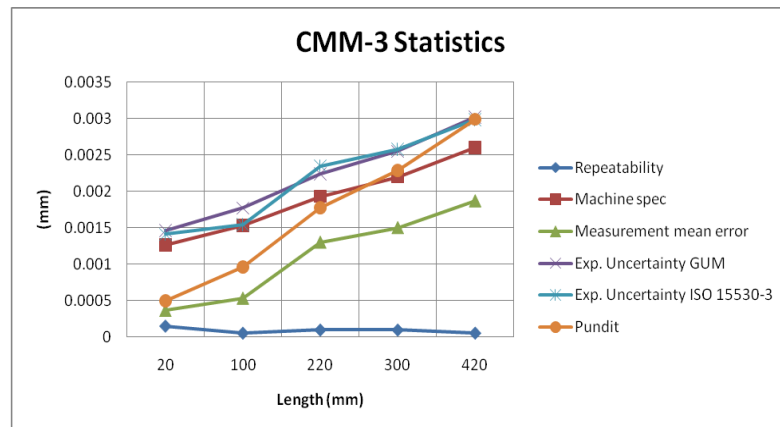
Figure-58 shows the uncertainty estimations obtained by Pundit/CMM, GUM and ISO 15330-3 (section 2.1 of this document). For all the results obtained Pundit/CMM uncertainty results were above the mean error results and the repeatability results with exception of CMM-1 30mm length where the reported UES uncertainty was found to be of very close to the mean error value. Although the comparison is provided was focused on mean error rather than absolute error, such comparison is still valid because it is an indication that the UES overestimation was consistent for more than one instance. The results obtained in section 2.1 for the uncertainty budgets were used for testing the comparison methodology described in section C.4 of the ISO 15530-4. It was found that for all CMMs the UES reported uncertainty was smaller when compared with the derived GUM uncertainty. For CMM-1 the magnitude of the expanded measurement uncertainty results from Pundit was found to be smaller when compared with the ISO-15530-3 results and GUM results. Nevertheless the trends of the results obtained (Figure-58) via Pundit were found to be very similar to the uncertainty budgets estimated from physical measurements. Pundit results for CMM-2 indicated that the simulation results were very similar to the ISO 15530-3 both in terms of magnitudes and trend when compared with the GUM results. The results for CMM-3 indicated that Pundit underestimated the magnitude of the expanded measurement uncertainty for the first two length bars when compared with the two other uncertainty budgets.



a)



b)



c)

Figure 58. a) Comparison of Pundit/CMM simulation with CMM-1 uncertainty budgets; b) Comparison of Pundit/CMM simulation with CMM-2 uncertainty budgets; c) Comparison of Pundit/CMM simulation with CMM-3 uncertainty budgets

Appendix 3 of this document contains further tests of Pundit/CMM where individual variables of the UES were tested based on known output responses.

3.2 Manufacture and inter comparison measurements of a multi feature artefact.

Some of the most common features found within critical parts of a gas turbine engine are:

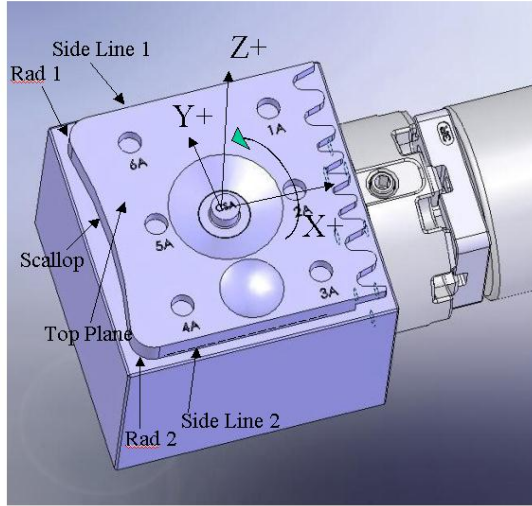
- a) Radi
- b) Holes
- c) Scallops
- d) Free for features

Such features were used to drive the design of a multi feature artefact. Most artefacts used for calibration/investigation of coordinate measuring machines capability comprise of a single type of feature or in some cases as shown in the figure 59 a small group of single features such as spheres, length bars, ring gauges. Due to traceability requirements such features will in most cases have very low form error both in terms of magnitude and uncertainty. A key requirement of the multi feature artefact was to be able to address the form error. For the purpose of this work two types of form error were applied to the “holes” features:

- a) Systematic
- b) Random

The Figures-59 a) and b) show how the two types of form error were applied to both artefacts

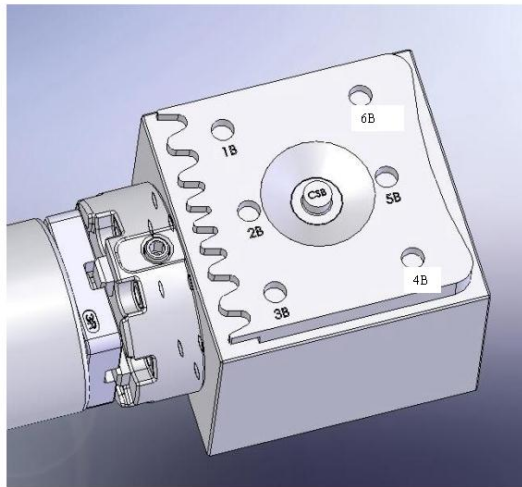
Name	Form Error	
	Feature Type	Feature Amplitude (mm)
CSA	3 lobes	0.025
1A	3 lobes	0.015
2A	4 lobes	0.015
3A	5 lobes	0.015
4A	5 harmonics	~ 0.022
5A	-	-
6A	-	-



CS: Central Spigot

a)

Name	Form Error	
	Feature Type	Feature Amplitude (mm)
CSB	-	-
1B	3 lobes	0.010
2B	4 lobes	0.020
3B	5 lobes	0.025
4B	3 harmonics	~ 0.022
5B	-	-
6B	-	-



CS: Central Spigot

b)

Figure 59. a) Features specification for artefact A; b) Features specification for artefact B

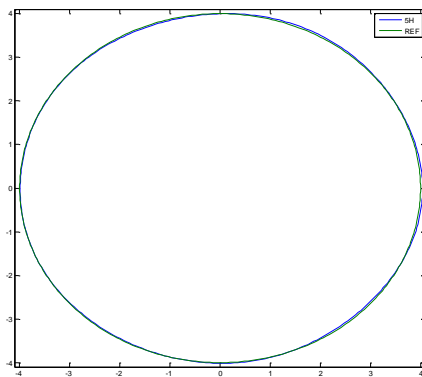
Both Artefact A and Artefact B were designed to be symmetrical with the main difference between the artefacts being the magnitude of the form in the features. Another key feature which differentiates the two artefacts were the central spigot CS. This feature was set up as a datum feature in both artefacts with the CS in artefact A having a systematic form error while the CS in artefact B had no form error. Fourier series was used to generate the features containing random form error as shown in the equations 3.2 and 3.3 for a feature with 5 and 3 lobes respectively. The formula to produce Fourier series with 5 harmonics was as follows:

$$r(\theta, b) = r_0 + s(\theta, b) \quad (3.2)$$

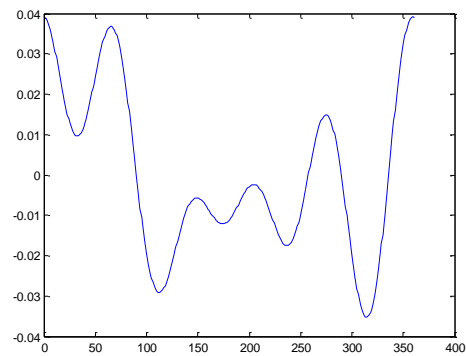
$$s(\theta, b) = \sum_{j=1}^5 [b_1(j) \sin j\theta + b_2(j) \cos j\theta] \quad (3.3)$$

$$b_1 = [0.014, 0.004, -0.001, 0.010, 0.012],$$

$$b_2 = [0.006, 0.013, 0.006, -0.006, -0.008];$$



a)



b)

Figure 60. a) Circular artefact with 5 harmonics; b) Fourier plot of the 5 harmonics

The point coordinates for the features were designed using a CAD package named Solidworks at CECA (Nottingham University). The material chosen for manufacturing the artefact was stainless steel. Both Artefacts were manufactured using a KernEvo CNC [139] with a claimed positioning accuracy in 3 axes mode of $\pm 2\mu\text{m}$.



Figure 61. KernEvo CNC 5 axis machining center and Zeiss F25 CMM

Due to the nature of the features in the artefact and the overall objective of this project, a Zeiss F25 CMM [140] was used to measure the machined artefacts and provide the calibration/reference data. The measuring volume of the CMM was the governing factor for the size of the artefacts manufactured. Appendix 1 contains all the CMM measurements for artefacts A and B. The measurements were taken using 177 probing points. Figure-62 shows the output measurement of feature 3A.



Figure 62. Fully assembled Multi feature artefact

3.3 Experimental design

For the experimental design of this project three different machines both in terms of specification and operational environment were selected. All machines selected were of the moving bridge type and all the probing strategy adopted was carried out in touch trigger mode. Table-24 summarises the main characteristic of each machine.

Table 24. CMM's specifications

	Machine M	Machine W	Machine C
Environment	Class A (+/- 0.5 °C)	Class B (+/- 1 °C)	Shop Floor (+/- 2 °C)
Specification (MPE μ m)	0.6+1.5L/1000	2.5+4L/1000	3+4L/1000

The experimental design of this project was to a certain extent governed by the CMM availability at each of the partners selected. The Table- 25 shows the probing strategy for Artefacts A and B. Each machine had to perform 3 repeat measurements of one artefact at

three different days. In a particular day the artefact would be rotated by 90° about the Datum-CS axis and applied probing strategy I-Basic. All features extracted from the machine measurements used LSC as the fitting algorithm.

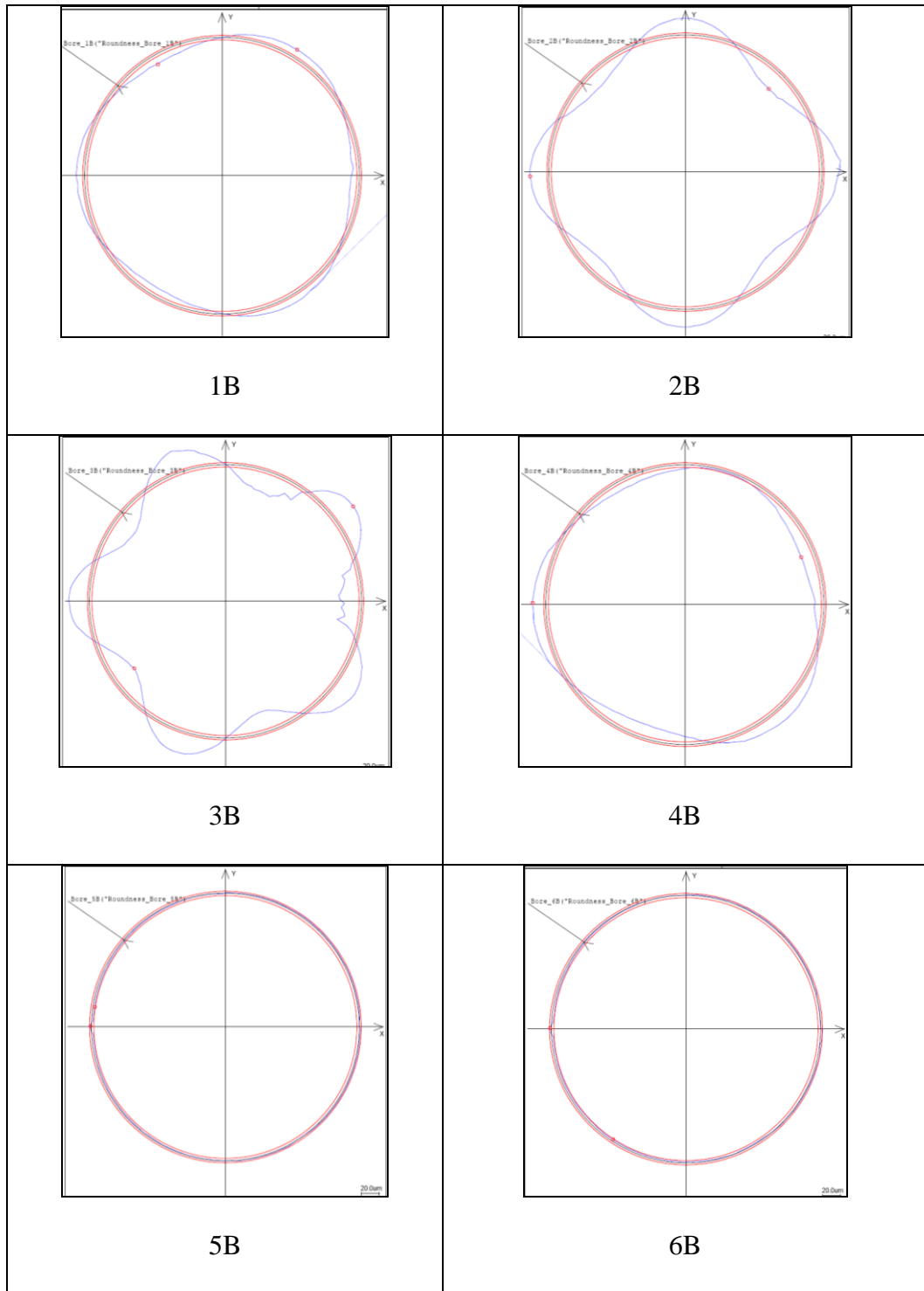
Table 25. Artefact A&B probing strategy

Hardware		Probing Strategy	I-Basic	III- 3xBasic
Probe calibration	5 or 9 points	Top plane	5	15
Probe stily	2mm ball	Side line 1	3	11
Probe Length	20mm	Side line 2	3	3
		Circle (Datum-CS)	4	13
		Cone	2X4	3X11
		Sphere	1X4+1	25
		Scallop	5	17
		Rad 1	4	4
		Rad 2	4	4
		Z Depth	2 mm	2 mm

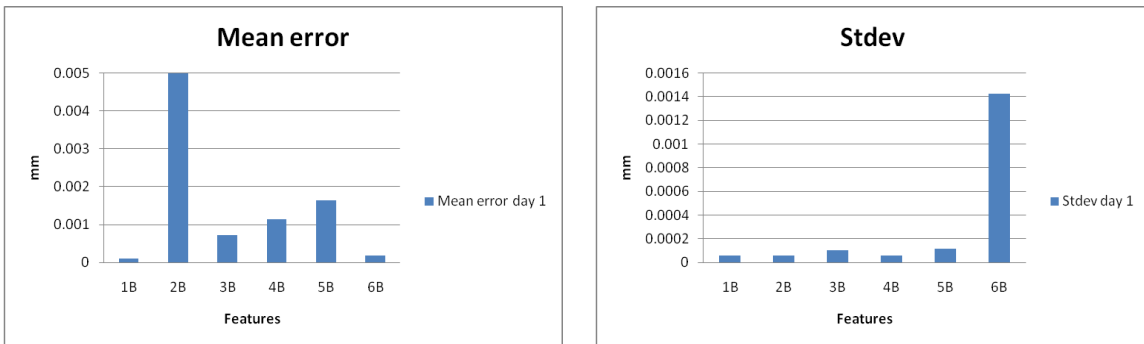
3.3 Physical measurements results

The results below are presented by each machine individually with a summary of all machines at the end of this section. The Table-27 shows the calibration plots for features 1B, 2B, 3B, 4B, 5B and 6B. The results obtained with the Zeiss F25 were used as the reference nominal values. No uncertainty values were provided with the reference nominal which under normal circumstances would affect experimental results due to the fact that the calibration uncertainty is required to build an uncertainty budget as shown in section 2.1 of this workbook. An assumption was made that the uncertainty resultant from the Zeiss CMM would be relatively small when compared with the magnitudes of the features being explored in this experiment.

Table 26. Artefact B features plots from Zeiss F25 CMM measurements.



3.3.1 Machine M Physical measurement results - Size

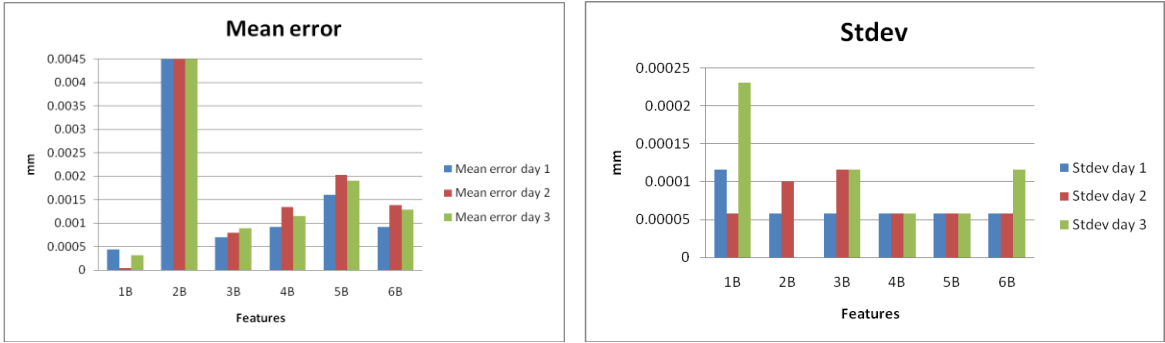


a)

b)

Figure 63. Day 1 I-Basic; a) Mean error of three repeats b) One standard deviation of three repeats

Figure-63 shows the results for the mean error and one standard deviation of the measurement results taken by machine M. The magnitude of the mean error for most features was found to be below 0.002mm with feature 2B showing a mean error value of 0.04mm. Feature 2B consisted of a circular feature with a systematic 4 lobe effect with a magnitude of 0.04mm. Table-26 shows the calibration plot for feature 2B. From the measured plot it is clear that the lobes are in phase with the X,Y datum lines. The basic measurement strategy for features 1B to 6B was 4 probing points equally distributed. It is clear that the probing points were also in phase with feature lobe during the measurement process which is a good indication that the datuming strategy was consistent with the one used during the calibration of the artefact. The standard deviation results obtained for all features were below 0.0005mm with the features 3B and 5B showing slightly higher Stdev values when compared to the remaining features.



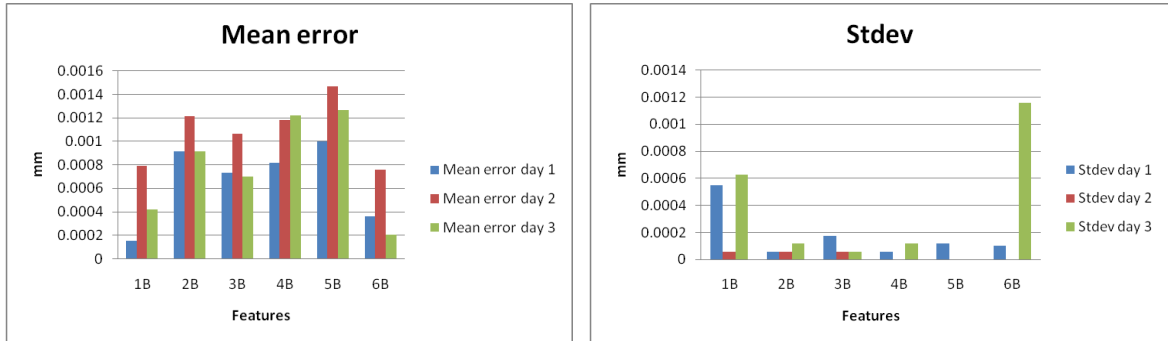
a)

b)

Figure 64. Three days I-Basic with 90 X,Y rotation about Datum-CS ; a) Mean error of three repeats b) One standard deviation of three repeats

Figure-64 shows the results for both mean error and standard deviation of the measurement results with a 90 rotation about the Z axis in the X,Y plane. Unlike the results show in Figure-63, Figure-64 shows the measurement results over a 3 day period. Although it was not shown, the magnitude of the mean error for Figure-64 a) was found to be consistent with one found for the mean error in Figure-64 of 0.039mm. Although there was a rotation of about the Z axis, due to phase of the lobe of this feature it was clear that the 4 probing points were once again in phase with the feature lobe. For the 3 days all features with exception of feature 2B show mean error values below 0.002mm with higher magnitudes found for day 1 of the experiment when compared with the 2 following days. Figure-64 b) shows that the magnitude of the standard deviation values for all three days for all the features was below 0.0008mm. Figure-65 shows the measurement results for all features using 13 probing instead of the 4 probing points. The mean error plot indicates that for all features during all days of the experiment the magnitude of the mean error was found to be below 0.001mm. Such results clearly indicates that the use of a higher number of probing points not only improved the

magnitude of the mean error for the experimental runs but it also deals with lobed features such as feature 2B in a more accurate manner.



a)

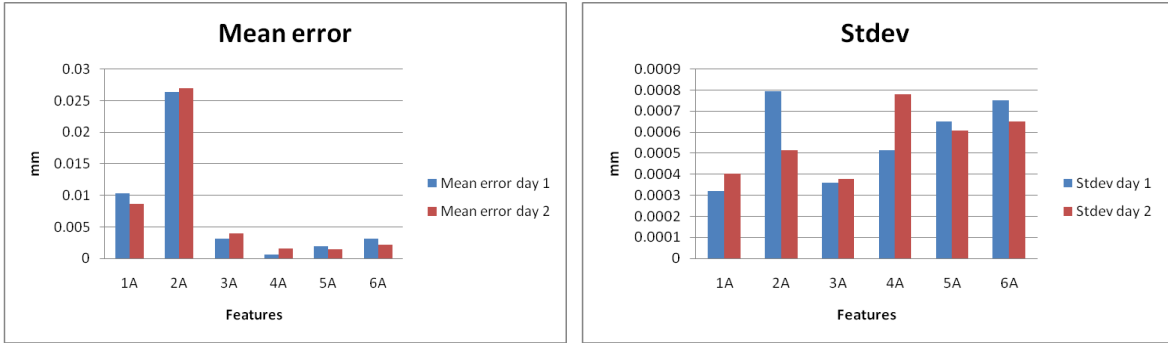
b)

Figure 65. Three days 3X-Basic; a) Mean error of three repeats b) One standard deviation of three repeats

The standard deviation plot for the 3 days of experimental trials indicates that the magnitude of the Stdev was found to be below 0.0012mm. Some of the values obtained were found to be slightly higher when using a higher density of probing points when compared with Figure-64 where a low density of points was used.

3.3.2 Machine C Physical measurement results - Size

The results presented for machine C were obtained using artefact A unlike machine M. Figure-66 contains the results for the mean error and the standard deviation. The magnitude of the mean error for all features measured (1A to 6A) were found to be below 0.005mm with feature 1A recording a mean error value of 0.010mm for both days. Feature 2A was found to have the highest mean error magnitude of 0.025mm.



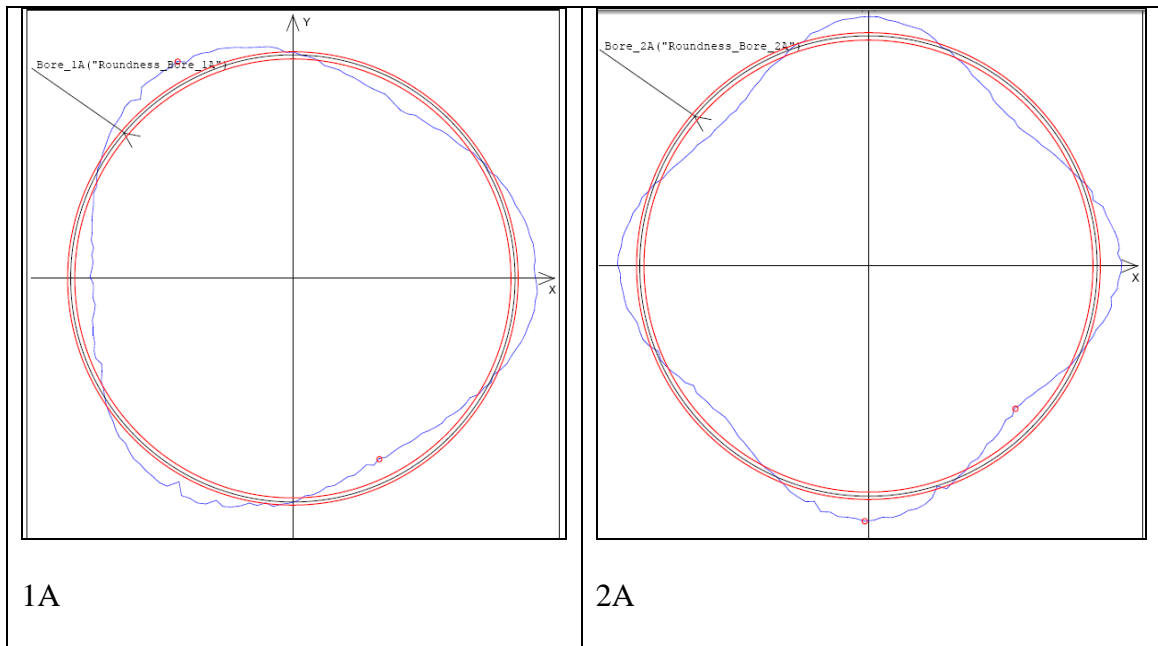
a)

b)

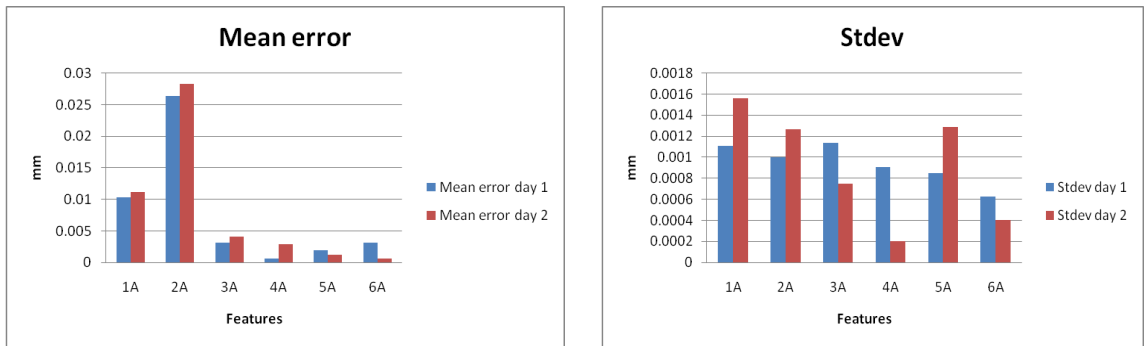
Figure 66. I-Basic; a) Mean error of three repeats b) One standard deviation of three repeats

These results were found to have some similarities with the results obtained for Machine M feature 2B. The Table- 27 shows the calibration plots for both features 1A and 2A.

Table 27. Zeiss F25 CMM measurement plots for features 1A and 2A.



From the reference plots in Table-20, it was clear that the magnitude of the mean error results was found to be higher for these two features due to the fact that the probing strategy was in phase with the features lobe. In the case of feature 1A the magnitude of the mean error measured when compared with form error applied was found to be approximately 1/3. This was due to the fact that only one of the four probing points used would ever touch the peak of the 3 lobe effect. The magnitude of the standard deviation obtained for all features was found to be below 0.0008mm.



a)

b)

**Figure 67. I-Basic with 90 X,Y rotation about Datum-CS ; a) Mean error of three repeats
b) One standard deviation of three repeats**

Figure-67 shows the results obtained for features 1A to 2A using the same probing strategy as the one applied to results shown in Figure-66 but with a rotation about the Z axis of 90. The mean error results obtained were very similar to the ones presented in Figure-66 with features 1A and 2A recording large mean error values while the remaining features recorded mean error values below 0.005mm. The standard deviation results were found to be of slightly higher magnitude when compared to the ones obtained without the X,Y rotation and mainly during day 2.

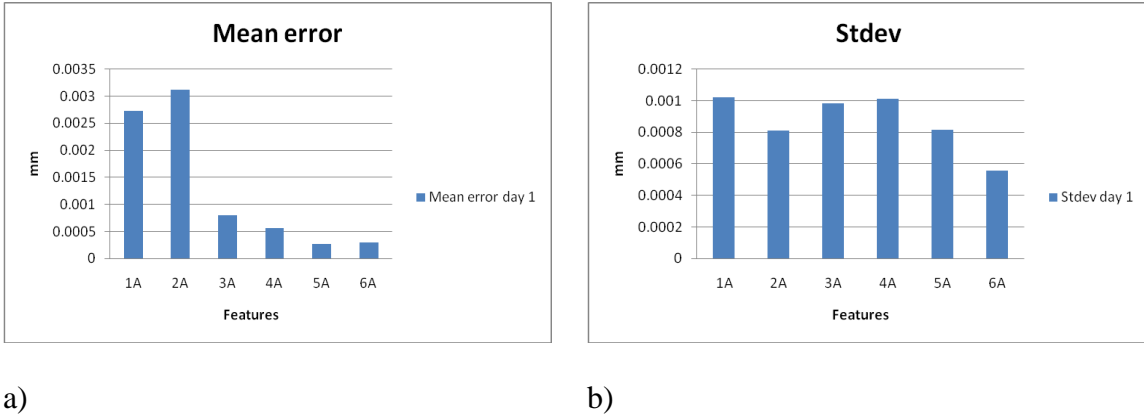


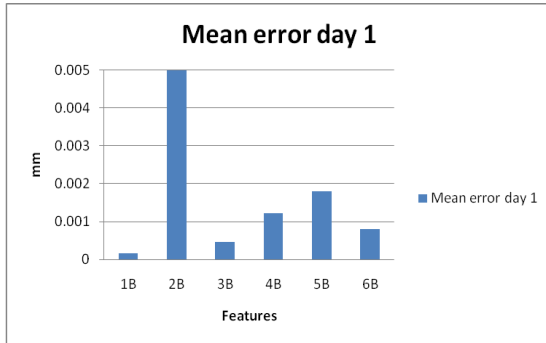
Figure 68. 3X-Basic; a) Mean error of three repeats b) One standard deviation of three repeats

Figure-68 shows the mean error and standard deviation results obtained using the high density probing strategy. The mean error results show that for all features there was a decrease in the magnitude of the mean error. For most features the magnitude of the mean error was found to be below 0.001mm with features 1A and 2A recording values of 0.0025mm and 0.0032mm respectively. The magnitude of the standard deviation results obtained for all features was found to be below 0.001mm. Such result was found to be slightly higher when compared with results obtained in Figure-66 where less probing points were used during the measurements.

3.3.3 Machine W Physical measurement results - Size

Figure-69 shows the measurement results obtained for features 1B to 6B. The magnitude of the mean error results was found to be below 0.002mm for all features with the exception of feature 2B where the mean error magnitude was found to be 0.04mm. The trend and magnitudes of the measurement results were found to be very consistent with the ones obtained by machine M. A similar result was found for the magnitudes of the

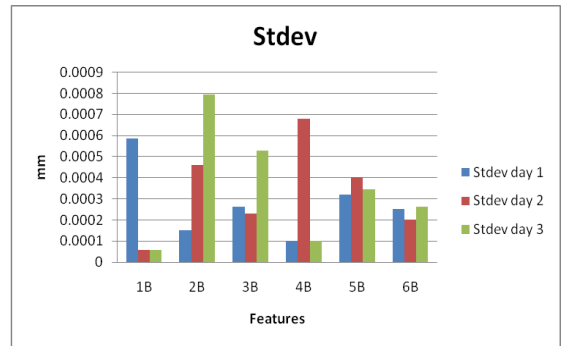
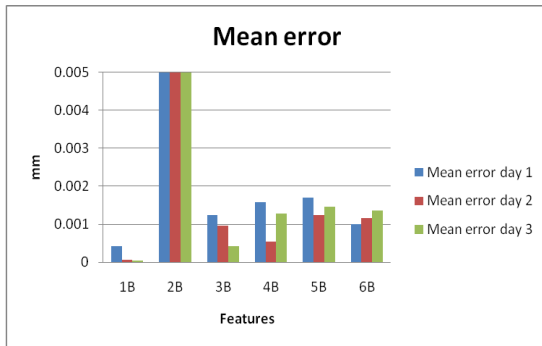
standard deviation for all the features measured when compared to Figure-70. Figure-71 indicates all standard deviation results for all features remained below 0.0005mm.



a)

b)

Figure 69. I-Basic; a) Mean error of three repeats b) One standard deviation of three repeats

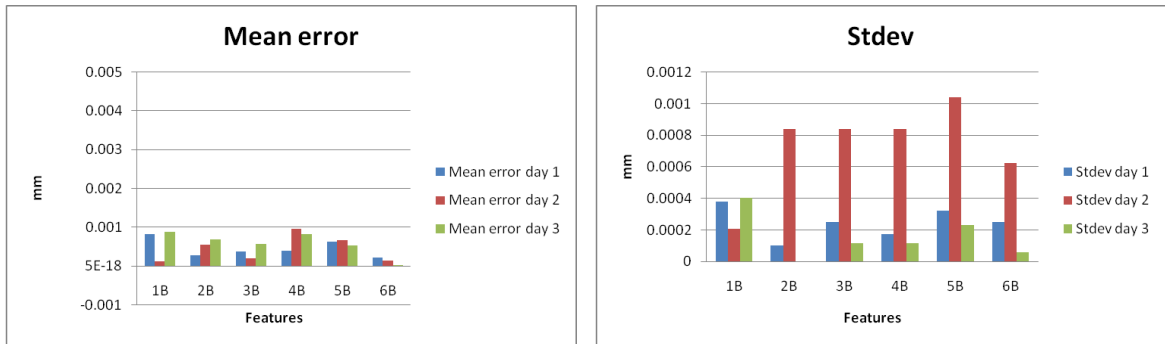


a)

b)

Figure 70. I-Basic with 90 X,Y rotation about Datum-CS ; a) Mean error of three repeats b) One standard deviation of three repeats

The results shown in Figure-70 indicate that magnitude of the mean error was found to be very similar to the one shown in Figure-69. Such result clearly shows that the X,Y rotation applied to the measurement strategy did not have a strong effect on the mean error results obtained. All standard deviation results shown in Figure-70 were found to be below a value of 0.0008mm.



a)

b)

Figure 71. 3X-Basic; a) Mean error of three repeats b) One standard deviation of three repeats

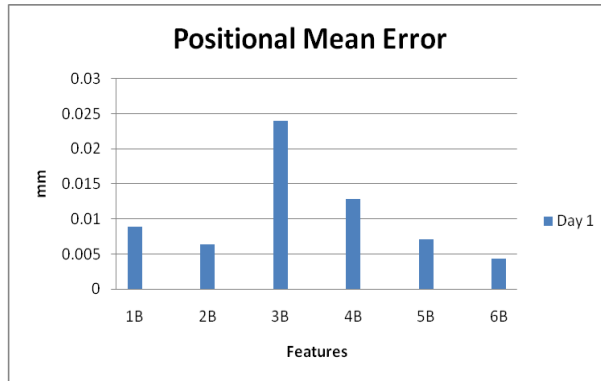
Figure-71 shows the mean error and standard deviation results obtained during the three days using the high number of probing points strategy. When compared with the results shown for the mean error plot in Figure-70, it was clear that by using a higher number of probing points reduces in general the magnitude of the mean error. All mean error values shown in Figure-71 a) were found to be below a value of 0.001mm including feature 2B which previously featured a mean error of 0.04mm. Standard deviation values were found to be below 0.0012mm with the higher values found during day 2 measurements.

3.3.4 Features Position results (M, C, W)

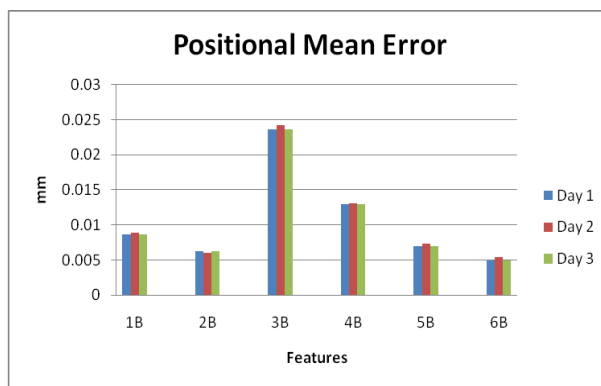
The positional error (P) for the features of artefact B was derived by summing the X and Y coordinates mean errors in quadrature.

Machine M

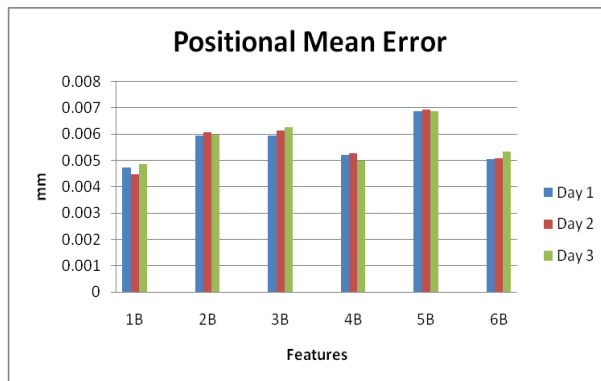
From the Figure-72 a),b) above the maximum positional error found was 0.025mm for feature 3B. This result was consistent when using the 1XBasic and 1XBasic XY rotation probing strategy for all days. Feature 3B consisted of a systematic 5 lobe effect with 0.025mm amplitude. Feature 4B was found to have a positional error of 0.013mm. This feature consisted of 3 harmonic lobbing effects with 0.022mm amplitude. The magnitude of the positional error for features 2B,5B and 6B was found to be 0.005mm. Both features 5B and 6B had no form error while feature 2B had a systematic 4lobed effect with amplitude of 0.020mm. Feature 1B had a 3 lobe systematic effect with amplitude of 0.010mm. Its positional error was found to be 0.0085mm. These results seem to indicate that both the phase and amplitude of the form error applied to a feature will have an impact on its positional accuracy. Figure-72 b) shows that for the different days of the experimental trials the results showed consistency which indicated that the factors affecting this experimental trial were of systematic nature. Figure-72 c) showed a reduction in the magnitude of the mean error for all features with a maximum value of 0.007mm recorded for feature 5B.



a) 1XBasic



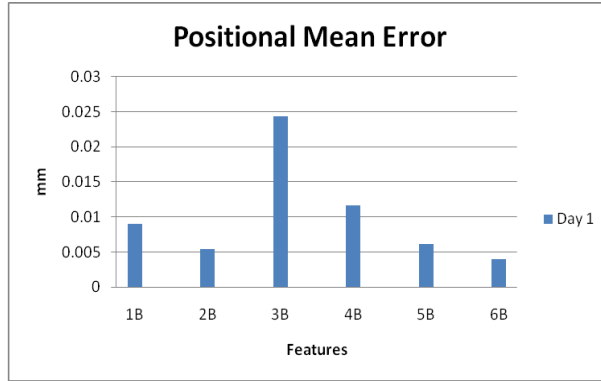
b) 1XBasic XY rotation



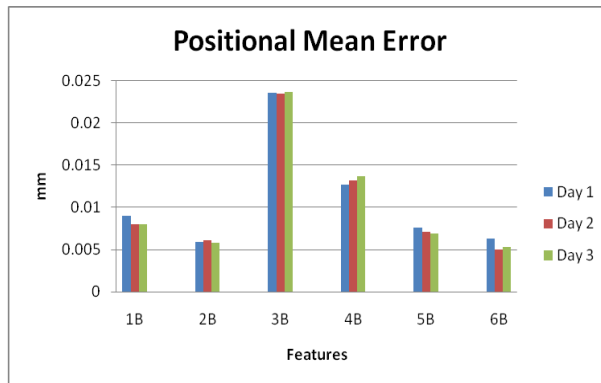
c) 3XBasic

Figure 72_ a) Mean error of three repeats 1XBasic; b) Mean error of three repeats 1XBasic XY; c) Mean error of three repeats 3XBasic

Machine W



a) 1XBasic



b) 1XBasic XY rotation



c) 3XBasic

Figure 73_ a) Mean error of three repeats 1XBasic; b) Mean error of three repeats 1XBasic XY; c) Mean error of three repeats 3XBasic

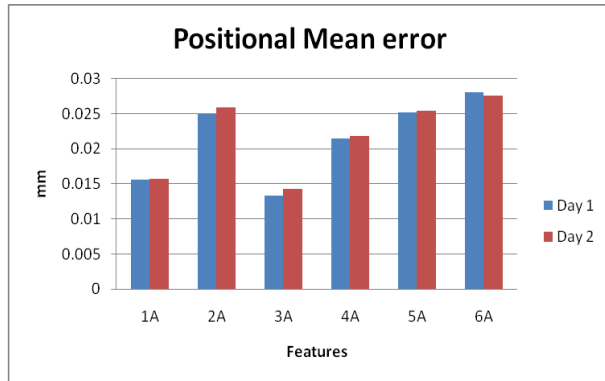
From the Figure-73 a),b) the maximum positional error found was 0.025mm for feature 3B. This result was consistent when using the 1XBasic and 1XBasic XY rotation probing strategy for all days. The results obtained were very similar to the ones obtained by Machine W (Figure 72).

Figure-73 c) showed a reduction in the magnitude of the mean error for all features with a maximum value of 0.007mm recorded for feature 5B. This result was obtained due to increase in the number of probing points.

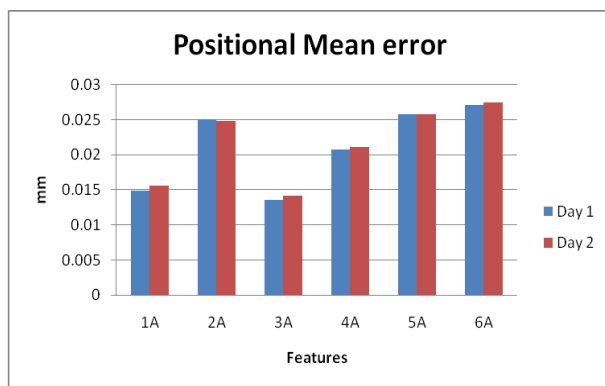
Machine C

Machine C results (Figure-74 a),b)) showed higher magnitudes of the mean error when using 1XBASIC strategy. The maximum value of the mean error found was for features 5A and 6A which. Both features did not have any artificial for error inferred. Similarly feature 2A was also found to have a high mean error value of 0.025mm. The 3XBASIC results showed an overall reduction in the mean error values for all features. Features 1A and 3A recorded the highest mean error values of 0.001mm.

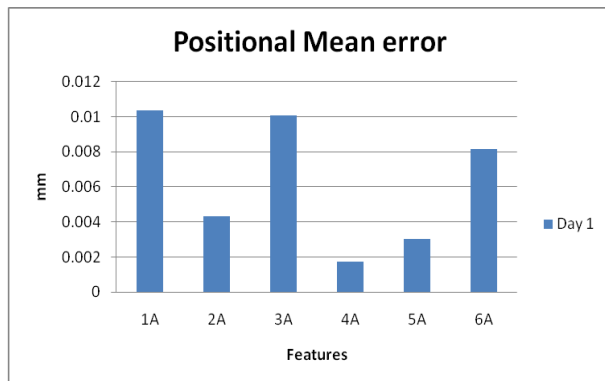
The standard deviation results for the position results can be found in Appendix 3.3.4.



a) 1XBasic



b) 1XBasic XY rotation



c) 3XBasic

Figure 74.a) Mean error of three repeats 1XBasic; b) Mean error of three repeats 1XBasic XY; c) Mean error of three repeats 3XBasic

3.4 VCMM multi feature artefact simulation

The Figure-75 shows an example of a hole positional tolerance for feature 3B set up in Pundit/CMM with the corresponding datum strategy.

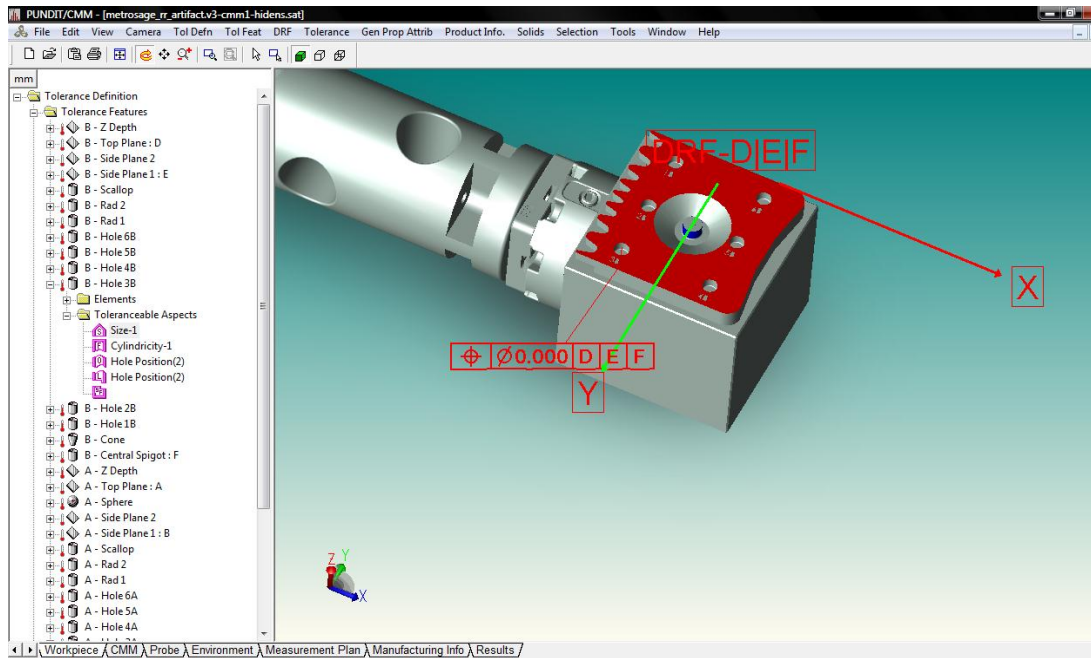


Figure 75. Datum set up for Artefact B in Pundit/CMM

The Figure-76 shows an example of the probing strategy (1XBasic) and the definition of form error for feature 3B. The sections below describe compare the original physical measurement results for size and position of the 6 circular features for artefacts A and B. Uncertainty values of the physical measurement results were calculated in accordance with Pundit's uncertainty calculation (ISO 15530-3).

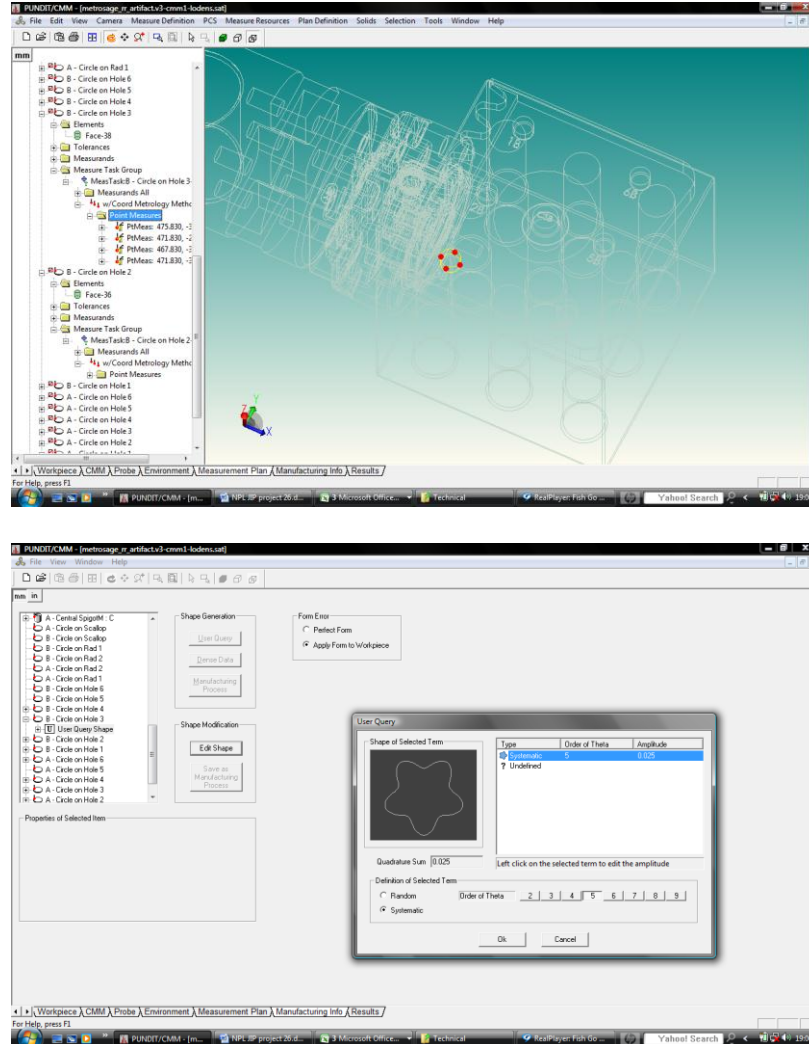


Figure 76. Probing strategy and form error definition in Pundit/CMM

3.4.1 VCMM vs Physical measurement results – Size

Machine M

Figure-77 shows the results indicate that there was good correlation for the results obtained via Pundit/CMM and the physical measurements of machine M. Figure-77 a)

feature 2B showed an uncertainty of 0.04mm during the physical measurement trails while the magnitude obtained via Pundit’s simulation was 0.058mm. Although the value obtained from the simulation was of higher magnitude when compared with the physical measurements, the trend of results obtained was very similar with feature 2B recording an extremely high uncertainty value.

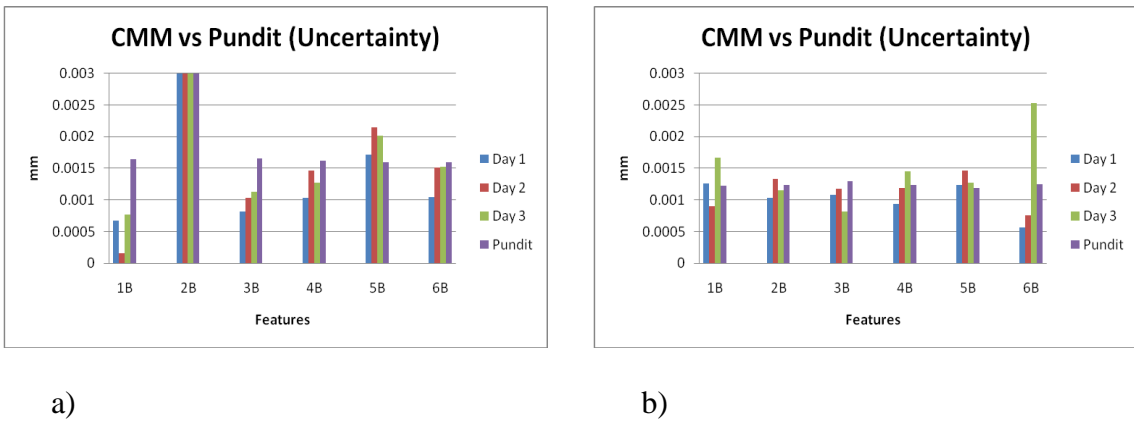


Figure 77. Pundit Simulation comparison for Machine M feature sizes a) 1XBasic; b) 3XBasic

The results obtained by Pundit/CMM also demonstrated that the UES reported uncertainty for all features in 1XBasic was higher when compared with the mean error results. When simulating the 3XBasic experiment the UES uncertainty values were also found to be higher than the mean error values obtained in the physical measurements section 3.3 (Figure-66,67,68) with the exception of features 4B and 5B where the UES reported uncertainty was very similar to the mean error values.

Machine W

From the results in the Figure-78 a) figure 2B recorded an uncertainty value of 0.040mm for the physical measurements and 0.057mm using Pundit/CMM. For the remaining features Pundit's results were very similar to the physical measurement results.

The results from Pundit/CMM shown in Figure-78 b) indicate that the simulation values for most of the features were overestimated when compared with Days 1 and 3 of the physical measurements. The uncertainty values obtained during day 2 of the physical measurements were found to be of approximately 100% higher magnitude when compared with the two other days.

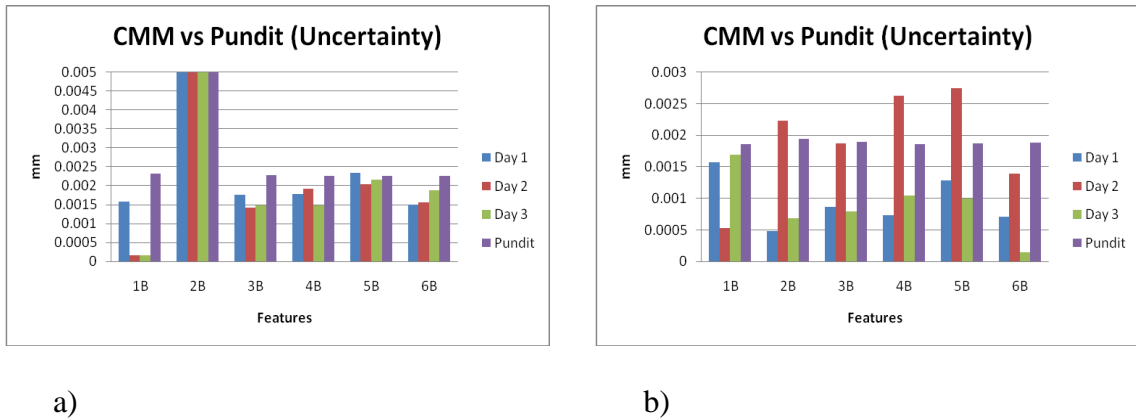
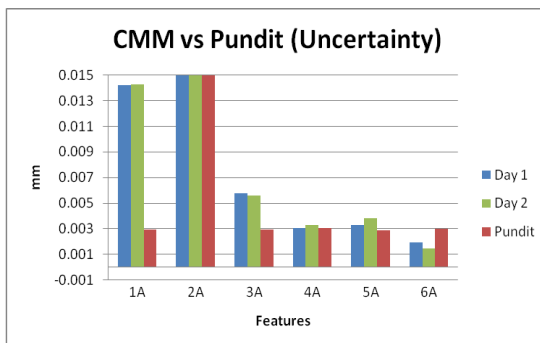


Figure 78. Pundit Simulation comparison for Machine W feature sizes a) 1XBASIC; b) 3XBASIC

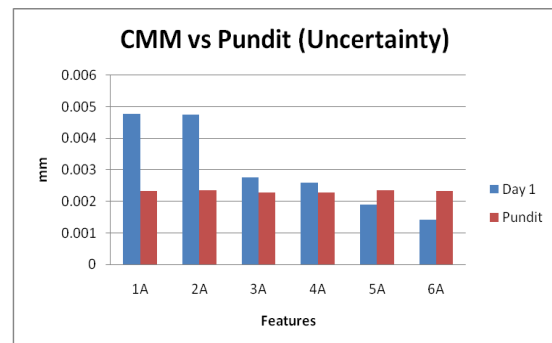
The uncertainty values reported for the 1XBASIC and 3XBASIC experiments were found to be above the mean error values reported in section 3.3 (Figure-69,70,71).

Machine C

The chart 79 summarises the uncertainty values obtained for the 6 features in Artefact A. The results indicated that there was good correlation for the results obtained via Pundit/CMM and the physical measurements of machine C. Figure-79 a) feature 2A showed an uncertainty of 0.028mm during the physical measurement trails while the magnitude obtained via Pundit's simulation was 0.042mm. Although the value obtained from the simulation was of higher magnitude when compared with the physical measurements, the trend of results obtained was very similar with feature 2A recording an extremely high uncertainty value. When compared with the physical measurement results presented in section 3.3 (Figure-66,67,68), the 1XBASIC UES reported uncertainty was found to higher than the mean error values. For the 3XBASIC features the UES reported for features 1A and 2A was found to be smaller when compared with the mean error values. While the mean error values were found to be 0.0025mm and 0.003mm, the reported UES uncertainty values were 0.0022mm for both features.



a)



b)

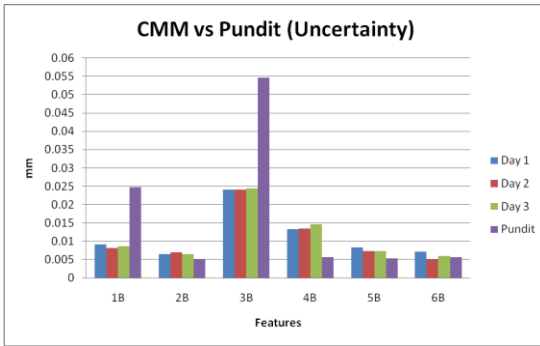
Figure 79. Pundit Simulation comparison for Machine C feature sizes a) 1XBasic; b) 3XBasic

3.4.2 VCMM vs physical measurement results – Position

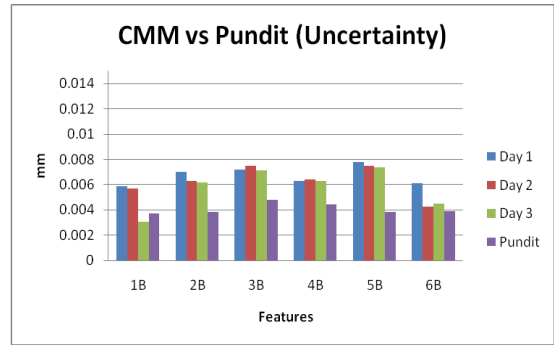
Machine – W

The chart 80 summarises the positional uncertainty values obtained for the 6 features in Artefact B. Uncertainty values were calculated in accordance with Pundit's uncertainty calculation. From the chart 80 the results indicate that there was good correlation for the results obtained via Pundit/CMM and the physical measurements of machine W. Figure-80 a)1XBasic feature 1B showed an uncertainty of 0.008mm during the physical measurement trials while the magnitude obtained via Pundit's simulation was 0.025mm. Feature 3B showed a similar trend where the uncertainty values of the physical measurements were found to be approximately 0.024mm and the simulation values 0.057mm. For the remaining features the uncertainty values obtained via Pundit CMM were very similar to the ones obtained via the physical measurements for the different days.

Figure-80 b)3XBasic showed that Pundit CMM results not only followed the trend of the results for the different features but the magnitudes also correlated extremely well.



a)



b)

Figure 80. Pundit Simulation comparison for Machine W features position a) 1XBasic; b) 3XBasic

When compared to the 3XBASIC mean error physical measurement results, the UES uncertainty values for all the features were found to be smaller. Most of the features mean error position results were found to be above 0.006mm while the reported UES values were 0.004mm for most features.

3.4.3 Impact of form error definition within Pundit/CMM

In order to investigate the overestimation of features 1B and 3B in Pundit/CMM, the systematic form error was loaded via the “dense data” within Pundit’s manufacturing tab menu. This option was previously used to load the data generated for features 4B and 4A of the multifeature artefact due to the nature of the lobes generated using Fourier series as opposed to totally random lobes.

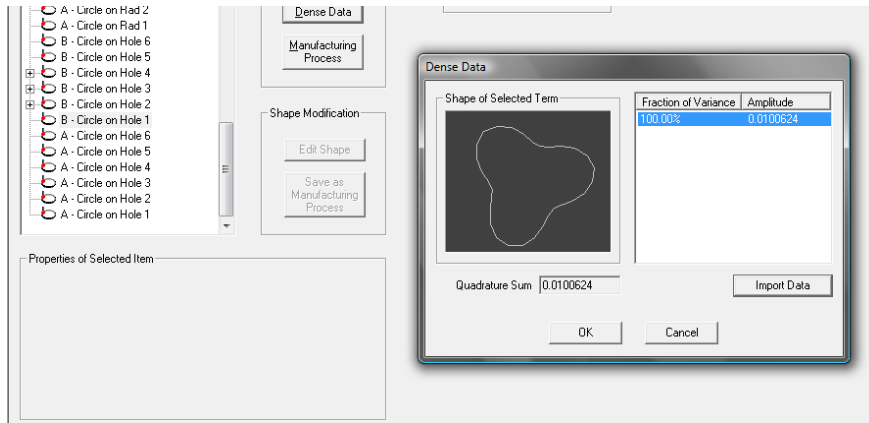
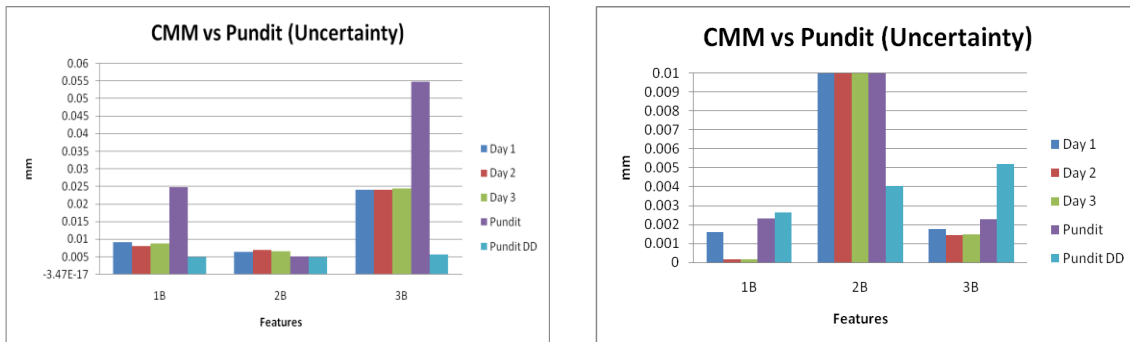


Figure 81. Pundit/CMM dense data option

The results below show the impact of using the dense data option for the application of form errors. Figure-82 a),b) show the simulation results for the positional and size measurements respectively using the 1XBasic Probing strategy.



a)

b)

Figure 82. Impact of dense data option using 1XBasic a) Feature position; b) Feature size

The results above indicated that for features 1B and 3B the magnitude of the positional uncertainty values obtained when using “dense data” option decreased to approximately 0.005mm. For feature 2B the magnitude of the positional uncertainty was found to be the same when using Pundit/CMM in both “User query” mode and “dense data” mode.

A similar result was found for the uncertainty associated with the size of feature 2B where its magnitude was found to be 0.004mm as opposed to 0.057mm. For feature 3B the uncertainty value increased to 0.005mm using the “dense data” mode.

Figure-83 a),b) show the simulation results for the positional and size measurements respectively using the 3XBasic Probing strategy.

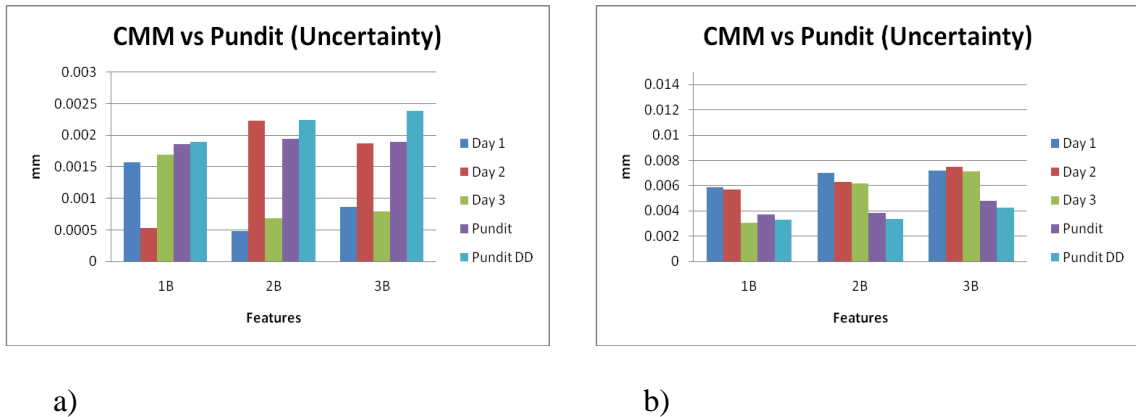


Figure 83. Impact of dense data option using 3XBasic a) Feature position; b) Feature size

The results above indicated that the magnitude of the uncertainty values for both size and positional uncertainty did not change significantly using both simulation options within pundit/CMM.

Machine – M

The simulation results from Figure-84 a) indicated that Pundit/CMM overestimated the uncertainty associated with features 1B and 3B. In both cases the overestimation was found to be approximately 100% when compared with the physical measurement results. For the remaining features, the simulation results indicated an underestimation when compared with the physical measurement results.

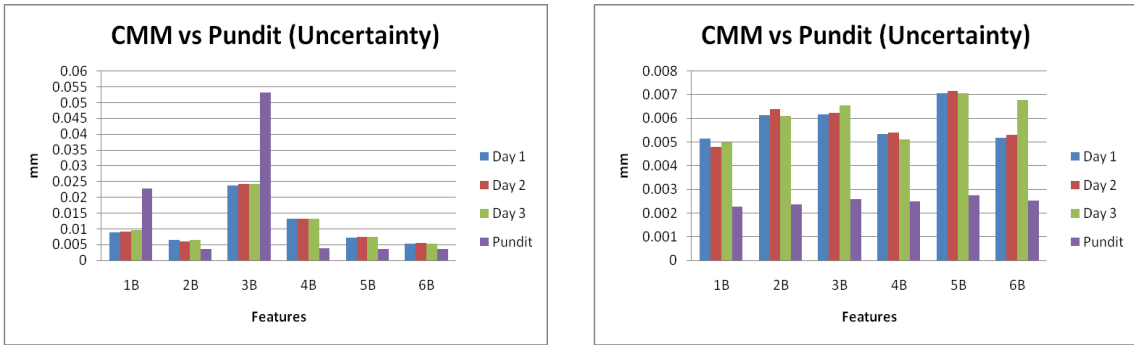


Figure 84. Pundit Simulation comparison for Machine M features position a) 1XBasic; b) 3XBasic

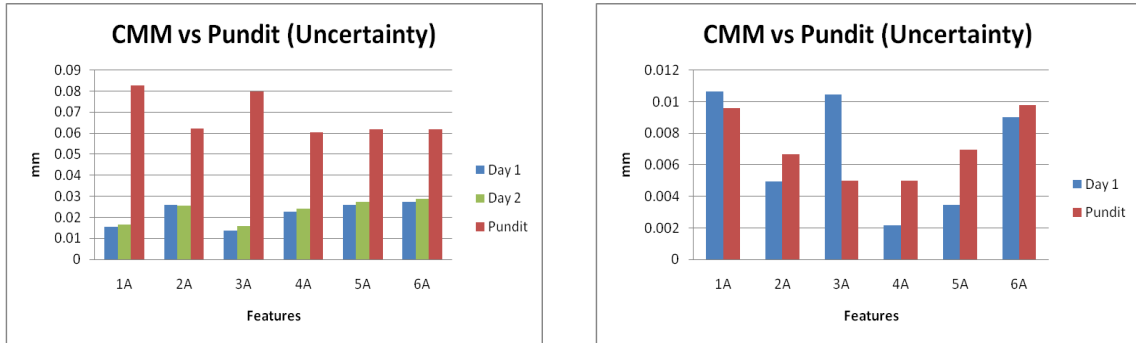
The results obtained using the 3XBasic probing strategy indicated that for all features Pundit/CMM underestimated the positional uncertainty when compared with the physical measurements of the artefact. For most of the features the underestimation was approximately 50%.

When compared with the mean error results found shown in section 3.3 for the 1XBASIC simulation the UES only overestimated the uncertainty for features 1B and 3B. For the remaining features the UES underestimated the measurement uncertainty when compared with the mean error results. Nevertheless the trends found for features 1B and 3B replicate d the trends found during the physical measurement trials.

Machine – C

The simulation results from Figure-85 a) indicated that Pundit/CMM overestimated the positional uncertainty associated with all features when compared with the physical measurement results. The overestimation obtained via Pundit/CMM was approximately

100%. For the 3XBaisc simulation, Pundit/CMM estimations were found to be very similar to the ones obtained for all the artefact features.



a)

b)

Figure 85. Pundit Simulation comparison for Machine C features position a) 1XBasic; b) 3XBasic

Unlike artefact B, artefact A contained a Datum features CSA with form error.

3.5 A Case study for application of Pundit CMM during dowell hole measurement of shafts

The drawing definition for the dowel holes measurement can be seen in Figure-86. Datum A and B were used to define a datum line across the centre of the shaft to which the centre of each dowell hole is referenced to. Datum C indicates the holes should be measured has cylinders and not circles.

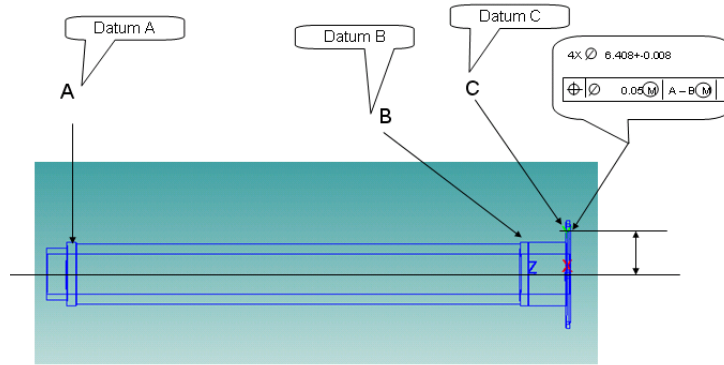


Figure 86. Definition for measurement of dowell holes

The measurement system used for this task is an Eley CMM with a specification of $5+6.7L/1000$ (μm) according to the ISO-10360-2. Within this particular CMM measurement system there were factors that influence the measurement result. The breakdown of these factors can be seen in Figure-87.

CTQC tree diagram

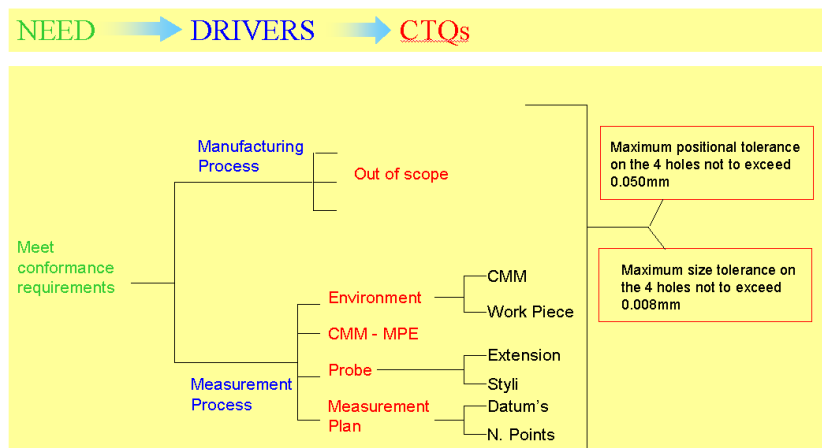


Figure 87. Critical to quality characteristics (CTQC) diagram for the specific CMM

The underlying methodology used in this study was based on the ISO-15530-3 approach where a reference artefact that represents the measurand under investigation was used to determine the task specific measurement uncertainty. Below are the steps used to determine the expanded measurement uncertainty for the physical measurement of the Master artefact:

- a) Calibration of the artefact/part using the same measurement strategy i.e datum's, planes.
- b) Measure the Master shaft 10 times on the Eley CMM under the same conditions
- c) Compute both standard deviation and mean error based on the calibration results
- d) Used the quantities in c) to determine expanded measurement uncertainty

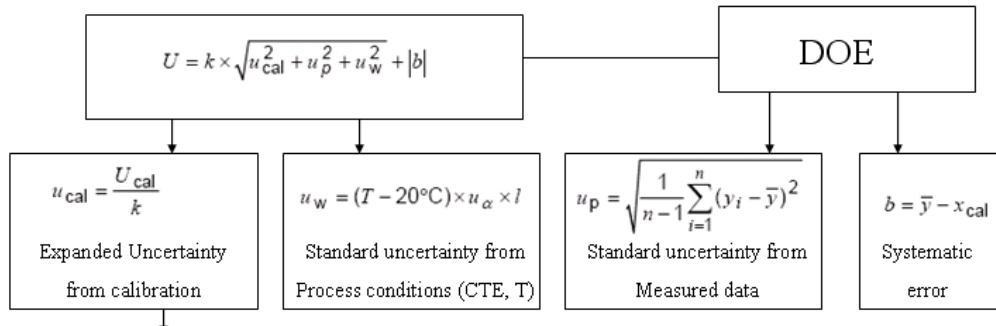


Figure 88. Experimental workflow using the ISO 15530-3 approach

The quantities used to determine the expanded measurement uncertainty can be seen in Figure-88 where:

U_{cal} was the standard uncertainty evaluated from the expanded uncertainty given on the calibration certificate of the calibrated ring gauge:

$$u_{cal} = \frac{U_{cal}}{k}$$

(3.4)

And k is the coverage factor with a value of 2 for a coverage probability of 95%. The standard uncertainty due to measurement process u_p is equal to $stdv$ as defined by equation-xx. u_w is the standard uncertainty from the manufacturing process:

$$u_w = (T - 20^\circ C) \times u_\alpha \times L$$

(3.5)

Where u_α is the standard uncertainty of the expansion coefficient of the master artefact, T is the average temperature during the experimental measurement and L the dimension under investigation. For this study the value attributed to u_α was 10% of the thermal expansion coefficient value.

Environment – According to the data logger present in the CMM room the temperature uncertainty for the facility was 20 +/- 2 C.

Probe Extension – No probe extensions were used during this study.

Styli – The styli used was 20 mm long with a 2mm ball tip.

Measurement plan – The measurement plan used for the master shaft followed the production practice. Probe 6 points in each of the datum's A and B to establish the centre of a circle. From the centre of the circle a datum line is established and the centre of each hole is then referenced in terms of position to the datum line. The artefact selected for the study was a Master Shaft which had the same features being assessed in this study. All the measurements were carried out using production parts datum's and alignments so that the results represent the production part as much as possible. Figure-89 illustrates the master shaft used in Pundit/CMM.

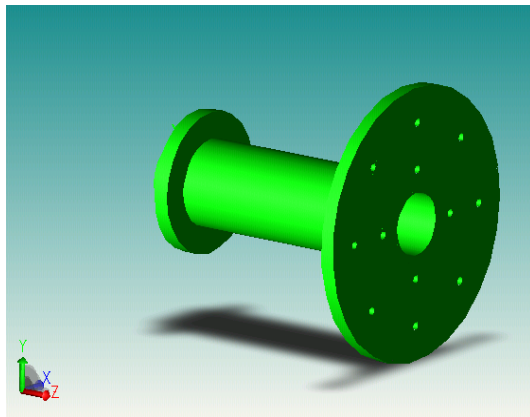


Figure 89. 3D visualisation of master shaft in Pundit/CMM

3.5.1 Physical measurement results of the master shaft

The Figure-90 contains the data for 10 repeated measurements of the size and position of the dowel holes seen in Figure-89. The calibration values were used as nominal values for the calculations below. From the chart below it was clear that the CMM repeatability was between 0.0005 and 0.0015mm for both size and position. The same value applied for the mean error in terms of the hole size. For the mean error in terms of hole positioning the values varied between 0.0005 and 0.01 mm. Since the machine specification fell within the 6 microns range and that most holes never reached such value, the 0.01 mm results could only be considered outliers. These were later identified as squareness error on the machine by an Eley technician. This error was only found when the Z axis was fully extended. For the purpose of uncertainty evaluation the value of 0.0045 mm was taken as being the mean error for both X and Y position. The sine wave effect seen on the screen may be due to factors such as fixturing concentricity during manufacture of the master shaft.

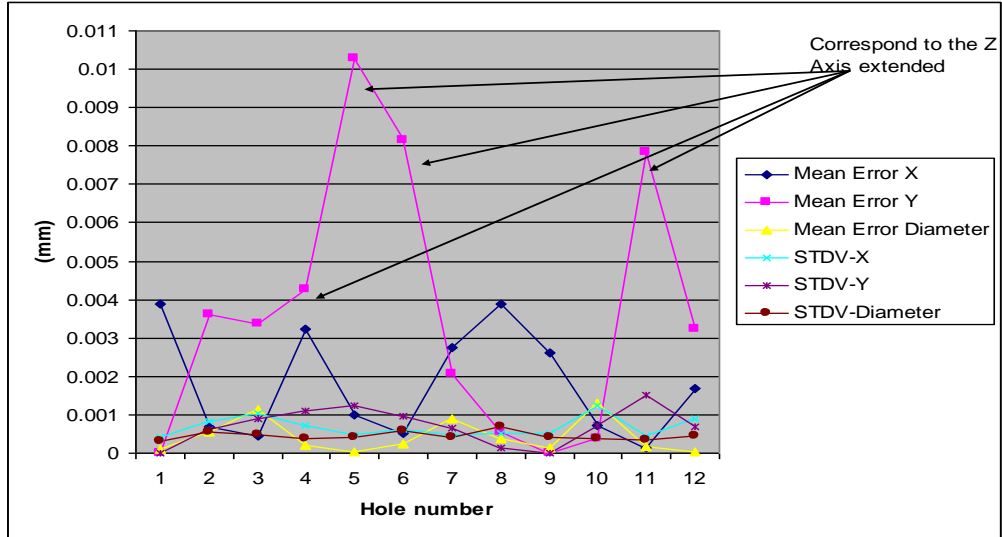


Figure 90. 10 repeated measurements of 12 holes on the master shaft

For the Expanded uncertainty calculation the following assumptions/values were used:

$$u_{cal} = \frac{U_{cal}}{k} \quad \text{where} \quad K = 2 \quad \text{and} \quad U_{cal} = 0.002$$

$$u_w = (T - 20^\circ C) \times u_\alpha \times L \quad \text{where} \quad T = 21 \quad u_\alpha = 10\% \text{ of CTE} \quad (3.6)$$

The calculated expanded measurement Uncertainty values for both X and Y was 0.006 mm. Given that it was a positioning tolerance (in terms of radii but referenced to a diameter) the following applied:

$$U = 2 \times \sqrt{X^2 + Y^2} = 0.0169 \text{ mm}$$

3.5.2 Pundit/CMM simulation results

All the assumptions/values used in section 3.5.1 were used when setting up the Pundit simulation. The datum set-up can be seen in Figure-91 . The only variable which was set using previous experience/knowledge was the probe set-up. Form errors were also not considered in this task given they could have had a severe impact on the measurement uncertainty values and there was no data available..

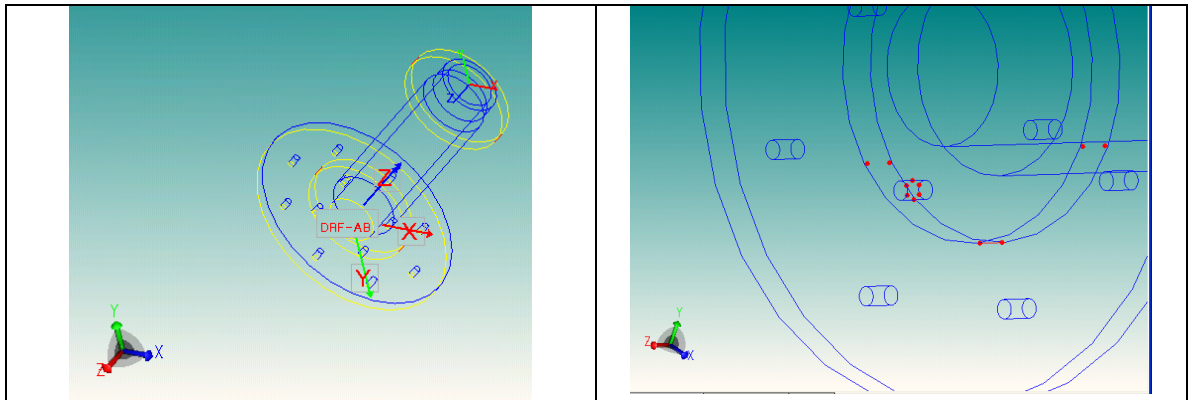


Figure 91. Pundit/CMM simulation shaft simulation set up

Figure-91 shows the probing strategy used, 6 points on both the datum's and holes. Two values were extracted from Pundit:

- 1 – X or Y position uncertainty for a hole
- 2 – Total positional uncertainty for a hole

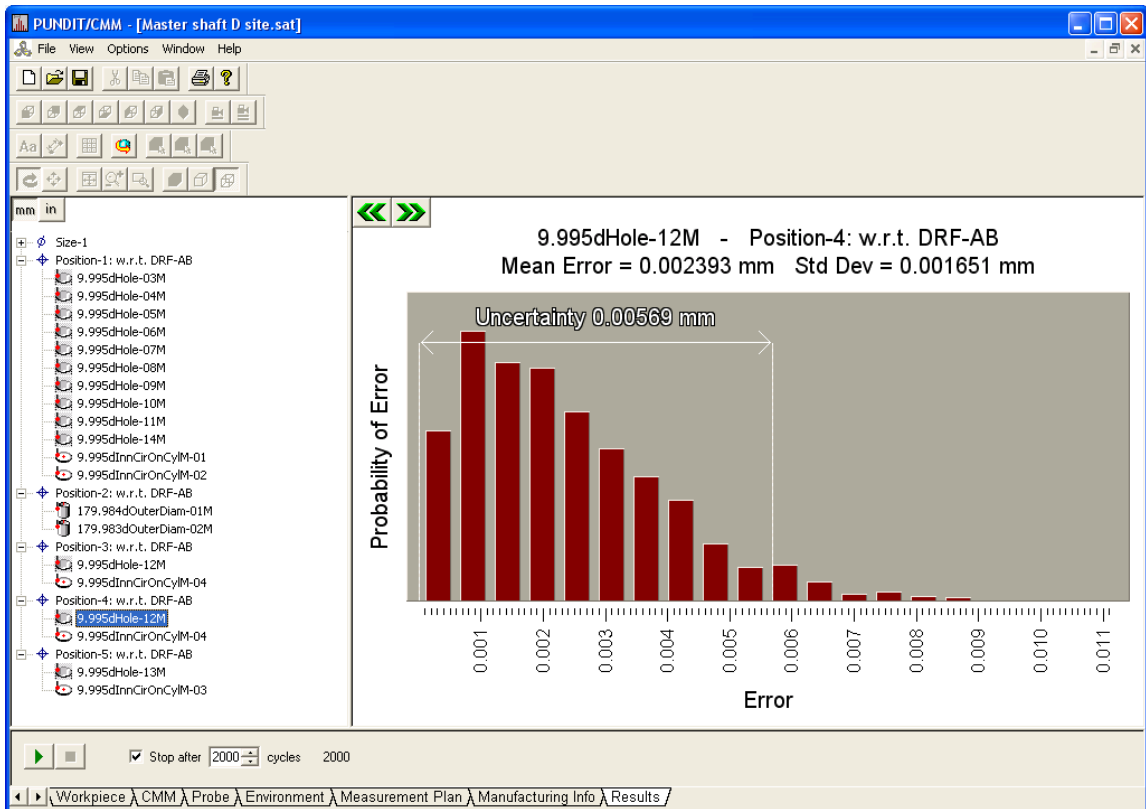


Figure 92. X,Y position uncertainty

Figure-92 shows the result for the total position uncertainty. The calculated expanded measurement uncertainty value for the total position in section 5.1 was 0.0169 mm. The value obtained via the simulation was 0.0134 mm. This results showed an underestimation in terms of comparing Pundit’s measurement uncertainty with the ISO 15530-3 but when comparing Pundit’s uncertainty estimation with the mean error added in quadrature for X,Y coordinates and ignoring the squareness errors showed in Figure-90, the mean error was found to be 0.011mm. Similarly to the length bar measurements,

Pundit overestimated the measurement uncertainty when compared with the mean error but slightly underestimated when compared with the ISO 15530-3 estimate.

3.6 Impact of measurement uncertainty in conformance decision associated with circular features

In section 2.1.3 of this document it was demonstrated how uncertainty played a major role in conformance decisions. Furthermore it was shown that under certain circumstances it was possible to use the CMM specification standard uncertainty as the only contributor for determining expanded measurement uncertainty. The results obtained for the circular features presented (sections 2.3 and 3.3) clearly indicated that using the CMM specification for features other than length bar measurements as expanded measurement uncertainty would imply a high underestimation of the expanded measurement uncertainty. As an example the CMM-1 featured in section 2.1.1 of this work was Machine M used in section 3.3. By comparing the uncertainty values obtained for the 30mm length bar with the circular feature 2B it was clear that the expanded measurement uncertainty would be highly underestimated $0.7\mu\text{m}$ vs $58\mu\text{m}$ in the case of 1XBASIC measurements. In the case of the 3XBASIC measurements of the same feature the underestimation would have been $0.7\mu\text{m}$ vs $1.1\mu\text{m}$ which equated to just over 50%. Such comparison was valid due to the control of factors such as temperature associated with CMM-1 (Machine M).

3.7 Summary

In this Chapter a VCMM or UES as defined by the ISO 15530-4 was tested by using physical measurements of calibrated artefacts in the case of the length bar measurements. For the three CMM's length measurements Pundit/CMM complied with the test provided in section C.2 of the ISO 15530-4. When compared with the mean error values obtained for all CMM's Pundit/CMM overestimated the uncertainty which complies with section C.3.

A multi feature artefact was designed and manufactured to test how UES would perform when trying to simulate physical measurements of three different CMM's on an artefact with predefined form error. When comparing the Pundit's uncertainty results for the size of all features investigated with the mean error of the physical measurements the UES overestimated the measurement uncertainty in the majority of cases. Of particular importance was the similarity in trends shown by the UES and the physical measurements. A similar result was found when comparing the uncertainty statements derived from the physical measurements and the ones obtained from Pundit/CMM. In order to compare both uncertainties, the uncertainty derived for the physical measurements was calculated in the same manner as the uncertainty calculated in Pundit/CMM.

For the positional measurement results it was found that for Machine M and W Pundit/CMM underestimated the measurement uncertainty with a few exceptions (features 1B and 3B show an overestimation by the UES). However the trends of the reported uncertainty for most feature was found to be very similar.

Chapter 4

Automated conformance assessment of airfoil edges

4.1 Assessing the significance of Leading edge shape

To investigate the significance of the leading edge shape of airfoil profiles, a 2D section along the stacking axis of a conventional compressor blade was selected.

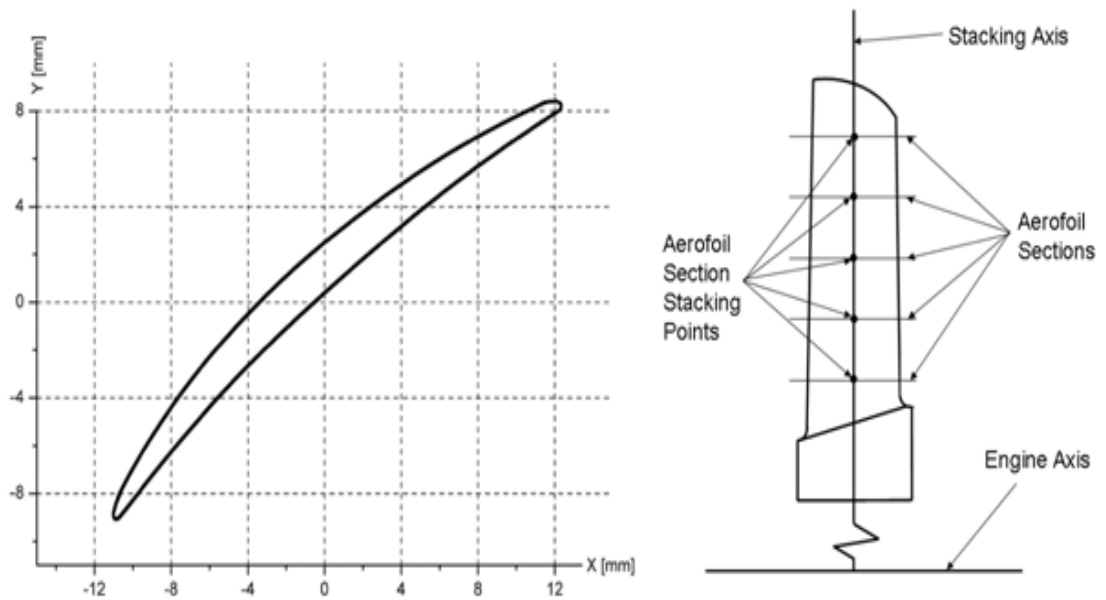


Figure 93. Compressor blade airfoil sections

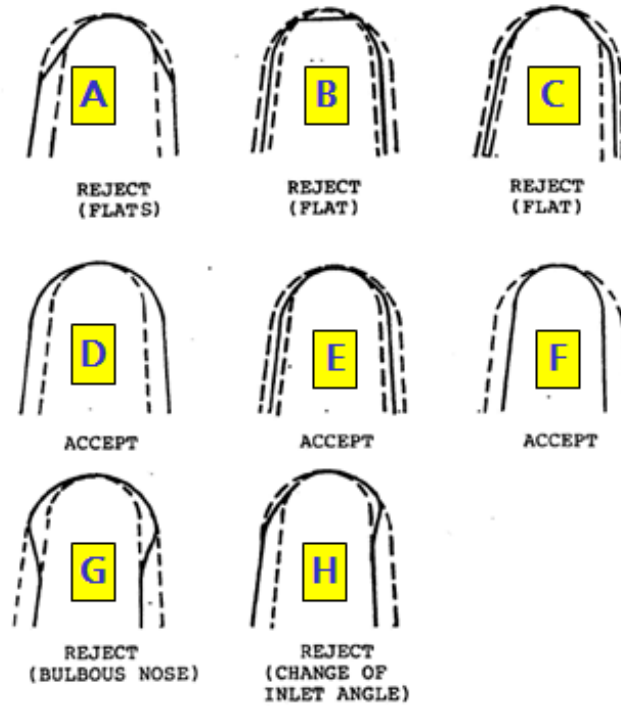


Figure 94. LESA standard for leading edge shape assessment

Figure-94 shows the leading edge standard assessment (LESA) diagram used by the inspectors during final sentencing of the airfoil. The assessment was carried out using output plots for the different airfoil sections from CMM measurements by superimposing the dashed tolerance line shown above.

4.2 Mathematical modelling of Leading edge shape

The mathematical modelling of the leading edge shape consisted of converting the point cloud data received from a measurement system into a mathematical quantity. Two initial requirements for the mathematical quantity were:

- Ability to deal with output data from different measurement systems
- Compatibility with current standards (LESA, Figure-94)

Initial work carried out by Rolls-Royce plc demonstrated that curvature could be used to detect certain features along a leading edge profile. The instantaneous curvature of a leading edge profile was therefore defined using $\kappa = \left| \frac{d\alpha}{ds} \right|$, where α was the angle of inclination and s the arc length.

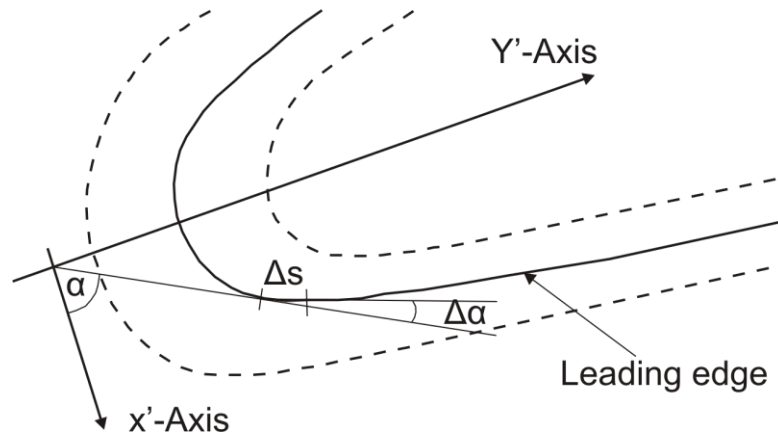


Figure 95. Leading edge curvature definition

Figure-95 illustrates the curvature of a leading edge planar curve.

$$\kappa = \left| \frac{d\alpha}{ds} \right| = \left| \frac{d\alpha/dt}{ds/dt} \right| = \left| \frac{d\alpha/dt}{\sqrt{(dx/dt)^2 + (dy/dt)^2}} \right| = \left| \frac{d\alpha/dt}{\sqrt{(x')^2 + (y')^2}} \right| \quad (4.1)$$

$$\tan \alpha = \frac{dy}{dx} = \frac{dy/dt}{dx/dt} = \frac{y'}{x'} \Rightarrow \frac{d(\tan \alpha)}{dt} = \sec^2 \alpha \cdot \frac{d\alpha}{dt} = \frac{x' \cdot y'' - x'' \cdot y'}{x'^2} \quad (4.2)$$

$$\frac{d\alpha}{dt} = \frac{1}{\sec^2 \alpha} \cdot \frac{d(\tan \alpha)}{dt} = \frac{1}{1 + \tan^2 \alpha} \cdot \frac{x' \cdot y'' - x'' \cdot y'}{x'^2} = \frac{1}{1 + \frac{y'^2}{x'^2}} \cdot \frac{x' \cdot y'' - x'' \cdot y'}{x'^2} = \frac{x' \cdot y'' - x'' \cdot y'}{x'^2 + y'^2}$$

(4.3)

$$\text{Joining (23) and (24)} \rightarrow \kappa = \left| \frac{x' \cdot y'' - x'' \cdot y'}{(x'^2 + y'^2)^{3/2}} \right| \quad (4.4)$$

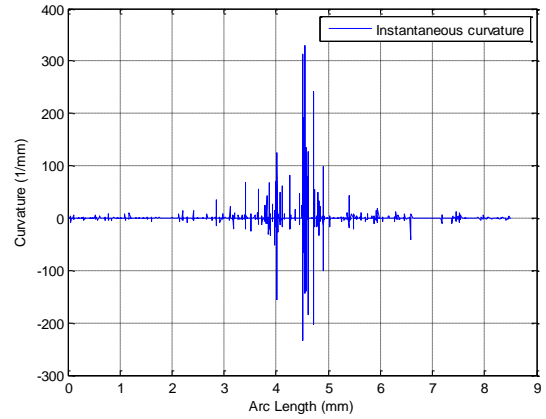
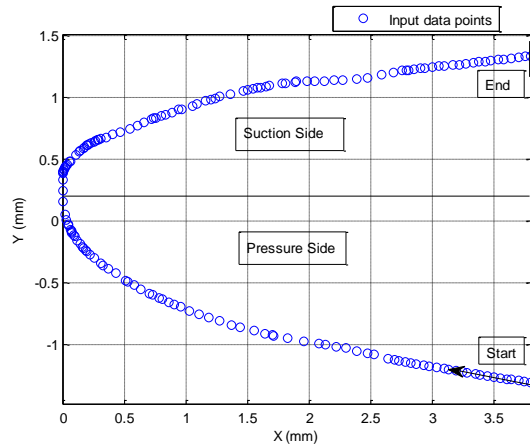
The mathematical models were developed in Matlab 2007.b using some numerical methods available within the Matlab library and literature [141].

4.2.1 Data manipulation

In this section unless otherwise stated the results presented were derived for airfoils under the conventional clockwise rotation direction as shown in Figure-96.

Due to the nature of the measurement system the data supplied was not always of the same amount, equally distributed and contained some “noise” from the measurement system due to factors such as the ones described in chapters 2 and 3 of this document.

The Figure-96 a) shows the typical point cloud data output from the CMM.



a)

b)

Figure 96. a) Leading edge point cloud data; b) Instantaneous curvature for input data points

Figure-96 b) shows the instantaneous curvature of the leading edge profile in Figure-96 a). The instantaneous curvature plot indicated that in order to extract information about the leading edge shape some level of smoothing was required. Two levels of smoothing were therefore developed:

Level 1 – Point cloud data smoothing

Level 2 – Curvature smoothing

The point cloud data smoothing parameter was developed by using a combination of linear and cubic spline interpolation with choice of control points as a function of arc length S . Firstly the input data was resampled using a linear interpolant using every input data point as a control point. Figure-97 shows the impact of using cubic spline interpolation and linear interpolation. The linearly interpolated data showed very good

maintenance of the original leading edge shape while the cubic spline interpolant caused some changes in direction between control points.

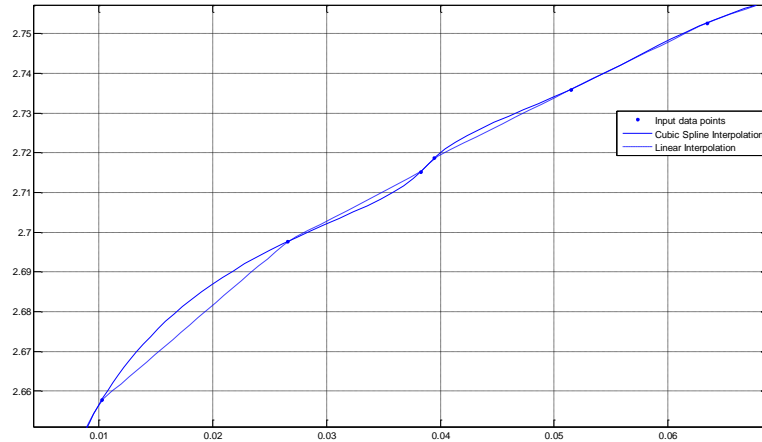


Figure 97. Linear interpolation vs Cubic spline interpolation

This step was required in order to maintain a high level of information about the original leading edge shape while providing an equally distributed point cloud of data points. The second step consisted of using the linear interpolated data to select the control points used for the interpolation function. Figure-98 shows the difference between cubic spline interpolation (not-a-knot end condition) and uniform B-spline interpolation. Due to accuracy requirements on control point approximation, Cubic spline was selected as the interpolating function. The choice of Control Points Distance (CPD) was generated as a function of the arc length. Table-28 shows how the curvature profile of the leading edge shape changed as a function of the CPD.

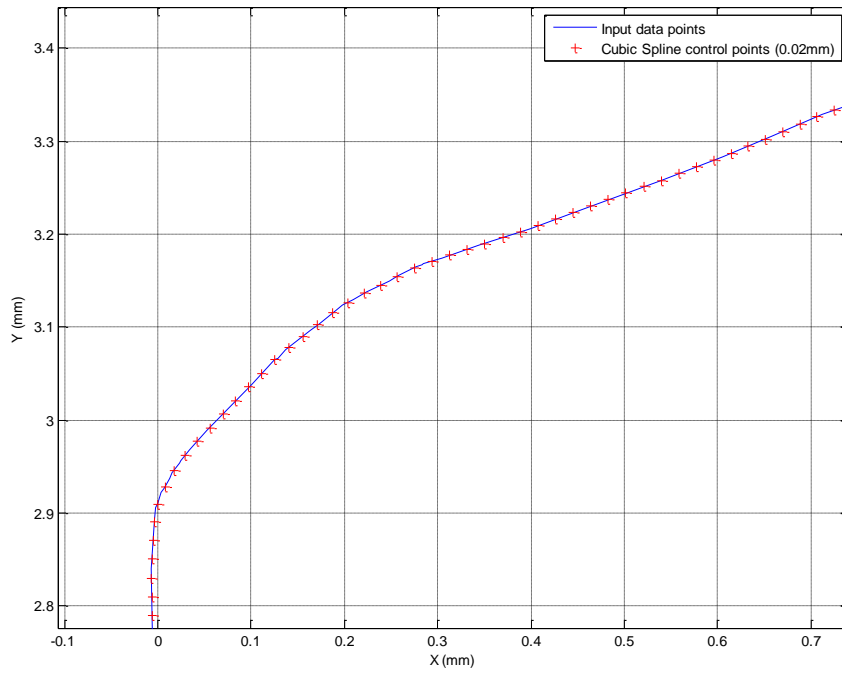
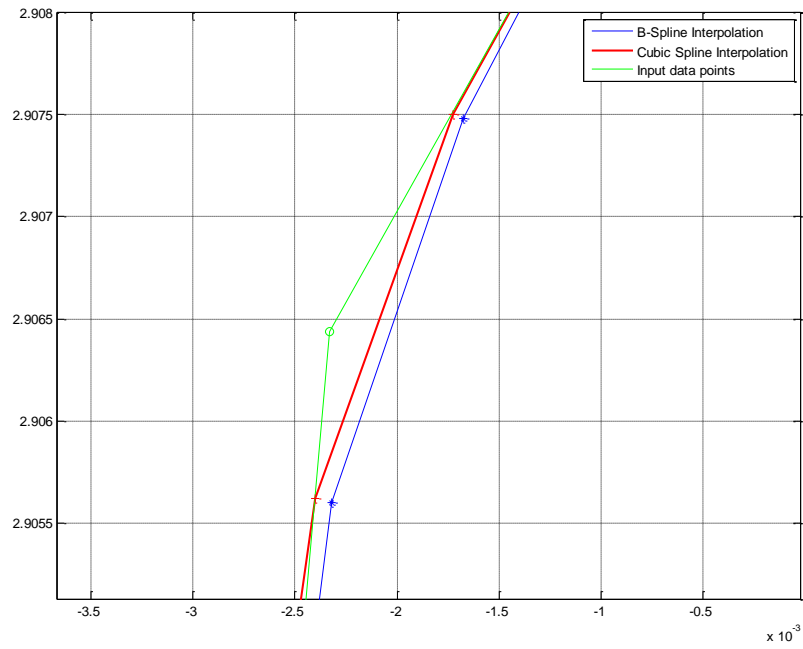
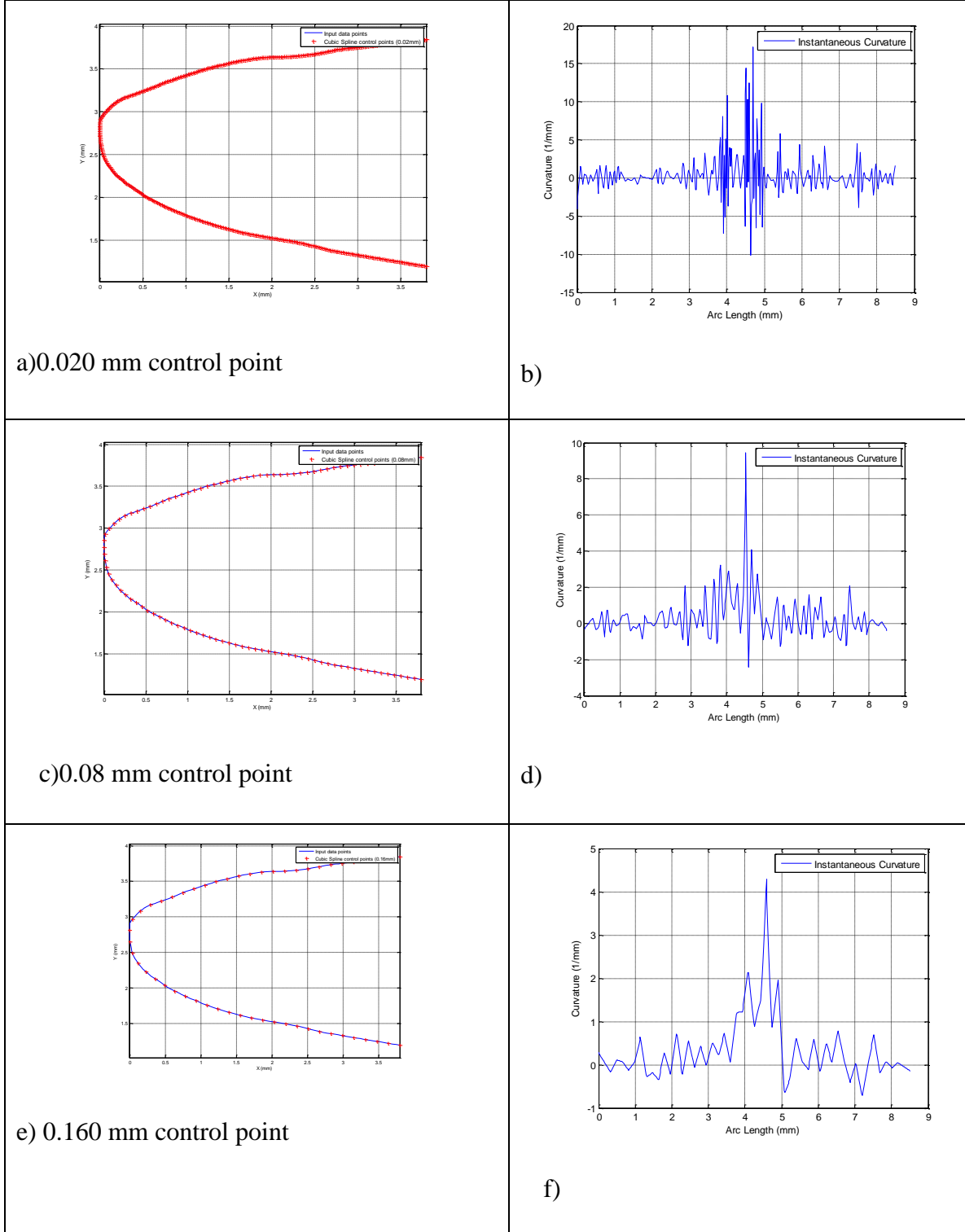


Figure 98. Cubic spline interpolation vs B-Spline interpolation

Table 28. Impact of control point choice on curvature smoothing



By increasing the distance for choice of control points even further, the curvature profile shown in Figure-99 was achieved. It was found that features such as peak/valleys curvatures and flat regions could be detected.

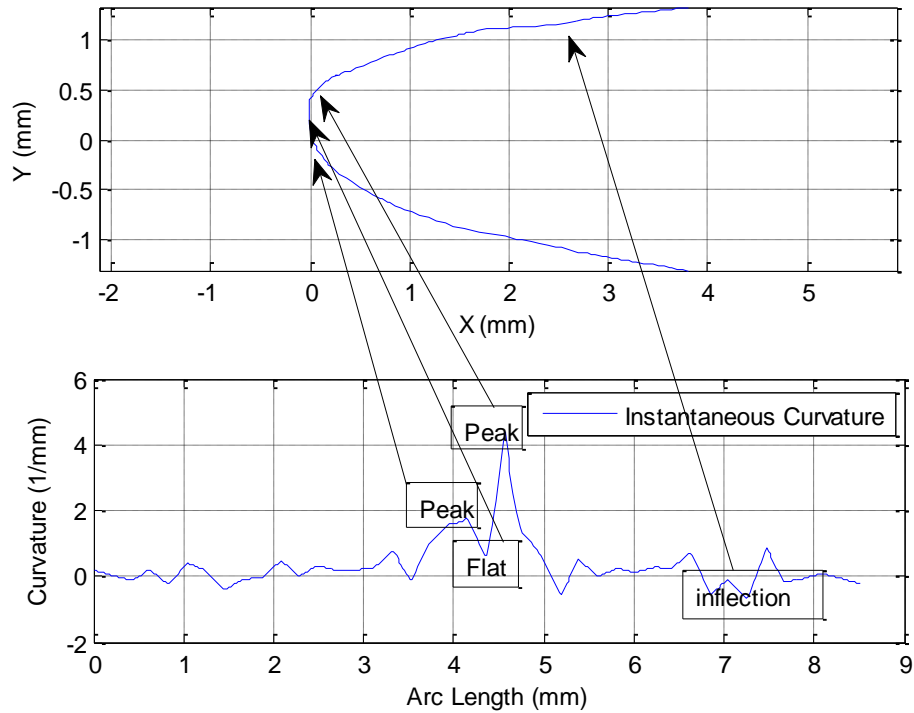
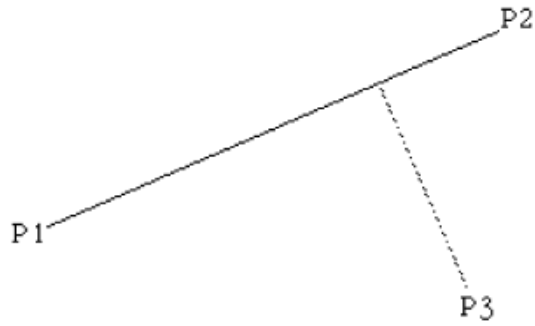


Figure 99. Instantaneous curvature profile using CPD of 0.2mm

By increasing the CPD it was found that the original LE shape was modified as shown in Figure-100 a). In order to determine the goodness of the spline fit, the distance between a point and a line was determined. The equation of a line through two points:

$$\mathbf{P1} (x_1,y_1) \text{ and } \mathbf{P2} (x_2,y_2) \text{ is } \mathbf{P} = \mathbf{P1} + u (\mathbf{P2} - \mathbf{P1})$$



The point **P3** (x_3, y_3) is closest to the line at the tangent to the line which passes through **P3**, that is, the dot product of the tangent and line is 0, thus

$$(\mathbf{P3} - \mathbf{P}) \text{ dot } (\mathbf{P2} - \mathbf{P1}) = 0$$

Substituting the equation of the line gives

$$[\mathbf{P3} - \mathbf{P1} - u(\mathbf{P2} - \mathbf{P1})] \text{ dot } (\mathbf{P2} - \mathbf{P1}) = 0$$

Solving this gives the value of u

$$u = \frac{(x_3 - x_1)(x_2 - x_1) + (y_3 - y_1)(y_2 - y_1)}{\| \mathbf{p2} - \mathbf{p1} \|^2} \quad (4.5)$$

Substituting this into the equation of the line gives the point of intersection (x, y) of the tangent as:

$$x = x_1 + u (x_2 - x_1) \quad (4.6)$$

$$y = y_1 + u (y_2 - y_1) \quad (4.7)$$

The distance therefore between the point **P3** and the line is the distance between (x,y) above and **P3**.

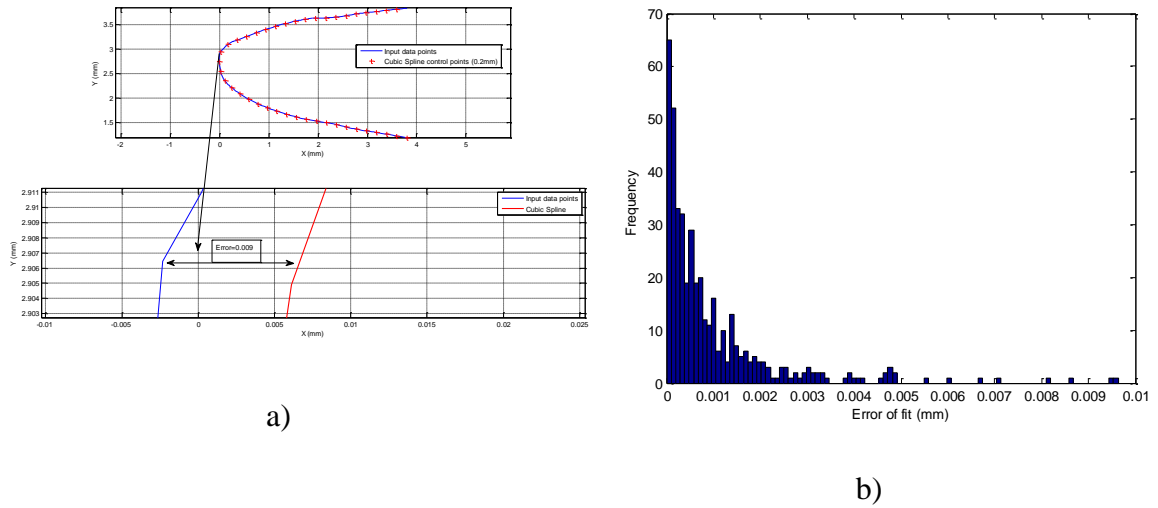


Figure 100. a) B-spline fit error with CPD of 0.2mm; b) Histogram of error of fit

The histogram shown in Figure-100 b) indicated a maximum error of fit of 0.096 mm with a very small frequency below 5. Most of the errors due to the cubic spline fit were found to be below 0.005 mm with higher frequencies of occurrence starting at approximately at the 0.001mm error of fit. To minimise the error of the spline fit the CPD was set at 0.02mm. The Figure-101 histogram shows an error of fit below 0.0016mm.

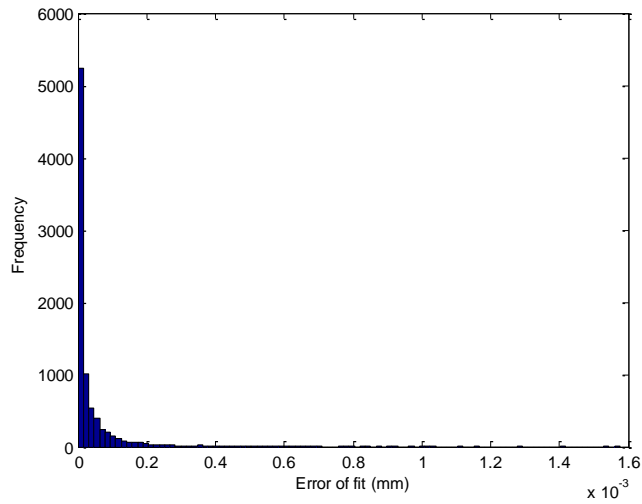


Figure 101. B-spline fit error with CPD of 0.02mm

A smoothing parameter was therefore developed for the curvature values based on a simple moving average where n represented the curvature values with a CPD of 0.02mm.

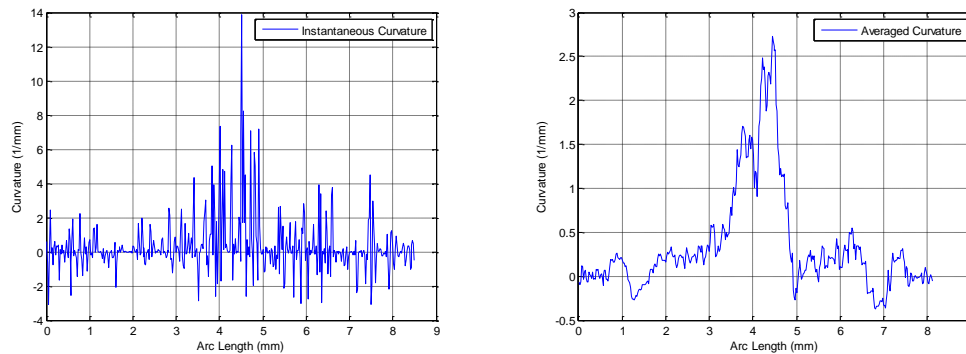
$$K_{SMA} = \frac{n + n - 1 + \dots + n - m}{m + 1} \quad (4.8)$$

Although the moving average was based on selection of number of curvature values n , a conversion to arc length S was developed using:

$$m = \frac{C_{avg}}{(S / n(\max))} \quad (4.9)$$

where C_{avg} was the specified distance along the arc length.

The effect of the simple moving average filter on a curvature plot is shown in Figure 102. By applying the smoothing parameter to the instantaneous curvature plot (Figure-102 a)), key features such as the ones described in Figure-99 became visible without lost accuracy in the cubic spline fit.



a) Curvature plot with no C_{avg} . b) Smoothed curvature plot with $C_{avg}=0.4mm$.

Figure 102. Comparison of a) instantaneous curvature, and b) smoothed curvature a single pass simple moving average filter.

Although some key features could be identified from Figure-102, the curvature plot was smoothed further by reapplying the simple moving average filter using a $C_{avg}=0.2$. This implied that the raw curvature plot was being filtered twice which allowed better visibility of key features required for the leading edge analysis.

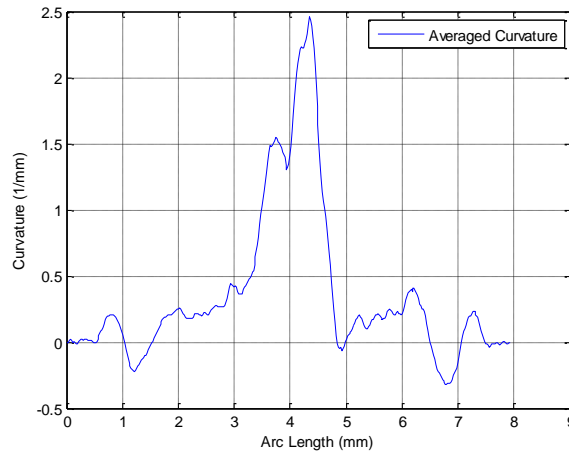


Figure 103. Smoothed curvature using a two pass simple moving average filter

To understand the impact of the C_{avg} parameter on the instantaneous curvature, a synthetic leading edge was generated using an ellipse in canonical position where:

$$\begin{aligned} x(\theta) &= a \cos(\theta) \\ y(\theta) &= b \sin(\theta) \end{aligned} \quad (4.10)$$

The ellipse shown in Figure-104 was generated with $a=1, b=4$ and $CPD=0.02\text{mm}$.

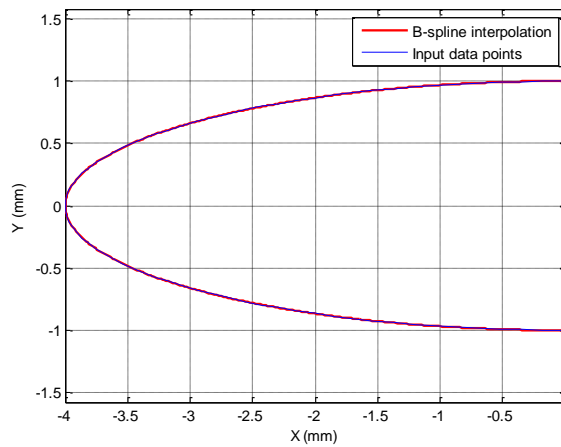


Figure 104. Generated ellipse with $a=1, b=4$.

Figure-105 a) showed a peak curvature of 4 while Figure-105 b) showed a peak curvature of 3.25 using a $C_{avg}=0.4$ on a single pass moving average filter. The use of the curvature smoothing parameter caused a reduction on the peak curvature value of 0.75.

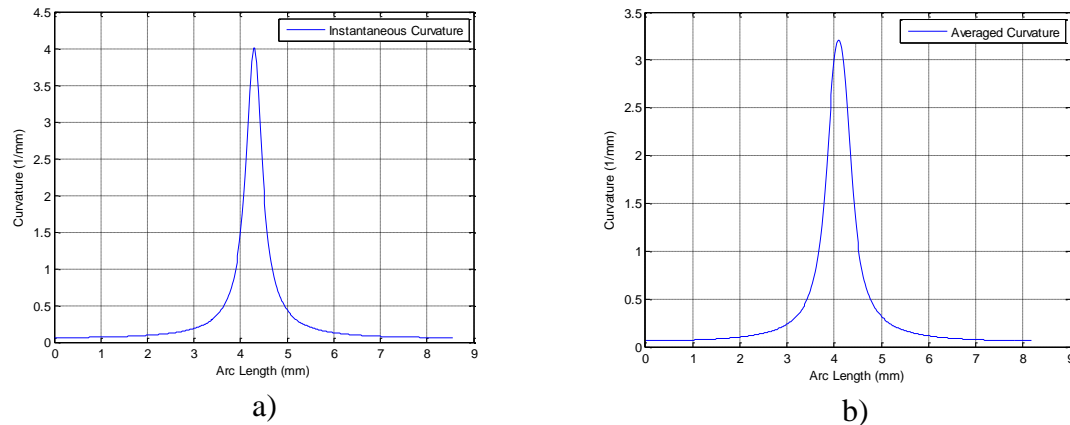


Figure 105. a) Instantaneous curvature b) Averaged curvature.

4.2.2 Types of curvature

In the previous section curvature was plotted as a function of the arc length but in order to extract key attributes of the leading edge profile, different approaches for manipulating the curvature quantity were investigated and summarised below as follows:

Type 1 - Conversion of curvature (1/mm) to a non-dimensional quantity via:

- a) Total thickness value between start and end points of the LE shape analysis (NTT)
- b) $\frac{1}{2}$ thickness value between start and end points of the LE shape analysis (NHT)
- c) Total arc length (NTAL)

Type 2 - Conversion of X axis to:

- a) Arc length
- b) Thickness position
- c) Normalising 2a) or 2b) from 0 to 1

Type 1

The conversion of curvature to a non-dimensional quantity was investigated using the synthetic shape (ellipse) generated in Figure-104. Figure-106 shows the three different types of instantaneous curvature non-dimensionalisation with $a=1,2$ and $b=4,8$. At first glance the plots indicated that non-dimensionalisation was only a scaling effect.

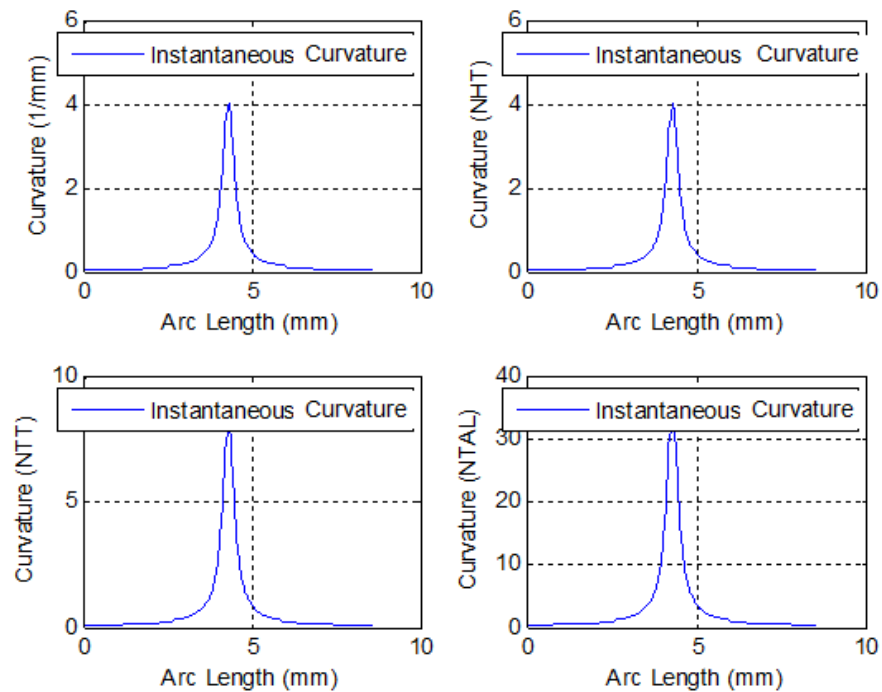


Figure 106. Instantaneous curvature vs non-dimensionalisation options.

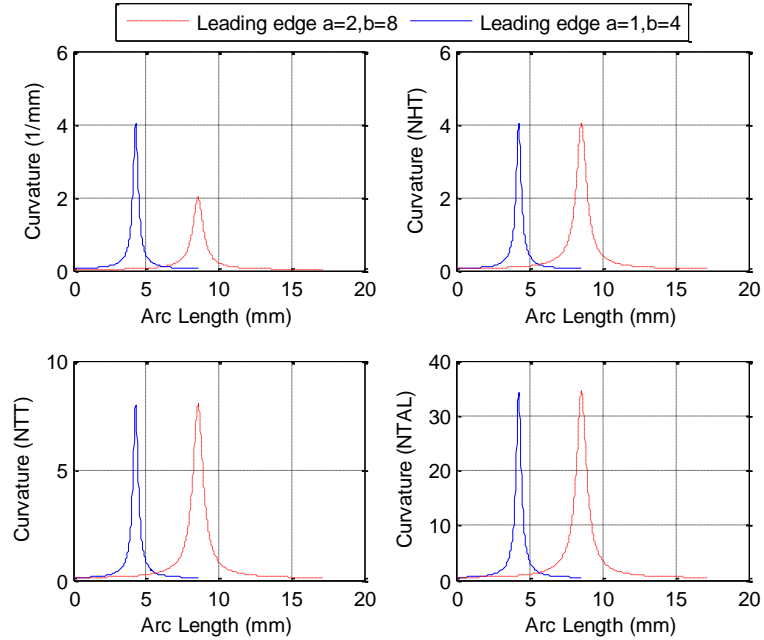


Figure 107. Instantaneous curvature non-dimensionalisation options for two synthetic shapes.

From Figure-107 it was clear that by non-dimensionalising the two synthetic shapes by $\frac{1}{2}$ the measured thickness (NHT), the non-dimensional curvature values remained unchanged when compared with the real curvature values shown in Figure-106 (1/mm). Both NTAL and NTT methods showed changes in the magnitude of the curvature plots when compared with original curvature values. Although such effect could be neglected due the fact that the main objective of non-dimensionalisation was to allow the possibility of plotting different leading edge shapes in a common plot, the aerodynamicists would not be able to extract an equivalent radius from the peak curvature. Although the smoothing parameters would eventually influence the extraction of a radius quantity based on the peak leading edge curvature the impact would much smaller when compared with the use of NTAL and NTT options.

Type 2

As previously mentioned, the leading edge profile “bias” was a quantity of particular interest to aerodynamic engineers due to its impact on aerofoil performance (section 1.6). In the context of this work “bias” was defined as the difference between the location of the sharpest point at the tip of the ideal leading edge profile and the manufactured profile sharpest point. Using the Equation-4.11, a bias was artificially added to $x(\theta)$ from Equation-4.10 to generate the leading edge bias shown in Figure-108.

$$x_s(\theta) = x(\theta) + \lambda \cos(\theta x(\theta)) \quad (4.11)$$

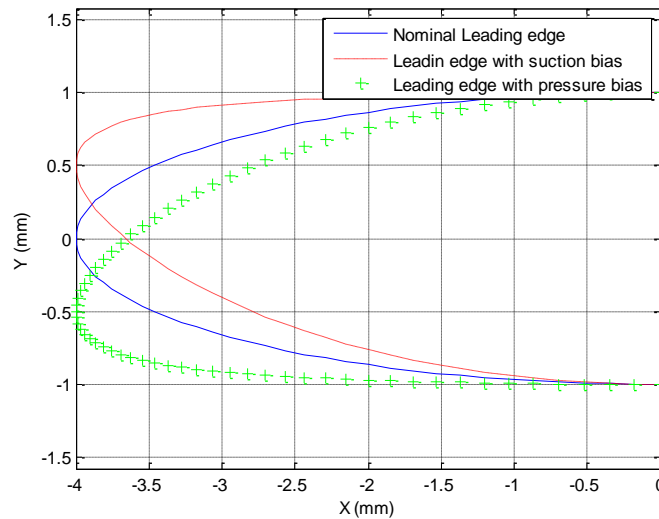


Figure 108. Examples of leading edge bias.

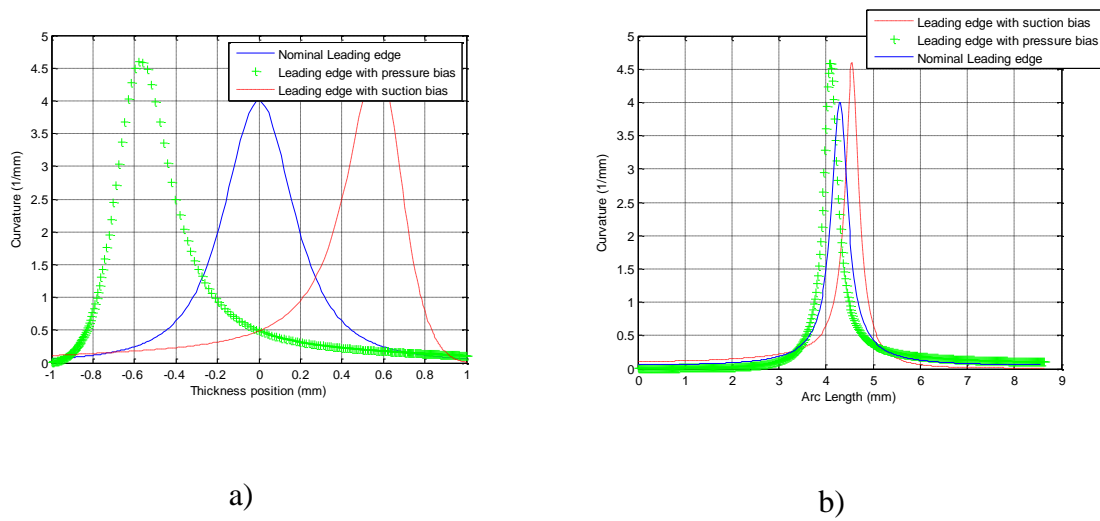


Figure 109. a) Instantaneous curvature vs Thickness; b) Instantaneous curvature vs Arc Length

Figure-109 shows the instantaneous curvature plots for the leading edge shapes in Figure 108. When comparing the plots of Figure-109 a) and b) it was clear that plotting curvature against measured thickness position emphasises any bias effect. Furthermore, any feature near the leading edge “tip” would be emphasised when compared with the curvature plots plotted against arc length.

The curvature plots results generated from ellipses presented only reflected ideal case scenarios for cases of constant thickness or arc length. In a manufacturing environment both the thickness/arc length of a series of leading edges can vary and ultimately influence the output of the curvature plots so far explored. In order to eliminate manufacturing variations caused to both of these quantities, the X axis on either curvature plots were normalised between 0 and 1 in the following way:

$$XN = \frac{\phi_i}{\phi_{\max}} \quad (4.12)$$

Where ϕ_i represents an arc length or thickness position value and ϕ_{\max} represents a maximum value of arc length or thickness position. Figure-110 a) shows the normalised curvature plot from Figure-109 a). Having the curvature plots normalised between 0 and 1 would also aid the development of the analysis of the features found by having a common limit within the X axis of the chart.

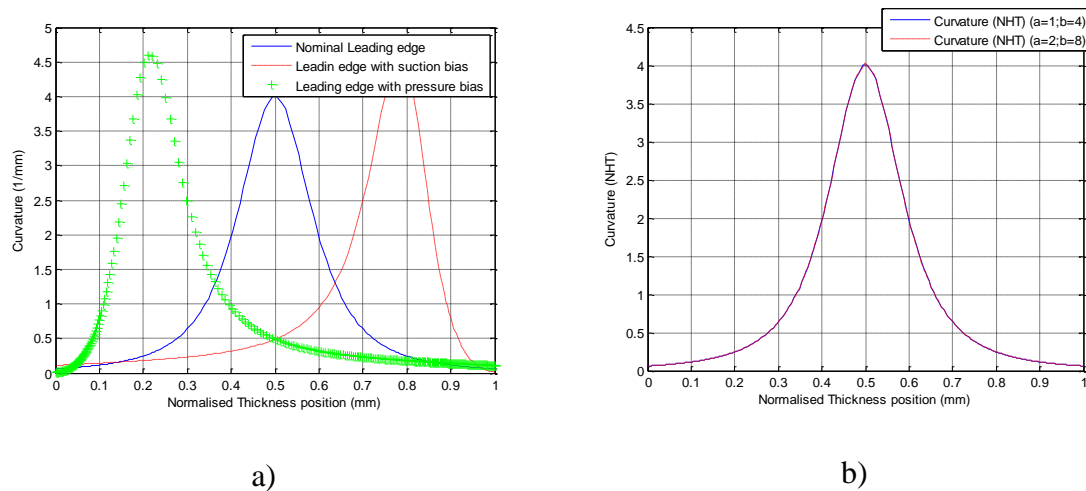


Figure 110. a) Instantaneous curvature vs Normalised Thickness position; b) Curvature NHT vs Normalised Thickness position

Figure 110 b) shows the NHT curvature from Figure-110 a) plotted against the normalised thickness. The use of both the NHT curvature and the normalisation of the X axis quantity allowed for manufacturing variations to be taken into account given that the ratio between the synthetically generated shapes was 2 for both a and b in eq(3).

To test the use of such parameters, leading edge shapes from three different blades of the same component family were chosen to compare the curvature (NHT) when plotted against normalised thickness position and arc length. The leading edges belonged to the same section of a blade along the staking axis of the three different blades.

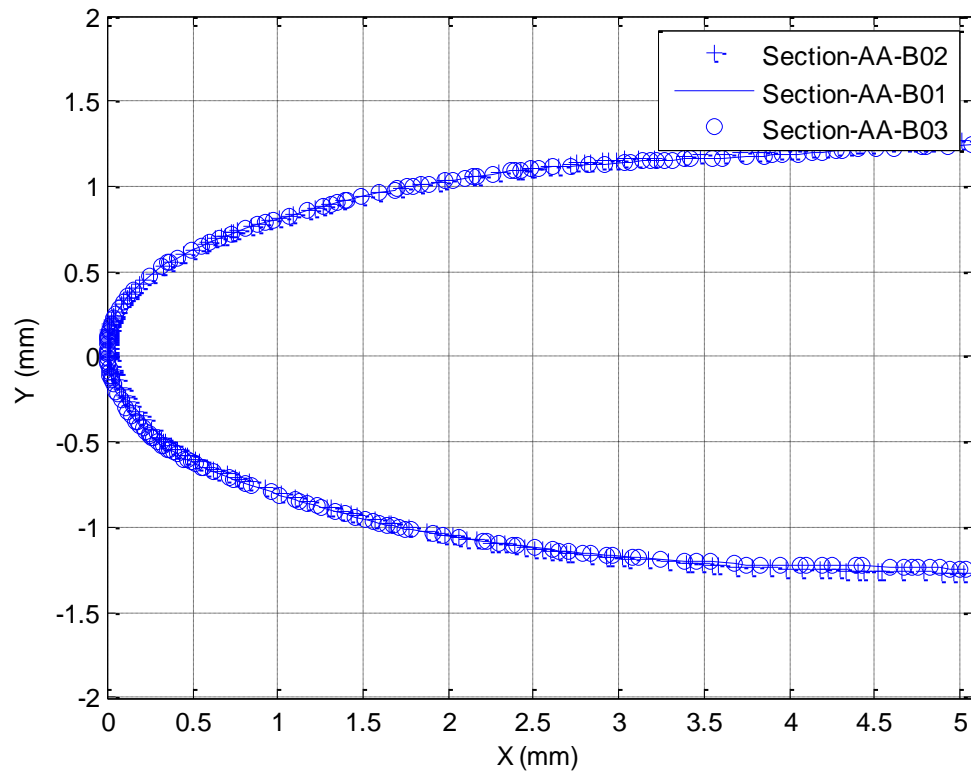


Figure 111. Section AA Leading edge plots for three different blades

Figure-111 above shows three leading edge shapes from the same section of three different blades. All three shapes appear to have similar geometries. Figure-112 shows the curvature (NHT) plots for the three leading edges. Both curvature plots highlight slight differences between the three leading edge shapes. Blade 2 showed higher peak

curvature when compared with Blades 1 and 3. The results obtained used the following smoothing parameters:

$$CPD = 0.1\text{mm}$$

$$C_{avg} = 0.4\text{mm}$$

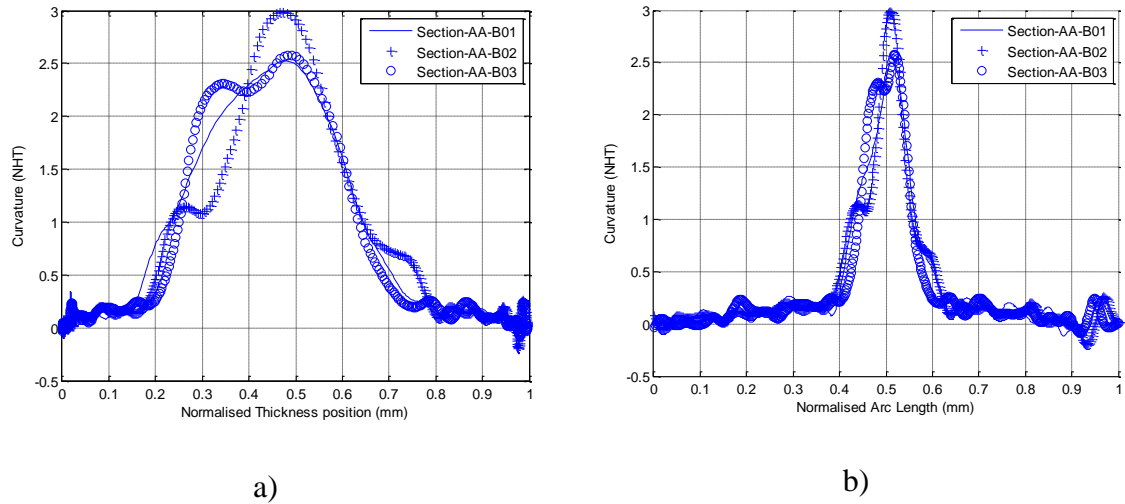


Figure 112. a)Curvature NHT vs Normalised Thickness position; b)Curvature NHT vs Normalised Arc Length

The curvature plots against the normalised thickness position clearly emphasised features present in the three blades when compared to the arc length curvature plots. This results was due to plotting curvature against a higher quantity in the case of the total arc length versus the leading edge thickness. Of particular concern it was noticed that features shown in Figure-112 b) between 0.9 and 1 (X axis) were very “compressed” and potentially overlapping in Figure-112 a). This observation led to further investigations in potential curvature shifts and or overlaps when using the normalised thickness position for the X axis of the curvature plots. Because curvature was plotted normal to the

thickness line, any minor changes to its angle caused a shift in the X axis of the curvature plot as shown in Figure 113. Curvature plots shift as a function of the thickness line angle

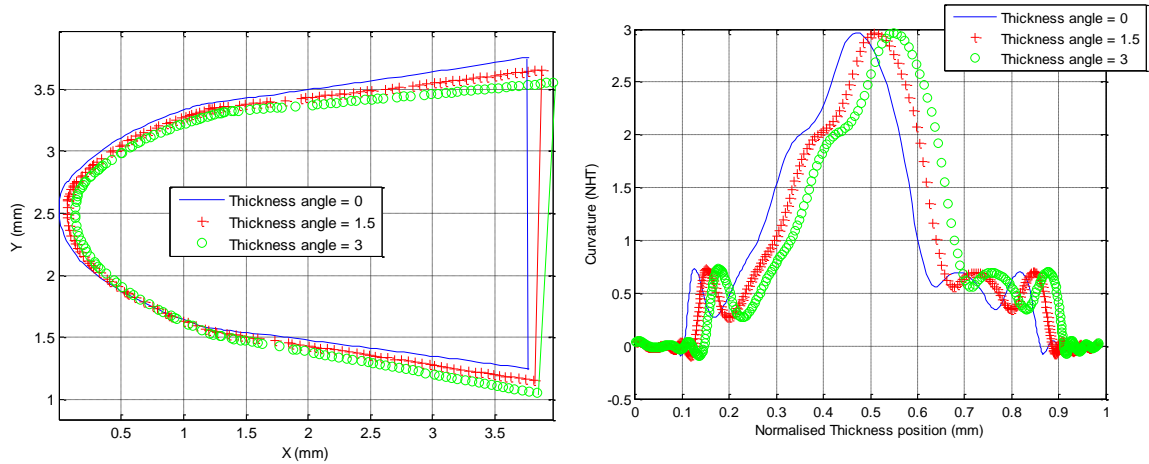


Figure 113. Curvature plots shift as a function of the thickness line angle

The shift observed along the X axis of the curvature plot was 0.04 mm for a thickness angle change of 1.5° and 0.08 mm for a thickness angle change of 3° . The magnitude of the changes is directly related to thickness magnitude of the leading edge shape and therefore it was foreseen that for thinner leading edge shapes such changes would not be acceptable. Figure-114 highlighted another potential issue of plotting curvature against normalised thickness position for leading edge shapes which may have curvature overlaps. A LESA shape was selected for the test. Due to the potential curvature plot shifts highlighted in Figure-113 and curvature of non ideal shapes Figure-114, it was decided to develop a sentencing strategy using both thickness and arc length quantities.

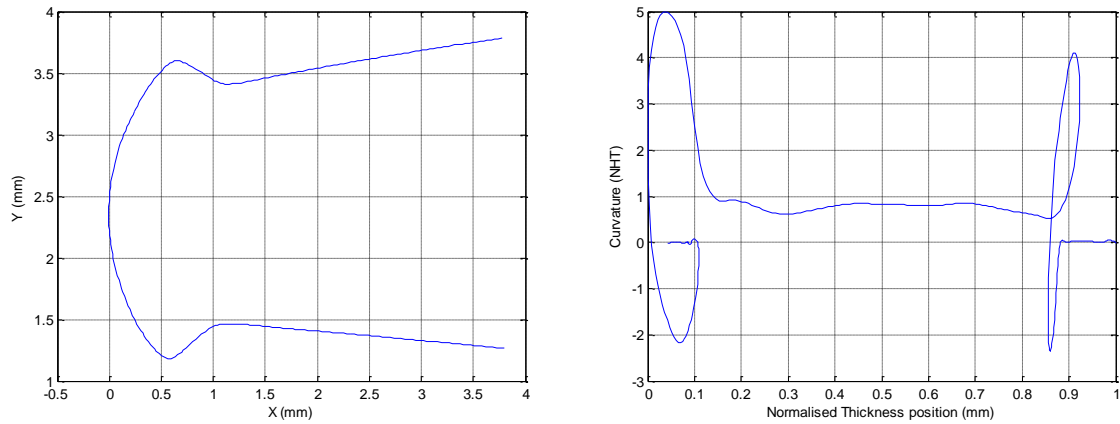


Figure 114. Curvature of a non-ideal shape (LESA)

4.3 Automated sentencing of the Leading edge shape

In the previous section Leading edges of airfoil profiles were successfully modelled mathematically by extracting their inherent curvature. The flowchart below shows the key stages of the automated sentencing development. Aachen University developed a software package in C++ according to the specifications written by Rolls-Royce plc (Appendix 4).

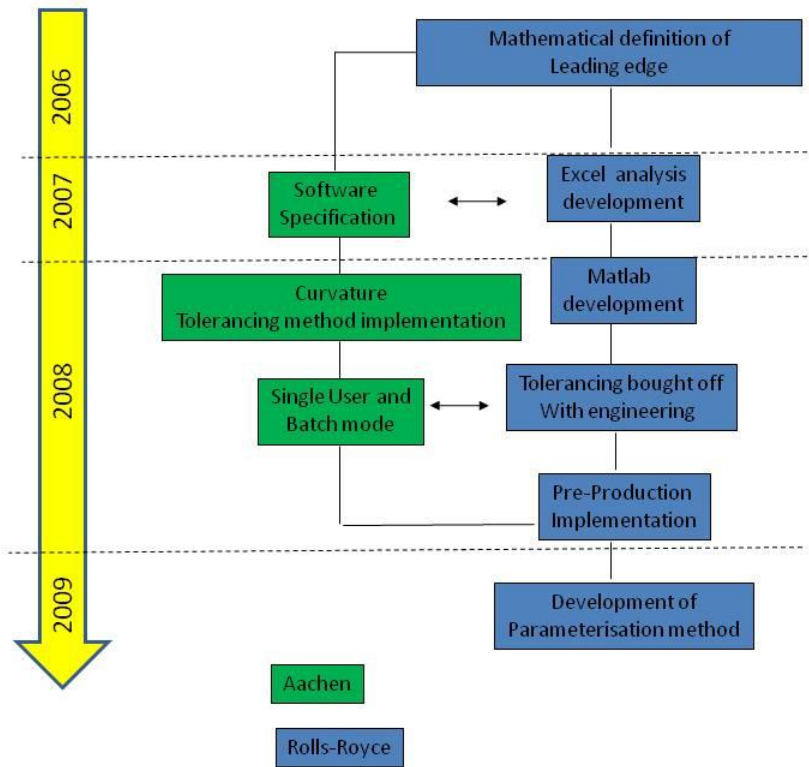


Figure 115. Flow chart for the automated leading edge assessment

A set of pre-production blades of the same airfoil section were classified by two aerodynamicists (Aero1, Aero2) and a senior production inspector in order to obtain acceptance/rejection reference. The classification of the airfoils was achieved by scoring each airfoil between 1 and 5. Airfoils that scored between 1 and 3 were classified as accepted while airfoils that scored 4 or 5 were classified as rejected. Figure-116 summarises the airfoil classification for 27 airfoils sections of different blades for one section common between each blade.

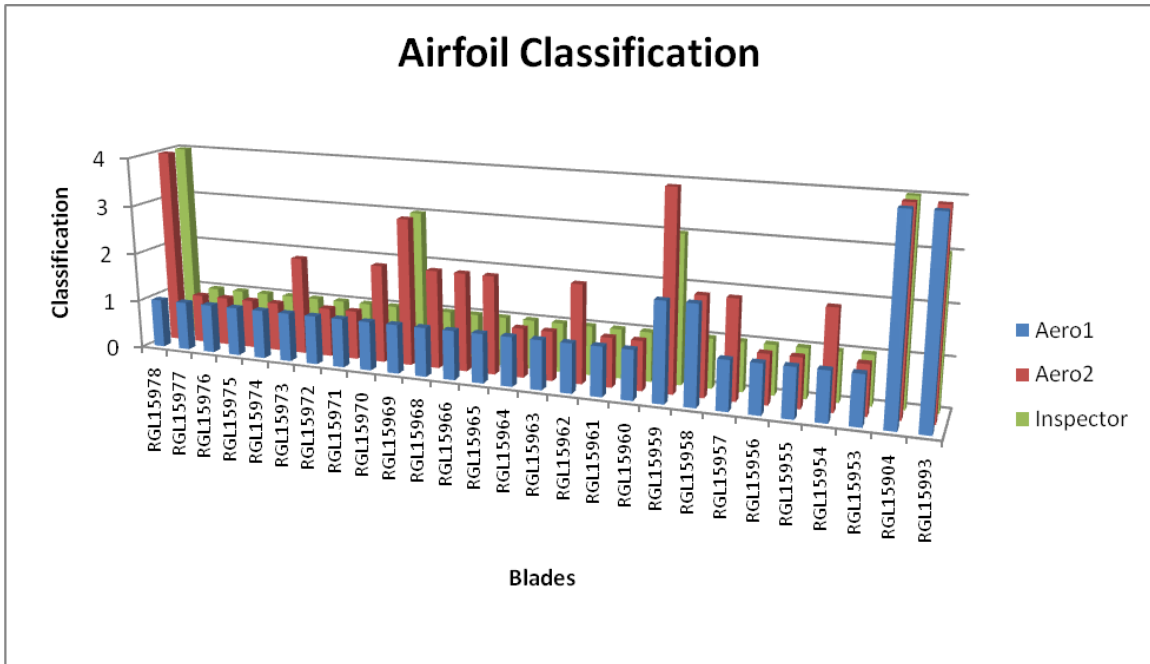


Figure 116. Airfoil classification for 14 blades.

4.3.1 Method 1 – Curvature Tolerancing

The curvature tolerancing method consisted of applying a set of upper and lower tolerance limits to the nominal curvature of an airfoil section as shown in the Figure-117. By controlling the curvature via a prescribed tolerance profile based on the nominal leading edge shape it was possible to check if the overall curvature profile fitted within the upper and lower tolerance bands, but also to check for any local changes in curvature. Visually it also provided the user with a quick visible way to verify the output results.

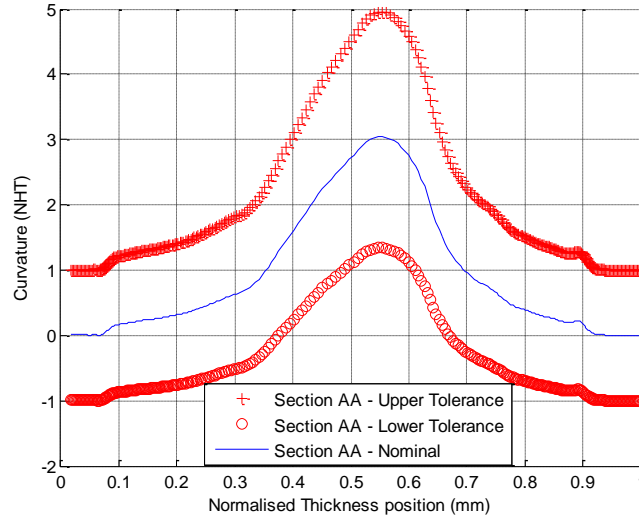


Figure 117. Upper and Lower tolerance bands derived from nominal curvature.

A set of parameters were developed to aid the tolerance bands definition. The curvature plot was split into two sides, a pressure side (0.5 to 1(X-axis)) and suction side (0 to 0.49(X-axis)). Using the (x, y) coordinates of the nominal curvature the $(\bar{x}_{uc}, \bar{y}_{uc})$ coordinates of the upper tolerance band were defined as follows:

$$(\bar{x}_{up} = x + (\varpi_{up}) + \psi_{xup}, \bar{y}_{up} = y(\delta_{up}) + \psi_{yup}) \text{ for } x \leq 0.5 \quad (4.13)$$

$$(\bar{x}_{us} = x + (\varpi_{us}) + \psi_{xus}, \bar{y}_{us} = y(\delta_{us}) + \psi_{yus}) \text{ for } x > 0.5 \quad (4.14)$$

$$\text{where } \varpi = \lambda(\cos(\frac{\pi}{2}(x \bullet 2) - 1))$$

and the lower tolerance band coordinates $(\bar{x}_{lc}, \bar{y}_{lc})$ were defined as follows:

$$(\bar{x}_{lp} = x + (\varpi_{lp}) + \psi_{xlp}, \bar{y}_{lp} = y(\delta_{lp}) + \psi_{y lp}) \text{ for } x \leq 0.5 \quad (4.15)$$

$$(\bar{x}_{ls} = x + (\varpi_{ls}) + \psi_{xls}, \bar{y}_{ls} = y(\delta_{ls}) + \psi_{y ls}) \text{ for } x > 0.5 \quad (4.16)$$

Having defined the tolerance bands, the sentencing method consisted of checking if the manufactured airfoil curvature plot fitted inside the area defined by the upper and lower tolerance bands as shown in the Figure-118. This was achieved by applying the same methodology described earlier in section 4.2.1 where the error of fit was estimated by determining the distance between the fitted shape and actual shape.

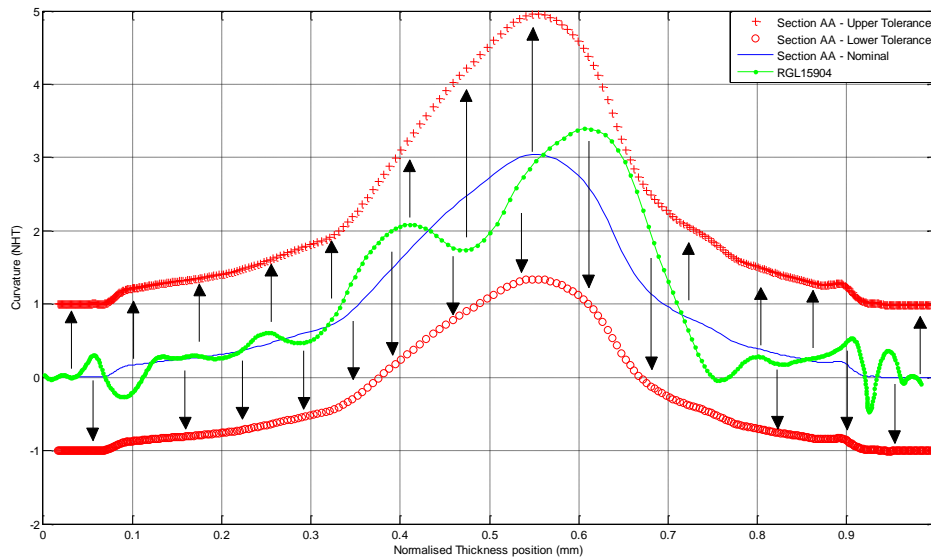


Figure 118. Curvature tolerancing sentencing method

The curvature tolerating method was applied to both curvature plots using thickness as position (CVNTP) as X-axis and curvature plots using arc length as X-axis (CVNAL).

Curvature Tolerancing using CVNTP

The Table-23 contains the initial values used for the upper and lower tolerance bands definition. Initial values were developed with design engineering iteratively because of potential changes to the manufacturing process for the leading edges.

Table 29. Upper and Lower band variables definition 1st pass.

Upper Tolerance							
ϖ_{up}	ϖ_{us}	ψ_{xup}	ψ_{xus}	δ_{up}	δ_{us}	ψ_{yup}	ψ_{yus}
0	0	0	0	1.3	1.3	1	1
Lower Tolerance							
ϖ_{lp}	ϖ_{ls}	ψ_{xlp}	ψ_{xls}	δ_{lp}	δ_{ls}	ψ_{ylp}	ψ_{yls}
0	0	0	0	1.3	1.3	-1	-1

The scored blades from Figure-116 (rgl5904 to15958) were used to set the tolerance bands although the focus was in ensuring the rejected blades failed the assessment. The Figure-119 shows the curvature plots for the six rejected blades. At the first iteration only two of the six blades failed the assessment.

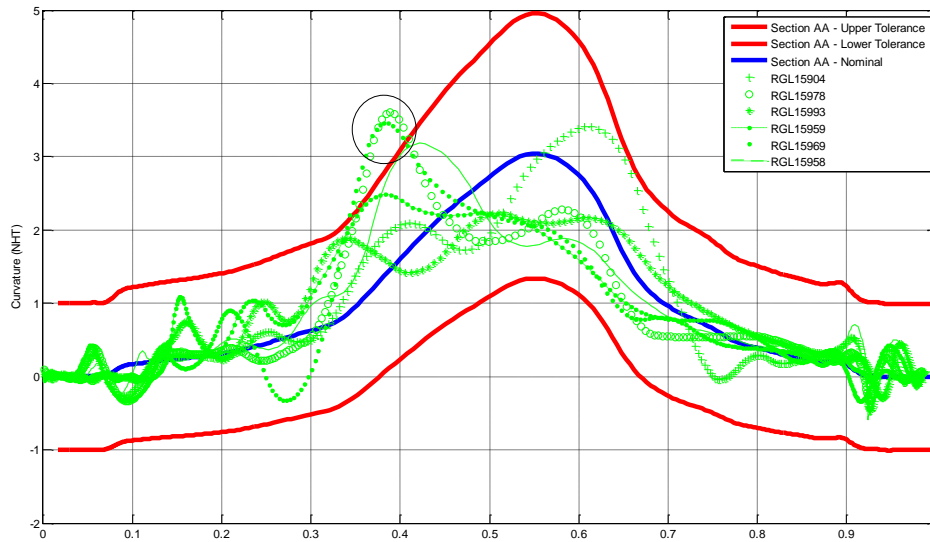


Figure 119. Curvature tolerancing sentencing method applied to the 6 blades.

Table-31 shows the 2nd iteration for the 6 rejected blades. This was achieved by changing the variables required until all the 6 blades were rejected.

Table 30. Upper and Lower band variables definition 2nd pass.

Upper Tolerance							
ϖ_{up}	ϖ_{us}	ψ_{xup}	ψ_{xus}	δ_{up}	δ_{us}	ψ_{yup}	ψ_{yus}
0	0	0	0	1.2	1.2	0.7	0.7
Lower Tolerance							
ϖ_{lp}	ϖ_{ls}	ψ_{xlp}	ψ_{xls}	δ_{lp}	δ_{ls}	$\psi_{y lp}$	$\psi_{y ls}$
0	0	0	0	0.9	0.9	-0.7	-0.7

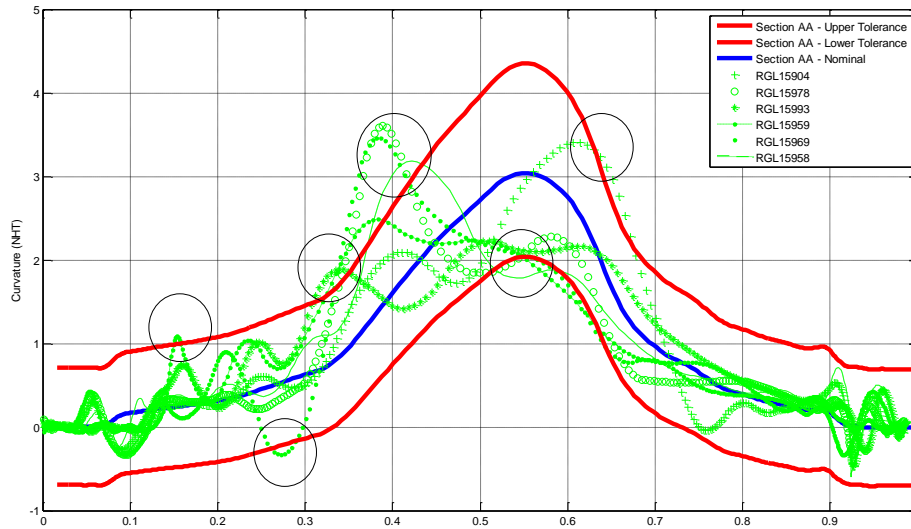


Figure 120. Curvature tolerancing sentencing method applied to 6 blades with updated tolerance bands 2nd pass.

The curvature plots in Figure-120 indicated that the updated tolerance bands failed the 6 selected blades. Results for accepted blades are shown at the end of this section for CVNAL.

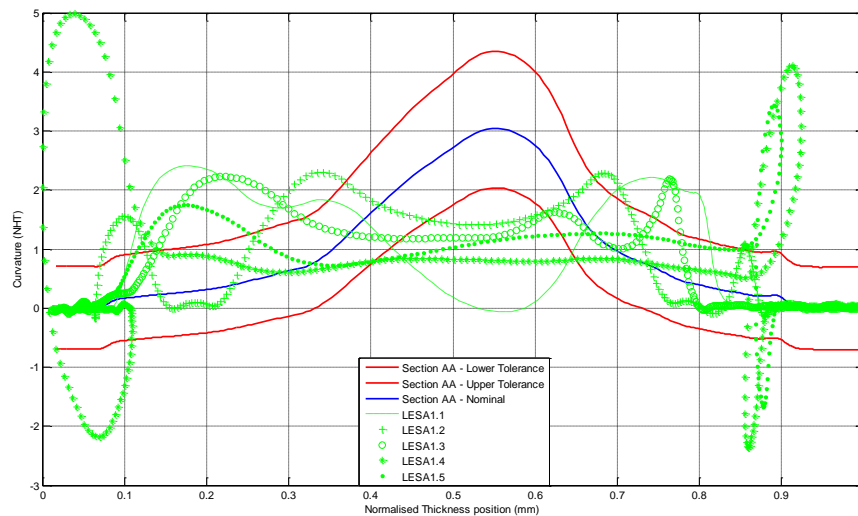


Figure 121. Curvature tolerancing method applied to LESA shapes.

To ensure the method could replace the current manual visual assessment technique, the LESA1 rejected shapes were also assessed using the parameters developed during the 2nd iteration of the tolerance bands. Figure-121 clearly indicated that the LESA1 shapes failed the assessment.

Curvature Tolerancing using CVNAL

Using the values defined for the variables in Table-31 the upper and lower tolerance bands were defined using the CVNAL plots. The Figure-122 indicated that most of the blades failed the assessment with the exception of two blades (RGL15959, RGL15958) as shown in Figure-123. This showed that although both CVNTP and CVNAL methods shared similar data, a read across from the variables defined during the 2nd iteration was not possible.

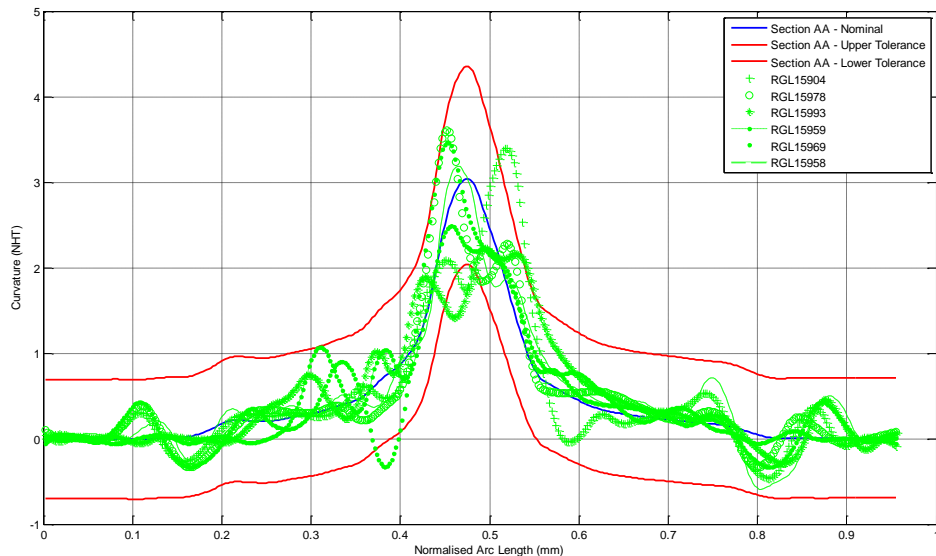


Figure 122. Curvature tolerancing sentencing method applied to 6 blades

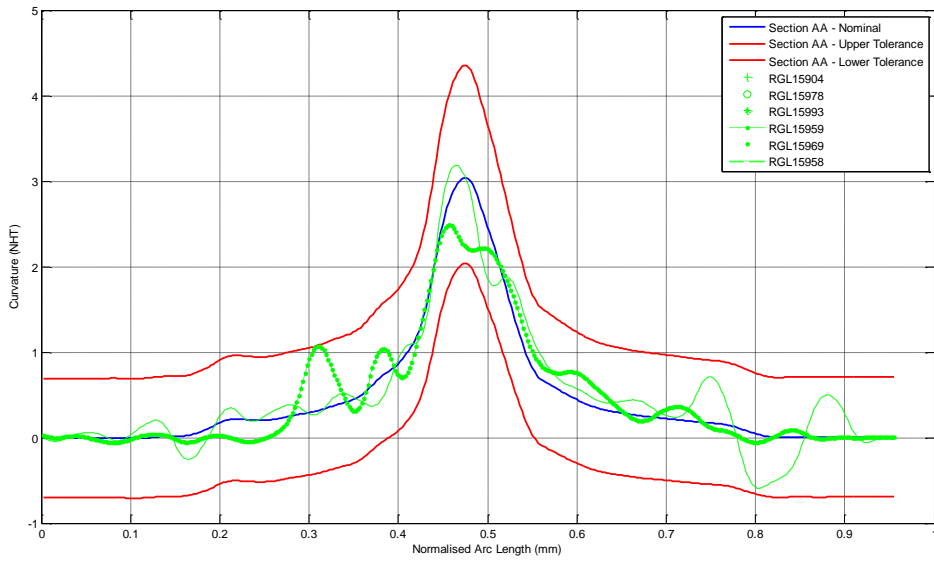


Figure 123. Curvature tolerancing sentencing failing to capture 2 blades.

The Table-32 contains the updated values for the upper and lower tolerance bands.

Figure-124 shows the updated tolerance bands failing the 2 remaining blades.

Table 31. Upper and Lower band variables definition final iteration.

Upper Tolerance							
ϖ_{up}	ϖ_{us}	ψ_{xup}	ψ_{xus}	δ_{up}	δ_{us}	ψ_{yup}	ψ_{yus}
0	0	0	0	1.1	1.1	0.6	0.6
Lower Tolerance							
ϖ_{lp}	ϖ_{ls}	ψ_{xlp}	ψ_{xls}	δ_{lp}	δ_{ls}	$\psi_{y lp}$	$\psi_{y ls}$
0	0	0	0	0.9	0.9	-0.6	-0.6

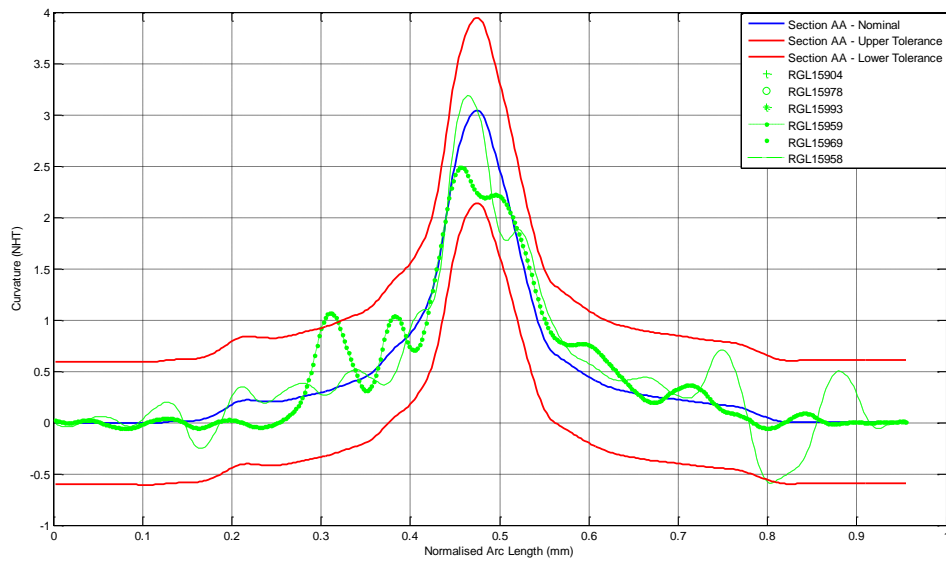
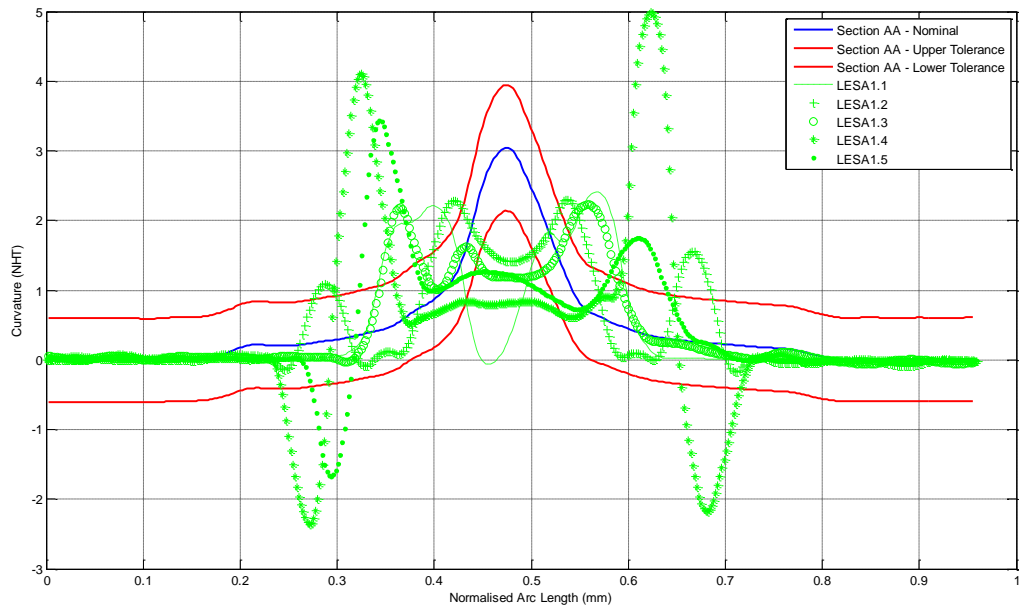
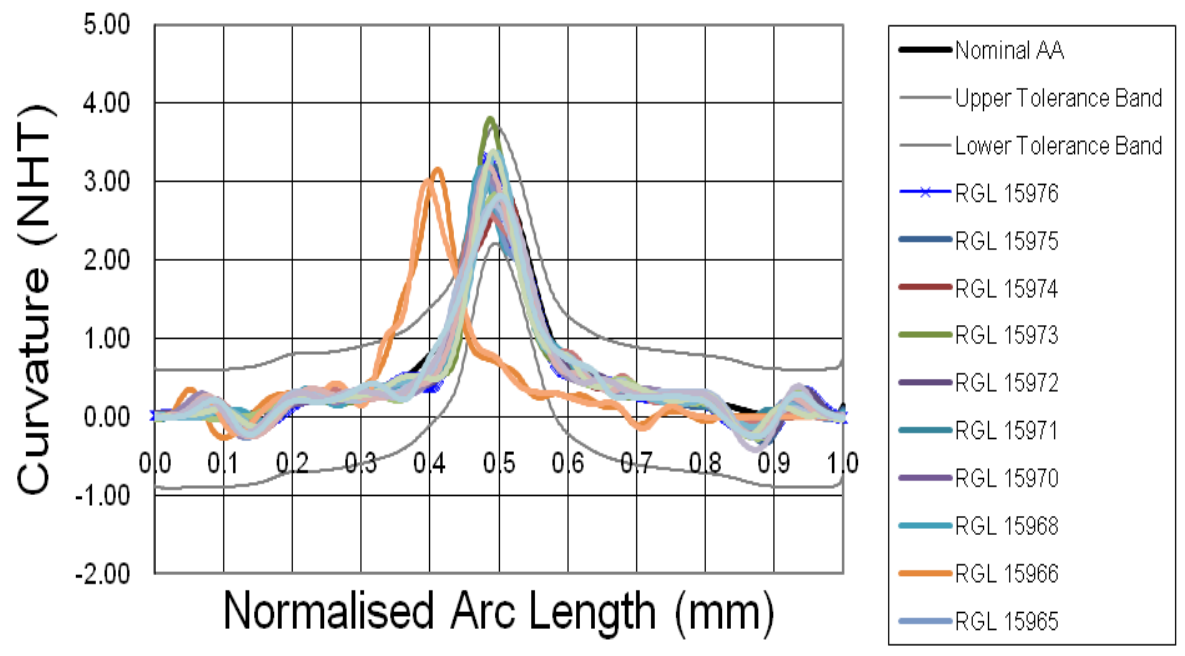


Figure 124. Updated tolerance bands final iteration.

The tolerancing method was also applied to the LESA1 standard as shown in Figure-125. The Figure-125a) above showed the final iteration of the tolerancing method for section AA. Figure-125b) shows the final iteration of the tolerancing method applied to the accepted shapes from Figure-116. Two of blades were found to be shifted to the left of the maximum curvature values along the X axis. This was later found to be due to an error related to the angle of extraction of the leading edge as previously highlighted in section 4.2.2 of this document. The blade RGL 15973 was also found to fail the assessment due to a high curvature peak value. Overall the majority of the shapes passed the Tolerancing assessment.



a)



b)

Figure 125. a) Curvature tolerancing method applied to LESA shapes final iteration; b) Curvature tolerancing method applied to accepted shapes.

While development of the this method was done at RR Derby/Bristol, Aachen University (Fraunhofer) developed in conjunction with RR a software package named Blade Inspect using the Curvature Tolerancing method. The development of the software package allowed for further testing of the tolerancing method and provided the user both graphical outputs in HTML and Excell formats. Such outputs were required due to the fact that the integrated project team (IPT) was not all located in RR Derby and allowed further flexibility for analysing the output data.

The above methodology was developed based on one airfoil section AA of a preproduction blade set. In order to fully test the proposed methodology a set of production blades from a different compressor stage was used. Each blade contained 7 sections “DC” to “DJ” hence 7 sets of upper and lower tolerance bands were generated. The Table-32 shows the values used for generating the tolerance bands.

Table 32. Upper and Lower band variables definition.

Upper Tolerance							
ϖ_{up}	ϖ_{us}	ψ_{xup}	ψ_{xus}	δ_{up}	δ_{us}	ψ_{yup}	ψ_{yus}
0	0	0	0	1.177	1.177	1	1
Lower Tolerance							
ϖ_{lp}	ϖ_{ls}	ψ_{xlp}	ψ_{xls}	δ_{lp}	δ_{ls}	ψ_{ylp}	ψ_{yls}
0	0	0	0	1.06	1.06	-1	-1

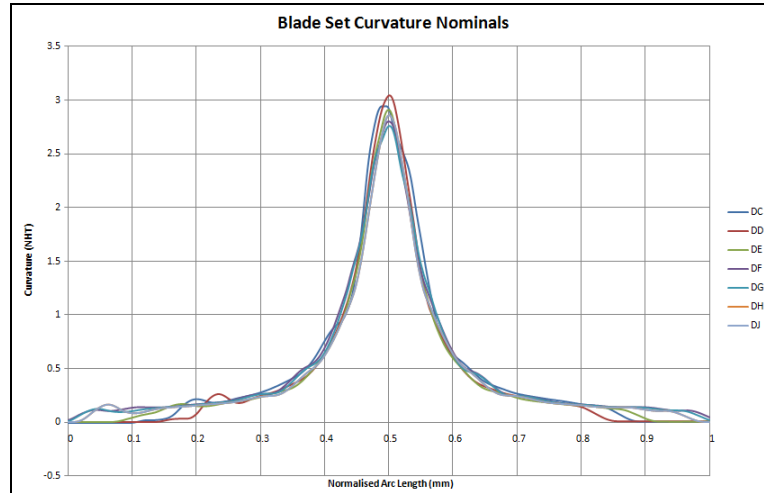


Figure 126. Blade set curvature nominal curvature

The Figure-126 above shows the 7 curvature profiles for the nominal airfoil leading edges. Figures-127 and Figure-128 shows the result for the blade set for sections “DC” and “DE” respectively.

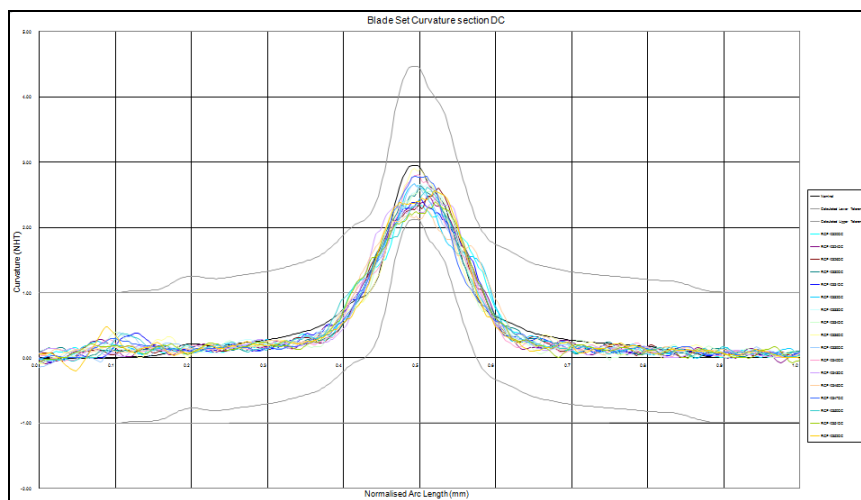


Figure 127. Section “DC” curvature assessment

The results for Section “DC” indicated that all blades passed the assessment with all peak curvature values located between the Nominal curvature profile and the Lower tolerance band.

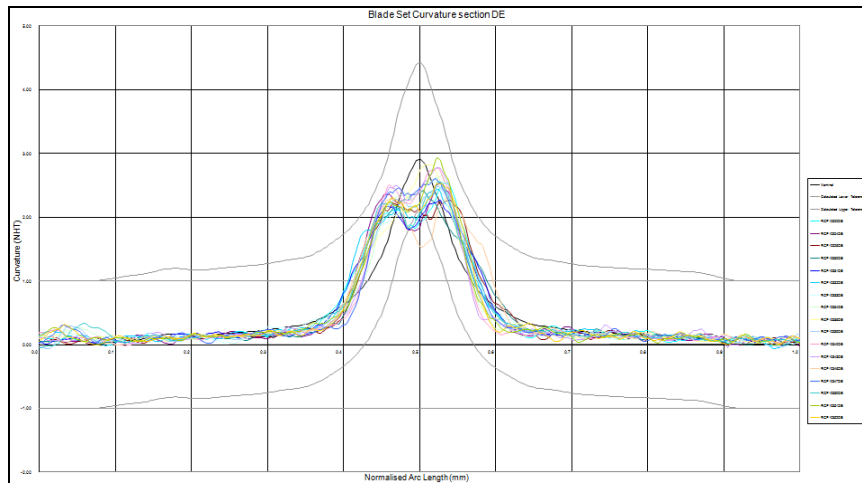


Figure 128. Section “DE” curvature assessment

The results from Figure-128 indicated that 6 blades (35%) failed the assessment. In all cases the airfoil sections failed at the Lower tolerance band minimum peak curvature. The Figure-129 a) shows one of the failed blade sections and its respective geometry. Although geometrically the airfoil section appears to be very symmetrical and smooth, when compared to the nominal shape, it was clear that the airfoil section was not as “sharp”.

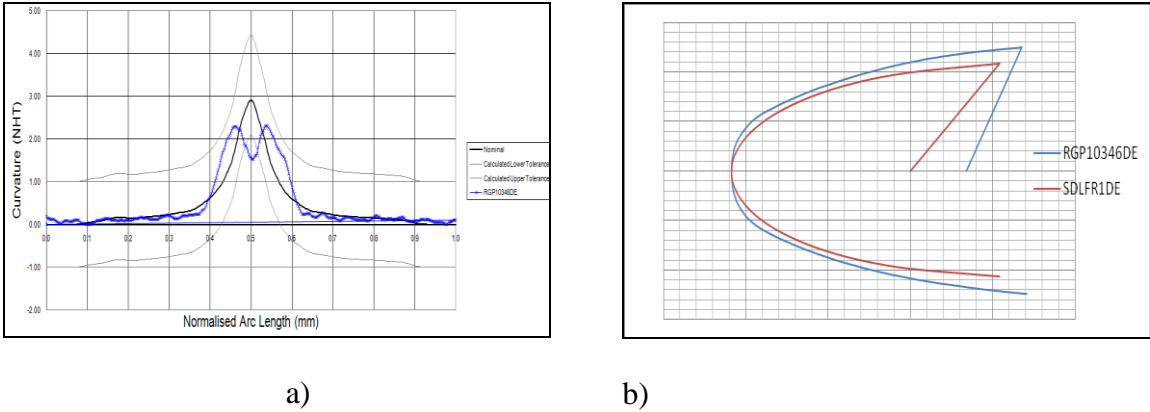


Figure 129. a) Curvature plot of a failed blade; b) Leading edge profile of nominal and measured blade

Appendix 5.3.1 contains the summary results for the blade set sections. During further examination with the aerodynamicists it was noticed that in most cases independently of the blade section, failing occurred due to “double peaks” as shown above. Although the tolerance bands provided a methodology for capturing such features, it was found that in some cases the tolerance bands may fail to capture “double peaks” as shown in the Figure-130.

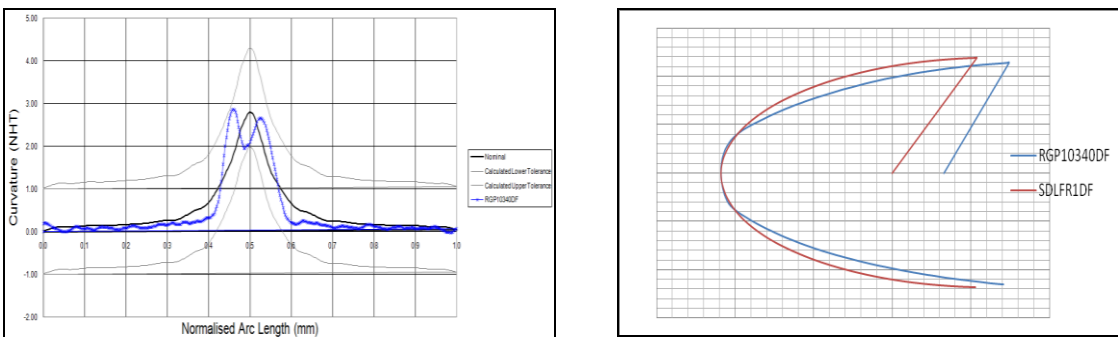


Figure 130. Tolerancing methodology failure to capture a double peak feature

From the Figure-130 it was noticed that the airfoil section had the “double peak” feature offset from the expected peak curvature location. Due to such offset, the “double peak” feature was not captured by either the upper tolerance band or the lower tolerance band. This event triggered further testing to investigate a potential scope of features that may not have been captured by the tolerancing methodology. As an example the curvature plot (Figure-131) was extracted from a blade at its early stages of manufacturing to highlight potential features that could be present in a finished blade.

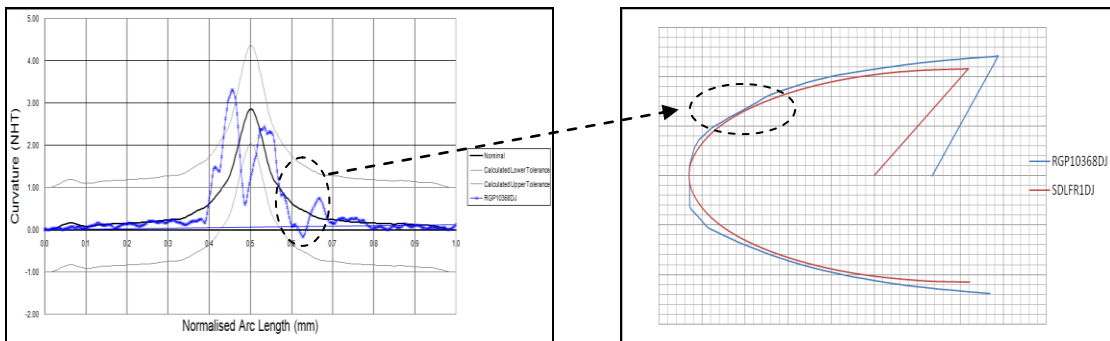


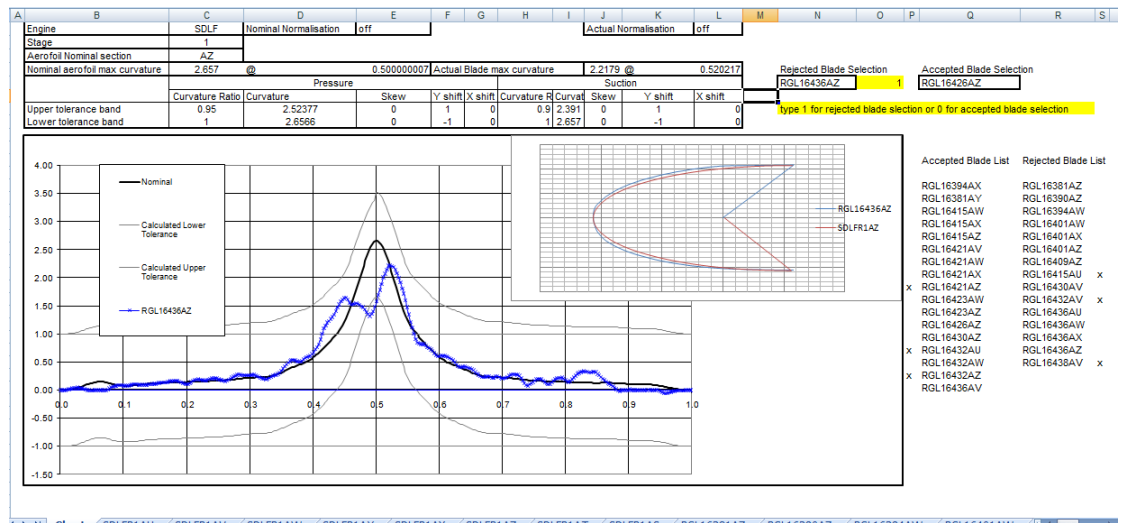
Figure 131. Failure to capture second double peak feature

Although the tolerance band failed the above shape, it was clear that features such as high curvature peaks/valleys could exist along the airfoil profile and not be captured by the tolerancing method. To capture such features a second method for assessing the leading edge shape was developed (section 4.3.3).

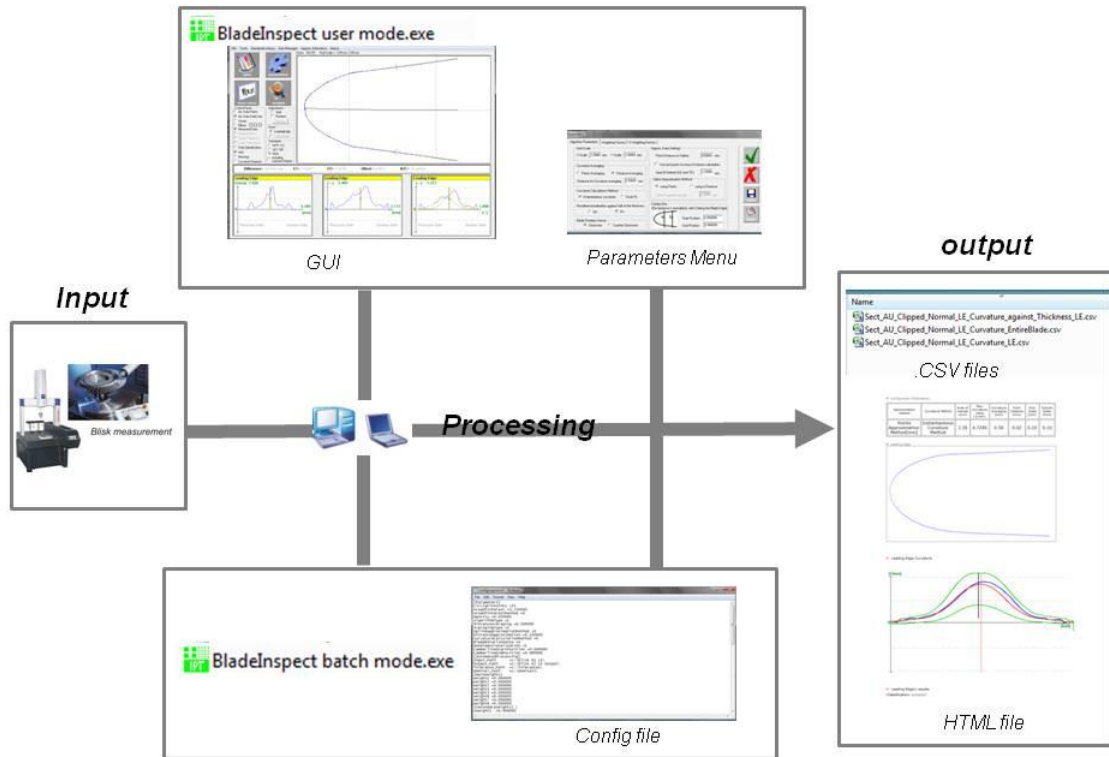
4.3.2 Industrial impact

A comprehensive software specification was developed with Aachen University at the Rolls-Royce pre-production facility where the blades were manufactured, to ensure that the software inputs and outputs could be controlled at different levels from the already existing manufacturing execution software within the facility. A configuration file was used to set all the software parameters and paths to located data such as the upper and lower tolerance bands but also to ensure the output data was located in the correct folder structure. The software was developed with two modes of operation, a user mode which allowed the user to process a single section of a blade and a batch mode which could process several blades.

The component selected for implementation of the software was a bladed disk also known as blisk. The Figure-132 shows a) the excel tool developed to visualise the Blade Inspect outputs and b) high level view of the two modes of operation within the software.



a)



b)

Figure 132. a) Excel tool for displaying Blade Inspect outputs; b) Blade Inspect integration with CMM inspection

Further tools were developed in Microsoft Excel to aid the development/updating of new tolerance bands. Although the work presented in this document was originally aimed at final inspection of airfoil leading edge shape, it was decided that the curvature plot could also be used as a process control tool throughout the different operations within the blade manufacturing process. The operation numbers chosen for software deployment were 690 (post-machining) and 870 (post-linishing(polishing)). The Figure-133 shows the software integration within the blisk measurement facility in Rolls-Royce plc.

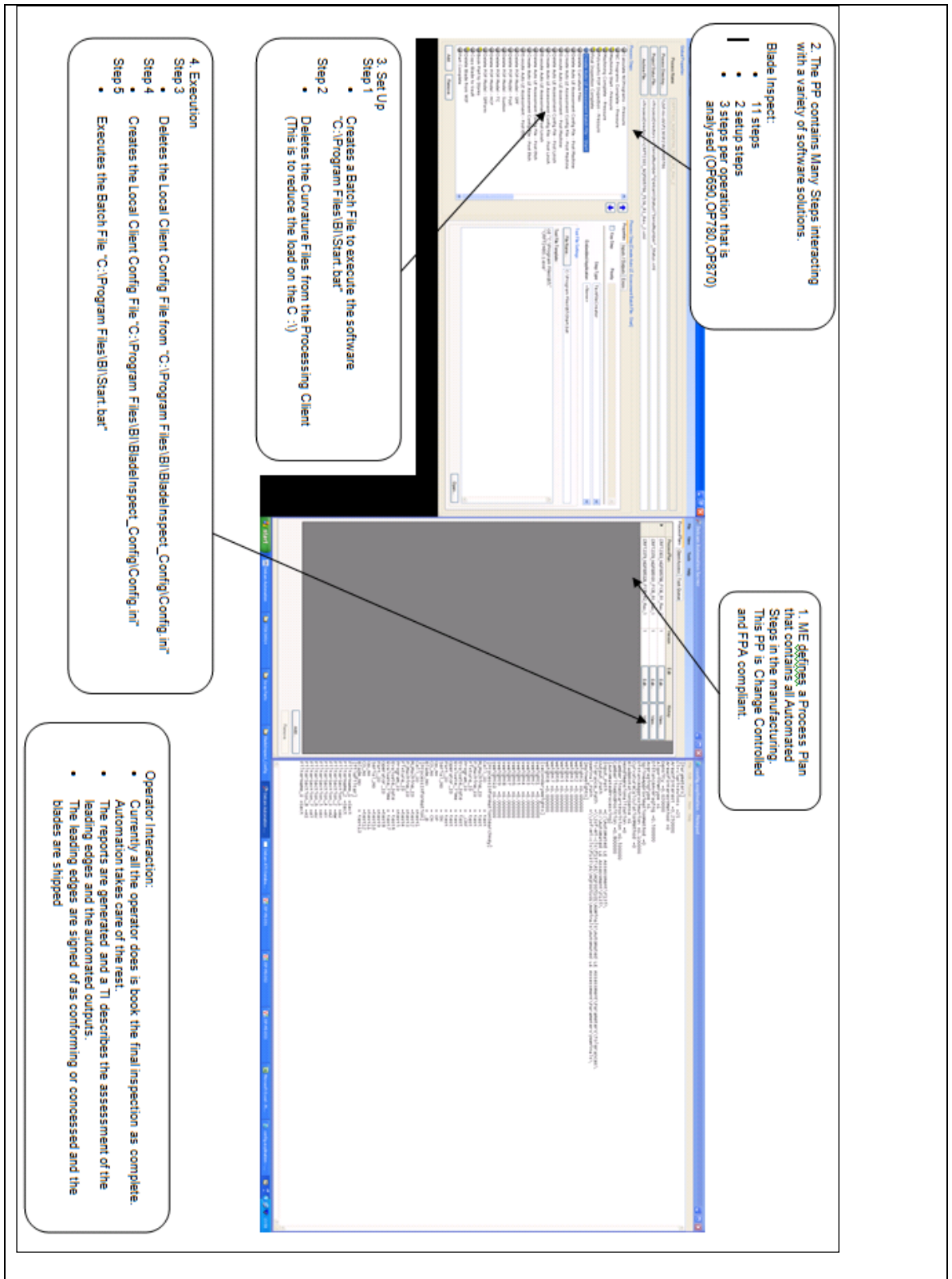


Figure 133. Detailed integration overview between Blade Inspect and inspection process operation sequence

As the naming convention indicates it was expected that leading edges of OP690 would have sharper features when compared with OP870. From a production perspective all OP690 (post machining operation) shapes should fail the assessment. The Figure-134 shows the results for a set of 180 blades with 17 sections using the curvature tolerancing method in both CVNTP and CVNAL mode. In both cases (CVNTP, CVNAL) for OP690 the fail rate was 89%. This result indicated that some leading edges may have a good shape after OP690. For OP870 the pass rate achieved was 91%.

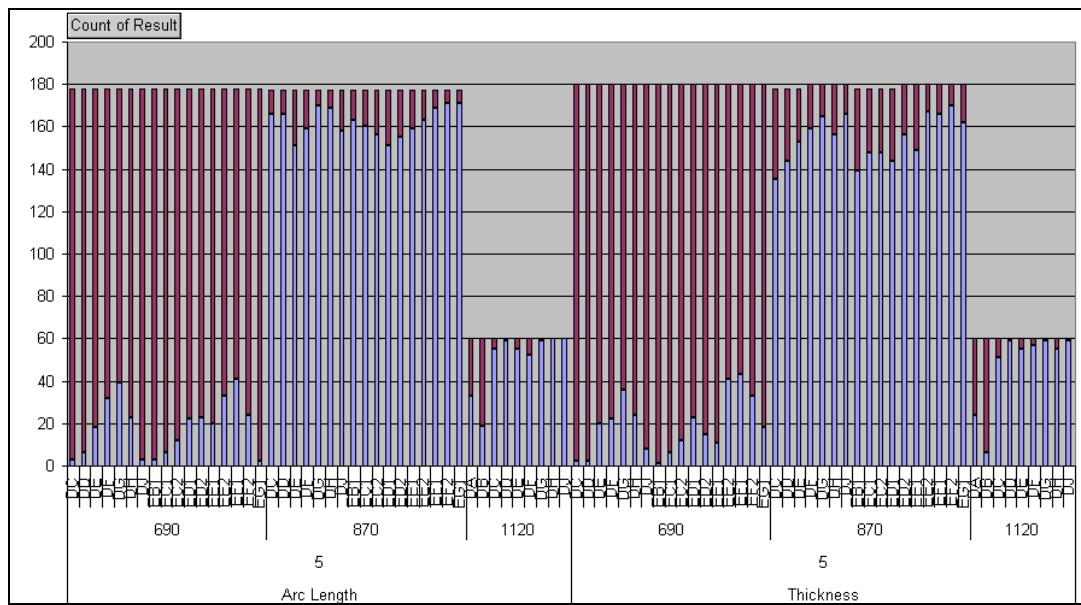


Figure 134. Blade Inspect output for a blisk assessment using both CNTP and CNAL.

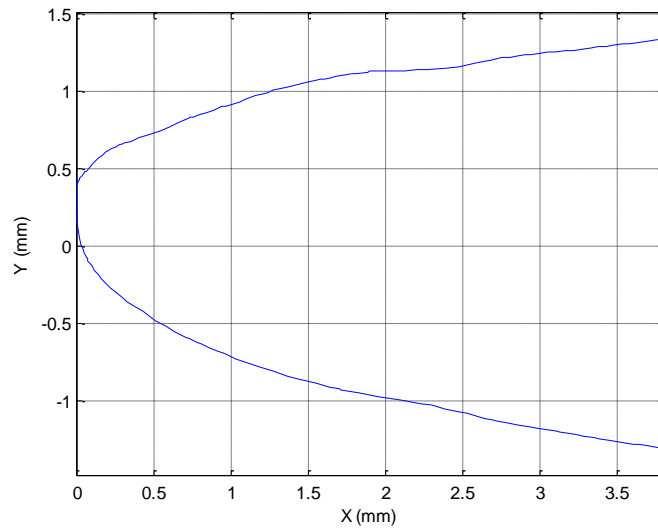
4.3.3 Method 2 – Parameterisation of curvature plot features

The parameterisation method consisted of identifying key distances between key features present in the curvature plots. Before key features could be identified the following smoothing settings were applied:

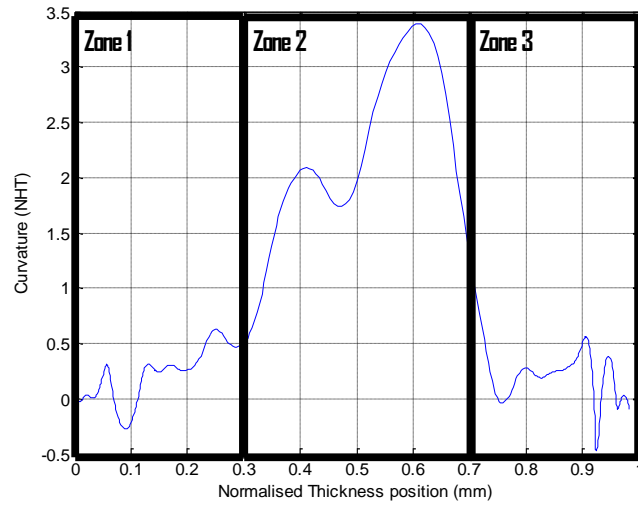
$$\text{CPD} = 0.2\text{mm}$$

$$\text{Cavg} = 0.4\text{mm}$$

Such settings were necessary because the parameterisation method consisted of searching for a set of values which represented a peak or a valley as shown in Figure-135. If the curvature plots were to have less smoothing the searching criteria for a peak or a valley could have multiple answers which would make the sentencing process more complex.



a) Leading edge shape from a production compressor blade



b) Curvature parameterisation variables Zones

Figure 135. Parameterisation of curvature plot zones

The nominal airfoil section chosen for testing was section AA as shown in the Figure-136.

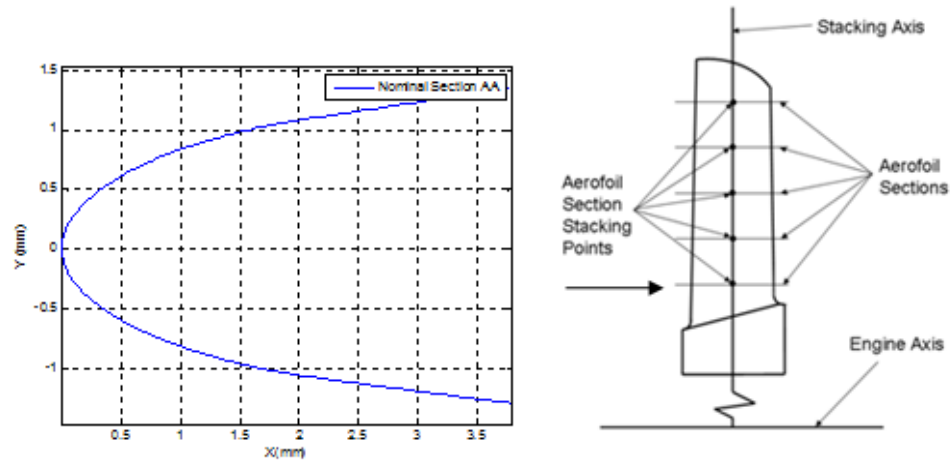


Figure 136. Nominal airfoil section AA.

Parameterisation using CVNTP

Three zones were selected in relation to the three key areas of interest within the leading edge geometry, the pressure side (Zone 1), the leading edge tip (Zone 2) and the suction side (Zone 3). The three zones of interest were defined from the curvature plots as follows:

CVNTP

- Zone 1 – 0 to 0.3
- Zone 2 – 0.3 to 0.7
- Zone 3 – 0.7 to 1

Figure-137 shows the curvature plots for the 6 blades with the highest scores from Figure-121 (section 4.3.1). These plots were used to create the first iteration of the parameterisation variables shown in Figure-138.

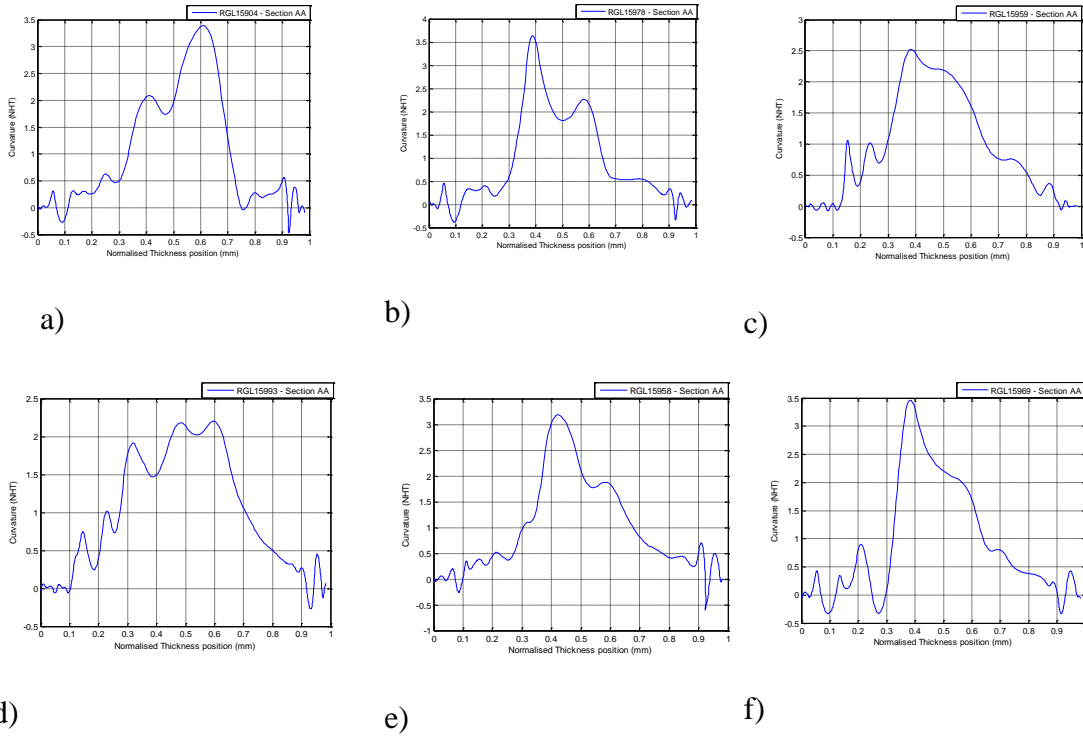


Figure 137. Curvature plots for the rejected airfoils section AA from classification summary.

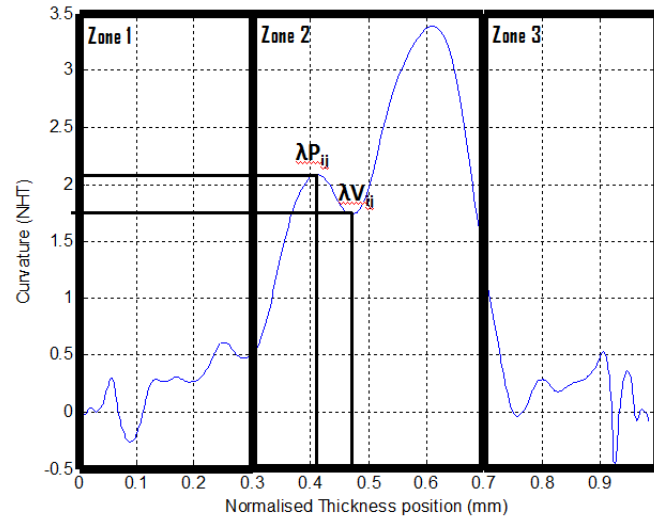


Figure 138. Parameterisation variables for all zones.

Zones parameterisation

Two variables were defined for extracting peaks and valleys information from the curvature plot as follows:

- λP_{ij} where P defined a “peak” with subscript i referring to a “zone” and subscript j an “incremental counter”.
- λV_{ij} where P defined a “valley” with subscript i referring to a “zone” and subscript j an “incremental counter”.

For zone2 extra variables were derived by extracting the (x_p, y_p) coordinates of λP_{ij} and (x_v, y_v) of λV_{ij} as follows:

$$Area_{ij} = \frac{abs((xp_{ij} \times yp_{ij+1} - xp_{ij+1} \times yp_{ij}) + (xv_{ij} \times yp_{ij} - xp_{ij} \times yv_{ij}) + (xp_{ij+1} \times yv_{ij} - xv_{ij} \times yp_{ij+1}))}{2} \quad (4.17)$$

A set of rules was developed using the results obtained for the 6 blades shown in Figure-137 to generate an output associated with λP_{ij} , λV_{ij} .

Table 33. Zone 1 variables and rules

Variable	Rule	Output if true	Output if false
λP_{11} (Yp4)	>1	1	0
λP_{12} ()	N/A	N/A	N/A
λV_{11} (Yv4)	<-0.3	1	0

Table 34. Zone 2 variables and rules

Variable	Rule	Output if true	Output if false
λP_{21} (Yp3)	>1.5	0	1
λP_{22} (Yp1)	N/A	N/A	N/A
Area ₂₁	>0.04	0	1
Area ₂₂	>0.04		
λV_{21}	<1.5	1	0

Table 35. Zone 3 variables and rules

Variable	Rule	Output if true	Output if false
λP_{31} (Yp5)	>1	1	0
λP_{32} ()	N/A	N/A	N/A
λV_{31} (Yv5)	<-0.3	1	0

Each variable output from the three zones was used as an input to a sentencing vector S using the following expression:

$$S = ([\lambda P_{11}] + [\lambda V_{11}] + [\lambda P_{21}] + [Area_{ij}] + [\lambda P_{31}] + [\lambda V_{31}]) \quad (4.18)$$

The Table-30 summarises the output of the sentencing vector S . The conditions for the vector S output were set in the following way:

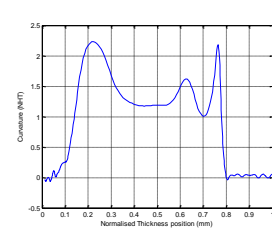
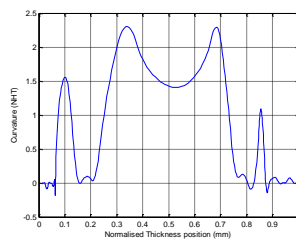
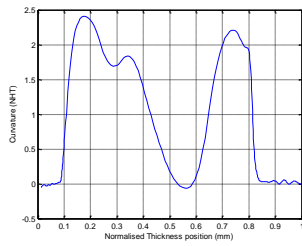
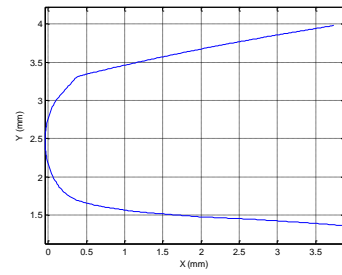
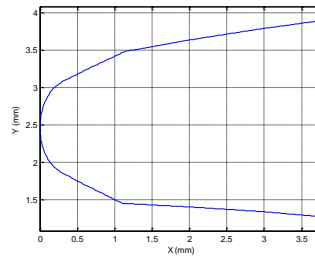
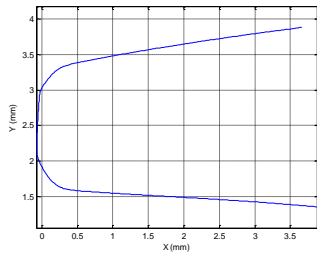
If $S = 0$, the airfoil passed the assessment; If $S > 0$, the airfoil failed the assessment

Table 36. Sentencing results for the 6 rejected leading edges

Blade	RGL15904	RGL15993	RGL15978	RGL15959	RGL15969	RGL15958
λP_{11}	0	1	0	1	0	0
λV_{11}	0	0	1	0	1	0
λP_{21}	0	0	0	0	0	0
λV_{21}	0	0	0	0	0	0
Area ₂₁	1	0	1	0	0	0
Area ₂₂	N/A	1	N/A	N/A	N/A	N/A
λP_{31}	0	0	0	0	0	0
λV_{31}	1	0	1	0	1	1
S	2	2	3	1	2	1
Automated Sentencing	Fail	Fail	Fail	Fail	Fail	Fail
Figure 123scoring	Fail	Fail	Fail	Fail	Fail	Fail

The sentencing vector was successfully able to sentence the 6 airfoils used from Figure-137 in accordance to the results showed in Figure-121. This result represented the first iteration of the sentencing vector using a small population of blades to define a set of rules. Like the toleracing method it was foreseen that an iterative process with design engineering and manufacture was required before agreeing on set variables.

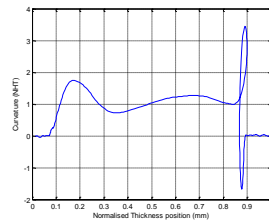
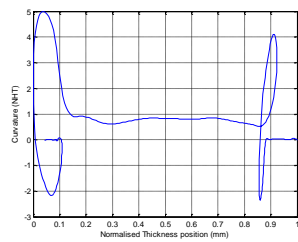
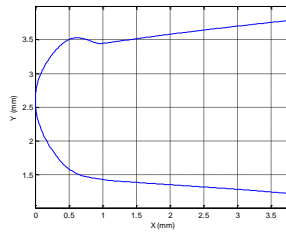
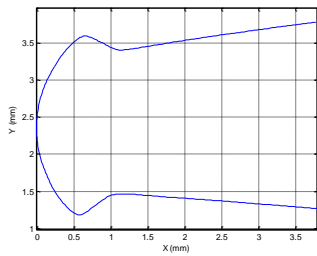
If such method was to be used in a production environment, it would have to be compatible with the current standards (LESA1) used for Leading edge shape assessment. Figure-139 shows the extracted LESA1 shapes and their corresponding curvature plots. The Table-38 summarises the output of the sentencing vector S for the standard LESA1.



a) LESA1.1

b) LESA1.2

c) LESA1.3



d) LESA1.4

e) LESA1.5

Figure 139. LESA1 Leading edge shapes and corresponding curvature plots using CVNTP

Table 37. LESA1 sentencing results using curvature parameterisation method

LESA1	LESA1.1	LESA1.2	LESA1.3	LESA1.4	LESA1.5
λP_{11}	1	1	1	1	1
λV_{11}	0	0	0	1	0
λP_{21}	0	0	0	1	1
λV_{21}	1	1	1	1	1
Area ₂₁	0	1	0	0	0
Area ₂₂	N/A	N/A	N/A	N/A	N/A
λP_{31}	1	1	1	1	1
λV_{31}	0	0	0	1	1
<i>S</i>	3	4	3	6	5
Automated Sentencing	Fail	Fail	Fail	Fail	Fail
LESA1 Standard	Fail	Fail	Fail	Fail	Fail

All LESA1 shapes failed the assessment. From the Table- above it was only shown the results for 1 Area although multiple areas were identified by the Matlab algorithm. Because 1Area was sufficient to fail the above leading edges no further development for n Areas took place.

Parameterisation using CVNAL

Similarly to CVNTP the parameterisation algorithm was developed for arc length quantity due to the reasons discussed earlier in this work. Zone 1 and 3 variables remained the same as the ones obtained for CVNTP. Zone 2 variables were changed as shown (Table-39).

CVNAL

- Zone 1 – 0 to 0.4
- Zone 2 – 0.4 to 0.6
- Zone 3 – 0.6 to 1

Table 38. Zone 2 variables and rules using CVNAL

Variable	Rule	Output if true	Output if false
λP_{21} (Yp3)	>1.5	0	1
λP_{22} (Yp1)	N/A	N/A	N/A
Area ₂₁	>0.02	0	1
Area ₂₂	>0.02		
λV_{21}	<1.5	1	0

The Table-39 summarises the output of the sentencing vector S . The conditions for the vector S output were set in the following way:

If $S = 0$, the airfoil passed the assessment

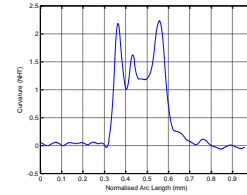
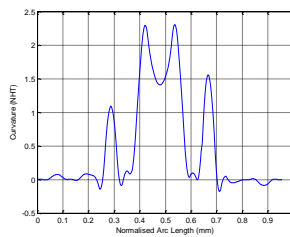
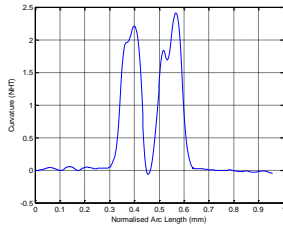
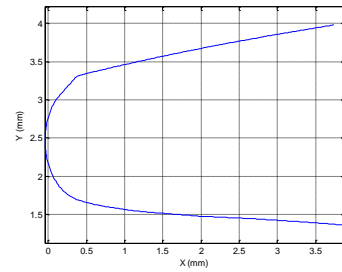
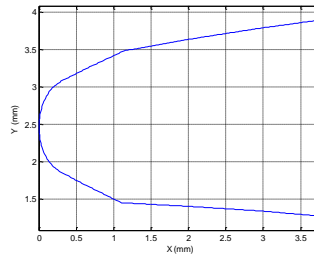
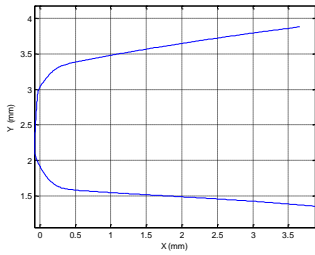
If $S > 0$, the airfoil failed the assessment

Table 39. Sentencing results for the 6 “Fail” blades and remaining RGL159 series “Pass”.

Blade	RGL 15904	RGL 15993	RGL 15978	RGL 15959	RGL 15969	RGL 15958	RGL 1595’’	RGL 1596’’	RGL 1597’’
λP_{11}	0	1	0	1	0	0	0	0	0
λV_{11}	0	0	1	0	1	0	0	0	0
λP_{21}	0	0	0	0	0	0	0	0	0
λV_{21}	0	0	0	0	0	0	0	0	0
Area ₂₁	1	0	1	0	0	0	0	0	0
Area ₂₂	N/A	1	N/A	N/A	N/A	N/A	N/A	N/A	N/A
λP_{31}	0	0	0	0	0	0	0	0	0
λV_{31}	1	0	1	0	1	1	0	0	0
S	2	2	3	1	2	1	0	0	0
Automated Sentencing	Fail	Fail	Fail	Fail	Fail	Fail	Pass	Pass	Pass
Figure 123 scoring	Fail	Fail	Fail	Fail	Fail	Fail	Pass	Pass	Pass

Table-39 shows the assessment results for the 6 rejected blades used through this work to set Tolerancing methods. Results showed that all 6 blades failed the assessment. The table also shows the remaining blade series from Figure-116 and all remaining blades

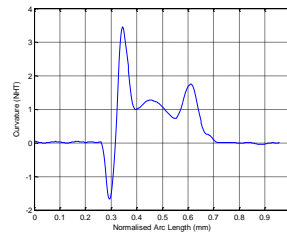
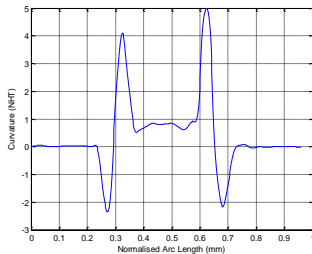
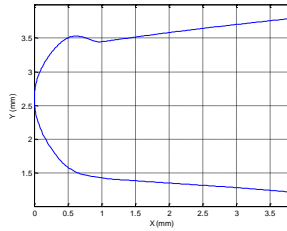
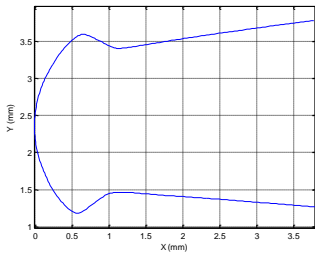
passed the assessment in accordance to the previous scores. The Figure-140 shows the results for the LESA1 standard using CVNAL. When compared with the curvature plots from Figure-139 d),e) with Figure-140 d),e) the CVNAL plots don't show any curvature overlap.



a) LESA1.1

b) LESA1.2

c) LESA1.3



e) LESA1.5

d) LESA1.4

Figure 140. LESA1 Leading edge shapes and corresponding curvature plots using CVNAL

Table 40. LESA1 results using CVNAL

LESA1	LESA1.1	LESA1.2	LESA1.3	LESA1.4	LESA1.5
λP_{11}	1	1	1	1	1
λV_{11}	0	0	0	1	1
λP_{21}	0	0	0	1	1
λV_{21}	1	0	0	1	1
Area ₂₁	1	1	1	0	0
Area ₂₂	N/A	N/A	N/A	N/A	N/A
λP_{31}	0	1	1	1	1
λV_{31}	0	0	0	1	0
S	3	3	2	5	4
Automated Sentencing	Fail	Fail	Fail	Fail	Fail
LESA1 Standard	Fail	Fail	Fail	Fail	Fail

From the Table-40 above it was clear that the automated sentencing using the predefined parameters failed all the LESA1 shapes. When compared to the CVNTP, the CVNAL test performed in the same manner by failing all the rejected LESA1 shapes.

Chapter 5

5.1 Conclusions

This thesis had two aims. The first was focused on the evaluation of task specific measurement uncertainty when using coordinate measuring machines. This was explored via the application of statistical analysis tools such as experimental designs and Monte Carlo simulation on how factors present on everyday coordinate measuring machine measurements affected measurement uncertainty. A first evaluation was the physical measurement of a known artefact under different thermal conditions. Further investigation of factors related to measurement strategy was explored via the integration of a Monte Carlo simulator with a full factorial experimental design to aid the analysis on the sensitivity of fitting algorithms for circular features. Finally the potential applications for a newly developed virtual CMM (VCMM) named pundit/CMM was explored via comparative tests when using length bars and parts with known form errors. Although the focus of this work was for CMMs equipped with touch trigger probes, its results can be read across to CMMs equipped with other types of probing systems. The experimental work and literature review indicated that measurement strategy was a significant factor that influenced measurement uncertainty. Strategy in this case not only covered typical factors such as probing point distribution and form error and its impact when selecting algorithms to extract circular features.

The main conclusions of the Engineering Doctorate thesis are summarized in the following 6 sections below.

- 1 Two methods for deriving uncertainty budgets for coordinate measuring machines were extracted for point to point measurements of length bars. Both methods showed good correlation, although the ISO 15530-3 method was found to be more sensitive to changes in the CMM repeatability when compared with GUM approach. This was due to the fact that the GUM approach relies heavily on the CMM specification data while the ISO 15530-3 relies on the output data of the measurement results in order to build to uncertainty budget. Using the CMM specification in as an uncertainty statement for part measurements in circumstances where environmental controls may be poor could lead to underestimation of the measurement uncertainty and ultimately influence a conformance assessment.
- 2 The sensitivity of circular features experiment revealed that there was a strong interaction between form error and probing strategy. The full factorial experimental design revealed that by applying LSC algorithm to extract circular features under different experimental conditions the uncertainty associated with both size and position of the features was of smaller magnitudes when compared to MIC and MCC algorithms. Nevertheless standard deviation (1 sigma) values of 0.0015mm were obtained when applying LSC when compared with MIC/MCC values of 0.0022mm. Mean error results were very sensitive to the standard to which such features should be extracted. The centre coordinates sensitivity study revealed a range of centre coordinates standard deviation values of up to 0.012mm when applying the MIC algorithm according to the main effects plot obtained. Although the main effects plot presents an averaged result for the study

of a particular quantity, error values of centre coordinates for particular runs of the experimental design were found to reach a magnitude of 0.04mm. The method chosen when using of statistical tools could affect the outputs of uncertainty studies. The magnitudes of the standard deviation values when applying LSC were found to be smaller when compared with MIC and MCC algorithms. As previously mentioned, clarity of the design intent is required when defining the feature function, because this will potentially impact the definition of the algorithm being used to extract the centre coordinates of the feature. A similar result could have been obtained for a circular datum feature in which case the results obtained for the uncertainty estimations would have been of higher magnitude hence a key recommendation is that stricter controls should be applied to datum features

- 3 The temperature effects during CMM measurements revealed that the major contributor to the measurement uncertainty was the mean error also known as the systematic error. Although care was taken to ensure that all factors selected for the experimental study were well controlled, the study confidence level was only 40%. Temperature did not influence the repeatability of the measurement results and caution is required when applying temperature variations to an uncertainty model.
- 4 A Virtual CMM named Pundit/CMM showed good correlation between simulated experiments and physical measurements of artefacts. Uncertainty budgets developed in the 2nd chapter for length bar measurements were used as a basis for a comparative study. Pundit/CMM was found to be very user friendly with an

intuitive user interface developed around the main factors that affect CMM measurement uncertainty. For the simulations of length bar measurements Pundit/CMM results were found to follow the same trend as the uncertainty budgets. Furthermore the magnitude of uncertainty values was found to always be above the mean error and close to the machine specification quantity. All these results were found to be positive indicators for Pundit/CMM capability to estimate CMM task specific measurement uncertainty. Similar results were obtained for the simulations associated with the multi-feature artefact experiment. For the circular features size uncertainty comparison, Pundit/CMM showed very similar trends and magnitudes to the results obtained during the physical measurement trials for machines M and W. Feature 2B (Artefact B) showed the highest uncertainty magnitude when compared with all the remaining features. When the probing strategy was modified from 1XBASIC to 3XBASIC there was an overall small improvement of the magnitudes of measurement uncertainty for all features including feature 2B. Machine A results showed that Pundit/CMM simulations results followed the trend of uncertainty results for most features with the exception of feature 1A. For all physical measurements and simulations results the uncertainty of measurement associated with the circular features size was as found to be between 0.0005mm and 0.003mm with the exception of features 1A, 2A and 2B during 1XBASIC measurements.

For the feature position results Pundit/CMM showed good correlation with the physical measurements for the 1XBASIC measurements. The 3XBASIC measurements showed that Pundit/CMM underestimated the positional

uncertainty values for machines M and W but for machine C the correlation was found to be very good.

It was also found that the options available within Pundit/CMM for defining form error associated with the features in this study were sensitive to the probing strategy used. The results for both modes of inputting form error showed that there was a clear difference between the two modes when simulating the 1XBASIC physical measurements. Finally both the physical measurements and the simulation results clearly showed a strong correlation between probing strategy and form error which reflected some of the results in chapter 2 of this work. The simulation of an artefact used for aero engine shaft measurements revealed very good correlation between Pundit/CMM results and the measured artefact. Chapters 2 and 3 clearly showed that the estimation of measurement uncertainty for coordinate measuring machines is still a very complex task and that the CMM specification does not always reflect the uncertainty values found for some of the experiments. Pundit/CMM was found to be a very useful tool where the user could explore the impact of key factors such as form error and probing strategies without having to carry out experiments such as the ones showed in this study.

- 5 The mathematical definition of the leading edge of compressor airfoil profiles was successfully developed via the use of curvature. By filtering the instantaneous curvature of the leading edge profiles undesirable features such as flat regions along the leading edge profile could be detected. It was shown by non dimensionalising curvature plots leading edges of different sections within a blade

profile could be compared in the same plot. It was also shown that the method successfully assessed the LESA shapes. Because the leading edge was described mathematically the subjectivity associated with the manual visual assessment of the leading edge profiles was removed from the process.

- 6 A software named blade inspect was successfully developed in conjunction with Aachen university using the curvature tolerancing method. It was found that the tolerancing method was required for each section of a compressor blade. Integration and demonstrated of the software package in a pre- production facility demonstrated that the curvature tolerancing method could successfully sentence the leading edge profiles. Furthermore, the sentencing method was quicker when compared to a trained inspector. 200 Leading edge shapes were assessed in just under 5 minutes, an operation that could take a trained inspector 3 hours. Because the software was successfully integrated with the shop floor execution system in the pre-production facility its applicability was expanded to other operations in the manufacturing process of the leading edge profile so that early potential defects could be detected early in the manufacturing process. During early trials of the curvature Tolerancing method it was found that there could be cases where the method could fail to identify rapid changes in curvature that would still fit within the tolerance bands defined. A second method was developed in Matlab 2007.b where rapid changes in curvature could be captured and assessed. Early trials of the method proved successful but were not implemented on time in Blade Inspect due to the end of the Engineering Doctorate programme.

5.2 Future work

The future work outcome from chapters 2 and 3 of this thesis will be focused on integration of tools such as Pundit/CMM with design tools available within the PLM environment. This integration will allow designers to understand the impact of CMM measurement uncertainty during tolerancing stages of a product. During this research it was identified that although Pundit/CMM provides a trained user with many possibilities for simulating how different factors affect measurement uncertainty, it still required a considerable amount of time for a trained user to simulate different measurement scenarios. Metrosage were commissioned to develop and add on module to Pundit/CMM which allowed the user to predefine several measurement scenarios via tools such Minitab. This feature was never fully tested but simple tests revealed that there was strong potential to explore this option further.

The second method developed for the assessment of leading edge profiles will be added to Blade Inspect to ensure both methods can combine to allow for improved capability when sentencing leading edge profiles. Exploration of the methodology developed for assessing the leading edge profiles could see applications in geometric tolerancing fields where free form features can be difficult if not impossible to sentence. Such features could include radii and scallops which are common features in aero engine parts. Free form features generally prove challenging in the aerospace industry because the methodology used to extract the feature geometry may be ambiguous and or subjected to very high uncertainties. The proposed algorithm could potentially support/replace the methods/standards associated with free form features geometric definitions and remove the subjectivity associated with conformance decisions of such features.

References

1. Schuh G, Rozenfeld H, Assmus D, Zancul E. Process oriented framework to support PLM implementation. *Computers in Industry* 2008; 59: 210–218
2. ISO 9001:2000 Quality management systems – Requirements, Geneva, 2000.
3. Salomons O, Houten F, Kals H. Review of Research in Feature-Based Design. *J. Manuf. Sys* 1993; 12: 113-132.
4. Gu Z, Zhang YF, Nee AYC. Identification of Important Features for Machining Operations Sequence Generation. *International Journal of Production Research* 1997; 35: 2285-2307.
5. Lee H, Cho MW, Yoon GS, Choi JH. A Computer- Aided Inspection Planning System for on-Machine Measurement- Part I. *Global Inspection Planning. KSME International Journal* 2004; 18: 1349-1357.
6. Cho MW, Lee H, Yoon GS, Choi J. A Feature-Based Inspection Planning System for Coordinate Measuring Machines. *The International Journal of Advanced Manufacturing Technology* 2005; 26: 1078-1087.
7. Hopp T. CAD-Directed Inspection. *Annals of the CIRP* 1984; 33: 357-361.
8. ElMaraghy HA, Gu P. Expert System for Inspection Planning. *Annals of the CIRP* 1987; 36: 85-89.
9. ElMaraghy HA. Evolution and Future Perspectives of CAPP. *Annals of the CIRP* 1993; 42: 739-751.
10. ASME Y14.5 Geometrical product specifications (GPS) – General concepts -- Part 1: Model for geometrical specification and verification, Geneva, 2005.
11. ISO/TR 14638:1995 Geometrical product specification (GPS) – Masterplan, Geneva, 1995.
12. ISO 1101 Geometrical product specifications (GPS) – General concepts -- Part 1: Model for geometrical specification and verification, Geneva, 2005.
13. ISO/TS 17450-1:2005 Geometrical product specifications (GPS) – General concepts - - Part 1: Model for geometrical specification and verification, Geneva, 2005.
14. ISO/TS 17450-2:2002 Geometrical product specifications (GPS) – General concepts - - Part 2: Basic tenets, specifications, operators and uncertainties, Geneva, 2002.

15. ISO 14660-1:1999 Geometrical Product Specifications (GPS) – Geometrical features -- Part 1: General terms and definitions," Geneva, 1999.
16. ISO/IEC Guide 99:2007 International vocabulary of metrology - Basic and general concepts and associated terms (VIM), Geneva, 2007.
17. John A. Bosch. Coordinate Measuring Machines and Systems. Marcel Dekker Inc; 1995.
18. Concheri G, Cristofolini I, Meneghello R, Wolf G. Geometric Dimensioning and Tolerancing (GD&T) versus Geometrical Product Specification (GPS). XII ADM International Conference Grand Hotel, Rimini, Italy 2001.
19. ISO 14253-1:1998 Geometrical Product Specifications (GPS) -- Inspection by measurement of workpieces and measuring equipment -- Part 1: Decision rules for proving conformance or non-conformance, Geneva, 1998.
20. ISO/IEC Guide 98:1995 Guide to the expression of uncertainty in measurement (GUM), Geneva, 1995.
21. ISO 10360-1:2000 Geometrical Product Specifications (GPS) – Acceptance and reverification tests for coordinate measuring machines (CMM) -- Part 1: Vocabulary, Geneva, 2000.
22. ISO 10360-2:2001 Geometrical Product Specifications (GPS) – Acceptance and reverification tests for coordinate measuring machines (CMM) -- Part 2: CMMs used for measuring size, Geneva, 2001.
23. ISO 10360-3:2000 Geometrical Product Specifications (GPS) – Acceptance and reverification tests for coordinate measuring machines (CMM) -- Part 3: CMMs with the axis of a rotary table as the fourth axis, Geneva, 2000.
24. ISO 10360-4:2000 Geometrical Product Specifications (GPS) – Acceptance and reverification tests for coordinate measuring machines (CMM) -- Part 4: CMMs used in scanning measuring mode, Geneva, 2000.
25. ISO 10360-5:2000 Geometrical Product Specifications (GPS) – Acceptance and reverification tests for coordinate measuring machines (CMM) -- Part 5: CMMs using multiple-stylus probing systems, Geneva, 2000.
26. ISO 10360-6:2001 Geometrical Product Specifications (GPS) – Acceptance and reverification tests for coordinate measuring machines (CMM) -- Part 6: Estimation of errors in computing Gaussian associated features, Geneva, 2001.

27. ISO/CD 10360-7 Geometrical Product Specifications (GPS) -- Acceptance and reverification tests for coordinate measuring machines (CMM) -- Part 7: CMMs equipped with imaging probing systems, Geneva.
28. VDI/VDE 2617 Part 1 Accuracy of coordinate measuring machines; characteristics and their checking; generalities, Düsseldorf, 1986.
29. VDI/VDE 2617 Part 2.1 Accuracy of coordinate measuring machines - Parameters and their reverification - Code of practice for the application of DIN EN ISO 10360-2 for length measurement, Düsseldorf, 2005.
30. VDI/VDE 2617 Part 2.2 Accuracy of coordinate measuring machines - Parameters and their reverification - Form measurement, Düsseldorf, 2000.
31. VDI/VDE 2617 Part 2.3 Accuracy of coordinate measuring machines - Characteristics and checking of characteristics - Acceptance and reverification tests for coordinate measuring machines of large dimensions, Düsseldorf, 2006
32. VDI/VDE 2617 Part 3 Accuracy of coordinate measuring machines; characteristic parameters and their checking; components of measurement deviation of the machine, Düsseldorf, 1989.
33. VDI/VDE 2617 Part 4 Accuracy of coordinate measuring machines - Characteristics and their checking - Manual for the use of DIN EN ISO 10360-3 for coordinate measuring machines with additional axes of rotation, Düsseldorf, 2006
34. VDI/VDE 2617 Part 5 Accuracy of coordinate measuring machines - Characteristic parameters and their verification - Interim check with artefacts, Düsseldorf, 2001.
35. VDI/VDE 2617 Part 5.1 Accuracy of coordinate measuring machines - Parameters and their reverification - Interim check with ball plates, Düsseldorf, 2000.
36. VDI/VDE 2617 Part 6 Accuracy of coordinate measuring machines; characteristic parameters and their checking - Coordinate measuring machines with optical probes – Basics, Düsseldorf, 1997.
37. VDI/VDE 2617 Part 6.1 Accuracy of coordinate measuring machines - Characteristics and their testing - Coordinate measuring machines with optical probing - Code of practice for the application of DIN EN ISO 10360 to coordinate measuring machines with optical sensors for lateral resolution, Düsseldorf, 2007.
38. VDI/VDE 2617 Part 6.2 Accuracy of coordinate measuring machines - Characteristics and their testing - Guideline for the application of DIN EN ISO 10360 to coordinate measuring machines with optical distance sensors, Düsseldorf, 2005.

39. VDI/VDE 2617 Part 6.3 Accuracy of coordinate measuring machines - Characteristics and their testing - CMM with multiple probing systems, Düsseldorf, 2007.
40. VDI/VDE 2617 Part 7 Accuracy of coordinate measuring machines - Parameters and their checking - Estimation of measurement uncertainty of coordinate measuring machines by means of simulation, Düsseldorf, 2006.
41. VDI/VDE 2617 Part 8 Accuracy of coordinate measuring machines - Characteristics and their testing - Test suitability of measurements with coordinate measuring machines, Düsseldorf, 2006.
42. VDI/VDE 2617 Part 9 Accuracy of coordinate measuring machines - Characteristics and their reverification - Acceptance and reverification tests for articulated arm coordinate measuring machines, Düsseldorf, 2006.
43. ANSI/ASME B89.4.1-1997 Methods for Performance Evaluation of Coordinate Measuring Machines, New York, 1997.
44. ANSI/ASME B89.4.10-2000 Methods for Performance Evaluation of Coordinate Measuring System Software, New York, 2000.
45. ANSI/ASME B89.4.19-2006 Performance Evaluation of Laser-Based Spherical Coordinate Measurement Systems, New York, 2006.
46. ISO/IEC 17025:2005 General requirements for the competence of testing and calibration laboratories, Geneva, 2005.
47. Wilhelm RG, Hocken R, Schwenke H. Task specific uncertainty in coordinate measurement. *Ann CIRP* 2001; 52: 553–63.
48. Weckenmann A, Eitzert H, Garmer M, Weber H. Functionality-oriented evaluation and sampling strategy in coordinate metrology. *Precision Eng* 1995; 17: 244–52.
49. Lobato H, Ferri C, Faraway J, Orchard N. Uncertainty due to experimental conditions in co-ordinate measuring machines. *Proceedings of the Institution of Mechanical engineers, Part B: Journal of Engineering Manufacture* 2009; 223: 499-509.
50. Hoop T. The sensitivity of three point circle fitting. NISTIR 5501. National Institute of Standards and Technology, Gaithersburg, MD, 1994.
51. Phillips SD, Borchardt B, Estler WT, Buttrees J. The estimation of measurement uncertainty of small circular features measured by coordinate measuring machines. *Precision Eng* 1998; 22: 87–97.

52. Jiang Q, Feng H, Yang D, Desta M. A roundness evaluation algorithm with reduced fitting uncertainty of CMM measurement data. *Journal of Manufacturing Systems* 2006; 25: 184-195.
53. Chan F, King T, Stout K. The influence of sampling strategy on a circular feature in coordinate measurements. *Measurement* 1996; 19: 73-81.
54. ISO/TS 15530-3:2004 Geometrical Product Specifications (GPS) – Coordinate measuring machines (CMM): Technique for determining the uncertainty of measurement -- Part 3: Use of calibrated workpieces or standards, Geneva, 2004.
55. ISO/PRF TS 15530-1 Geometrical product specifications (GPS) -- Coordinate measuring machines (CMM): Technique for determining the uncertainty of measurement -- Part 1: Overview and metrological characteristics
56. ISO/CD TS 15530-2 Geometrical Product Specifications (GPS) – Coordinate measuring machines (CMM): Technique for determining the uncertainty of measurement -- Part 2: Use of multiple measurements strategies in calibration artefacts, Geneva.
57. ISO/TS 15530-4 Geometrical Product Specifications (GPS) – Coordinate measuring machines (CMM): Technique for determining the uncertainty of measurement -- Part 4: Evaluating task-specific measurement uncertainty using simulation, Geneva.
58. Feng C-X, Wang X. Subset selection in predictive modeling of CMM digitization uncertainty. *J Manuf Syst* 2002; 21: 419–439
59. Feng C-X, Pandey V. Experimental study of the effects of digitizing parameters on digitizing uncertainty with a CMM. *Int J Prod Res* 2002; 40: 683–97.
60. Piratelli-Filho A, Giacomo BD. CMM uncertainty analysis with factorial design. *Precision Eng* 2003; 27: 283–8.
61. Saal, T. Applying regression analysis to CMM measurement uncertainty study. MS project report, Bradley University, 61625 Peoria, IL, USA: Department of Industrial & Manufacturing Engineering & Technology; May 2003.
62. Barini E, Tosello G, De Chiffre L. Uncertainty analysis of point-by-point sampling complex surfaces using touch probe CMMs DOE for complex surfaces verification with CMM. *Precision Engineering* 2010; 34: 16–21
63. Lee G, Mou J, Shen Y. Sampling strategy design for dimensional measurement of geometric features using coordinate measuring machine. *International Journal of Machine Tools and Manufacture* 1997; 37: 917-934.
64. ISO/TS 14253-2:1999 Geometrical Product Specifications (GPS) – Inspection by measurement of workpieces and measuring equipment -- Part 2: Guide to the estimation

of uncertainty in GPS measurement, in calibration of measuring equipment and in product verification, Geneva, 1999.

65. ISO 14253-3:2011 Geometrical product specifications (GPS) -- Inspection by measurement of workpieces and measuring equipment -- Part 3: Guidelines for achieving agreements on measurement uncertainty statements 2011.

66. Fang C, Sung C. Measurement uncertainty analysis of CMM with ISO GUM. ASPE Annual meeting 2005.

67. Dhanish P, Mathew J. Effect of CMM point coordinate uncertainty on uncertainties in determination of circular features. *Measurement* 2006; 39: 522–531

68. ISO 5459:1981 Technical drawings -- Geometrical tolerancing -- Datums and datum-systems for geometrical tolerances

69. ISO/TS 16610-30:2009 Geometrical product specifications (GPS) -- Filtration -- Part 30: Robust profile filters: Basic concepts

70. ISO/TS 16610-31:2010 Geometrical product specifications (GPS) -- Filtration -- Part 31: Robust profile filters: Gaussian regression filters

71. Wilhelm R, Hocken R, Schwenke H. Task specific uncertainty in coordinate measurement. *Annals of the CIRP* 2001; 50: 553–563.

72. Miguela P, Kingb T, Abackerlia A. A review on methods for probe performance verification. *Measurement* 1998; 23: 15-33.

73. Sun A, Anand S, Tang J. Comprehensive design of experiments-based framework for optimal CMM inspection and uncertainty analysis of form tolerances. *International Journal of Production Research* 2002; 40: 2097– 2123.

74. Chang H, Lin T. Evaluation of circularity tolerance using Monte Carlo simulation for coordinate measuring machine, *International Journal of Production Research* 1991; 30: 2079–2086.

75. Starczak M, Jakubiec W. Optimisation Of Measuring Strategies in Coordinate Measuring Technique. *Measurement Science Review* 2001; 1: 191.

76. Roman D, Vicari G. Baseline Uncertainty in Geometric Tolerance Inspection by Coordinate Measuring Machines: the Case of Position Tolerance with Maximum Material Condition. ENBIS Second Annual Conference on Business and Industrial Statistics Rimini, Italy, September, 2002

77. Liu Q, Zhang C, Wang H. On the effects of CMM measurement error on form tolerance estimation. *Measurement* 2001; 31: 33–47.

78. Odayappan O, Raja J, Hocken R, Chen K. Sampling strategies for circles in coordinate measuring machines, in: Proceedings of the American Society of Precision Engineering, 1993; 70–72.
79. Dowling M, Griffin P, Tsui K, Zhou C. Statistical Issues in Geometric Feature Inspection Using Coordinate Measuring Machines. *Technometrics* 1997; 39: 3-17.
80. Draper NR, Smith H. Applied regression analysis. 3rd ed. New York: Wiley; 1998.
81. Montgomery D, Peck EA, Geoffrey Vining C. Introduction to linear regression analysis. 3rd ed. New York: Wiley; 2001.
82. Montgomery D. *Des Anal Exp*. 6th ed. New York: John Wiley & Sons; 2005.
83. Dean A, Voss D. *Design and Analysis of Experiments*. Springer; 2000.
84. Mathews P. *Design of Experiments with Minitab*. ASQ; 2005.
85. R Development Core Team. A Language and environment for statistical computing. R Foundation for Statistical Computing, Vienna, Austria. URL: www.r-project.org . 2008.
86. Kruth J, Van Gestel N, Bleys P, Welkenhuyzen F. Uncertainty Determination for CMMs by Monte Carlo Simulation Integrating Feature form Deviations. *Annals of CIRP* 2009; 58: 463–466.
87. Beaman J, Morse E. Experimental evaluation of software estimates of task specific measurement uncertainty for CMMs. *Precision Engineering* 2010; 34: 28–33.
88. Baldwin J, Summerhays K, Campbell D, Henke R. Application of Simulation Software to Coordinate Measurement Uncertainty Evaluations. *Measure* 2007; 2:40–52.
89. Trapet, E, Waldele F. The Virtual CMM Concept. In *Advanced Mathematical Tools in Metrology II*. World Scientific 1996; 238-247.
90. Phillips, S.D., et al. The Calculation of CMM Measurement Uncertainty via the Method of Simulation by Constraints. *Am. Soc. For Precision Engineering* 1997; 16: 443-446.
91. Haitjema H, Van Dorp B, Morel M, Schellekens P. Uncertainty estimation by the concept of virtual instruments. *Proc. SPIE 4401 Recent Developments in Traceable Dimensional Measurements*. 2001.

92. Balsamo A, Di Ciommo M, Mugno R, Rebaglia B, Ricci E, Grella R. Evaluation of CMM uncertainty through Monte Carlo simulations. *Annals of the CIRP*, 1999; 48: 425-428.
93. Trenk M, Franke M, Schwenke H. The “Virtual CMM” a software tool for uncertainty evaluation – practical application in an accredited calibration lab. Physikalisch-Technische Bundesanstalt, Department Coordinate Metrology, Braunschweig, Germany.
94. Schwenke H, Wäldele F. R&D Activities of PTB in the field of coordinate metrology. Physikalisch-Technische Bundesanstalt (PTB). *Simposio de Metrología* 2006.
95. Wilhelm R, Hocken R, Schwenke H. Task specific uncertainty in coordinate metrology. *Annals of CIRP*. 2001; 50: 553-563.
96. Van Dorp B, Haitjema H, Delbressine F, Bergmans R, Schellekens P. Virtual CMM using Monte Carlo methods based on frequency content of the error signal. *Proc. SPIE 4401 Recent Developments in Traceable Dimensional Measurements*. 2001.
97. Van Dorp B, Delbressine F, Haitjema H, Schellekens P. Calculation of measurement uncertainty for multi-dimensional machines, using the method of surrogate data. *Advanced Mathematical and Computational Tools in Metrology* 2001; 344-351.
98. Zhang G, Veale R, Charlton T, Borchardt B, Hocken R. Error compensation of coordinate measuring machines. *Annals of CIRP* 1985; 34: 445–448.
99. Barakat M. Kinematic and geometric error compensation of a coordinate measuring machine. *Spence International Journal of Machine Tools & Manufacture* 2000; 40: 833–850
100. Lim C, Burdekin M. Rapid volumetric calibration of coordinate measuring machines using a hole bar artefact. *Proceedings of the Institution of Mechanical Engineers, Part B: Journal of Engineering Manufacture* Augus 2002; 216: 1083-1093
101. Kunzmann H, Waldele F, Trapet E. Results of the international comparison of ball plate measurements in CIRP and WECC. *Ann. CIRP* 1995; 44: 479-482.
102. Trapet, E, Waldele F. Determination of the parametric errors of coordinate measuring machines and machine tools using reference objects. *VDI Berichte* 1989; 761: 175.
103. Wendt K, Schwenke H, Wäldele F, Krawczyk M. Error mapping of large CMMs by sequential multi-lateration using a laser tracker. *Kniel Physikalisch Technische Bundesanstalt (PTB), Germany*.

104. Hughes B, Wilson A, Peggs G. Design of a High-Accuracy CMM Based on Multi-Lateration Techniques. *Annals of the CIRP* 2000; 49: 391-394
105. Takatsuji T, et al. The first measurement of a three-dimensional coordinate by use of a laser tracking interferometer system based on trilateration. *Meas. Sci. Technol.* 1998; 9: 38-41
- 106 Takamasu K. Final Research Report International Standard Development of Virtual CMM (Coordinate Measuring Machine). NEDO International Joint Research Project. 2001.
107. Cox M, Harris P. Software specifications for uncertainty evaluation. NPL Report DEM-ES-010. 2006.
108. Forbes A. Harris P. Simulated Instruments and Uncertainty Estimation. NPL Report CMSC 01/00.
109. Pahk H, Burdekin M, Peggs G. Development of virtual coordinate measuring machines incorporating probe errors. *Proceedings of the Institution of Mechanical Engineers, Part B: Journal of Engineering Manufacture* 1998; 212: 533–548.
110. Hu Y, Yang Q. Development of A Novel Virtual Coordinate Measuring Machine. *International Instrumentation and Measurement Technology Conference Singapore.* 2009.
111. Phillips S, Borchardt B, Sawyer D, Estler W, Ward D, Eberhardt K, Levenson, M, McClain M, Melvin B, Hopp T, Shen Y. The Calculation of CMM Measurement Uncertainty via The Method of Simulation by Constraints. *Proceedings of the 12th Annual Meeting of the American Society for Precision Engineering, 1997.*
112. Ramu P, Yagiie J, Hocken R, Miller J. Development of a parametric model and virtual machine to estimate task specific measurement uncertainty for a five-axis multi-sensor coordinate measuring machine. *Precision Engineering* 2011; 35: 431–439.
113. Summerhays K, Henkea M, Brownb C, Richard P, Baldwin J. A Tool for Determining Task-Specific Measurement Uncertainties in GD&T Parameters Obtained from Coordinate Measuring Machines. MetroSage, LLC and Honeywell Inc. Federal Manufacturing and Technologies.
114. Volcano, CA, USA: Metrosage LLC.
<<http://www.metrosage.com//punditcmm.html>>
115. Hamburg-Piekar D, Donatelli G. A Hybrid approach to the uncertainty analysis of coordinate measurements. XVIII IMEKO World Congress Metrology for a Sustainable Development 2006, Rio de Janeiro, Brazil.

116. Barbato, G., Levi, R., Vicario, G., 2006, Method of Determining the Uncertainty of a Coordinate Measuring Machine, European Patent EP1836454.
117. Barini, E.M., 2008, Evaluation of CMM Measurement Uncertainty: Simulation and DoE Approaches, PhD Thesis, Politecnico di Torino.
118. Forbes A. Measurement uncertainty and optimized conformance assessment. *Measurement* 2006; 39: 808–814
119. Weckenmann A, Gebauer U. The impact of uncertainty of measurement on process control in micro- and nanotechnology. *Mikro- und Nanotechnologie 4th International Colloquium Berlin, Germany, 1997; 6: 141.*
120. Weckenmann A, Rinnagl M. Acceptance of processes: do we need decision rules? *Precision Engineering Journal of the International Societies for Precision Engineering and Nanotechnology* 2000; 24: 264–269.
121. Phillips S, Estler W, Levenson M, Eberhardt K. Calculation of measurement uncertainty using prior information. *J Res Natl Inst Stand Technol* 1998; 103: 625–32.
122. Goodhand M, Miller R. Compressor leading edge spikes: a new performance criterion. *Proceeding of ASME Turbo Exp, Power for Land Sea and Air. 2009.*
123. Bailey M. (GEAE). Integrated Multidisciplinary Design of High Performance Multistage Compressor Systems First Order Manufacturing Constraints & Requirements AGARD RTO Lecture Series No. 211
[http://ftp.rta.nato.int/public//PubFulltext/RTO/EN/RTO-EN-001///\\$EN-001-03.pdf](http://ftp.rta.nato.int/public//PubFulltext/RTO/EN/RTO-EN-001///$EN-001-03.pdf)
124. Lebele-Alawa B, Hart H, Ogaji S, Probert SD. Rotor-blades' profile influence on a gas-turbine's compressor effectiveness. *Appl Energy* 2008; 85:494–505.
125. Hamakhana I, Korakianitis T. Aerodynamic performance effects of leading-edge geometry in gas-turbine blades, *Applied Energy* 2010; 87: 1591–1601
126. Lamballais E, Silvestrin J, Laizet S. Direct numerical simulation of flow separation behind a rounded leading edge: Study of curvature effects. *International Journal of Heat and Fluid Flow* 2010; 31: 295–306.
127. <http://www.gom.com/>
128. <http://www.mitutoyo.com/pdf/Section-L-1001.pdf>
129. <http://www.zeiss.com.ar/c12568ef003df8fe/ContentsFrame/ccdab22f7c6280e8c12572b10051ca75>

130. <http://www.am-inc.com/MSES.shtml>
131. Coolidge J. A Treatise on Algebraic Plane Curves. D.o.v.e.r Publications 2004.
132. Mcleod R, Baart M. Geometry and interpolation of curves and surfaces. Cambridge University Press. Cambridge 1998.
133. Saltelli A, Ratto M, Andres T, Campolongo F. Global Sensitivity Analysis: The Primer. Wiley-Interscience 2008.
134. Press W, Teukolsky S, Vetterling W, Flannery B. Numerical Recipes in Fortran, The Art of Scientific Computing, Second Edition, Cambridge University Press. Cambridge Reprinted 1995.
135. Henrici P. Essential of Numerical Analysis. John Wiley & Sons, New York, 1982.
136. McKinley S, Levine M. Cubic Spline Interpolation.
<http://online.redwoods.cc.ca.us/instruct/darnold/laproj/Fall98/SkyMeg/Proj.PDF>.
138. www.Renishaw.co.uk
139. http://www.kern-microtechnic.com/page.php?page_id=54&lid=2
140. <http://www.zeiss.com/imt>
141. Otto S, Denier J. An introduction to programming and numerical methods in MATLAB. Springer 2005.